EPFL

Transient Electronics for Smart Biodegradable Medical Implants

I don't know where the limits are,
but I would like to go there.
— Eliud Kipchoge

A mes parents. . .

Acknowledgements

The PhD is a unique experience which is made of up and down times. Fortunately, in the end only the up times remain and these were possible only thanks to numerous people who helped me along this journey.

First of all, I would like to thank Prof. Jürgen Brugger for giving me the opportunity to work in the Microsystems Laboratory (LMIS1), for his advice and for supporting and trusting me all along my PhD. I also would like to thank Dr. Giovanni Boero for his scientific advice, relevant comments and intense discussions which enabled to keep me on the right track and to present this thesis today.

I am also grateful to Prof. Anja Skrivervik, Dr. Clémentine Boutry, Dr. Michel Despont and Dr. Danick Briand for accepting to review my work by being the members of my thesis jury. Special thanks go to Clémentine for the invaluable discussions we had half way through my thesis and for her help with the synthesis of PGS and POMaC.

Next, I would like to acknowledge my colleagues at LMIS1 for their help related to my work and for making this journey enjoyable by providing a great atmosphere in the office and in the lab. I would like to thank the current members, Ana, Ya, Xia, Nergiz, Thomas, Henry, Pierrick, Deeke, Reza, Mohammad, Jack, Zhiwei and Roberto, as well as the former members, Enrica, Yuliya, Marco, Mario, Valentin, Gabriele, Jongmoon, Xiaosheng, Alessandro and Chris. I am also very grateful to Séverine and Lucie for always taking care of the administrative matter and making my life as a PhD student much easier. Special thanks go to my office mates. Claudio for taking over the microfabrication and bringing new ideas over the last year of my thesis. I can leave knowing the project is in good hands. Dr. Samuel for his precious advice and your unwavering positive thinking. It was a pleasure working with you during these last 5 years. Lorenz for being a close friend in addition to an amazing colleague. Thank you for sharing memorable work and after-work times.

I am also very grateful to many colleagues from other groups at EPFL who helped me at different points in my thesis. Prof. Guillermo Villanueva, Kaitlin, Annalisa, Andrea and Tom from ANEMS for your scientific advice. Jonathan, Benoît and Arnaud B. from LMIS4 for the brainstorming, taking EDX images and your advice about COMSOL and chemistry. Maria, Alice, Sabrina, Lisa and Jacques from LP for helping me with the materials-related aspects of my thesis.

Acknowledgements

I also had the chance to work with highly motivated and skilled students who contributed to numerous aspects of my thesis. Thank you Remo, Tomas, Ruixi, Audrey, Paul, Gaspard and Lucas.

I am thankful to the medical doctors Dr. Brigitte Jolles-Haeberli, Dr. Marc-Etienne Corthésy, Dr. Thierry Buclin and Dr. Robert Gurny from CHUV, Clinique Bois-Cerf and HUG for helping me defining the specifications at the beginning of the project, and for allowing me to attend a knee arthroplasty in order to better understand the associated challenges.

I would like to warmly thank all the staff members from the the EPFL Center of Micronanotechnology (CMi), Philippe F., Cyrille, Philippe L., Georges-André, Julien, Niccolo, Joffrey, Rémy, Zdenek, Giancarlo, Jean-Marie, Guy, Giovanni, Miguel and Gatera. Without your advice and the great facilities you provide day after day I wouldn't have been able to develop the technology behind my thesis. In particular I would like to thank Didier and PAM for sharing coffees, discussions and your positive energy.

Besides working hard, doing sport also helped me changing my mind and getting rid of my frustration when nothing was working in the lab. Thank you to my lunch running friends Josué, David B., Guillaume, Marc, Colin, Arnaud G. and David F. for actually also sharing good scientific discussions while staying in good shape. I always came back to the office with less problems and more solutions. Thank you to my team mates from my triathlon team the Rushteam Ecublens and to my biking mates from Les Mardistes for helping me keeping a good balance between my work and my health.

I am also thankful to my friends Line, Daphné, Isabelle, Mélanie, Julie, Valentine, Flavien, Gaëtan, David R., Julien S, Kizito, Valentin, J-C, Daniel, Giulia, Flaminia for reminding me that social life is also important through apéros, weekends, holidays or simply relaxing moments. Special thanks go to Ludovic, Nicolas and Daniel for your friendship since the beginning of our studies in Microengineering and your help all along my thesis, and to Carine for her support and the good times we had sharing this experience together.

I want to thank Rachel for proofreading my thesis and for keeping me alive throughout the intense writing months in confinement. I cannot thank you enough for listening to me, supporting me and always finding the right words to lift me up.

Last but not least, I would like to thank my family. My parents, Patricia and Olivier, for supporting me all along my studies and my PhD and for giving me the love of learning and discovering new things since I was a kid. I also would like to thank my brothers, Julien and David, for proofreading my thesis, asking relevant questions and pointing out flaws in my manuscript. Thanks also for sharing good times and making me feel part of a great family.

Lausanne, May 20th 2020   Matthieu Rüegg

Abstract

Bioresorbable implantable medical devices show great potential for applications requiring medical care over well-defined periods of time. Such implants naturally degrade and resorb in the body, which eliminates adverse long-term effects or the need for a secondary surgery to extract the device. Since biodegradable materials are water-soluble, their fabrication requires special care and relies solely on dry processing steps without exposure to aqueous solutions. Another challenge is the in vivo powering of medical implants that are only constituted of biodegradable materials. The objective of this thesis is to develop a fully biodegradable drug delivery implant with multiple reservoirs for on-demand wireless drug delivery. Then to integrate and miniaturize all the components to reduce the volume of material used, whilst limiting the fabrication process complexity.

The design, fabrication and characterization of selectively addressable biodegradable magnesium microheaters is presented, together with the development of an innovative microfabrication process. It consists of four steps: physical vapor deposition, photolithography, ion beam etching and resist stripping. The microheaters consist of several spiral resonators. An electrical current is induced in a specific spiral resonator when coupling an external magnetic field at a matching frequency. Adding a meander to the resonator increases the current density locally and creates a hot-spot. Slightly varying the geometry of the devices enables the tuning of their resonance frequency and makes them selectively addressable. The frequency-selective wireless heating of different resonators is demonstrated in air and in liquid, plus enables the melting of the surrounding environment. Additionally, small geometrical variations by design induce large frequency shifts. As a result, several resonators with multiple resonance frequencies can be integrated in one device without much of an increase in diameter.

These microheaters are used as power receivers and triggering elements to selectively release drugs from multiple reservoirs in a wirelessly controlled drug delivery capsule. This prototype is made of non-biodegradable materials to demonstrate the feasibility of the concept. It consists of a 3D printed capsule with several reservoirs filled with drugs. Each reservoir is sealed with a polyimide membrane and a resonant gold microheater on top of it. These microheaters are used to thermally trigger the breaking of the membranes and release the drugs from the reservoirs. The powering and triggering mechanisms are combined into one element, minimizing the volume of material and maximizing the drug-to-implant volume ratio. The successful fabrication of leak-free capsules and the wireless release of liquid from

the reservoirs is demonstrated. This capsule is compatible with the drug requirements needed in the context of local analgesia after a knee arthroplasty. However, to have a clinical outcome, it should be fabricated from biodegradable materials to prevent a second surgery to extract the device.

Finally, to explore the development of a fully biodegradable version of the device, biodegradable microheaters are fabricated on biodegradable membranes by transfer printing. The capsules are then micro-molded from biodegradable elastomers.

Keywords: transient electronics, drug delivery systems, medical implants, biodegradable, wireless powering, microheater, spiral resonator, capsule, knee arthroplasty, pain management

Résumé

Les implants médicaux biodégradables montrent un grand potentiel pour les applications nécessitant un traitement pour une durée limitée. De tels implants se dégradent et sont éliminés naturellement par le corps, ce qui évite les effets à long terme et le besoin d'une deuxième opération pour extraire le dispositif. Etant donné que les matériaux biodégradables sont solubles dans l'eau, leur mise en œuvre nécessite des procédés de de fabrication spéciaux. Alimenter en énergie ces implants médicaux qui ne sont constitués que de matériaux biodégradables représente un autre défi. L'objectif de cette thèse est de développer un implant biodégradable capable de délivrer sur demande et de manière sans fil des médicaments en les relâchant depuis plusieurs réservoirs. Ceci en intégrant et miniaturisant au maximum tous les composants afin de réduire le volume de matière, tout en limitant la complexité des procédés de fabrication.

Le design, la fabrication et la caractérisation de micro corps de chauffe biodégradables en magnésium et contrôlables sélectivement sont présentés. Ces micro corps de chauffe sont constitués de résonateurs spiraux. Sous la présence d'un champ magnétique ayant une fréquence identique à celle d'un des résonateurs, un courant électrique est induit spécifiquement dans ce résonateur. En ajoutant un méandre au résonateur, la densité de courant augmente localement et crée un point chaud. En modifiant légèrement la géométrie des résonateurs, leur fréquence de résonance peut être ajustée, ce qui les rend sélectifs. L'échauffement des résonateurs de manière sans fil est démontré dans l'air et dans un liquide, et permet de faire fondre les matériaux à proximité. De plus, de petites variations géométriques induisent de grands changements de fréquence. Cet effet permet d'intégrer plusieurs résonateurs avec des fréquences différentes dans un seul dispositif, sans devoir fortement augmenter leur diamètre.

Ces dispositifs sont ensuite utilisés comme récepteurs d'énergie et éléments déclencheurs pour relâcher des médicaments depuis les réservoirs d'une capsule implantable. Le prototype développé ici n'est pas biodégradable car son but est de démontrer la faisabilité du concept. Il est constitué d'une capsule imprimée en 3D avec plusieurs réservoirs remplis de médicaments. Chaque réservoir est fermé au moyen d'une membrane en polyimide avec un micro corps de chauffe en or par-dessus. Ce dernier est utilisé pour induire la rupture de la membrane grâce à la chaleur dégagée, ce qui libère le médicament. Les mécanismes liés à la réception d'énergie et à l'actionnement du dispositif sont combinés en un seul système ce qui minimise le volume de matière et maximise le ratio entre le volume de médicament et de l'implant. La

Abstract

fabrication de capsules et leur activation de manière sans fil entrainant la libération de liquide sont démontrés avec succès. Le design des capsules est compatible avec les spécifications requises pour le traitement de la douleur après une arthroplastie du genou. Néanmoins, afin d'avoir un avenir clinique le système doit être fabriqué à base de matériaux biodégradables pour éviter de devoir l'extraire lors d'une deuxième opération.

Finalement, afin de développer une version du système entièrement biodégradable, des micro corps de chauffe biodégradables sont fabriqués sur des membranes biodégradables au moyen d'un procédé d'impression par transfert. Les capsules sont quant-à-elles micro-moulées à base d'élastomères biodégradables.

Mots-clés : électronique biodégradable, systèmes d'administration de médicaments, implants médicaux, biodégradable, transfert d'énergie sans fil, micro corps de chauffe, résonateur spiral, capsule, arthroplastie de genou, traitement de la douleur

Contents

List of Figures

List of Tables

List of abbreviations

- AFM: atomic force microscope

- Al: aluminum

- Ar: argon

- Au: gold

- C: carbon

- Ca: calcium

- CD: critical dimension

- Cl: chlorine

- Co: cobalt

- Cr: chromium

- Cu: copper

- CPS: coplanar stripline

- CPW: coplanar waveguide

- ddH_2O: double distilled water

- DDS: drug delivery system

- dECM: decellularized extracellular matrix

- EDX: energy-dispersive X-ray spectroscopy

- Fe: iron

- FEM: finite element method

- FGMRES: Flexible Generalized Minimum Residual

- Ge: germanium

- GUI: graphical user interface

- H: hydrogen

- H_2: hydrogen gas

- IBE: ion beam etching

- IMD: implantable medical device

- IR: infrared

- IPA: isopropyl alcohol

- IUPAC: International Union of Pure and Applied Chemistry

- MEMS: microelectromechanical system

- Mg: magnesium

- $MgCl_2$: magnesium chloride

- MgO: magnesium oxide

- $Mg(OH)_2$: magnesium hydroxide

- Mo: molybdenum

- MRI: magnetic resonance imaging

- N: nitrogen

- N_2: nitrogen gas

- NM: nanomembrane

- NRIC: near-field resonant inductive coupling

- O: oxygen

- OM: optical microscope

- PBS: phosphate-buffered saline

- PCL: polycaprolactone

- PDMS: polydimethylsiloxane

- PDO: polydioxanone

- PGA: poly(glycolic acid)

- PGS: poly(glycerol sebacate)

- PI: polyimide

- PKR: partial knee replacement

- PLA: poly(lactic acid)

- PLGA: poly(lactic-co-glycolic acid)

- PMMA: poly(methyl methacrylate)

- POC: poly(1,8-octanediol-co-citrate)

- POMaC: poly(octamethylene maleate (anhydride) citrate)

- PPy: polypyrole

- PR: photoresist

- PVDF: polyvinylidene fluoride

- QUCS: Quite Universal Circuit Simulator

- RF: radio-frequency

- RMS: root mean square

- Si: silicon

- Si_3N_4: silicon nitride

- SiO_2: silicon dioxide

- $Si(OH)_4$: orthosilicic acid

- SAR: specific absorption rate

- SEM: scanning electron microscope

- SR: spiral resonator

- SOG: spin-on-glass

- TBC: transition boundary condition

- TKR: total knee replacement

- Tg: glass transition temperature

- UV: ultraviolet

- W: tungsten

List of Tables

- WPT: wireless power transfer

- Zn: zinc

1 Introduction

Disclaimer: This chapter (1) is adapted from the following article with permissions of all co-authors and journal:

M. Rüegg, R. Blum, G. Boero and J. Brugger, "Biodegradable Frequency-Selective Magnesium Radio-Frequency Microresonators for Transient Biomedical Implants", *Advanced Functional Materials*, 2019, 29, 1903051.

My contribution: conceptualization, modeling, design, fabrication, experiments, figures and writing.

The purpose of this introduction is to define the problems to be addressed and the challenges behind the aims of this thesis. First, the use of implantable devices in medicine is introduced, with a specific focus on drug delivery systems, followed by the advantages and challenges of biodegradable electronics and medical devices. Finally, wireless power transfer strategies for implantable bioelectronics are also discussed.

1.1 Implantable medical devices in medicine

In recent years, thanks to a combination of scientific advances and to the development of new types of medical devices, medicine has evolved to become more personalized, precise, preventive and less invasive. Minimally-invasive angioplasty and the use of surgical robots decrease the recovery time and the risks associated with surgeries, and wearable devices enable the personalized monitoring of a patient's physiological information over a long period of time. Additionally, the use of implantable medical devices (IMDs) provides effective solutions for some clinical challenges thanks to the proximity between the implant and the targeted organ or medical condition to diagnose or treat.

IMDs can be divided in two main categories: passive and active, as illustrated in Figure 1.1. Energy is the main difference between those categories: active devices require energy from an internal or external source, whereas passive devices require none. Among passive devices, physical supports are required for reconstructive surgeries on body parts such as the nose, jaw and chest. Orthopedic implants are used to fix or repair broken or damaged bones and joints, following an injury or aging. These include simple devices such as fixation plates and screws, as well as more complex systems such as prosthesis for total joint replacement. For mechanical purposes, these implants are typically made of stainless steel or titanium alloys. [1] Another type of passive implant is surgical mesh used to mechanically fix an organ after a surgery. In order to avoid a mechanical mismatch with the soft surrounding tissues, polymeric meshes made of polypropylene or polyvinylidene fluoride (PVDF) are used. Finally, vascular stents are also widely used as passive IMDs in order to avoid re-stenosis of blood vessels and these can be made of polymeric materials or metals.

On the other hand, active devices include electronic components in order to perform advanced functions such as electrophysiological sensing or stimulation for neural and cardiac applications. Among neural implants, deep brain stimulation implants are used in the treatment of Parkinson's disease and depression, while cochlear implants enable the restoration of hearing capabilities for some patients with auditory disorders. For cardiac treatments, implantable defibrillators and pacemakers are used for heart diseases such as arrhythmia or myocardial infarction. Such systems are able to analyze electrical signals from the heart and to react accordingly using a closed-loop feedback regulation. In order to protect the sensitive electronics from the corrosive environment in the body, these systems are packaged in titanium and silicone housing. Finally, another type of active medical implants are those used for drug delivery, including insulin and intrathecal pumps to treat patients with diabetes and chronic pain. In such cases, pumps are implanted subcutaneously in the abdomen and deliver the drug to a specific site through a catheter. The drug release can be controlled wirelessly by a user interface and the system can be easily re-filled by injecting a large amount of drug in the reservoir of the pump. Such implantable pumps enable not only a reduction in the number of injections for the patient, but also improve the therapeutic effect by delivering the drug locally with a catheter. As a result, lower drug doses are required and the systemic effect of the drug over the whole body is limited.
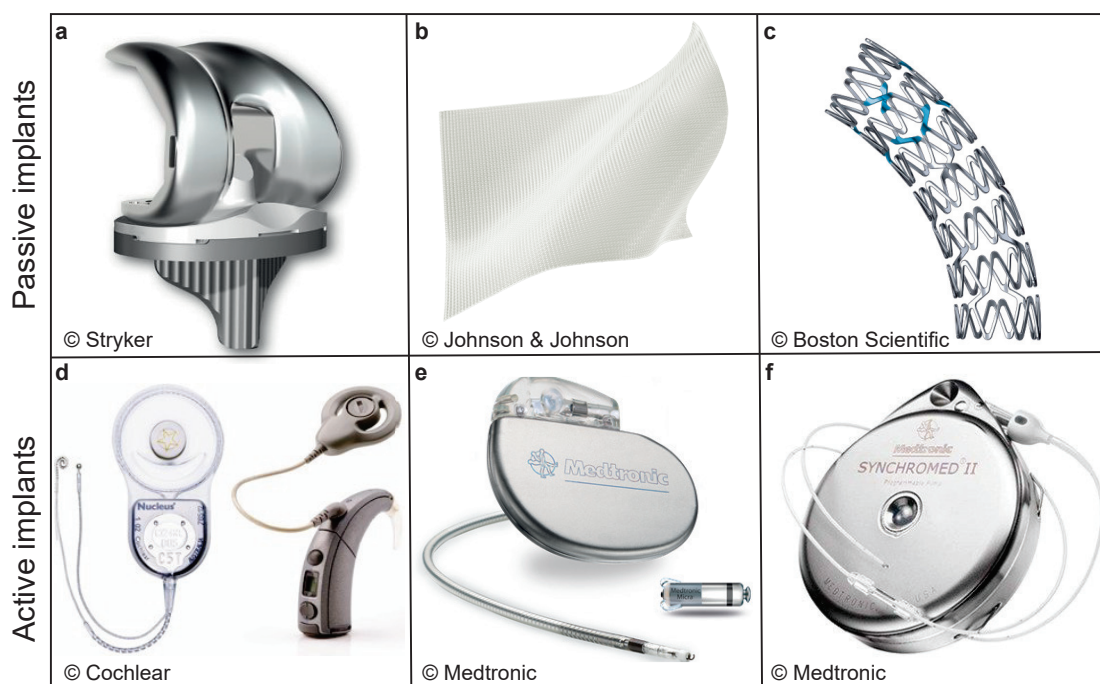
Figure 1.1 – **Examples of implantable medical devices. a**, Triathlon® total knee prosthesis from Stryker. **b**, PROLENE® polypropylene surgical mesh from Johnson and Johnson. **c**, REBEL™ platinum chromium coronary stent from Boston Scientific. **d**, Nucleus cochlear implant from Cochlear consisting of an implantable receiver and electrode array (left) and an external sound processing unit and emitter (right). **e**, Standard (left) and lead-free miniaturized Micra (right) pacemakers from Medtronic. **f**, SynchroMed II intrathecal pump from Medtronic.

1.1.1 Drug delivery systems

Currently, the two most common methods of drug administration are oral pills and injections however both suffer from several limitations. Firstly, in both cases, the entire body is exposed to the drug, causing systemic toxicity to healthy tissues. Furthermore, the drug has to travel through several physical barriers such as the stomach and the blood brain barriers before reaching the targeted location. Consequently, the administration of large molecules is difficult and the bioavailability of the drug is limited, which requires the intake of larger drug doses. Repeated injections are also painful and invasive for the patients and expose them to a high bolus level of drug just after the administration, as shown in Figure 1.2a. Finally, none of these two techniques enable advanced therapeutic needs such as controlled and sustained release or targeted delivery.

To overcome these limitations, drug delivery systems (DDS) are being developed. DDS are defined as technologies able to address the challenges associated with the rapid development in novel pharmaceutical compounds, by improving their specificity, localizing their effect and controlling their release. [2–4] Several types of DDS exist, including antibody-drug conjugates, micro- and nanoparticles, transdermal patches, inhalers, oral drug delivery systems and

drug delivery implants. [5] As depicted in Figure 1.2, each of these systems achieve different pharmacokinetics to keep the drug level within the therapeutic window. The therapeutic window is defined as the drug concentration in blood, plasma or tissue, at which the drug is efficient. At lower levels, the drug is less efficient than it should be, and at higher levels, the drug shows side-effects and toxicity for the patient.
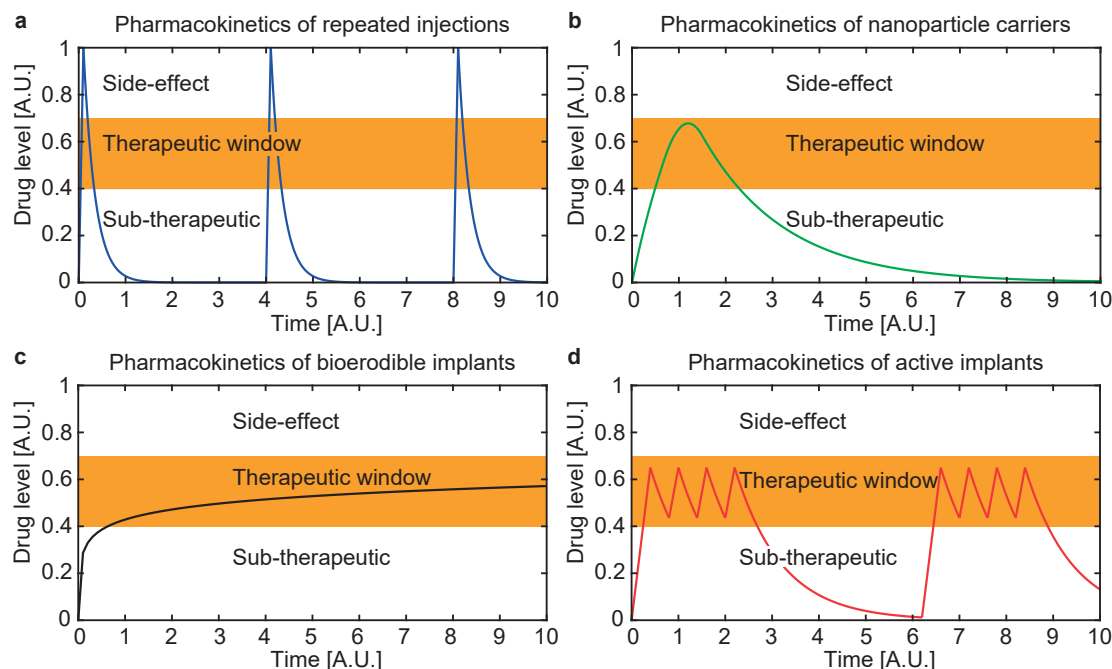
Figure 1.2 – **Pharmacokinetics of drug delivery systems.** Typical pharmacokinetics behavior of various administration ways, including injections (**a**), nanoparticle carriers (**b**), bioerodible implants (**c**) and active implants (**d**)

In comparison to other types of drug delivery systems, drug delivery implants can achieve the most advanced functionalities and pharmacokinetics. Similar to general IMDs, drug delivery implants are divided between passive and active devices. While the drug release from passive devices can be triggered by natural stimulus such as temperature, [6, 7] pH, [8] or polymer degradation, [9–11] the drug release from active devices can be triggered by external stimuli such as a magnetic field, [12–14] electric field, [15–17] electrochemical reaction, [18–20] electrothermal heating, [21–25] light, [26–29] or ultrasound. [30–32]

Passive devices do not require the use of active circuit elements and are thus generally simpler systems than active devices. However, they lack the ability to provide the patient or the clinician an external control on the release kinetics of the drug. On the other hand, active devices can be wirelessly controlled after the implantation in order to achieve precise controlled drug delivery over time as well as data telemetry. Thanks to the recent developments in microelectromechanical systems (MEMS) technology, several types of drug delivery systems including microneedles, [33–35] microchips, [18, 23, 36, 37] microvalves, [16, 17, 19, 38] and micropumps were developed. [39–43]

One of the first active drug delivery implants ever developed was unquestionably the microchip system originating from Robert Langer's lab in 1999 and shown in Figure 1.3a. [18] This device consists of several reservoirs fabricated in a silicon wafer and closed with a thin gold membrane. The release of the drug from the reservoirs is triggered by the electrochemical dissolution of the gold membranes when an electrical potential is applied between the membranes and a reference electrode.
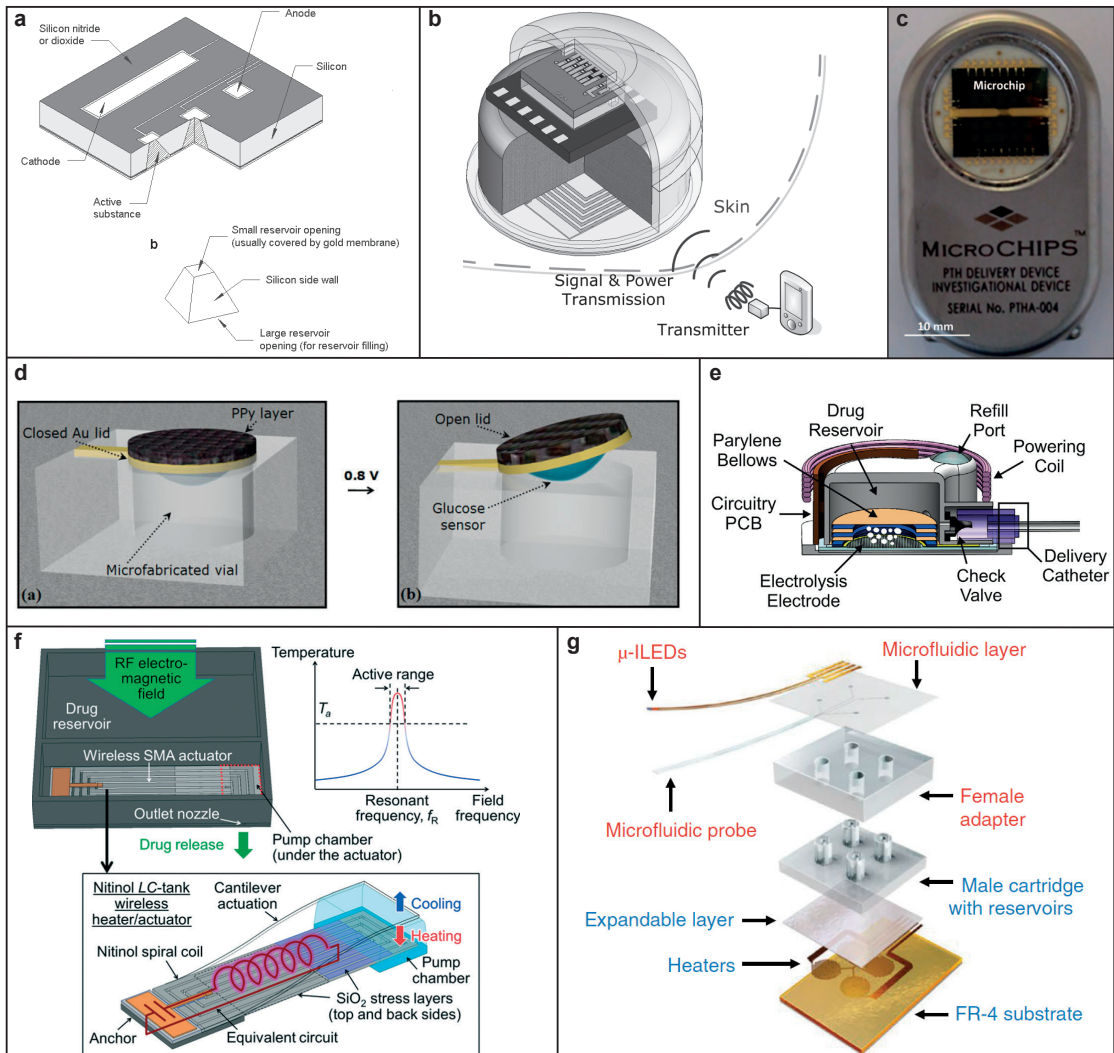
Figure 1.3 – **Implantable active drug delivery systems. a**, Original microchip drug delivery system based on the electrochemical dissolution of gold membranes to release the drug. [18] **b, c**, Fully functional microchip drug delivery systems. [23,37] **d**, Microvalve based on polypyrrole, an electroactive polymer, for a combined glucose sensing and drug delivery system. [19] **e,f,g**, Drug delivery micropumps based on water electrolysis (**e**, [42]), shape memory alloys (**f**, [40]), and thermally expendable layers **g**, [44]).

The development of this microchip technology has then been pursued by Langer's group as well as by Anthony Walton's and Shey-Shi Lu's groups and led to fully functional drug delivery devices with up to 100 reservoirs shown in Figure 1.3b and 1.3c. [23, 37] The overall design didn't change much from the original device but the triggering principle changed from the electrochemical to the electrothermal dissolution of the gold membrane to release the drug. These devices are single-use and need to be extracted from the body once empty. Their commercialization was further investigated under the company Microchips Biotech and bought by Daré Bioscience in 2019.

Among other more complex drug delivery systems, Marc Madou's group developed a combined glucose sensing and drug delivery system based on a polypyrrole microvalve (Figure 1.3d, [19]). Polypyrrole, an electroactive polymer, changes it's volume under small bias voltages. Several implantable micropumps for drug delivery based on different thermal actuation principles were also investigated. Ellis Meng's group developed pumps based on the deformation of a Parylene membrane resulting from the creation of hydrogen bubbles by water electrolysis between two electrodes (Figure 1.3e, [42]). Kenichi Takahata's group developed several valve and pump systems based on the shrinkage of thermosensitive hydrogels, and the thermal deformation of shape memory alloys (Figure 1.3f, [40]). Finally, John Roger's and Jae-Woong Jeong's groups developed optofluidic microsystems based on the expansion of a thermally expandable layer which show great potential for neuropharmacology and optogenetic stimulation (Figure 1.3g, [44]). Extensive recent reviews of MEMS based drug delivery devices can be found in [4] and [3].

1.2 Biodegradable electronics and medical devices

Although implantable medical devices and drug delivery systems undoubtedly bring advantages in terms of bio-sensing accuracy and therapeutic efficacy, they also suffer from some limitations. Two of the main challenges related to implantable medical devices are the powering of the system inside of the body, as well as the extraction of the system once it's function has been achieved or after the device failure. One way to overcome the extraction problem is to use biodegradable systems which naturally resorbs from the body.

Before entering into the details of biodegradable implantable medical devices, their advantages and limitations, it is worth first defining what is biocompatibility, biodegradabliliy, and bioresorbability. According to the International Union of Pure and Applied Chemistry (IUPAC), biocompatibility is defined as the ability to be in contact with a living system without causing any adverse biological effect. [1] When a foreign body is implanted into a living host, a host response consisting of three overlapping stages of inflammation, proliferation and tissue remodeling naturally occurs. [45]

The specific pathways and the intensity of this response, and thus the level of biocompatibility of the foreign implanted body, strongly depends on some implant- and host-related factors. On the host side, the implantation site and the degree of injury during the implantation are important parameters. On the implant side, the composition, geometry, mechanical properties, topography and porosity are modulating the host response. Porous, smooth and soft implants usually show better biocompatibility. Biocompatible materials can be bioinert such as titanium, or on the contrary biodegradable if they show some gradual breakdown mediated by specific biological activity in vivo. Furthermore, a material is considered to be bioadsorbable or bioresorbable if the degradation products are metabolized or eliminated by the organism through natural pathways.

Finally, transient is used in the field of biodegradable electronics to describe a system which achieves a function over a defined amount of time and then naturally decomposes to be eliminated. In the framework of this thesis, the words biodegradable, bioresorbable, bioadsorbable and transient are used interchangeably with the meaning of describing a system which naturally degrades and resorbs in vivo.

Materials used to develop biodegradable implantable medical devices can be classified into five categories which are metals, semiconductors, dielectrics, natural and synthetic polymers. The exact degradation pathways as well as specific material examples for each of these categories are discussed in Section 2.1.1 but the degradation is mainly based on hydrolysis and enzymatic action. Additionally, the degradation products are important factors in the host response and thus in the biocompatibility of biodegradable implantable devices. It is not only the nature of the degradation products but also their amount over time which dynamically modulates the host response. High local concentration of some degradation products such as lactic acid or hydrogen might cause toxicity although they are safe at lower concentrations. Properly setting the degradation rate of the device enables the concentration of the degrada-

tion products to be kept below the tolerance limits of the body. [46, 47] Finally, the hydrolytic degradation of biodegradable materials implies the use of special fabrication processes which minimize their exposure to aqueous media to produce biodegradable electronics and devices. Specific microfabrication processes used to produce biodegradable electronics are discussed in more details in Section 2.1.2.

Among implantable medical devices discussed in Section 1.1, it is obvious that some of them such as cardiac pacemakers and cochlear implants, need to persist in time and should not degrade once implanted in the body. However, there are medical conditions which require implantable devices to work only over well-defined periods of time. These include various applications such as monitoring, stimulating, and treating central and peripheral nervous systems after a surgery or a traumatic injury. [48–53] Plus, localized drug delivery for wound healing or following a surgical procedure, [54, 55] as well as pressure and strain monitoring on tendons and blood vessels during rehabilitation after surgical repair. [56, 57] For such usage, transient medical devices which resorb after some time are beneficial. Once its aim is achieved, a biodegradable implant naturally degrades and is eliminated by the body, thus avoiding adverse long-term effects or the need for a second surgery for its removal. [50, 58–62] As detailed in Section 2.1.1, the degradation time varies between minutes and months depending on the types of materials used.

The list of biodegradable IMDs and electronics is large and has been covered by multiple reviews in the recent years. [1, 58, 63–65] The first main breakthrough in term of transient electronics originated in John Roger's lab in 2012. This device consisted of several biodegradable electronic components, sensors, actuators, power supply systems and wireless control strategies made of biodegradable materials on a biodegradable silk substrate as shown in Figure 1.4a. In the following years, many biodegradable sensors and devices were developed based on this technology for various kind of applications.

Hereafter, the most representative examples of biodegradable drug delivery systems with active electronic components are detailed. Passive biodegradable drug delivery systems such as Zoladex® or Gliadel® implants are not within the scope of this thesis. Figure 1.4b shows a device based on the increased diffusion of drug out of a silk layer when the device is heated using a magnesium (Mg) microheater developed in Roger's and Fiorenzo Omenetto's groups. The device is used to release ampicilin into growth media containing *S. aureus* and *Escherichia coli*. Similarly, Figure 1.4c from Ali Khademhosseini's group shows a biodegradable patch made of electrospun poly(glycerol sebacate)-polycaprolactone (PGS-PCL) fibers loaded with antibiotics. The drug release is triggered by heating the patch with a zinc (Zn) heater to increase the diffusion of the drug out of the nanofribrous sheet. The device performance is tested by releasing ceftriaxone against *Escherichia coli* and cefazoline against *S. areus* cultures.
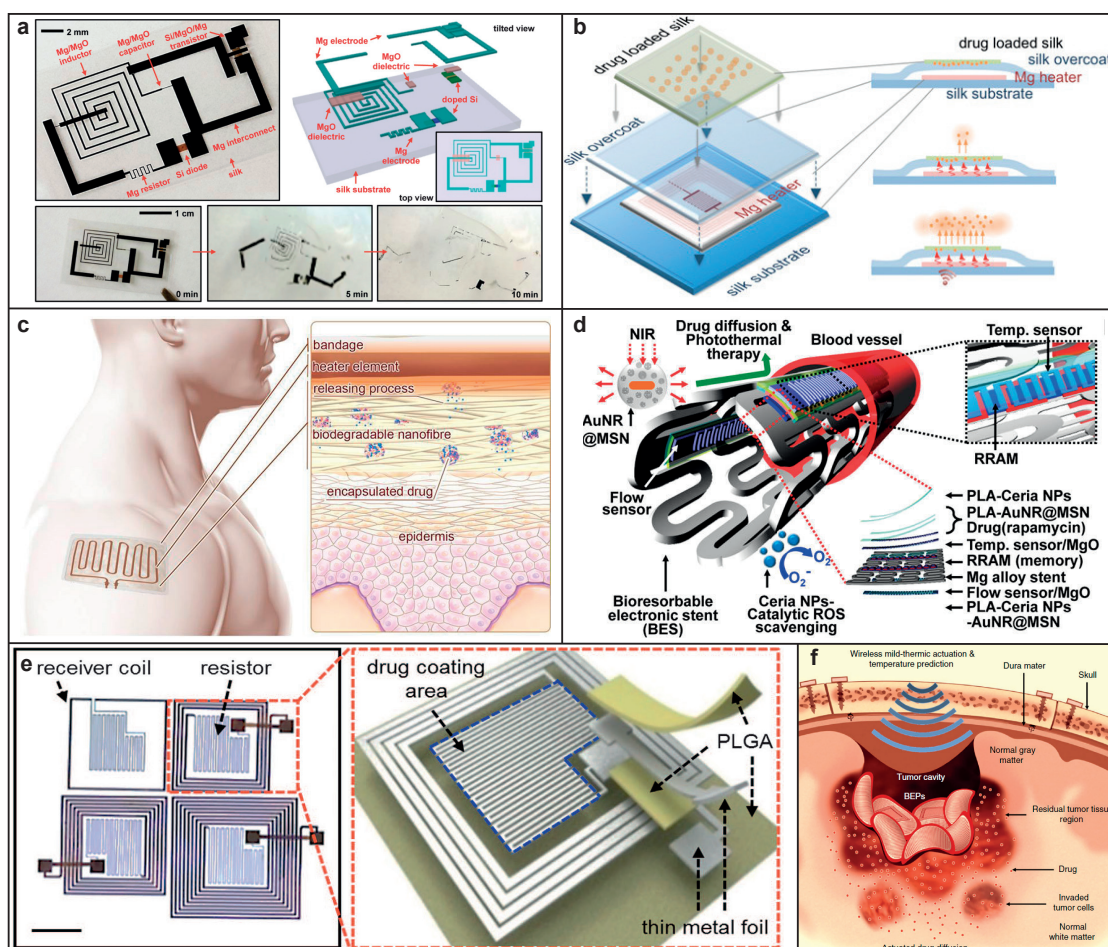
Figure 1.4 – **Biodegradable active drug delivery implants. a**, First transient electronics device consisting of electronic components, sensors, actuators, power supply systems and wireless control strategies. [59] **b**, **c**, Biodegradable drug delivery system based on the increased diffusion of drug out of thermally actuated polymeric materials. [54, 55] **d**, Bioresorbable electronic stent including multiple functionalities such as flow sensing, temperature monitoring, data storage, wireless power/data transmission, inflammation suppression, localized drug delivery and hyperthermia therapy. [28] **e**, Biodegradable DDS with the ability to selectively release drug from different areas by tuning the frequency at which the energy is wirelessly transferred to the device. [66] **f**, Bioresorbable electronic patches with heating and temperature sensing capabilities for the release of doxorubicin to brain tumors. [67]

Figure 1.4d shows a bioresorbable electronic stent including multiple functionalities such as flow sensing, temperature monitoring, data storage, wireless power/data transmission, inflammation suppression, localized drug delivery and hyperthermia therapy. The device developed in Dae-Hyeong Kim's group releases drugs from drug-loaded gold nanoparticles under infrared (IR) irradiation.

Finally, Figure 1.4e shows another drug delivery device from Roger's group based on the diffusion of parathyroid hormone (1-34) and doxorubicin through thermally actuated lipid membranes. The electronics is made of molybdenum (Mo) on a poly(lactic-co-glycolic acid) (PLGA) substrate and the specificity of the device is its ability to selectively release drugs from different areas by tuning the frequency at which the energy is wirelessly transferred to the device. Figure 1.4f demonstrates another more recent biodegradable DDS from Kim's group which releases doxorubicin from oxidized starch bioresorbable electronic patches with heating and temperature sensing capabilities. For this device the heating element is based on eddy currents in a Mg layer encapsulated with a poly(lactic acid) (PLA) layer. Despite the fact that all these devices show great potential and are promising candidates for several applications, the lack of performance prevents their use in clinical settings yet. [4, 45]

1.3 Wireless power transfer strategies

The second key challenge associated with active implantable medical devices is powering and communicating with the device in the body. One solution is to power the system using a battery and to remotely control it using a wireless communication system. [24, 37, 44] Additionally, other solutions exist which do not require the use of a battery, where the energy is directly harvested in vivo [68] or wirelessly transferred through near-field inductive, [36, 66, 69–71] near-field capacitive, [72] mid-field [73, 74] and far-field electromagnetic coupling, [75] ultrasounds, [76] and light. [26–28] Wired trans-cutaneous powering is also possible but shows a higher risk of infection.

A further challenge is the powering of medical implants that only consist of biodegradable materials. Some of the proposed mechanisms to power these types of implants include biodegradable energy harvesters, supercapacitor, batteries and photovoltaic cells. [77–87] In all of these examples, additional volume and mass are added to the device. In the case of photovoltaic cells, power is only efficiently generated closely underneath the skin surface. As for non-biodegradable IMDs, near-field resonant inductive coupling (NRIC) is a good and widely used alternative to power biodegradable implantable devices. A radio-frequency (RF) magnetic field carries the energy to the implant location in the body and a resonant RLC circuit is used as an energy receiver on the implanted device. [48, 50, 55, 57, 59, 88, 89]

In comparison to batteries and solar cells, this approach reduces the amount of material implanted in the body and integrates the power supply and the wireless control of the implant into one system. Using resonant circuits also adds another relevant dimension to the control, as the system becomes frequency-selective. When implementing multiple resonators with distinct resonance frequencies in one or several implants, each RLC circuit can be selectively addressed by matching the frequency of the external excitation magnetic field to that of the resonator of interest. Selective drug delivery or differentiating drug delivery and optical stimulation in an implantable optofluidic system were demonstrated using this technique. [66, 75]

The optimal choice of the wireless power transfer (WPT) method depends on several parameters such as the device size, the transmission frequency, the WPT range and the type of medium. [90, 91] Ultrasound propagation highly depends on the coupling between the transducer and the skin as well as on the type of tissue. The acoustic impedance of bones for instance is so high that all the ultrasound wave energy is reflected back. [91] Capacitive coupling is limited by the distance at which the power can be delivered and is restricted to subcutaneous applications only. [91] Radiative power transfer is limited by the ability to design efficient small antennas in the centimetre size range to be used in implantable devices, which becomes feasible only in the GHz range. However, at these frequencies, the absorption in the biological tissues becomes important. The penetration depth is defined as the distance at which the power is 0.135 of its surface value. At 1 GHz for example, it is about 3 cm in muscle tissue. [92] At 10 GHz, it is only 0.27 cm.

Despite recent progresses in the design of small antennas for implantable and wearable applications, [93] inductive coupling remains currently the most common WPT technique. With inductive coupling, a near-field magnetic field is used to couple the energy from a primary coil into a secondary coil. A typical inductive coupling link schematic is shown in Figure 1.5.
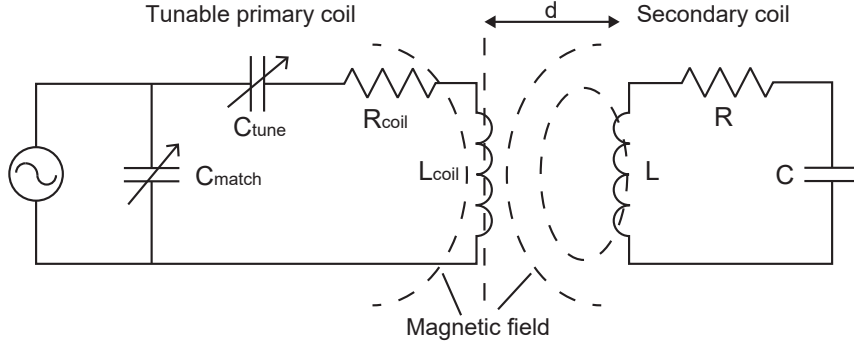
Figure 1.5 – **Inductive coupling link schematic.** The inductive coupling link consists of a primary excitation coil and a secondary receiving coil. The primary coil can be tuned and matched to a specific frequency and impedance using variable capacitors.

Multiple implantable devices powered by NRIC at various frequencies from 10 kHz to hundreds of MHz exist. [16, 57] The choice of the operating frequency at which the power is transmitted from the primary coil to the secondary coil is depending on several parameters. Faraday's law of induction is described in Equation 1.1, with ϵ the electromotive force, Σ a surface bounded by the closed contour $\partial\Sigma$, $\vec{E}$ the electric field, $\vec{B}$ the magnetic flux density, t the time, $d\vec{l}$ an infinitesimal vector element of the contour $\partial\Sigma$, and $d\vec{A}$ an infinitesimal vector element of surface Σ.

$$\epsilon = \oint_{\partial\Sigma} \vec{E} \cdot d\vec{l} = -\int_{\Sigma} \frac{\partial \vec{B}}{\partial t} \cdot d\vec{A} \qquad [V] \tag{1.1}$$

It appears clearly from Equation 1.1 that the electromotive force is proportional to the frequency of the magnetic field, the intensity of the magnetic field and the area of the secondary coil. Thus, high values of these parameters should be used to maximize the efficiency of the inductive link. However, there are other considerations which limit their upper value. A first effect is the increase of the primary and secondary coils electrical resistance with the frequency, due to the skin effect. An increase of the primary coil resistance induces a decrease of the magnetic field intensity which is directly proportional to the current in the primary coil. An increase of the secondary coil resistance decreases the induced electrical current for a given value of the electromotive force.

Additionally, tissue losses also increase with frequency. [94] At 1 GHz, the wavelength is around 30 cm in air and 4 cm in muscles. This means that up to low GHz frequencies and with separation distances between the primary and secondary coils of millimeters to a few centimeters, only near-field electromagnetic fields need to be considered. In the near-field region, tissue losses are due to conduction and displacement currents resulting from the

induced electric field created by the time-variant magnetic field. Below 10 MHz, these currents are too low to disturb the source magnetic field and thus losses can be neglected. [90] At higher frequencies, losses should be considered and can be computed by finite element method (FEM). The spatial distribution of the source magnetic field should be optimized to minimize the electric field and thus the losses.

Regarding the intensity of the magnetic field, its maximal value is specified by health and safety regulations which limit the induced current density and the power dissipated in the human body. At frequencies below 100 kHz, electrical current can have direct physiological effects such as muscle and nerve stimulation. At frequencies above 100 kHz however, direct physiological effects are negligible and only thermal effects due to tissue losses must be considered. [90]

The specific absorption rate (SAR) is defined to limit the temperature increase in the tissue to less than 1°C to prevent physiological damage. [92] Limits of 0.4 W/kg over the whole body, 10 W/kg localized over the head or the trunk and 20 W/kg localized over the limbs are applicable for continuous exposure at frequencies from 100 kHz to 10 GHz. In terms of magnetic field, a 0.4 W/kg exposition level is equivalent to 0.2 to 0.45 µT fields between 10 MHz and 2 GHz. [95] For short pulse exposure, higher magnetic field values can be applied without exceeding the SAR values. For example, in magnetic resonance imaging (MRI) scanners, maximum RF magnetic fields of 100 µT for a pulse duration of about 1 ms and repetition rates of about 100 ms are commonly used. [96]

Finally, dimensional considerations also limit the operating frequency range as well as the area of the secondary coil, as the final purpose of the implantable system imposes a restriction on the size of the device. Often, the working frequency range is strongly affected by the device dimensions and is not a free design choice. Generally, miniaturization of implantable systems implies a smaller secondary coil area and higher working frequencies, and thus more tissue losses. Another problem when working at frequencies above 1 GHz is the ability to design primary coils in the centimetre size range at these frequencies. If the primary coil has to be miniaturized in order to achieve high enough frequencies, then the decay of the magnetic field intensity also becomes more important.

To conclude, it is also important to keep in mind that all the parameters discussed above regarding the efficiency of WPT for implantable devices relate to an optimum configuration. In reality, the efficiency of NRIC links is further limited by additional factors such as the misalignment between the primary and secondary coils and the detuning of the resonance frequency due to the surrounding environment or to the implant deformation.

1.4   Aims and outline of this work

General objective   The overall objective of this thesis is to work towards the development a fully biodegradable drug delivery implant with multiple reservoirs for on-demand wireless drug delivery. The goal is to further integrate and miniaturize all the components to minimize the volume of material used, while limiting the fabrication process complexity. A new fabrication process was therefore developed to produce frequency-selective biodegradable microheaters. These microheaters were then used in a first time as power receivers and triggering elements in a non-biodegradable drug delivery capsule to selectively release drugs from multiple reservoirs. Finally the technology was further developed to produce a fully biodegradable version of the drug delivery capsule.

Aims   This work is subdivided into several aims in order to achieve the final objective:

- Design frequency-selective microresonators, to be used as power receivers and microheaters in implantable medical devices.

- Develop a water-free microfabrication process to fabricate the microresonators out of biodegradable materials.

- Demonstrate the heating and degradation capabilities of the frequency-selective microheaters.

- Design a wirelessly controlled multi-reservoir drug delivery system using the developed microheaters as power receivers and triggering elements for the drug release.

- Demonstrate the wireless selective release from different reservoirs of the developed drug delivery system.

- Develop a microfabrication process to fabricate biodegradable resonators on biodegradable membranes contributing to the development of a fully biodegradable version of the drug delivery system.

Outline   This thesis is divided into five chapters:

1. Introduction to implantable medical devices, drug delivery systems, biodegradable electronics and wireless power transfer schemes for implantable medical devices.

2. Design and fabrication of Mg wireless microheaters with a robust process based on ion beam etching (IBE), in view of a versatile approach for implantable transient electronics. This new and innovative fabrication process reduces the devices exposure to aqueous media without the need to fabricate and use fragile stencils. The fabrication consists of four main steps including a) the deposition of a Mg thin film by thermal evaporation,

b) pattern definition by photolithography, c) pattern transfer into the Mg film by ion beam etching and d) resist stripping with oxygen plasma and acetone. The wireless microheaters shapes are designed in order to be able to produce the devices by a single iteration of the aforementioned process. Slightly varying the geometry of the devices in the design process enables the tuning of their resonance frequency from 0.5 to 5 GHz and makes them selectively addressable. The frequency-selective wireless heating of different resonators is demonstrated. This represents a significant step towards their use as power receivers and microheaters in biodegradable implantable medical devices, for applications such as triggered drug release.
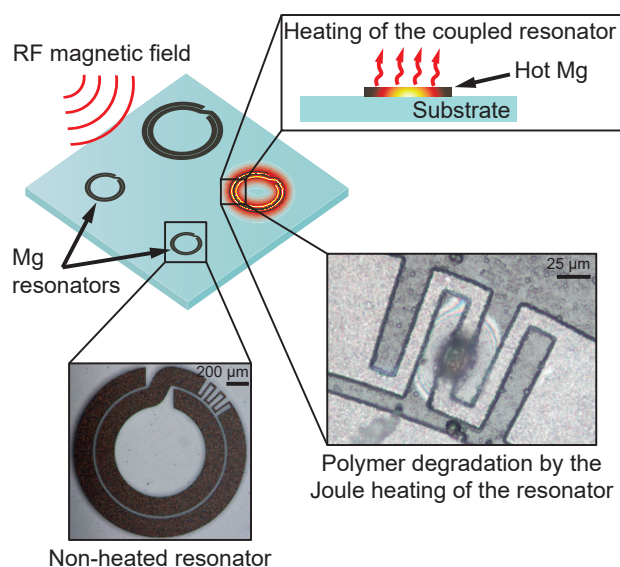
Figure 1.6 – Concept of selectively-addressable wireless biodegradable microheaters.

3. Design and fabrication of a wirelessly controlled drug delivery capsule enabling the on-demand selective release of drugs from multiple reservoirs. Resonant microheaters are used both as power receivers for near-field resonant inductive coupling, and electrothermal triggering elements to release the drug. Thus, the device powering and triggering mechanisms are combined into a single element, minimizing the volume of implanted material and maximizing the drug-to-implant volume ratio. The integration and miniaturization of all the components of such a system enables multiple drug reservoirs of several tens of μl in a minimal volume. Additionally, the design of the active elements is such that only one metal layer is required and the fabrication is based on dry processes only. This makes the technology readily available to be translated towards a fully biodegradable DDS which could be used for releasing local anesthetic for post-operative pain treatment following knee arthroplasty. The capsule is filled with a colored DI water solution by pipetting and the wireless release of liquid from the reservoirs is demonstrated.
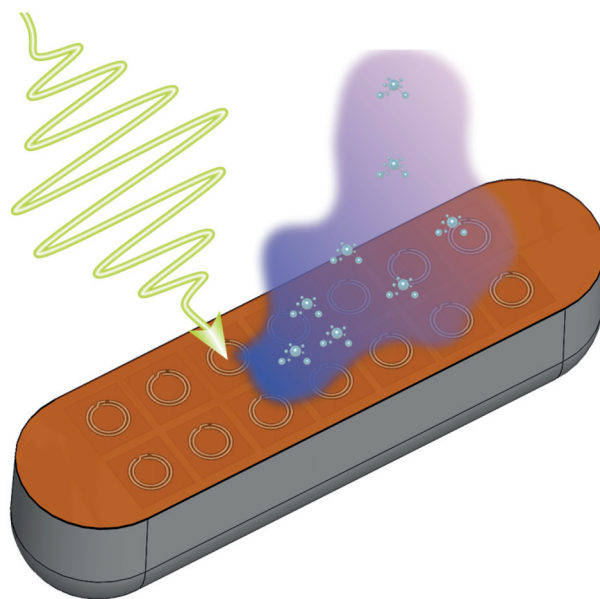
Figure 1.7 – Concept of a wirelessly controllable drug delivery capsule.

4. Translation of the fabrication processes developed in chapters 2 and 3 in order to fabricate biodegradable microheaters on biodegradable membranes. This progresses towards the development of a fully biodegradable version of the drug delivery system presented in chapter 3. At this stage, this work is facing some technological challenges preventing the fabrication of a fully functional prototype. However, it gives some strong guidelines in order to its fulfillment.

5. Conclusion and perspectives on biodegradable electronics and drug delivery implants.

2 Biodegradable frequency-selective magnesium microheaters

The purpose of this chapter is to present the design, the fabrication and the characterization of biodegradable Mg resonant microheaters. First, the materials used in transient electronics are introduced. Then, the concept of using microresonators as power receivers and microheaters is presented, followed by the design considerations, the modeling of the system and the microfabrication of the biodegradable microresonators. Finally, the electrical properties of the resonators are characterized. Their degradation and heating capabilities are also studied.

2.1 Introduction

In Chapter 1, the concept of using biodegradable implantable medical devices to avoid adverse long-term effects or the need for a second surgery to remove the implant was introduced. Two of the main challenges related to these implants are the fabrication of electronics out of water-soluble materials, plus powering and communicating with the implanted devices. Hereafter we introduce the state of the art materials used for transient electronics, their degradation pathways and the current fabrication techniques used to produce biodegradable electronics. Then, the concept of biodegradable frequency-selective resonant microheaters is introduced. The main goal here is to combine the powering, the communication and the active heating elements of implantable devices into a unique and miniaturized element.

2.1.1 Biodegradable materials for transient electronics

Biodegradable metals as conductive materials Biodegradable conductors include several alkaline metals such as magnesium (Mg) and calcium (Ca), as well as transitions metals such as molybdenum (Mo), Zinc (Zn), iron (Fe) and tungsten (W). [1, 65] Among them, Mg is widely present in cells and contributes to metabolic pathways. Additionally, it shows excellent biocompatibility and is already used to fabricate bioresorbable coronary stents and transient electronic circuits. [28, 48, 50, 55, 59, 97–99] Mg naturally dissolves in aqueous media by hydrolysis and Mg thin films show a rapid degradation rate of 0.05-5 µm/h depending on the solution composition, pH, temperature and stirring. Additionally, the degradation rate also depends on the Mg thin film deposition method and on the definition of the degradation rate itself. [100] Consequently, in vitro and in vivo degradation rates can be different, but generally, unprotected Mg microstructures have a lifetime of a few minutes when immersed in an aqueous solution. [59, 101] For in vivo applications, Mg is usually passivated by other materials in order to extend it's lifetime and to avoid short-circuits due to the conductivity of body fluids.

Mg dissolves by hydrolysis at the implant site and produces oxides, hydroxides and hydrogen gas as degradation products, which are resorbed by the body. The detailed dissolution process is described in the following equations: [102]

$$\text{Anodic reaction: } Mg \longrightarrow Mg^{2+} + 2\,e^- \tag{2.1}$$

$$\text{Cathodic reaction: } 2\,H_2O + 2\,e^- \longrightarrow H_2 + 2\,OH^- \tag{2.2}$$

$$Mg^{2+} + 2\,OH^- \longrightarrow Mg(OH)_2 \tag{2.3}$$

Mg reacts with water to produce slowly dissolvable magnesium hydroxide ($Mg(OH)_2$). Then $Mg(OH)_2$ reacts with Cl^- to form highly soluble magnesium chloride ($MgCl_2$). Dissolved ions can induce either positive or negative physiological reactions depending on their concentration. Additionally, H_2 creates gas pockets which can cause tissue displacement. It is thus important to have a controlled dissolution rate either by limiting the amount of Mg exposed to

biofluids or by using Mg alloys, such as Mg-Zn alloys, which dissolve more slowly. [64]. Other biodegradable metals, also dissolve more slowly than Mg. The dissolution rate of Mo is 7 nm/-day in water and 20 nm/day in phosphate-buffered saline (PBS), Fe dissolves at 7 nm/day in PBS, and W at 20 nm/day in PBS. [65, 100] Mo, Fe, W, Zn foils can be used as substrates for transient electronics, [64] and these materials were also used to fabricate biodegradable batteries and microsupercapacitors, [79, 80, 84] electrodes, [49, 103] and wires. [50] However, Mg remains the most widely used biodegradable metal and is already certified for commercial applications. Therefore, it is our primary material choice to fabricate the biodegradable resonant microheaters discussed in this chapter.

Semiconductors   As opposed to biodegradable metals which were already used in passive implantable orthopedic devices before the first appearance of transient electronics, the use of semiconductors as biodegradable materials started about 10 years ago. Although semiconductor materials show low dissolution rates in biofluids and are considered as non-biodegradable in their bulk form because of oxides formation, silicon (Si), germanium (Ge), SiGe, and ZnO, are biodegradable when used in the form of nanomembranes (NMs) and nanowires. [65] These semiconductor materials, which are compatible with conventional microfabrication processes, show tunable electrical characteristics with doping concentrations and enable the fabrication of active devices such as transistors. They determine the overall performance of the active electronics.

Organic semiconductors, such as indigo and melanin are also used in transient electronics for their soft mechanical properties and have potential for large-scale synthesis, but they show issues related to performance and uniformity. Finally, synthetic semiconducting polymers including those that are polypyrole-based (PPy) are also investigated. Several applications including energy harvesters, [77] photodetectors, [103] optical waveguides, [104] dopamine monitors, [105] temperature and pressure sensors, [50] electrodes, [49] and transistors [59] use biodegradable semiconductors.

The degradation of biodegradable semiconductors occurs by hydrolysis, and the degradation rate depends on the crystalline structure of the material. In addition, the rate increases with the solution pH, ionic concentration and temperature. It also decreases with proteins in the solution and the concentration of dopants in the material. [64] Si-NMs dissolve at 2-4 nm/day in PBS and 23 nm/day in artificial cerebrospinal fluid. [1, 65] Furthermore, the degradation products are biocompatible, even when the semiconductor materials are doped. [1]

Dielectrics   Oxides such as MgO and SiO_2, nitrides such as Si_3N_4, and spin-on-glass (SOG) have low dissolution rates in biofluids and are thus ideal candidates for electrical insulation and the encapsulation of transient electronics devices. Furthermore, they are also compatible with microfabrication processes. [1, 65] Their degradation occurs by hydrolysis and the rate depends on the pH, ions concentration, and temperature. The rate is also strongly related to

the material porosity and density, which depends on the deposition technique used. [64, 65] The hydrolysis of SiO_2 produces orthosilicic acid ($Si(OH)_4$) which dissolves in biofluids. Si_3N_4 is first converted in SiO_2 and then degrades in orthosilicic acid. Finally, the degradation of MgO depends on the pH and produces $Mg(OH)_2$. In terms of degradation rates, MgO degrades faster than SiO_2 which degrades faster than Si_3N_4, [65] but the rate strongly varies between 0.1 to 100 nm/day depending on the experimental conditions and deposition technique used. [106]

Biodegradable polymers as structural and encapsulation materials   Biodegradable polymers can be divided in two main categories: natural and synthetic. Natural biodegradable polymers include among others, silk, decellularized extracellular matrix (dECM), collagen, fibrin, starch, alginate, chitin and chitosan. The two most commonly used for IMDs are dECM and also silk thanks to its good biocompatibility, mechanical properties and easily tunable degradation. Natural biodegradable polymers generally exhibit a low inflammatory response but have a low manufacturing control and purification steps are required. While dECM is mainly used as scaffold for tissue growth after surgical repair and reconstruction, [45] silk is used as substrate material, [59, 101, 107] encapsulation layer, [108], drug-loaded layer in implantable biodegradable DDS, [55, 109, 110] as well as in triboelectric nanogenerators, batteries, [83, 111] and optics. [112]

Silk dissolution in vivo is mainly due to enzymatic degradation by protease, which is itself regulated by immune cells. [45] The degradation rate depends on parameters such as molecular weight, molecular structure, crystallinity, porosity, geometry, and surface topography, and can be tuned from minutes to years. Silk with a low beta-sheet amount and a porous structure degrades faster. The drying rate and ethanol treatment also change the degradation rate. [65] However, there is still a lack in the understanding of the exact degradation pathway and clearing mechanisms of silk. [45] Similar to silk, dECM also undergoes enzymatic degradation and is influenced by the presence of inflammatory cells, dECM density, its tissue source and crosslinking level. dECM dissolution products are eliminated through the blood stream and the kidneys or exhaled as CO_2. The full degradation of dECM typically takes between 3 to 24 months.

On the other hand, synthetic biodegradable polymers include among others polydioxanone (PDO), polycaprolactone (PCL), poly(glycolic acid) (PGA), poly(lactic acid) (PLA), poly(lactic-co-glycolic acid) (PLGA), poly(1,8-octanediol-co-citrate) (POC), poly(glycerol sebacate) (PGS) and poly(octamethylene maleate (anhydride) citrate) (POMaC). They can be manufactured in a reproducible way and exhibit controlled degradation rates but usually cause more inflammatory response than natural biodegradable polymers. PLA, PGA, PLGA and their derivatives are the most widely used synthetic biodegradable polymers. They are used in commercial surgical suture such as Neosorb®, drug delivery systems such as Zoladex®, and stents such as DESolve®. PLGA is also used as substrate and encapsulation layer in transient electronics devices. [48, 49, 87, 103, 104, 113, 114] Thanks to their elastomeric properties, PGS and POMaC

show great potential and have been recently used in biodegradable sensors, [56, 57, 115] drug delivery systems [54, 116] and scaffolds for tissue engineering. [117, 118]

The degradation of synthetic polymers follows three possible pathways which are hydrolysis, enzymatic degradation and oxidation. However, for some polymers such as polyesters, polyanhydrides and polyamides, the main pathway is hydrolysis. [45] The water causes the cleavage of ester bonds, degrading the polymers into oligomers or monomers such as lactic acid, glycolic acid or 6-hydroxyhexanoic acid. These degradation products are then processed in the tricarboxylic acid cycle and are eliminated from the body as carbon dioxide and water. The degradation can be of two types: bulk and surface. In bulk degradation, the water molecules penetrate in the implanted device and the whole implant degrades in a uniform way, resulting in the change of mechanical properties and molecular mass. As a result the implant breaks into big debris. Whereas, in surface degradation, only the outer part of the implanted devices is degraded. As a result, the size and the mass of the implant decrease with time while its molecular weight and mechanical properties remain relatively unchanged. PLGA and other polyesters mainly degrade through bulk degradation and the degradation rate can be tuned by the polymer composition. In the case of PLGA for instance, the ratio between glycolic and lactic acid content modulates the degradation time from weeks to months, with the fastest rate for PLGA 50:50. The degradation rate can be reduced by increasing, the molecular weight, crystallinity and hydrophobicity. On the other hand, blending and copolymerization both increase the degradation rate.

Having a controlled degradation rate is important to prevent the accumulation of acidic degradation products such as lactic acid. A reduced pH has an autocatalytic effect on the degradation, intensifies the inflammatory response and creates complications such as bone demineralization and reduced angiogenesis. [45] When used as a passivation layer to protect and prevent the rapid degradation of biodegradable metals, synthetic biodegradable polymers suffer from swelling caused by bulk degradation and from the permeation of water through the polymer layer. Both effects damage the electronics of the implanted device. [64] Polyanhydrides are good candidates for encapsulation thanks to their slow surface erosion. [1] Finally, the use of biodegradable polymers as substrates for transient electronics requires specific microfabrication techniques, because of their low glass transition temperatures (Tg) and poor chemical compatibility with solvents and water. [64]

2.1.2 Microfabrication of transient electronics

Since biodegradable materials are water-soluble, the fabrication of transient electronic circuits and devices made from these materials requires special care. More specifically, it needs to rely on dry processing steps which limit the exposure to aqueous solutions. This is especially important for fast dissolving metals such as magnesium. Various Mg microfabrication methods have been reported in literature, including electroplating, wet etching and laser-cutting of thick Mg foils, [119] and evaporation of thin Mg structures through stencils. [50, 59, 120]

Stencil lithography is used to pattern thin films of fragile materials because it completely avoids aqueous process steps, as shown in Figure 2.1a. Although stencil lithography - a high resolution shadow mask technique - is convenient to produce simple microstructures, it becomes less applicable when complex shapes such as coils are involved. Indeed, the stencils become fragile and difficult to manipulate when large suspended structures are involved. Stencil lithography also suffers from physical limitations such as blurring and clogging, [121] and is limited in the combination of thickness and resolution and in materials options. [122] The lift-off technique which consists of the deposition of a material by evaporation directly into a pattern of photoresist is another way to avoid wet etching and its associated rinsing steps. However, it suffers from limitations in resolution, shape uniformity, and maximal thickness of the deposited film. In our case, as described below in Section 2.2, the required resolution and film thickness are not compatible with such a technique.
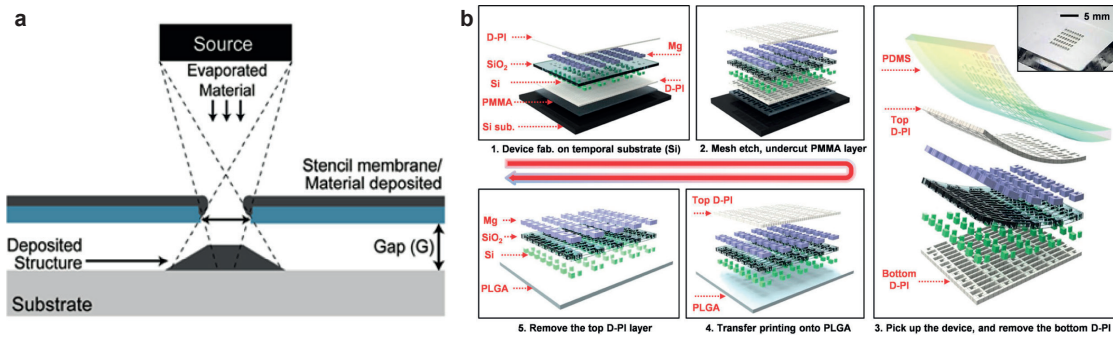
Figure 2.1 – **Microfabrication of transient electronics. a**, Diagram showing the concept of stencil lithography. The material to deposit is evaporated through the stencil aperture. Clogging of the stencil occurs over time as the material also deposit in the stencil aperture. [121] **b**, Schematic illustrations showing the concept of transfer printing of fabricated biodegradable microstructures on a biodegradable substrate. [122]

Regarding the fabrication of PLGA and silk films, they are mainly produced by drop-casting and spin-coating polymers solutions on Si wafers or glass substrates coated with silanes in order to prevent stiction. The polymers are dissolved in solvents such as water, acetone, ethyl acetate, anisole or chloroform, to achieve suitable viscosity to produce films with thicknesses varying from a few hundreds of nm to a few hundreds of μm. [78, 87, 104, 113, 114, 123] Since polymeric substrates are soluble in most solvents and their glass transition temperature can be as low as 50°C, they are not compatible with most of the microfabrication processes. Therefore, fabrication processes based on transfer printing were developed in order to transfer metal and semiconductor microstructures from a non-biodegradable to a biodegradable substrate. [107, 122, 124]

As shown in Figure 2.1b, the electronics is first fabricated on a stack of materials consisting of a Si wafer, a poly(methyl methacrylate) (PMMA) sacrificial layer and a polyimide (PI) mechanical layer. At the end of the fabrication process, the PI film with the metallic microstructures or Si-NMs on top, is released by dissolving the PMMA layer in acetone. It is then transferred

from the Si wafer to a biodegradable substrate using a polydimethylsiloxane (PDMS) stamp. The PI layer provides mechanical stability during the transfer. In order to ensure that the microstructures detach from the PDMS stamp and stick to the biodegradable substrate, it is heated to a temperature close to its Tg before the transfer process. Finally, the last step consists of etching the PI layer in oxygen plasma. Although the transfer printing process is widely used for the fabrication of biodegradable electronics it remains relatively complex, takes time and is costly since it is not easily scalable. Hence, alternative fabrication processes such as printing of Zn nanoparticles or laser cutting and screen printing have also been investigated. [1, 66, 114, 125, 126]

Following all the challenges presented above, we developed a new microfabrication process based on ion beam etching to improve and simplify the fabrication of biodegradable electronics. The detailed process is further described in Section 2.4.

2.1.3 Biodegradable microresonators as power receivers and microheaters

In order to improve the current means of powering biodegradable IMDs, we designed microresonators which combine the powering, the communication and the active heating elements into a unique and miniaturized element. Consequently, the volume of material used is minimized and the circuit complexity is reduced, which improves the overall system integration. Figure 2.2 illustrates the use of frequency-selective, biodegradable microresonators as power receivers and microheaters for transient electronics.
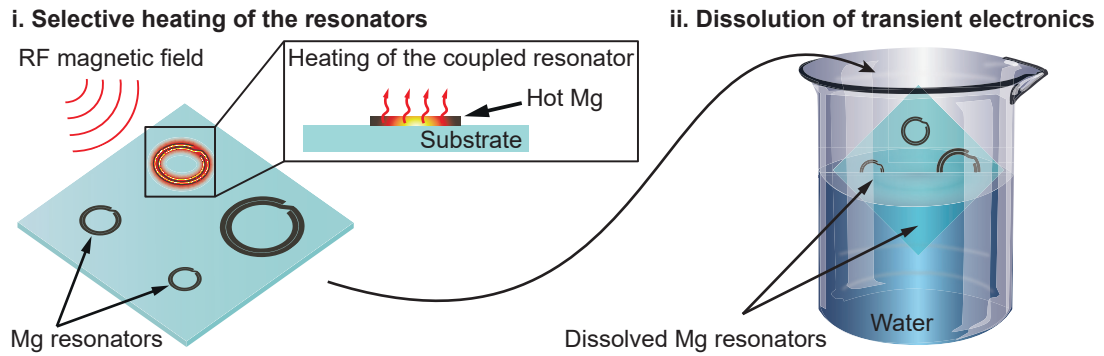
Figure 2.2 – **Biodegradable wireless microheaters.** Concept of using frequency-selective, biodegradable microresonators as power receivers and microheaters for transient electronics.

Several Mg resonators are fabricated on a substrate. Each resonator has a different resonance frequency (f_0) tuned by its geometrical parameters, which makes them selectively addressable. Using an external RF magnetic field, energy is coupled only into the frequency matched resonator where an electrical current is induced by electromagnetic induction. It results in the Joule heating of that particular device only.

Once immersed in water, the resonators naturally degrade by hydrolysis. To focus on the fabrication of biodegradable Mg electronics while demonstrating the concept of frequency-selective microheaters, the fabrication is done on a non-biodegradable glass substrate. Additionally, some of the resonators are passivated with a thin Parylene layer in order to characterize them in water, to mimic the permittivity of the in vivo environment.

As illustrated in Figure 2.3 and detailed in Section 2.2, a spiral resonator (SR) design is used for the microheaters. The time-varying RF magnetic field induces an electrical current in the resonator. By adding a meander hot-spot in the design of the resonator, the current density locally increases by one to two orders of magnitude, which creates a local hot-spot at a specific location. The increase of the current density in the meander is computed by finite element method as detailed in Section 2.3. All along this thesis, the terms microresonators and microheaters are used interchangeably.
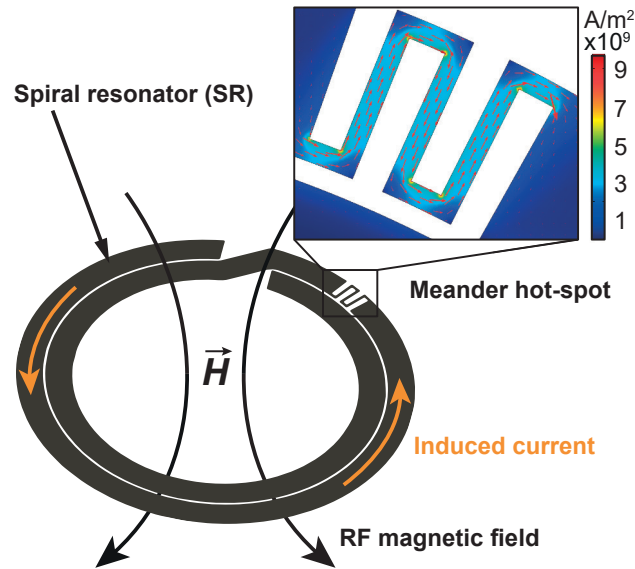
Figure 2.3 – **Spiral resonator microheater.** Design and FEM simulation of a spiral resonator (SR) with a meander hot-spot to increase the induced current density by one to two orders of magnitude.

2.2 Design considerations

Geometry of the resonator   The geometry of the developed microresonator, shown in Figure 2.4, is commonly referred to as spiral resonator. SRs can be used as secondary coils for NRIC on implantable devices, and as shown in Figure 1.5, they can be electrically considered as RLC series circuits. [127] The geometrical parameters such as the radius (R), the track width (W), and the gap between the two turns of the resonator (G) define the values of the R_{el}, L and C elements and thus the resonance frequency, as detailed in Section 2.3. The opening between the two turns of the resonator (W_o) has only a little influence on the resonance and is thus fixed to $W_o = 115\,\mu$m for all the resonators used in this chapter.
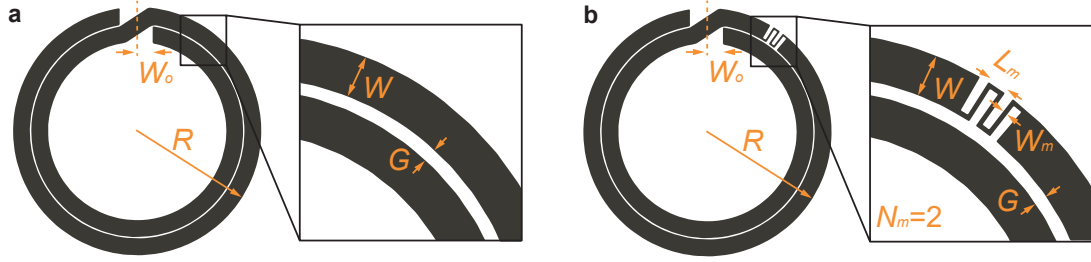
Figure 2.4 – **Spiral resonator design. a**, Geometry of a spiral resonator without a meander hot-spot as well as the geometrical parameters used to tune the resonance to specific frequencies by design. **b**, Geometry of a spiral resonator with a meander hot-spot as well as the geometrical parameters used to tune the resonance frequency and the heating properties of the meander hot-spot.

As discussed in Section 1.3, the size of the secondary coils and thus the resonance frequency range are partially defined by the final application of the implanted device. More specifically, when miniaturizing the implant, the frequency tends to increase towards values where the tissue losses are important. Lowering the frequency of miniaturized secondary coils then becomes a challenge. The spiral resonator design enables the maximization of the capacitance and thus the minimization of the resonance frequency for a given diameter. [127]

Alternatively, it enables the reduction of the secondary coil diameter compared to similar devices working in the same frequency range reported in the literature. [59, 75] Typically, SRs with a diameter from 2 to 5 mm resonate at frequencies from 1.5 to 5 GHz in air and from 0.5 to 2 GHz in water, depending on their exact geometry and specific surrounding environment. Another advantage of the SRs is that they are planar geometries and consist of only one layer. Consequently, they are easily fabricated by only four steps: one physical vapor deposition, one photolithography, one dry etching, and one resist stripping step, as detailed in Section 2.4.

Spiral resonators consist of only two turns by design. Increasing the number of turns in order to increase the impedance and to further decrease the resonance frequency would be possible but it implies a few other considerations. Firstly, With a design having more than two turns, the analytical formulae used to compute the inductance and capacitance of the resonator are not readily valid anymore and must be corrected. [127] Additionally, the effect of

having more turns on the power dissipated in the meander is not trivial. Indeed, as described below in Equation 2.38 in Section 2.3, having more turns increases the electromotive force in itself. Nevertheless, the fact that the resonance frequency and the average radius are lowered decreases the electromotive force. Finally, since the diameter of the resonators is limited by the application it is not easy to add many turns. Because of all these reasons, we decided to use only two turns for the first prototype. However, it might be interesting to study a design with more turns by FEM modeling in a future version of the device.

Design of the meander hot-spot   As shown in Figure 2.4b, the meander hot-spot design can be modified by several parameters such as the number of meanders (N_m), the meander length (L_m), and the meander width (W_m). As a result, the current density modification, and thus the heating properties of the meander can be tuned. Models of the system developed in Section 2.3 enable to quantify the current density in the meander. These models showed that the current density is slightly higher at the half of the length of the resonator, which explains the location of the meander. However, the final temperature value is difficult to predict as the cooling of the system depends on many parameters. Experimental data are thus required to quantify the heating capabilities of the resonators. Moreover, depending on the application, the final temperature might not be the most important parameter, as a lower temperature over a larger area might be required.

Thickness of the resonator   Finally, a last design consideration exists regarding the thickness (T) of the resonator, which requires a tradeoff between the heat focusing in the meander, the increase in frequency, and the fabrication technique. The power dissipated in the meander at resonance can be computed according to Equation 2.4, with P_m the power dissipated in the meander, ϵ the electromotive force induced by the RF magnetic field, R_m the electrical resistance of the meander, and R_r the electrical resistance of the resonator except the meander. Assumptions and detailed calculations to obtain to this formula are described in Section 2.3.

$$P_{m,\omega_0} = \frac{\epsilon^2 R_m}{(R_r + R_m)^2} \qquad \text{[W]} \qquad\qquad (2.4)$$

To maximize the dissipated power and thus the heating, the derivative of Equation 2.4 must be equal to 0.

$$\frac{\partial P}{\partial R_m} = \frac{\epsilon^2 (R_r - R_m)}{(R_r + R_m)^3} = 0 \qquad\qquad (2.5)$$

This condition is satisfied when $R_m = R_r$ and the maximal dissipated power in the meander is:

$$P_{m,\omega_0,max} = \frac{\epsilon^2}{4R_m} \qquad \text{[W]} \qquad\qquad (2.6)$$

Consequently, the resistance of the meander and of the resonator should be minimized. Taking into account the skin effect, the electrical resistance (R_{el}) of a conductive track is computed according to the following equations, with δ the skin depth, ρ the electrical resistivity of the material, μ_0 the vacuum permeability, μ_r the relative permeability of the material, ω the angular frequency, l the length of the track, W the width of the track, and T the thickness of the track: [128]

$$\delta = \sqrt{\frac{2\rho}{\mu_0 \mu_r \omega}} \qquad [\text{m}] \tag{2.7}$$

$$R_{el} = \frac{\rho l}{W\delta\left(1 - e^{-\frac{T}{\delta}}\right)} \qquad [\Omega] \qquad W >> T, \delta \tag{2.8}$$

To minimize the resistance, the thickness should be much larger than the skin depth. At 300 MHz and 3 GHz, the skin depth is 9.4 and 3 μm respectively, using a resistivity of 105 nΩ·m as measured for Mg thin films in Section 2.5.3. This implies having resonators with thicknesses of tens of μm. Although using thick Mg foils is possible, it is not compatible with common microfabrication techniques, which limits the lateral resolution of the fabricated structures. [119] A limited lateral resolution induces two other issues. Firstly, a good resolution is required to satisfy the condition $R_m = R_r$. Indeed, if we assume a meander 20 times shorter than the resonator length, then the resonator track width must be 20 times larger than the meander width ($W = 20W_m$) to satisfy $R_m = R_r$. For a track width of 120 μm, the meander width is 6 μm. Secondly, a resolution of a few μm for the gap (G) between the two turns of the resonator is required to maximize the capacitance of the resonators, and thus minimize their resonance frequency. As described in Equation 2.9 with L and C the inductance and capacitance values of the resonator, a large capacitance minimizes the resonance frequency f_0.

$$f_0 = \frac{1}{2\pi\sqrt{LC}} \qquad [\text{Hz}] \tag{2.9}$$

Microfabrication techniques enable to achieve these resolutions. Therefore, the choice was made to use thin film technology to deposit Mg, but maximizing the thickness to the extent of guarantying compatibility with microfabrication tools as well as a good lateral resolution. A thickness of 2 μm is still reasonable to be deposited by evaporation without excessive deposition times and stresses in the film, while it remains in the same order of magnitude as the skin depth. For all the subsequent results in this chapter, a thickness of 2 μm of Mg is used, for all the resonators.

2.3 Analytical and finite elements method models

2.3.1 Introduction

In order to design resonators at specific resonance frequencies and to get a better understanding of the system, two models were developed. Firstly, an analytical model enables to rapidly compute the resonance frequency, the quality factor and the energy dissipated in the meander for a specific resonator geometry. Secondly, a more precise FEM model enables to validate the analytical model and to understand how the electromagnetic field and the induced electrical current behave exactly.

2.3.2 Methods

Analytical model   This model was computed using Matlab and is based on the inductive link design shown in Figure 1.5. The primary coil is not modeled, and a uniform RF magnetic flux density (B_{RF}) over the whole area of the secondary coil is considered instead. The secondary coil, i.e. the spiral resonator, is modeled as an RLC series circuit in series with an electromotive force. The resistance of the resonator consists of two resistances in series, one for the meander (R_m) and one for the rest of the resonator (R_r). Such an assumption considers that the current is uniform over the whole resonator and is verified with the FEM model in Sections 2.3.3 and 2.3.4. The values of the R_{tot}, L and C elements to model the spiral resonator are computed according to the geometrical parameters of the resonators defined in Figure 2.4 (R, W, T, G, W_o, W_m, L_m, N_m). Additionally, the following is also considered. The values of R_r and R_m are taking into account the skin effect and are computed according to Equation 2.10 and 2.11, with δ the skin depth defined in Equation 2.7, l_r and l_m the resonator and meander lengths, $\bar{R}$ the average radius of the SR, and N_t the number of turns of the resonator. However, this formula doesn't take into account the resistance increase due to the temperature increase. [20] The total resistance of the SR is computed according to Equation 2.15.

$$R_r = \frac{\rho l_r}{W\delta\left(1 - e^{-\frac{T}{\delta}}\right)} \qquad [\Omega] \tag{2.10}$$

$$R_m = \frac{\rho l_m}{W_m\delta\left(1 - e^{-\frac{T}{\delta}}\right)} \qquad [\Omega] \tag{2.11}$$

$$l_r = N_t(2\pi\bar{R} - W_o) - 2N_mL_m \qquad [\text{m}] \tag{2.12}$$

$$l_m = 2N_mL_m + (2N_m - 1)W \qquad [\text{m}] \tag{2.13}$$

$$\bar{R} = R - W - \frac{G}{2} \qquad [\text{m}] \tag{2.14}$$

$$R_{tot} = R_r + R_m \qquad [\Omega] \tag{2.15}$$

The inductance (L) of a spiral resonator is equivalent to the inductance of a single ring, with a radius equal to the average radius ($\bar{R}$) of the spiral resonator computed in Equation 2.14, and a width equal to the track width of the resonator. [127, 129] It is computed according to Equation 2.16, [130, 131] with μ_0 the vacuum permeability, P and F unitless constants to correct for the track width and the thickness of the resonator.

$$L = \frac{\mu_0 \bar{R} P F}{4\pi} \qquad \text{[H]} \tag{2.16}$$

Finally the capacitance (C) is computed similarly to the capacitance of a coplanar stripline (CPS), [127, 129] a widely studied problem. [132–135] This assumption is only valid for resonators with two turns, i.e. $N_t \equiv 2$. First, the per unit length capacitance (C_{pul}) is computed, and multiplied by the length of the gap between the two turns of the SR (l_c) to get the total capacitance.

$$C = C_{pul} l_c \qquad \text{[F]} \tag{2.17}$$

$$l_c = 2\pi \bar{R} - 2W_o - 2N_m L_m \qquad \text{[m]} \tag{2.18}$$

For a CPS on a dielectric substrate with a finite thickness (h) such as illustrated in Figure 2.5a, $C_{pul,CPS}$ is equal to the CPS capacitance in free space when the dielectric is replaced by air (C_a), multiplied by an effective permittivity to take into account the substrate material (ϵ_{eff}).
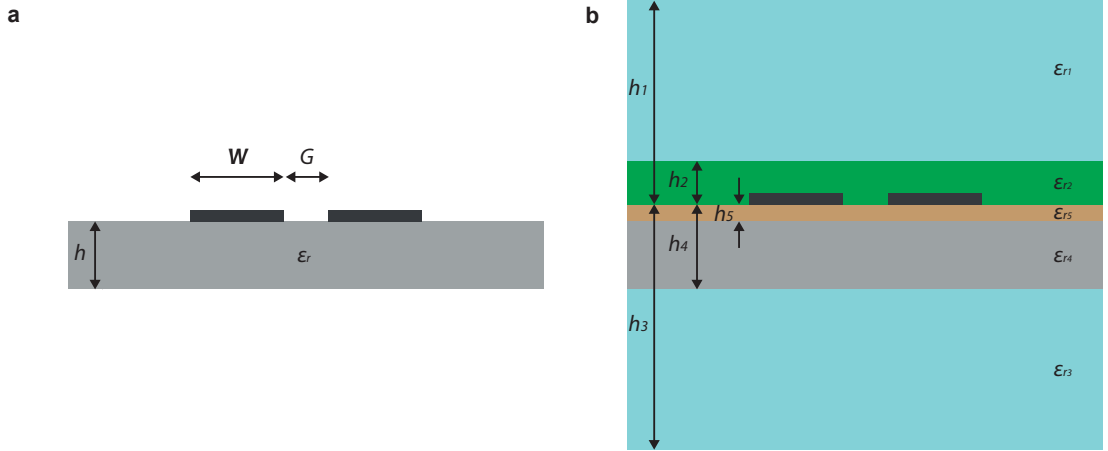
Figure 2.5 – **Analytical model - Coplanar stripline capacitance. a**, Geometry of a coplanar stripline on a finite thickness dielectric substrate. **b**, Geometry of a coplanar stripline taking into account the surrounding material (index 1 and 3), the substrate (index 4), a thin film between the substrate and the stripline (index 5) and a passivation layer (index 2).

$$C_{pul,CPS} = \epsilon_{eff} C_a \qquad \text{[F/m]} \tag{2.19}$$

$$C_a = \epsilon_0 \frac{K(k')}{K(k)} \qquad \text{[F/m]} \tag{2.20}$$

29

$$k = \frac{G}{G + 2W} \tag{2.21}$$

$$k' = \sqrt{1 - k^2} \tag{2.22}$$

$$\epsilon_{eff} = 1 + \frac{\epsilon_r - 1}{2} \frac{K(k')K(k_1)}{K(k)K(k'_1)} \tag{2.23}$$

$$k_1 = \frac{sinh\left(\pi \frac{G}{2} \frac{1}{2h}\right)}{sinh\left(\pi \left(\frac{G+2W}{2}\right) \frac{1}{2h}\right)} \tag{2.24}$$

$$k'_1 = \sqrt{1 - k_1^2} \tag{2.25}$$

With ϵ_0 the vacuum permittivity, ϵ_r the relative permittivity, and K the complete elliptic integral of the first kind. The ratio $K(k)/K(k')$ can be approximated by:

$$\frac{K(k)}{K(k')} = \begin{cases} \left[\frac{1}{\pi} \ln\left(2\frac{1+\sqrt{k'}}{1-\sqrt{k'}}\right)\right]^{-1} & \text{for } 0 < k < \frac{1}{\sqrt{2}} \\[3mm] \frac{1}{\pi} \ln\left(2\frac{1+\sqrt{k}}{1-\sqrt{k}}\right) & \text{for } \frac{1}{\sqrt{2}} < k < 1 \end{cases} \tag{2.26}$$

To also take into account the surrounding material, a thin film between the substrate and the stripline, and a passivation layer as shown in Figure 2.5b, the effective permittivity computed in Equation 2.23 must be replaced by Equation 2.27. [136]

$$\begin{aligned} \epsilon_{eff} = 1 &+ \frac{\epsilon_{r1} - 1}{2} \frac{K(k')K(k_1)}{K(k)K(k'_1)} \\ &+ \frac{\epsilon_{r2} - \epsilon_{r1}}{2} \frac{K(k')K(k_2)}{K(k)K(k'_2)} \\ &+ \frac{\epsilon_{r3} - 1}{2} \frac{K(k')K(k_3)}{K(k)K(k'_3)} \\ &+ \frac{\epsilon_{r4} - \epsilon_{r3}}{2} \frac{K(k')K(k_4)}{K(k)K(k'_4)} \\ &+ \frac{\epsilon_{r5} - \epsilon_{r4}}{2} \frac{K(k')K(k_5)}{K(k)K(k'_5)} \end{aligned} \tag{2.27}$$

$$k_i = \frac{sinh\left(\pi \frac{G}{2} \frac{1}{2h_i}\right)}{sinh\left(\pi \left(\frac{G+2W}{2}\right) \frac{1}{2h_i}\right)} \tag{2.28}$$

$$k'_i = \sqrt{1 - k_i^2} \tag{2.29}$$

When computing the capacitance of a CPS, the thickness of the track is considered to be infinitely thin, and the dielectric substrate and surrounding materials are considered to be infinitely large. In order to take into account the track thickness, we can add in parallel to the CPS capacitance a parallel plate capacitance $C_{pul,//}$. The computation of the parallel plate capacitance assumes that the gap (G) is much smaller than the thickness of the track (T). If this condition is not satisfied, the parallel plate term ($C_{pul,//}$) is negligible compared to the CPS term ($C_{pul,CPS}$).

$$C_{pul} = C_{pul,CPS} + C_{pul,//} \qquad [\text{F/m}] \tag{2.30}$$

$$C_{pul,//} = \frac{\epsilon_0 \epsilon_{r2} T}{G} \qquad [\text{F/m}] \qquad G << T \tag{2.31}$$

The electromotive force induced in the spiral resonator (ϵ) is described by Faraday's law of induction in Equation 2.32, with Σ a surface bounded by the closed contour $\partial\Sigma$, $\vec{E}$ the electric field, $\vec{B}_{RF}$ the magnetic flux density, t the time, $d\vec{l}$ an infinitesimal vector element of the contour $\partial\Sigma$, and $d\vec{A}$ an infinitesimal vector element of surface Σ. As described in Equation 2.33, thanks to the small size of the SR, $\vec{B}_{RF}$ is considered to be uniform over the whole area of the resonator, with $\hat{B}_{RF}$ the peak value of the flux density and ω the angular frequency. Additionally, the surface Σ of the resonator is not changing over time, thus equation 2.32 can be rewritten according to Equations 2.34 and 2.35, with $\vec{n}$ a unit vector perpendicular to the SR, A the surface of the SR defined in Equation 2.36, $N_t \equiv 2$ the number of turns of the resonator, and $\bar{R}$ the average radius defined in Equation 2.14.

$$\epsilon = \oint_{\partial\Sigma} \vec{E} \cdot d\vec{l} = -\int_\Sigma \frac{\partial \vec{B}_{RF}}{\partial t} \cdot d\vec{A} \qquad [\text{V}] \tag{2.32}$$

$$\vec{B}_{RF}(t) = \hat{B}_{RF} cos(\omega t) \qquad [\text{T}] \tag{2.33}$$

$$\epsilon = -\frac{d}{dt}\int_\Sigma \vec{B}_{RF} \cdot d\vec{A} \tag{2.34}$$

$$\epsilon = -\frac{d}{dt}\left(\vec{B}_{RF} \cdot \vec{n} A N_t\right) \tag{2.35}$$

$$A = \pi \bar{R}^2 \qquad [\text{m}^2] \tag{2.36}$$

Finally, we get the time-varying electromotive force as described in Equation 2.37, with γ the angle between the RF magnetic flux density and the vector $\vec{n}$. If we consider a perfect alignment ($\gamma = 0$), the root mean square (RMS) value of the electromotive force can be computed according to Equation 2.38.

$$\epsilon(t) = \omega A N_t cos(\gamma)\hat{B}_{RF} sin(\omega t) \tag{2.37}$$

$$\epsilon = \omega A N_t B_{RF} \tag{2.38}$$

The active power dissipated in the SR (P_{tot}) is described in Equation 2.39, with I the electrical current, $cos(\phi)$ the power factor, and Z_{tot} the total impedance of the SR.

$$P_{tot} = \epsilon I cos(\phi) = \epsilon \frac{\epsilon}{|Z_{tot}|} \frac{R_{tot}}{|Z_{tot}|} \qquad [W] \tag{2.39}$$

This equation considers that the spiral resonator behaves as an RLC series circuit in series with an electromotive force, and assumes a uniform current over the whole resonator. As mentioned above, this assumption is verified with the FEM model in Sections 2.3.3 and 2.3.4. The power and the energy dissipated specifically in the meander hot-spot are described in the following equation, with τ the time pulse during which the SR is exposed to B_{RF}:

$$P_m = \frac{\epsilon^2 R_m}{(R_{tot})^2 + \left(\omega L - \frac{1}{\omega C}\right)^2} \qquad [W] \tag{2.40}$$

$$E_m = P_m \tau \qquad [J] \tag{2.41}$$

It appears clearly from equation 2.40 that there is a resonance frequency (ω_0) at:

$$\omega_0 = \frac{1}{\sqrt{LC}} \qquad \left[s^{-1}\right] \tag{2.42}$$

Then, the power dissipated in the meander at resonance (P_{m,ω_0}) and the quality factor Q are:

$$P_{m,\omega_0} = \frac{\epsilon^2 R_m}{(R_{tot})^2} \qquad [W] \tag{2.43}$$

$$Q = \frac{1}{R_{tot}} \sqrt{\frac{L}{C}} \tag{2.44}$$

All the code to compute the analytical model is detailed in Appendix A. In order to ease the way of computing the resonance of specific SR geometries, a graphical user interface (GUI) was developed in order to enter the input parameter such as the magnetic flux density (B_{RF}) intensity, the pulse length (τ), and all the geometrical parameters defined in Figure 2.4. The SR material can be selected from a list (Mg, Au, Al, Cu), as well as the substrate, underlying layer, passivation layer and surrounding materials (Parylene, PLGA, PI, FR4, float glass, water, air) and their respective thicknesses. As an output, the energy dissipated in the meander hot-spot is plotted as a function of the frequency, and the values of the resonance frequency, the quality factor, the current density in the meander, the maximum energy dissipated in the meander, R_{tot}, R_m/R_r, L and C are displayed.

FEM model   In order to have a better understanding of the behavior of the SRs and to validate the analytical model, a FEM model was developed. Similar to the analytical model, it includes 2 μm thick Mg spiral resonators with various geometries, a 550 μm thick glass substrate, an optional 5 μm thick Parylene passivation layer and multiple surrounding medium such as air or water. Unlike the analytical model, the primary excitation system to produce the RF magnetic field is also modeled. It consists of a coplanar waveguide (CPW), the system used to experimentally characterize the resonators as detailed in Section 2.5.2. The FEM simulations were performed using COMSOL Multiphysics 5.3. A 3D model is required since there is no symmetry in the problem, as shown in Figure 2.6a.

The model takes into account dielectric losses in the glass substrate, in the Parylene passivation layer, and in water. Since the resistive losses in water are negligible, the water electrical conductivity is set to zero. The Electromagnetic Waves, Frequency Domain physics from the Radio Frequency module is used. Lumped port boundary conditions are used at the input (10 V, peak value), and at the output of the coplanar waveguide (50 Ω). The entire modeling domain is bounded by scattering boundaries that represent an open space. As shown in Figures 2.6b and 2.6c, the resonator can be facing up or down, and the distance between the CPW and the resonator can be tuned.
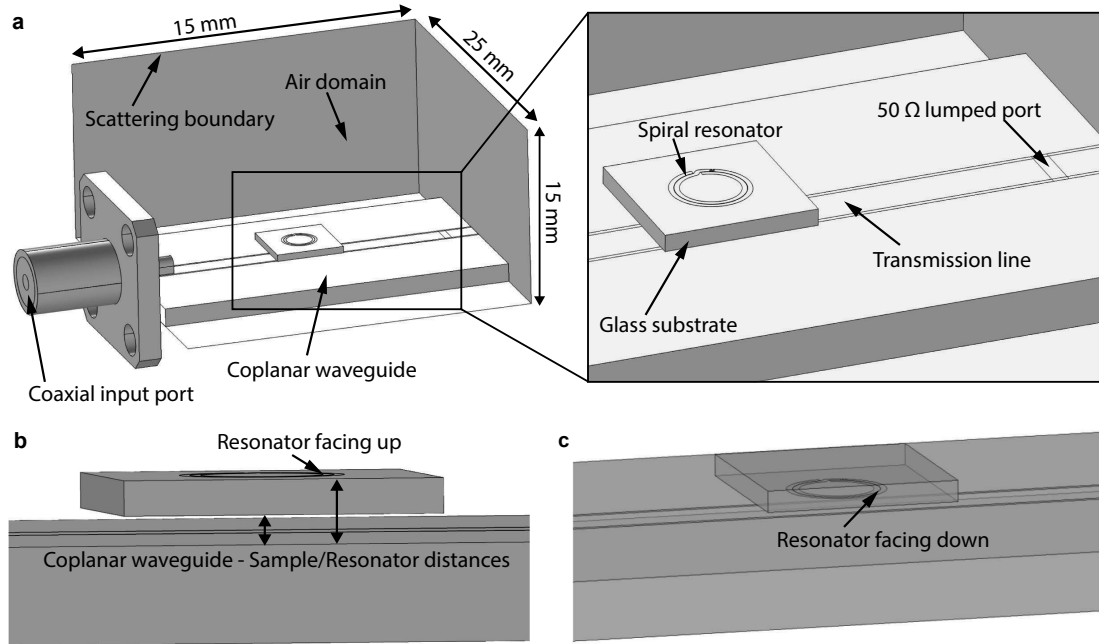
Figure 2.6 – **FEM model - Inductive link design. a**, 3D model of the inductive link including the coplanar waveguide used as primary excitation system, the spiral resonator and the surrounding environment. **b**, **c**, Configurations with the resonator facing up and down respectively.

A free tetrahedral mesh is used for all domains except for the thin Mg and Parylene layers where a free triangular swept mesh is used, as shown in Figure 2.7. One mesh element through the whole Mg layer is used. Meshing the thin Mg layer implies a high computational power due to the large number of mesh elements required. Indeed, the domain is several mm wide but only 2 um thick, and the gap between the two turns of the coil is in the micrometer range as well. Instead of including the Mg domain in the simulation, a transition boundary condition (TBC) could be used on this domain. When a TBC is used, it is not required to mesh the Mg domain and the resonance is still computed properly. However, it doesn't enable the computation of the electrical current in the resonator.
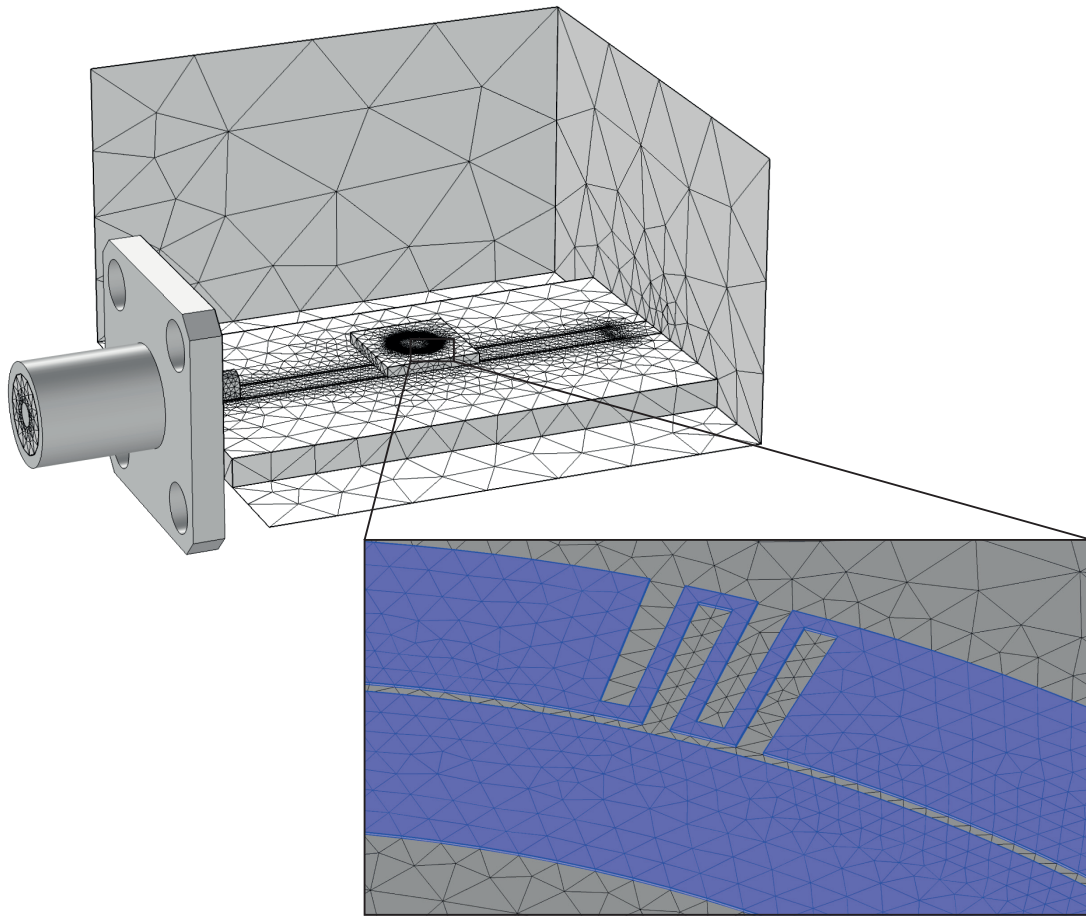
Figure 2.7 – **FEM model - Mesh.** A free tetrahedral mesh is used for all domains except for the thin Mg layer where a free triangular swept mesh is used.

Finally, a Frequency Domain study with an iterative Flexible Generalized Minimum Residual (FGMRES) solver is performed. The FEM model enables to compute the electric and magnetic fields, as well as the current in the resonator and in the meander. It also enables to compute f_0 and Q and takes into account the effect of the distance between the CPW and the resonator. As detailed in Section 2.5.2, some energy is coupled from the waveguide to the resonator, which results in a drop in the voltage signal at the output of the waveguide. The energy coupled

into the resonator depends on the frequency of the input signal, with the maximum coupling occurring when the frequency of the input signal matches the resonance frequency of the resonator. As a result, the output voltage signal can be used to determine the resonance frequency and the quality factor of the resonator. In order to suppress artifacts, a baseline removal operation is performed by subtracting the signal obtained with a broken resonator by design, from the signal obtained with a normal resonator. A broken resonator is shown in Figure 2.8.
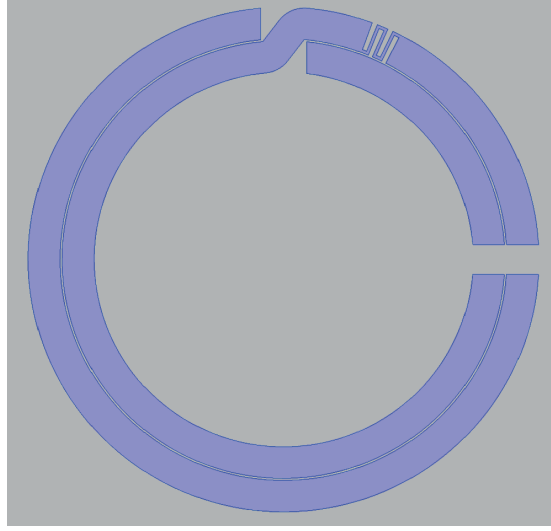
Figure 2.8 – **Spiral resonator cut by design.** A resonator cut by design enables to generate the reference signal used for baseline removal.

The resulting signal after the baseline removal operation is the voltage attenuation at the output of the waveguide (ΔV_{out}). The resonance frequency is defined as the frequency at which the voltage attenuation is maximal. As shown in Equation 2.45, the Q factor is defined as the resonance frequency divided by the full width at half maximum (Δf) of the voltage attenuation signal at the output of the CPW.

$$Q = \frac{f_0}{\Delta f} \tag{2.45}$$

The assumption of using the voltage attenuation signal to compute f_0 and Q was verified by making a lumped-element model of the system with Quite Universal Circuit Simulator (QUCS) as shown in Figure 2.9. Table 2.1, compares f_0 and Q values computed using the lumped-elements values of R, L and C directly, with the values obtained using the voltage attenuation signal from the QUCS simulation and give identical results.
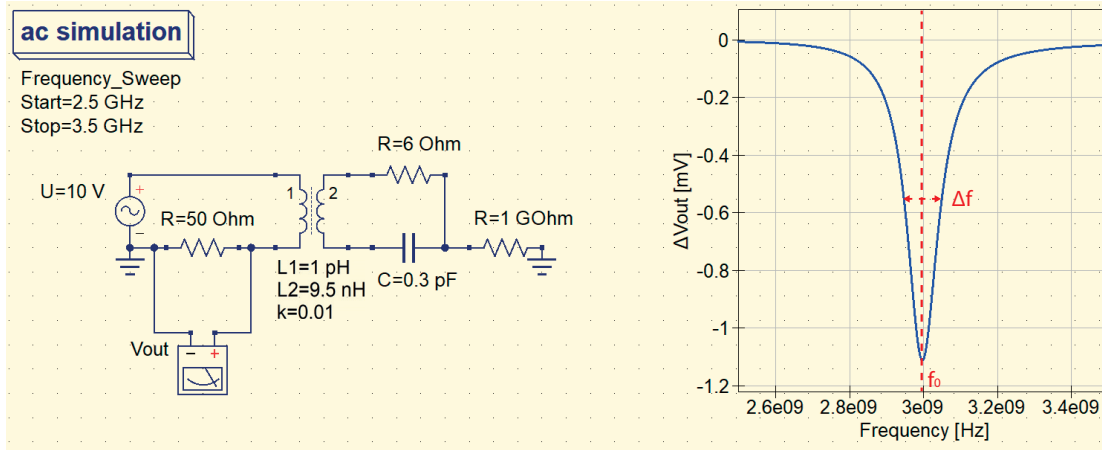
Figure 2.9 – **Lumped-element simulation of the inductive link.** The lumped-element model includes the primary and secondary coils of the inductive link. A frequency sweep simulation is performed with a 10V input voltage applied to the primary coil. The change in voltage at the output of the primary coil (ΔV_{out}) is displayed as a function of the frequency and this signal is used to determine the resonance frequency and the quality factor of the secondary coil.

Table 2.1 – **Lumped-element model vs. voltage attenuation.** In the lumped-element model, f_0 and Q values are computed using Equations 2.9 and 2.44 with the R, L and C values from the lumped-elements in the QUCS simulation. With the voltage attenuation technique, f_0 is defined as the minimum of the voltage attenuation signal (ΔV_{out}) from the QUCS simulation, and Q is computed according to Equation 2.45.

	f_0 [GHz]	Q
Lumped-element model	2.997	29.5
Voltage attenuation	2.998	29.4

2.3.3   Results

Analytical model   Figure 2.10 shows the graphical user interface of the analytical model. The energy dissipated in the meander as a function of the frequency is displayed for a specific resonator geometry and surrounding environment. Computing the model for a specific resonator geometry takes less than one second. Changing the geometrical parameters of the resonator as well as the surrounding environment both induce changes in the resonance frequency, the quality factor, and the current density in the meander. An extensive comparison of the resonance between the analytical model, the FEM model and experimental results is done in Sections 2.5.3 and 2.5.4. For a reference resonator geometry ($R = 1000\,\mu m$, $W = 120\,\mu m$, $G = 5\,\mu m$, $T = 2\,\mu m$, $W_m = 20\,\mu m$, $L_m = 40\,\mu m$, $N_m = 2$) and a 8.1 µT magnetic flux density, the current density in the meander is 4.95×10^9 A/m^2, when the resonator is surrounded by air. 8.1 µT is the average value of the magnetic flux density in the spiral resonator when a 10 V$_{peak}$ input voltage is applied to the CPW, as computed by FEM and shown in Figure 2.11a.
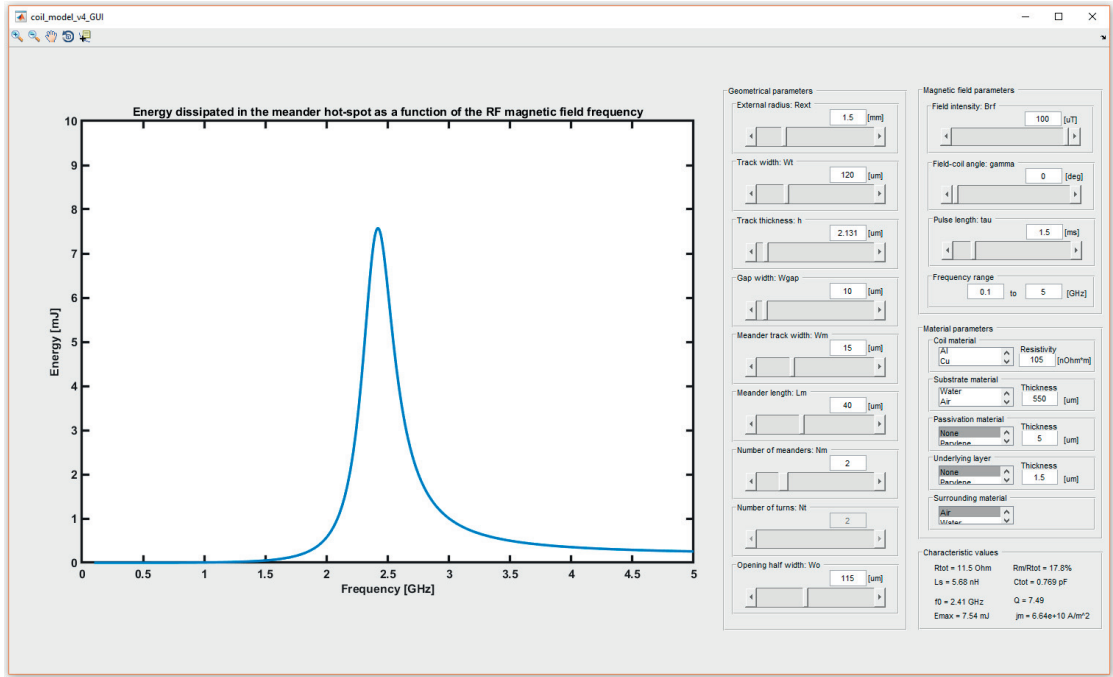
Figure 2.10 – **Analytical model - Energy dissipated in the meander.** Graphical user interface of the analytical model showing the energy dissipated in the meander as a function of the RF magnetic field frequency, as well as the main characteristics of the resonator such as the resonance frequency, the quality factor, and the current density in the meander.

FEM model FEM simulations enable to precisely determine the values of the magnetic field generated by the CPW, the resonance frequency and quality factor of the modeled spiral resonator, as well as the current density in the meander hot-spot. However, because of the 3D geometry and of the fine mesh required, the FEM simulation for one resonator takes several hours to converge. Figure 2.11a shows the RMS value of the vertical component of the magnetic flux density, when a $10\,\mathrm{V_{peak}}$ input voltage is applied to the CPW and the surrounding environment is air with a broken resonator on a glass substrate facing up (i.e. $850\,\mu\mathrm{m}$ above the CPW). Indeed, as shown in Equation 2.35, only the perpendicular component contributes to the induced electromotive force. Due to the geometry of the CPW, the B field intensity varies between 11.3 and $4.4\,\mu\mathrm{T}$ over the resonator area, with an average value of $8.1\,\mu\mathrm{T}$.

Figure 2.11b shows the RMS value of the current density for a non-broken reference resonator geometry ($R = 1000\,\mu\mathrm{m}$, $W = 120\,\mu\mathrm{m}$, $G = 15\,\mu\mathrm{m}$, $T = 2\,\mu\mathrm{m}$, $W_m = 20\,\mu\mathrm{m}$, $L_m = 40\,\mu\mathrm{m}$, $N_m = 2$) exposed to this magnetic flux density (i.e. $850\,\mu\mathrm{m}$ above the CPW). Compared to the reference geometry used in the analytical model, there is a difference in the gap value ($G = 5$ and $15\,\mu\mathrm{m}$), in order to have resonators with the same resonance frequency. The validity of both models in terms of resonance frequency is compared to experimental results in Sections 2.5.3 and 2.5.4, but here the frequency is kept constant in order to compare the induced current density for a given magnetic flux density. Indeed, the current density value is proportional to the electromotive force, which is itself proportional to the frequency, as shown in Equation 2.38.

In this specific case, the gap is varied to keep a constant frequency because it is the parameter which requires the smallest absolute variation to do so. The current density in the meander hot-spot and in the track of the resonator are 2.3×10^9 and 1.9×10^8 A/m^2 respectively.

A: 8.5 μT   B: 11.3 μT   C: 4.4 μT   A: 2.3×10^9 A/m^2 B: 1.9×10^8 A/m^2 C: 3.7×10^7 A/m^2
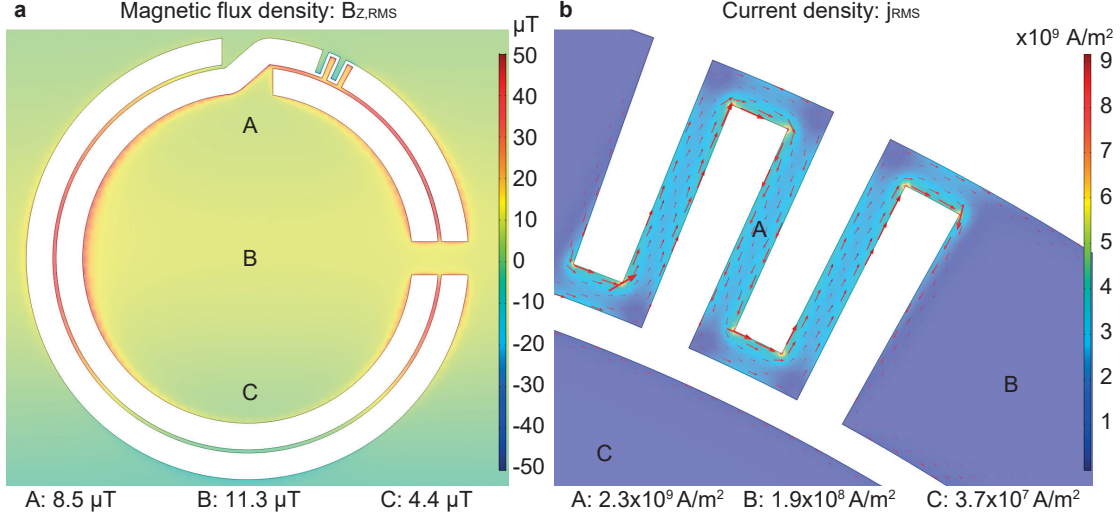
Figure 2.11 – **FEM model - Magnetic flux density and current density. a**, RMS value of the vertical component of the magnetic flux density, when a $10\,V_{peak}$ input voltage is applied to the CPW and the surrounding environment is air with a broken resonator on a glass substrate facing up (i.e. 850 μm above the CPW). **b**, RMS value of the current density for a non-broken reference resonator geometry ($R = 1000$ μm, $W = 120$ μm, $G = 15$ μm, $T = 2$ μm, $W_m = 20$ μm, $L_m = 40$ μm, $N_m = 2$) exposed to this magnetic flux density (i.e. 850 μm above the CPW) in air.

Similar to the analytical model, changing the geometrical parameters of the resonator as well as the surrounding environment both induce changes in the resonance frequency, the quality factor, and the current density in the meander. An extensive comparison of the resonance between the analytical model, the FEM model and experimental results is done in Sections 2.5.3 and 2.5.4. Figure 2.12 shows the resonance of a resonator in several media and orientations, while the resonance frequency and quality factor values for each configuration are shown in Table 2.2. We can observe that both the resonance frequency and the signal intensity depend on the resonator orientation, and thus on the distance between the coplanar waveguide and the resonator.

A detailed study of the effect of CPW-resonator distance on the resonance is shown in Figure 2.13. The scattering parameter S_{21} is plotted as a function of the frequency for several distances. S_{21} is defined according to Equation 2.46, with V_{in} and V_{out} the voltage waves at the input and output ports of the CPW.

$$S_{21} = 20 log_{10}\left(\frac{V_{out}}{V_{in}}\right) \tag{2.46}$$
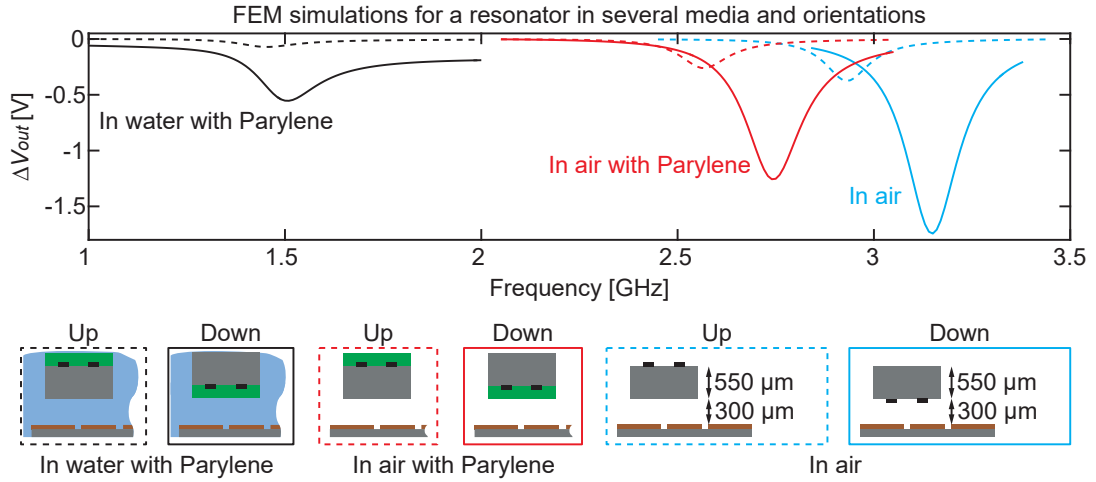
Figure 2.12 – **FEM model - Media and orientation effect.** Resonance of a resonator ($R = 1280\,\mu m$, $W = 160\,\mu m$, $G = 10\,\mu m$, $T = 2\,\mu m$, no meander) computed by finite element method in several media and orientations. Cyan curves are for data in air without any passivation layer, red curves for data with a $5\,\mu m$ thick Parylene passivation layer in air and black curves for data with a Parylene passivation layer in water. Solid lines are for data with the resonator facing down and dashed lines for data with the resonator facing up as illustrated in the schematic cross-sections at the bottom.

Table 2.2 – **FEM model - Media and orientation effect.** Resonance frequencies and Q factors of the FEM simulations in Figure 2.12, in several media and orientations. Δf is the full width at half maximum of the voltage attenuation signal at the output of the CPW (ΔV_{out}).

	Medium and orientation	f_0 [GHz]	Δf [GHz]	Q
——	In air, down	3.15	0.17	19
----	In air, up	2.93	0.13	22
——	In air with Parylene, down	2.74	0.17	16
----	In air with Parylene, up	2.57	0.15	17
——	In water with Parylene, down	1.51	0.25	6
----	In water with Parylene, up	1.45	0.18	8

Another interesting parameter to study is the effect of the resistance of the resonator on the resonance. Two different modifications in the model enable to study this effect. Figure 2.14 shows the resonance of a resonator in several media, with and without a meander hot-spot, while the resonance frequency and quality factor values for each configuration are shown in Table 2.3. Figure 2.15 shows the resonance of a resonator when different resistivity values are used to model the Mg domain.
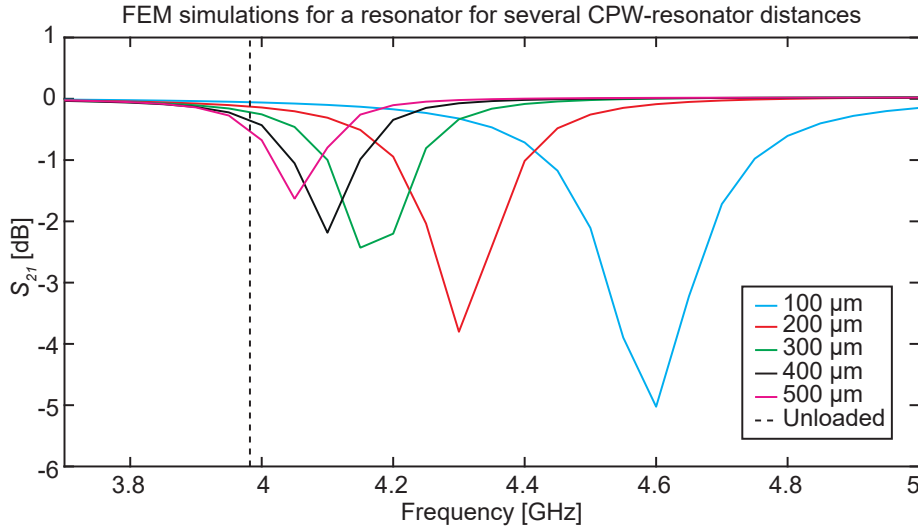
Figure 2.13 – **FEM model - CPW-resonator distance effect.** FEM simulations of the resonance frequency of a resonator as a function of the distance between the coplanar waveguide and the resonator. The simulation is performed in air without any passivation layer. The resonator is facing down, has no meander and its dimensions are $R = 1000\,\mu m$, $W = 120\,\mu m$, $G = 15\,\mu m$, $T = 2\,\mu m$. The unloaded resonance frequency is computed by FEM simulation using an eigenfrequency study.
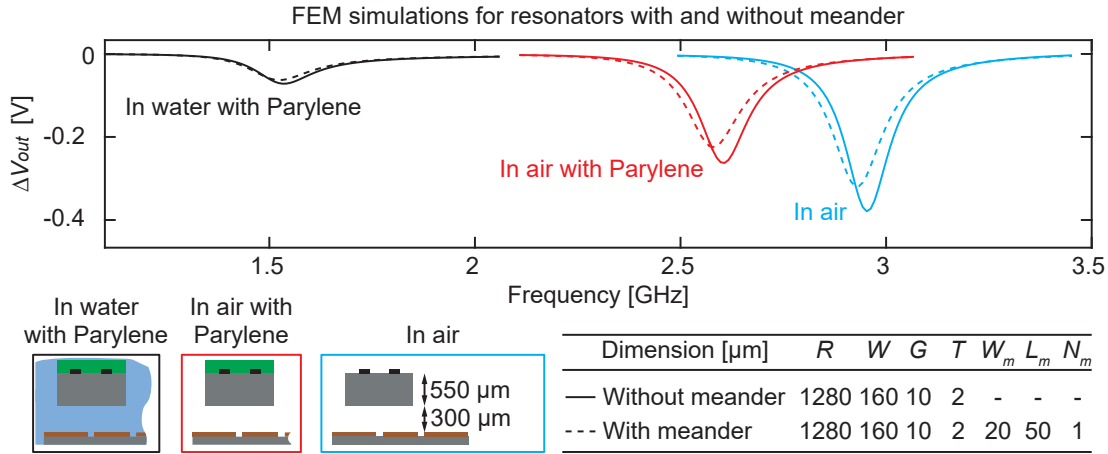
Figure 2.14 – **FEM model - Meander effect.** FEM simulations comparison between resonators with and without meanders in several media. Solid lines are for the resonator without meander and dashed lines for the resonator with meanders. The geometrical parameters are the resonator radius (R), the track width (W), the gap between the two turns of the resonators (G), the resonator thickness (T), the meander width (W_m), the meander length (L_m) and the number of meander (N_m). The plots color represents the medium in which the resonator is characterized and is illustrated by the cross-sections at the bottom. For all the simulations the resonator is facing up.

Table 2.3 – **FEM model - Meander effect.** Resonance frequencies and Q factors of the FEM simulations in Figure 2.14, in several media, with and without a meander hot-spot.

Medium and resonator type	f_0 [GHz]	Q
—— In air, no meander	2.93	22
- - - In air, with meander	2.91	19
—— In air with Parylene, no meander	2.57	17
- - - In air with Parylene, with meander	2.54	16
—— In water with Parylene, no meander	1.45	8
- - - In water with Parylene, with meander	1.44	8
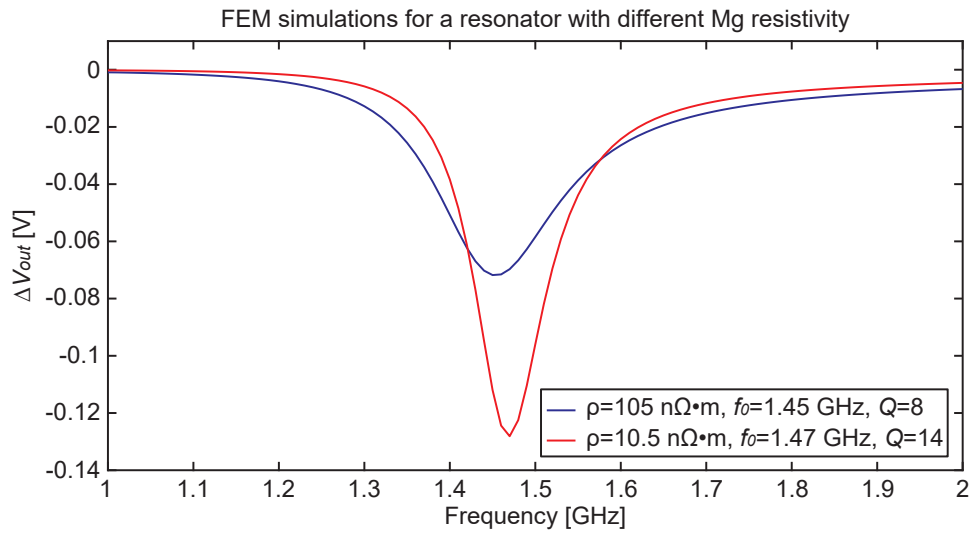
Figure 2.15 – **FEM model - Resistivity effect.** FEM simulations comparison between resonators with different resistivity values to model the Mg domain. The blue curve is for a resistivity of 105 nΩ·m, which is the Mg thin film resistivity measured in Section 2.5.3. The red curve is for a Mg resonator with a resistivity 10 times smaller. A resonator without a meander hot-spot is used ($R = 1280$ μm, $W = 160$ μm, and $G = 10$ μm, $T = 2$ μm), and the simulation is performed with a 5 μm thick Parylene passivation layer, in water with the resonator facing up.

Finally, the influence of the primary excitation system on the current density in the meander is also studied. Figure 2.16a shows the RMS value of the current density in the meander when a 6 W signal is applied at the input of the CPW used for all the simulation so far. This setup is used and detailed in Section 2.5.2 to electrically characterize the resonators. Figure 2.16b shows the RMS current density in the meander when a 6 W input signal is applied to a lambda-over-two (λ/2) CPW resonator. Such an excitation system is used to increase the intensity of the magnetic field, and thus the current in the resonator. This setup is used and detailed in Section 2.7.2 to characterize the heating capabilities of the resonators. When a normal CPW is used, the current density in the meander is 2.6×10^9 A/m^2, whereas it increases to 2.2×10^{10} A/m^2 when a resonant λ/2 CPW is used.

a   Current density with normal CPW: j_{RMS}

$\times 10^9$ A/m^2

A: 2.6x10^9 A/m^2

b   Current density with λ/2 CPW: $j_{RMS, \lambda/2}$

$\times 10^{10}$ A/m^2

A: 2.2x10^{10} A/m^2
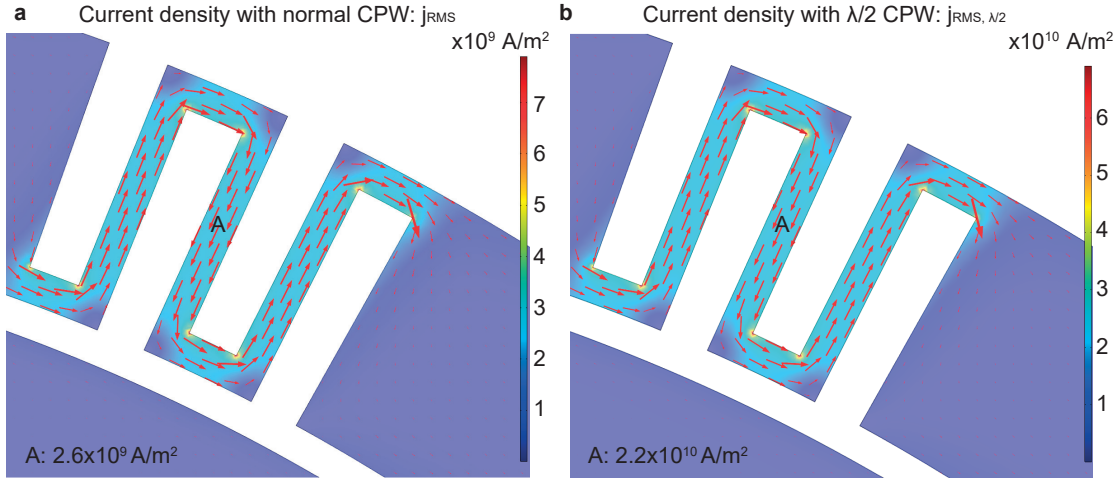
Figure 2.16 – **FEM model - Primary excitation system effect. a**, RMS value of the current density in the meander when a normal CPW is used as primary excitation system, with a 6 W input signal. **b**, RMS value of the current density in the meander when a λ/2 CPW resonator is used as primary excitation system, with a 6 W input signal. In both cases, a reference resonator geometry ($R = 1000$ μm, $W = 120$ μm, $G = 15$ μm, $T = 2$ μm, $W_m = 20$ μm, $L_m = 40$ μm, $N_m = 2$) passivated with a 5 μm thick Parylene layer is used. The resonator is facing up and the surrounding environment is water.

2.3.4   Summary and discussion

Summary   Analytical and FEM models of the resonators were developed in order to predict the resonance and the energy dissipated in the meander hot-spot for a given resonator geometry. The analytical model is based on Faraday's law of induction, where the SR is modeled as an RLC series circuit. It takes into account the resonator geometry, the skin effect and the surrounding environment, but considers a uniform magnetic field. The FEM model considers the same parameters as the analytical model, but also takes into account the primary excitation system and the losses in the surrounding environment. Both model enable to quantify the changes in resonance frequency, quality factor and current in the meander hot-spot as a function of the geometry, the surrounding environment and the intensity of the magnetic field. Additionally, the FEM model enables to see the effect of the primary excitation system design and of the distance between the primary system and the spiral resonator. It also enables to study in details effects such as the decrease of quality factor in lossy environments, and adding a meander hot-spot to the resonator.

Analytical model validity   The validity of the analytical model in terms of resonance frequency and quality factor is discussed in details in Sections 2.5.3 and 2.5.4, where the analytical and FEM models are compared to experimental results. However some considerations can already be discussed here. Since the analytical model considers a uniform B field, it doesn't take into account the CPW-resonator distance. As a result, the resonance frequency computed

in the analytical model is the unloaded resonance frequency, i.e. without considering the influence of the primary excitation system. The resonance frequencies computed from the FEM model and measured experimentally are the loaded resonance frequencies, i.e. they are influenced by the primary excitation system. However, in Section 2.5.3, we show that the unloaded resonance frequency computed with the analytical model lies within 10% of the loaded values obtained by FEM simulations or measured experimentally. The analytical model is thus a good option to rapidly estimate the resonance of spiral resonator with a specific geometry.

Additionally, the analytical model makes the assumption that the spiral resonator can be modeled as an RLC series circuit, and consequently that the current is uniform over the whole resonator. Looking at the current density in the meander, values obtained with the analytical model are approximately twice that of the FEM simulation (4.95×10^9 A/m^2 and 2.3×10^9 A/m^2). This difference can be explained in two ways. Firstly, the B field value given as input parameter in the analytical model is an average value of the non-uniform field produced by the coplanar waveguide. Secondly, the exact electrical model of an SR is probably more complex than a simple RLC series circuit, and several distributed R, L, and C elements should be considered. Nevertheless, more comparisons between the analytical model and the FEM simulations are still required to validate the preliminary evidence that the difference in the estimation of the current density is in the order of a factor of two. However, a factor of two in the current density between the analytical and the FEM models still allows a gross sizing of the SRs with the analytical model. More specifically, it shows that the analytical model can be used to study the power dissipation in the meander, for a rapid first approximation with a large number of resonators. Then, the fine tuning of a small number of resonators can be performed using time-consuming FEM simulations.

CPW-resonator distance   As shown in Figure 2.13, changing the distance between the CPW and the SR, induces a change in the resonance frequency as well as in the signal intensity. When the distance is large, the resonance frequency gets closer to its unloaded value. Nevertheless, the signal intensity also decreases with the distance. This observation show that the FEM model is able to take into account the loading of the resonator by the excitation system. In practice, this means there is a tradeoff between working close to the resonance frequency at which the SR was designed, and having enough energy coupled into the resonator. Additionally as shown in Figure 2.16, the FEM model also demonstrate that using a $\lambda/2$ CPW instead of a normal CPW as the primary excitation system increases the current density in the resonator by one order of magnitude.

Changes from air to water   As shown in table 2.2, for a given resonator geometry, the resonance frequency as well as the Q factor decrease when going from air to water. Such a frequency shift is expected and is due to the increase in the permittivity of the surrounding

environment ($\epsilon_{air} = 1$, $\epsilon_{water} \approx 77$), which results in an increase of capacitance. The relation between the Q factors at two different resonance frequencies can be written as:

$$\frac{Q_1}{Q_2} = \frac{\dfrac{f_1}{\Delta f_1}}{\dfrac{f_2}{\Delta f_2}} \tag{2.47}$$

$$Q_2 = \frac{f_2}{f_1} \frac{\Delta f_1}{\Delta f_2} Q_1 \tag{2.48}$$

The term $\frac{f_2}{f_1}$ depicts the change in Q due to the frequency shift (i.e. change in ϵ_r) while the term $\frac{\Delta f_1}{\Delta f_2}$ expresses the change in Q due to dielectric losses. According to the FEM data in Table 2.2, 60% of the quality factor drop is due to the frequency shift and 40% to the dielectric losses.

Effect of the resistance of the resonator   As shown in Table 2.3, adding a meander hotspot to the resonator has negligible effect on the values of f_0 and Q. Indeed, the resonance frequency decreases by 1% only and the quality factor by less than 10%, which doesn't affect the overall performance of the resonator. Additionally, as shown in Figure 2.15, decreasing the resistivity by one order of magnitude reduces Q by a factor of two only. It is not negligible but it is similar to the effect of going from air to water, as shown in Table 2.2.

2.4 Microfabrication of Mg microresonators on glass

2.4.1 Introduction

A robust and innovative microfabrication process based on ion beam etching is developed to fabricate magnesium-based, water-soluble electronic components. The process reduces the devices exposure to aqueous media without the need to fabricate and use fragile stencils. The fabrication consists of four main steps which are a) the deposition of a Mg thin film by thermal evaporation, b) pattern definition by photolithography, c) pattern transfer into the Mg film by ion beam etching and d) resist stripping with oxygen plasma and acetone.

2.4.2 Methods

Figure 2.17 shows the details of the process flow used to produce the Mg resonators. Firstly a 2 μm thick Mg thin film (99.95% purity, 1/4"x1/4" pellets, Kurt J Lesker, USA) is deposited by thermal evaporation ($2x10^{-6}$ mbar, 8 Å/s, joule evaporator) on a 550 μm thick float glass substrate. No specific cleaning of the substrate is required.

Secondly, a photolithography step is performed: after a dehydration step of 10 min on a hotplate at 120°C, a 2 μm thick layer of photoresist (PR) (AZ9260, Microchemicals GmbH, Germany) is spin-coated on top of the Mg film. Patterns are exposed by direct laser writing, with a dose of 150 mJ/cm^2 at a wavelength of 405 nm. The targeted critical dimension (CD) is 4 μm. After developing the resist (AZ400K 1:3.5 in DI water, Microchemicals GmbH, Germany), a reflow is performed on a hotplate at 120°C during 2 min to smoothen the resist profile. This avoids re-deposition of Mg on the resist sidewalls during the subsequent ion beam etching step. The Mg thin film is etched through by ion beam etching with argon (Ar) ions, at a rate of 120 nm/min and a tilt of -10°.

Finally, the photoresist is removed in acetone after a 1 min oxygen plasma step and the wafer is rinsed in isopropyl alcohol (IPA) and dried with N$_2$. The final DI water rinsing step usually performed with robust materials is waived in this case. For the electrical characterization in air, the devices can be directly used without any further processing step. In order to mimic the permittivity of the in vivo environment, the Mg SRs are also characterized in water. For this purpose, a 5 μm thick Parylene passivation layer is deposited on top of the Mg structures to prevent their degradation and to enable us to study the device in water without any time constraint. Parylene is not biodegradable but passivating the device with a biodegradable layer instead of Parylene would not imply major changes in the fabrication process.

#	Process description	Cross-section
1	**Substrate: float glass** Thickness: 550 µm	Glass Mg PR
2	**Mg thin film deposition** Thermal evaporation Thickness: 2 µm P=2×10^{-6} mbar, R=8 Å/s	
3	**Photolithography** 10 min dehydration, 120°C AZ9260 2 µm, 150 mJ/cm^2	CD=4 µm
4	**Reflow** 2 min reflow, 120°C On a hotplate	
5	**Mg dry etch** IBE: -10° tilt, 100 nm/min	
6	**Photoresist strip** 1 min oxygen plasma Acetone - IPA - N$_2$	

Figure 2.17 – **Mg microfabrication on glass.** Fabrication process to produce biodegradable Mg electronics on a glass substrate with minimal exposure to aqueous media. Mg is first deposited by thermal evaporation and then patterned using photolithography and ion beam etching. The photoresist is finally stripped with oxygen plasma and acetone.

The resonators are fabricated on a 4" wafer and their geometry is tuned using the six geometrical parameter R, W, G, W_m, L_m, and N_m. The layout file for the photolithography is generated using the same Matlab script as for the analytical model and given in Appendix A, with the layout software Clewin4. The variation of the six geometrical parameters is performed according to a full factorial design and to a star design from the design of experiment theories. [137]

The parameters variation range is shown in Table 2.4. In total, there are 36 chips of 1x1 cm, each containing four resonators, on one wafer. The final layout of the wafer and of the chips is shown in Figure 2.18. Some standalone meander structures with contact pads for the electrical characterization are also added in the corner of each chip. At the end of the fabrication process, the chips are diced to facilitate the handling during the characterization. Before dicing, a 4 µm thick photoresist layer (AZ9260, Microchemicals GmbH, Germany) is coated on the front face of the wafer to protect the Mg structures. After dicing, the PR layer is stripped in acetone, and the chips are rinsed in IPA and dried with N$_2$.

Table 2.4 – **Parameters variation range.** Column 0 describes the central points of the design. Column -1 and +1 describe the range for the full factorial design. The full factorial design consists of all the possible combinations of these two columns. The columns -α and +α describe the range for the star design. The star design consists of changing one parameter at once from the central point value to the parameters in columns -α and +α. All values are in µm.

Parameter	-α	-1	0	+1	+α
R	472	720	1000	1280	1528
W	45	80	120	160	195
G	6	10	15	20	24
W_m	6	10	15	20	24
L_m	21	30	40	50	59
N_m	0	1	2	3	4
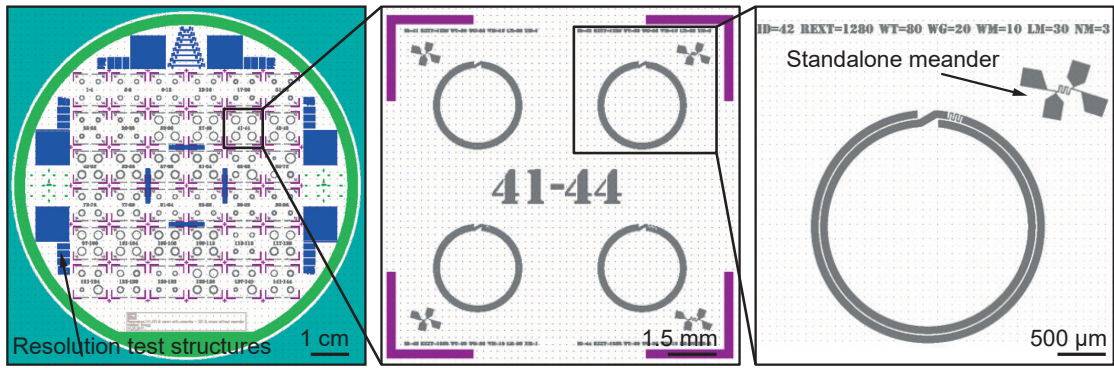
Figure 2.18 – **Wafer layout.** Layout of the Mg resonators on a 4" wafer. The wafer is divided into 36 chips, each containing four resonators. Some standalone meander structures with contact pads for the electrical characterization are also added next to each resonator. Resolution test structures are also included in the layout, on the edge and at the center of the wafer.

2.4.3 Results

Figure 2.19 shows typical fabricated Mg SRs with and without a meander hot-spot. The geometrical parameters designed to tune the resonance frequency and the meander hot-spot are highlighted. As discussed in Section 2.2, the thickness of all the resonators is constant and set to 2 µm in order to keep their electrical resistance to a few ohms only, while still being able to deposit the Mg thin film by thermal evaporation. Figure 2.20 shows Mg test structures demonstrating 4 µm resolution and 0.5 aspect ratio. The resolution is defined as the minimum line width that can be etched in the Mg film and the aspect ratio as the Mg film thickness divided by the resolution. Finally, Figure 2.21 shows scanning electron microscope (SEM) images demonstrating the quality and uniformity of the fabricated Mg resonators at the end of the fabrication process. Figure 2.22 shows a SEM closeup view and a quantitative analysis of the surface roughness of the Mg thin film. The arithmetical mean deviation (Ra) of the surface measured with an atomic force microscope (AFM) in Figure 2.22b is $Ra = 100$ nm.
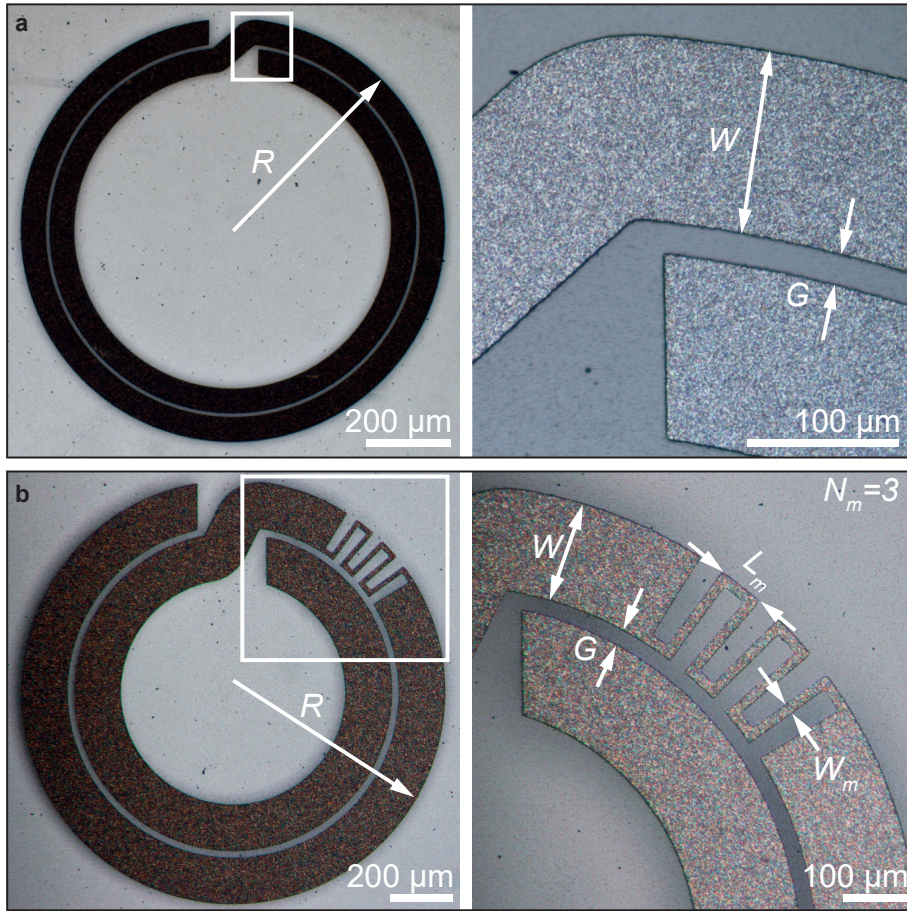
Figure 2.19 – **Fabricated Mg resonators. a,b**, Optical microscope (OM) images of fabricated Mg microresonators without (**a**) and with (**b**) a meander hot-spot. The specific geometrical parameters enabling the tuning of the resonance frequency and of the meander hot-spot are highlighted.
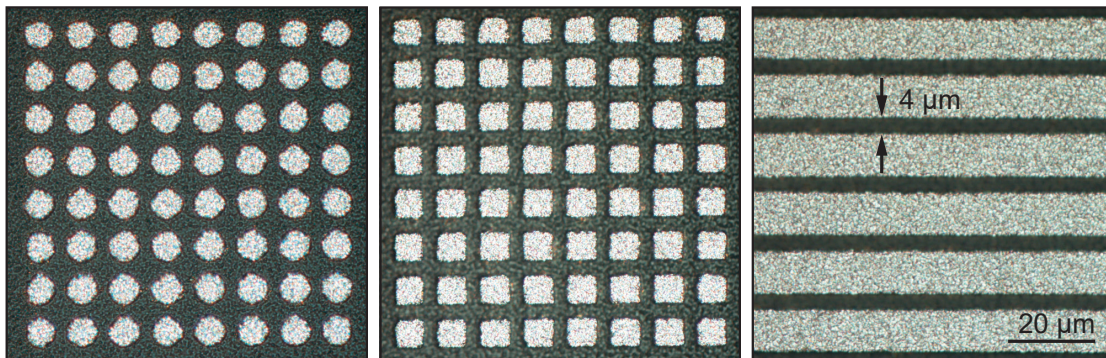
Figure 2.20 – **Resolution test patterns.** OM images of some fabricated Mg microstructures showing 4 µm resolution and 0.5 aspect ratio.
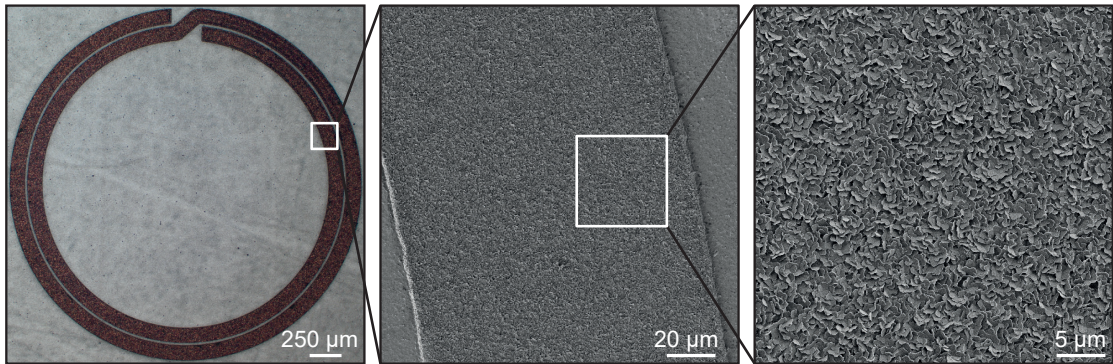
Figure 2.21 – **SEM images of the resonator.** OM (left) and scanning electron microscope (SEM) (center, right) images showing a Mg resonator at the end of the fabrication process. The Mg film quality is uniform over the entire width of the resonator and there are no cracks.
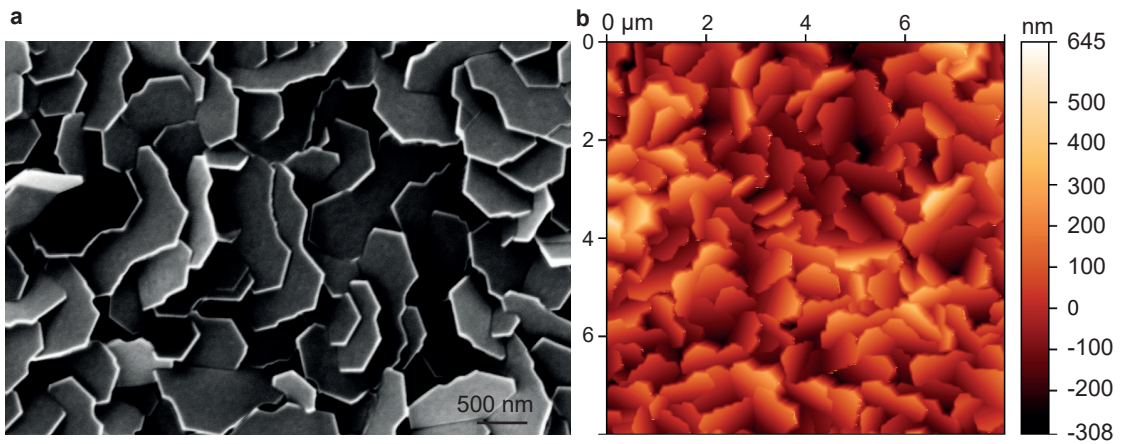
Figure 2.22 – **Surface roughness of the Mg film. a,b**, SEM (**a**) and AFM (**b**) images showing the surface roughness of the Mg film.

2.4.4 Summary and discussion

This new process based on ion beam etching enables producing Mg microresonators without exposing the Mg layer to water based solutions over the entire fabrication process. A resolution of 4 µm is achieved for a 2 µm thick Mg layer with this process. Additionally, the process consists of only four main steps and doesn't require the fabrication and the manipulation of fragile stencils. It is a promising versatile alternative for the fabrication of transient electronics out of water-soluble materials. In comparison, using polyimide stencils to deposit and pattern Mg enables to achieve a resolution of 20 µm for a 3 µm thick layer. [101]

The transfer of Mg microstructures from a non-biodegradable to a biodegradable substrate has been already demonstrated using microfabrication processes based on transfer printing, as discussed in Sections 2.1.1 and 2.1.2. The combination of our new fabrication process with these well established transfer printing processes is used in Chapter 4 to fabricate Mg

resonators on biodegradable membranes. Finally, the good uniformity over the entire width of the resonator and the absence of cracks observed in Figure 2.21 ensure a reliable fabrication and performance of the resonators. The relatively high surface roughness of the Mg film measured in Figure 2.22b is not a problem in itself, since it doesn't alter too badly the film resistivity measured in Section 2.5.3.

2.5 Electrical characterization of the resonators

2.5.1 Introduction

In this section, the electrical performance of the resonators is studied by measuring their resonance frequencies and quality factors in multiple configurations and different surrounding environments. The substrate material consists of a 550 μm thick float glass wafer. In order to characterize the resonant properties of the Mg microresonators, a wireless excitation setup is required because contacting the devices with microprober needles would alter both their resonance frequency and quality factor (Q).

2.5.2 Methods

The sheet resistance of the Mg thin film deposited by evaporation is measured using a conventional four-point resistivity meter (OmniMap RS75, KLA-Tencor, USA). The resistivity is then computed by multiplying the sheet resistance by the film thickness (2 μm).

In order to characterize the electrical performance of the resonators, f_0 and Q values are measured using the wireless characterization setup shown in Figure 2.23a. The working principle of the setup is the following. A signal generator (SG384, Stanford Research Systems, USA) creates a -40 dBm RF signal and couples it into a CPW above which is placed a Mg microresonator. The signal is pulse-modulated at 5 kHz to perform synchronous detection and, hence suppresses the influence of low frequency noise sources on the measured transmission and reflection spectra.

The signal frequency is swept between 1 and 4 GHz, and when it matches the resonator resonance frequency, some electromagnetic energy is coupled from the CPW into the resonator. This results in a drop in the transmitted power and voltage at the output of the CPW. The efficiency of this coupling as a function of the signal frequency is depicted in the transmitted power at the output of the CPW, which is amplified using a power detector (ZX47-60+, Mini-Circuits, USA) and a lock-in amplifier (7260 DSP lock-in amplifier, EG&G Instruments, USA). Finally, an acquisition card is used to record the signal (BNC-2110 + PCIe6361, National Instruments, USA) and the setup control is performed using LabVIEW.

As described previously in Section 2.3.2, the resonance frequency is defined as the frequency at which the voltage attenuation at the output of the waveguide is maximal. The Q factor is defined as the resonance frequency divided by the full width at half maximum (Δf) of the voltage attenuation signal at the output of the CPW (c.f Equation 2.45). Without an SR above the CPW, all the energy is transmitted through the CPW and the recorded signal can be used as a baseline. Baseline removal is performed for each measurement by subtracting the signal obtained with a broken resonator on top of the CPW.
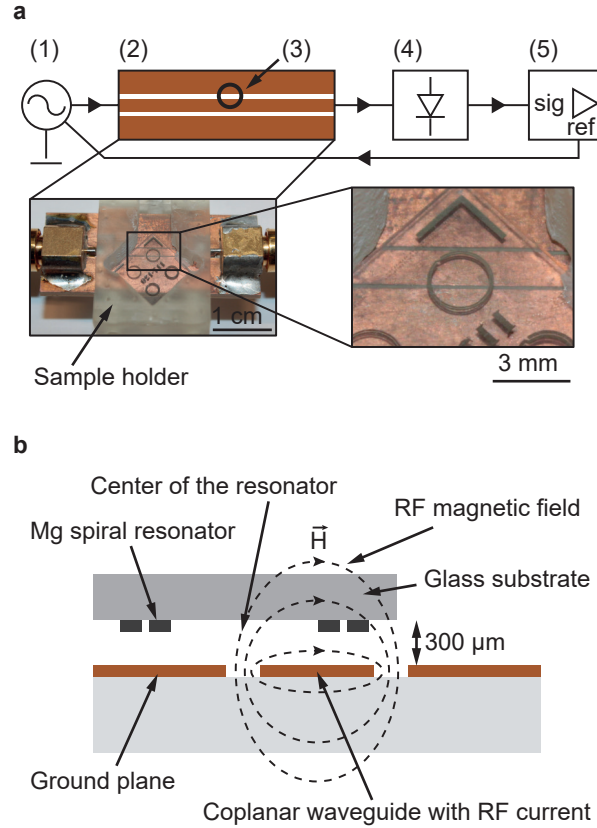
Figure 2.23 – **Electrical characterization setup. a**, The characterization setup consists of (1) a signal generator, (2) a coplanar waveguide, (3) a spiral resonator, (4) a power detector, and (5) a lock-in amplifier. Insets show top-view photographs of the CPW with a SR on top of it. A 3D printed sample holder is used to position the chip 300 µm over the CPW and to align it with the gap of the CPW. **b**, Schematic cross-section view of the characterization setup showing how the magnetic field generated by the current in the CPW interacts with the resonator.

Figure 2.23b shows a schematic cross-section view of the Mg-microresonator on top of the CPW. To maximize the power coupling, the magnetic flux through the resonator should be maximized. Thus, the center of the SR is aligned over one of the two gaps of the CPW. The vertical distance between the device and the CPW is also important since it is a tradeoff between the signal intensity and the loading of the resonator, as discussed previously in Sections 2.3.3 and 2.3.4. In our case, a distance of 300 µm is chosen. A shorter vertical distance results in a larger signal but also in a larger shift from the unloaded resonance frequency of the resonator. As shown in Figure 2.24a and 2.24c, a custom-made 3D printed sample holder is used to precisely set the vertical and horizontal position of the SR with respect to the CPW.

A three screws system is used to to align the center of the resonator over one of the two gaps of the waveguide. As illustrated in Figure 2.24b, for the characterization in water, a 5 µm Mylar film is glued below the sample holder in order to protect the CPW and avoid a short circuit. Additionally, a 5 µm thick Parylene passivation layer is coated on top of the Mg resonators.
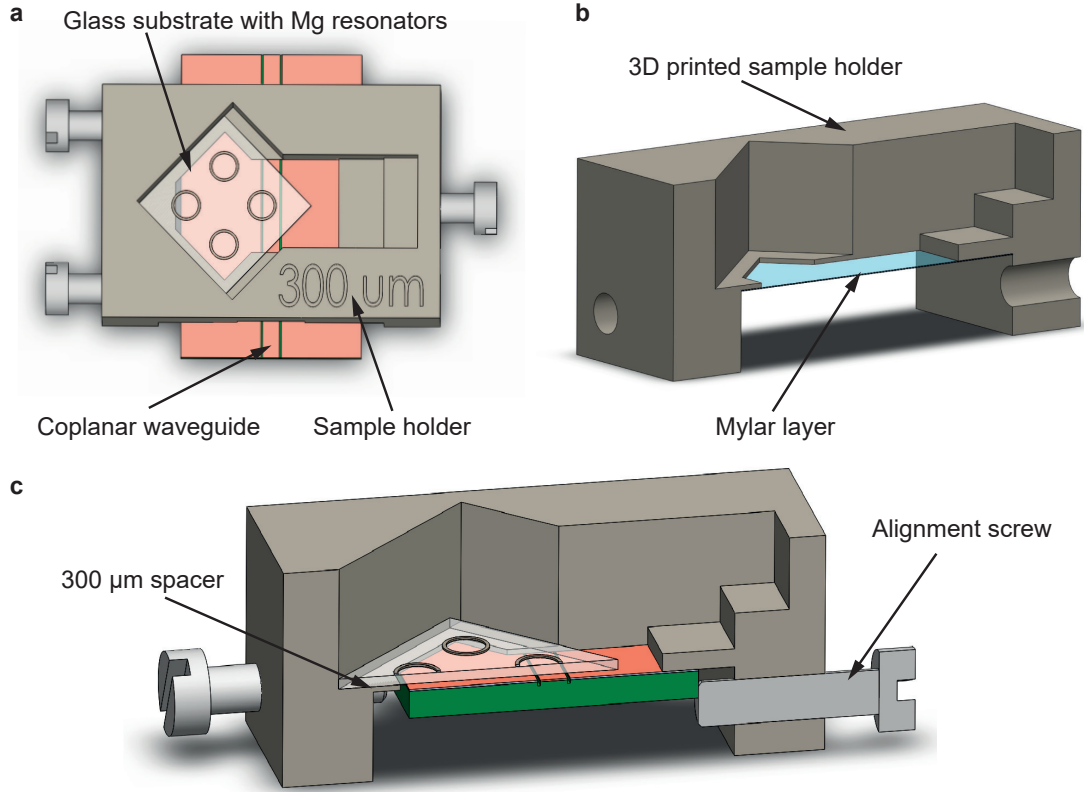
Figure 2.24 – **Sample holder for the characterization setup. a**, A 3D printed sample holder is used to position the chip 300 μm over the CPW and to align the resonator with the gap of the CPW. **b**, Cross-section view showing that to perform the characterization in water, a thin Mylar layer is glued at the bottom of the sample holder, to contain the water in a closed cavity and prevent short circuiting the CPW. **c**, A close-up cross-section view of the characterization setup shows how the sample holder enables to create a 300 μm gap between the chip and the waveguide, and how the resonator can be aligned on top of the CPW using screws.

2.5.3   Results

The thin Mg films deposited by thermal evaporation exhibit a resistivity value of about 100 nΩ·m. For comparison, the resistivity of bulk Mg is 44 nΩ·m. [119] The difference partially comes from the surface roughness of the Mg film measured in Figure 2.22, but a factor of two in the resistivity is not unusual for thin metal films.

As predicted with the analytical and FEM models in Section 2.3, changing the geometrical parameters of the resonator as well as the surrounding environment both induce changes in the resonance frequency and the quality factor. Figure 2.25 shows the resonance of a specific resonator geometry ($R = 1280$ μm, $W = 160$ μm, $G = 10$ μm, $T = 2$ μm, no meander) in several media and orientations, while the resonance frequency and quality factor values for each configuration are shown in Table 2.5. An extensive comparison of the resonance between the analytical model, the FEM model and experimental results is also given in this table.
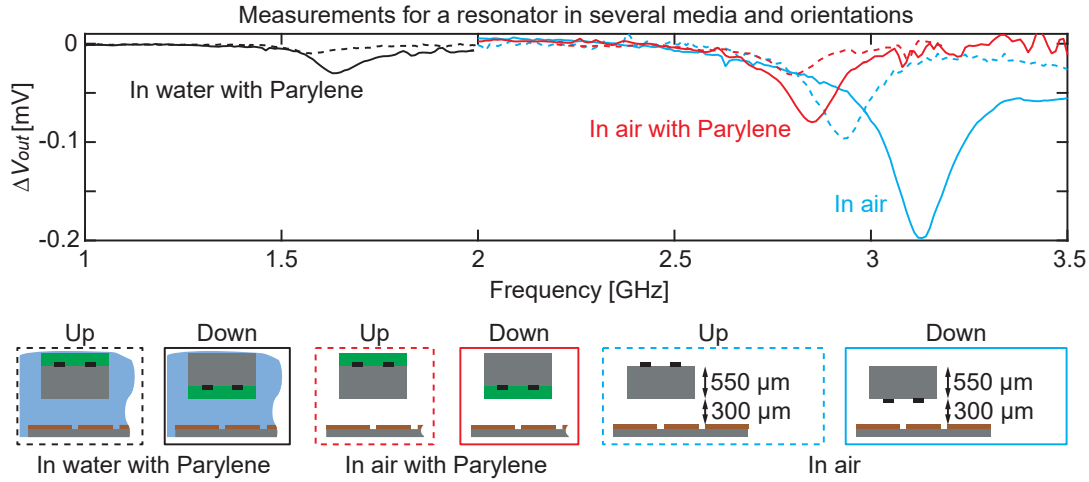
Figure 2.25 – **Electrical characterization - Media and orientation effect.** Resonance of a resonator ($R = 1280\,\mu m$, $W = 160\,\mu m$, $G = 10\,\mu m$, $T = 2\,\mu m$, no meander) measured in several media and orientations. Cyan curves are for data in air without any passivation layer, red curves for data with a 5 μm thick Parylene passivation layer in air and black curves for data with a Parylene passivation layer in water. Solid lines are for data with the resonator facing down and dashed lines for data with the resonator facing up as illustrated in the schematic cross-sections at the bottom.

Table 2.5 – **Models validation and comparison.** Comparison of the resonance frequencies and Q factors measured experimentally, computed by FEM simulation and with the analytical model, in several media and orientations. All the values are for a reference resonator geometry with no meander hot-spot ($R = 1280\,\mu m$, $W = 160\,\mu m$, and $G = 10\,\mu m$, $T = 2\,\mu m$). For the analytical model, there is no difference between the up and down configurations, since it doesn't take into account the distance between the CPW and the resonator, as explained in Section 2.3.4. The last line is for a configuration with the resonator immersed in water without a Parylene passivation layer. The water conductivity is considered to be 0 in the FEM model.

| Medium and orientation | f_0 [GHz] | | | Q | | |
	Measured	FEM	Anal.	Measured	FEM	Anal.
—— In air, down	3.13	3.12	3.12	15	19	13
···· In air, up	2.93	2.92		17	21	
—— In air with Parylene, down	2.85	2.87	3.03	18	19	13
···· In air with Parylene, up	2.80	2.81		19	20	
—— In water with Parylene, down	1.63	1.38	0.97	10	6	5
···· In water with Parylene, up	1.57	1.33		10	7	
In water no Parylene, up	N.A.	0.85	0.87	N.A.	4	4

The measured resonance frequencies of different SR geometries in air (solid lines) and in water (dashed lines) are shown in Figure 2.26. In both cases, the Mg structures are covered with a 5 µm thick Parylene layer to protect them. Geometrical variations of the resonators, resulting in distinct resonance frequencies and Q factors, are described in the table at the bottom left ($1000 < R < 1280$ µm, $80 < W < 160$ µm, $10 < G < 20$ µm) and depicted by different colors in the plots. Detailed numerical values of f_0 and Q for each measurement are described in Table 2.6.
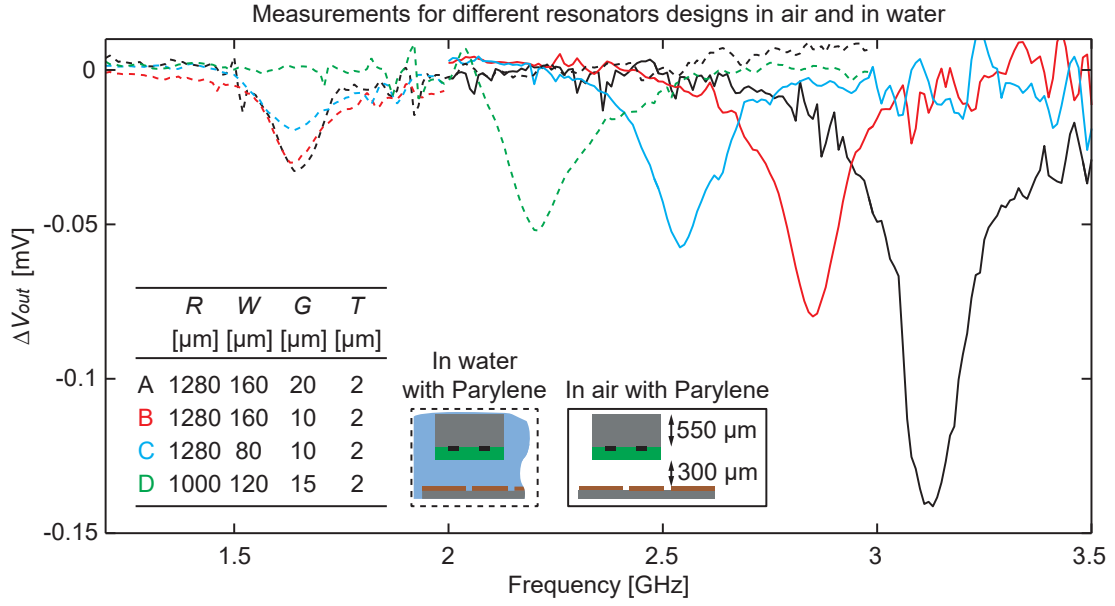
Figure 2.26 – **Electrical characterization - Resonator geometry effect.** Resonance of different resonator geometries in air (solid lines) and in water (dashed lines). In both cases, the devices are passivated with a 5 µm thick Parylene layer and the resonators are facing down, as illustrated by the cross-sections in inset. Geometry changes are described in the table at the bottom left ($1000 < R < 1280$ µm, $80 < W < 160$ µm, $10 < G < 20$ µm) and depicted by different colors in the plots. Resonators without a meander hot-spot are used.

Table 2.6 – **Electrical characterization - Resonator geometry effect.** Resonance frequencies and Q factors of the measurements in Figure 2.26, for several resonator geometries in air and in water. Measurement for resonator D in air is not available because it is higher than 4 GHz which is the maximum frequency of the signal generator used.

	In air with Parylene		In water with Parylene	
	f_0 [GHz]	Q	f_0 [GHz]	Q
A	3.13	18	1.64	13
B	2.85	18	1.63	10
C	2.54	14	1.64	9
D	N.A.	N.A.	2.21	12

Finally, the effect of the resistance of the resonator on the resonance is also studied. Figure 2.27 shows the resonance of a resonator in several media, with and without a meander hot-spot, while the resonance frequency and quality factor values for each configuration are shown in Table 2.7.
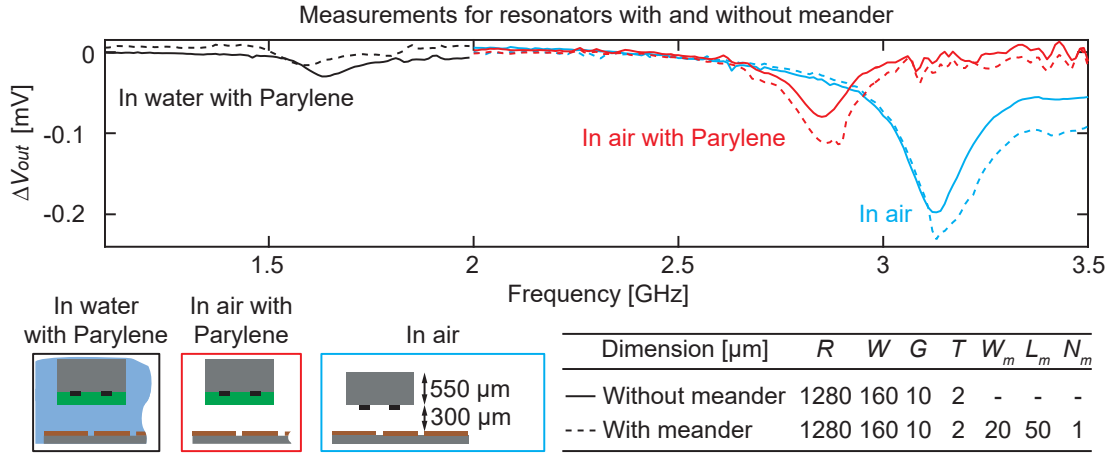
Figure 2.27 – **Electrical characterization - Meander effect.** Measurements comparison of resonators with and without meanders in several media. Solid lines are for the resonator without meander and dashed lines for the resonator with meanders. The geometrical parameters are the resonator radius (R), the track width (W), the gap between the two turns of the resonators (G), the resonator thickness (T), the meander width (W_m), the meander length (L_m) and the number of meander (N_m). The plots color represents the medium in which the resonator is characterized and is illustrated by the cross-sections at the bottom. For all the simulations the resonator is facing down.

Table 2.7 – **Electrical characterization - Meander effect.** Resonance frequencies and Q factors of the measurements in Figure 2.27, in several media, with and without a meander hot-spot.

	Medium and resonator type	f_0 [GHz]	Q
—	In air, no meander	3.13	15
---	In air, with meander	3.13	13
—	In air with Parylene, no meander	2.85	18
---	In air with Parylene, with meander	2.89	16
—	In water with Parylene, no meander	1.63	10
---	In water with Parylene, with meander	1.59	10

2.5.4 Summary and discussion

Summary   The electrical characterization of the resonators is performed by measuring their resonance frequencies and quality factors in multiple media and orientations. For this purpose, a wireless characterization setup is designed and consists in using a coplanar waveguide to couple some electromagnetic energy into the resonator. By recording the power at the output of the CPW as a function of the frequency, f_0 and Q values can be determined. The resonators are characterized in air with no passivation layer, in air with a 5 µm thick Parylene passivation layer, and in water with a 5 µm thick Parylene passivation layer. The characterization is performed for multiple resonator geometries, with and without a meander hot-spot.

Media and CPW-resonator distance effect   As shown in Figure 2.25 and table 2.5, for a given resonator geometry, the resonance frequency, the Q factor, and the signal intensity depend on the surrounding media and on the distance between the CPW and the resonator. These results are in good agreement with the FEM simulations from Sections 2.3.3 and 2.3.4. The decrease in the resonance frequency when the resonator is further away from the CPW (i.e. facing up) comes from the reduced loading of the resonator by the excitation system. However, it results in a lower signal intensity. We can see that a spacing of 300 µm is a good tradeoff between the loading and the signal intensity, particularly in water, where a spacing of 850 µm results in a signal close to the detection limit of the setup.

Furthermore, the decrease in the resonance frequency when going from air to water is due to the increase in the permittivity of the surrounding environment. As discussed in Section 2.3.4, the decrease in the Q factor is due to this frequency shift and to the dielectric losses in water. However, according to the experimental data in Table 2.2, the decrease in the quality factor between air and water is smaller than the expected drop due to the frequency shift alone (i.e. $Q_{air}/Q_{water} < f_{0,air}/f_{0,water}$). This phenomenon can be explained as follow. Firstly, the quality factor is sensitive to the CPW-resonator distance, and two different sample holders were used for the measurements in air and in water. Secondly, due to interference and signal distortion, the accuracy of the quality factor from the measured data is limited.

Models comparison and validity   As shown in Table 2.5, very good agreement exists between the FEM simulations and the measurements in air, with and without a Parylene passivation layer, for both f_0 and Q (Δf_0=<1% and ΔQ=<30%). In water however, there is a 16% mismatch in the resonance frequency between the FEM simulations and the experimental data. A possible explanation is to consider that, for the experimental data, there are air bubbles trapped in the 300 µm gap between the CPW and the sample, which shifts the resonance frequency upwards. Another explanation comes from the accuracy of the Parylene passivation layer thickness. Indeed, as shown in Figure 2.28, the thickness of the passivation layer strongly influences the resonance frequency, especially for thin films. A slightly thicker Parylene layer would shift the resonance frequency upwards.
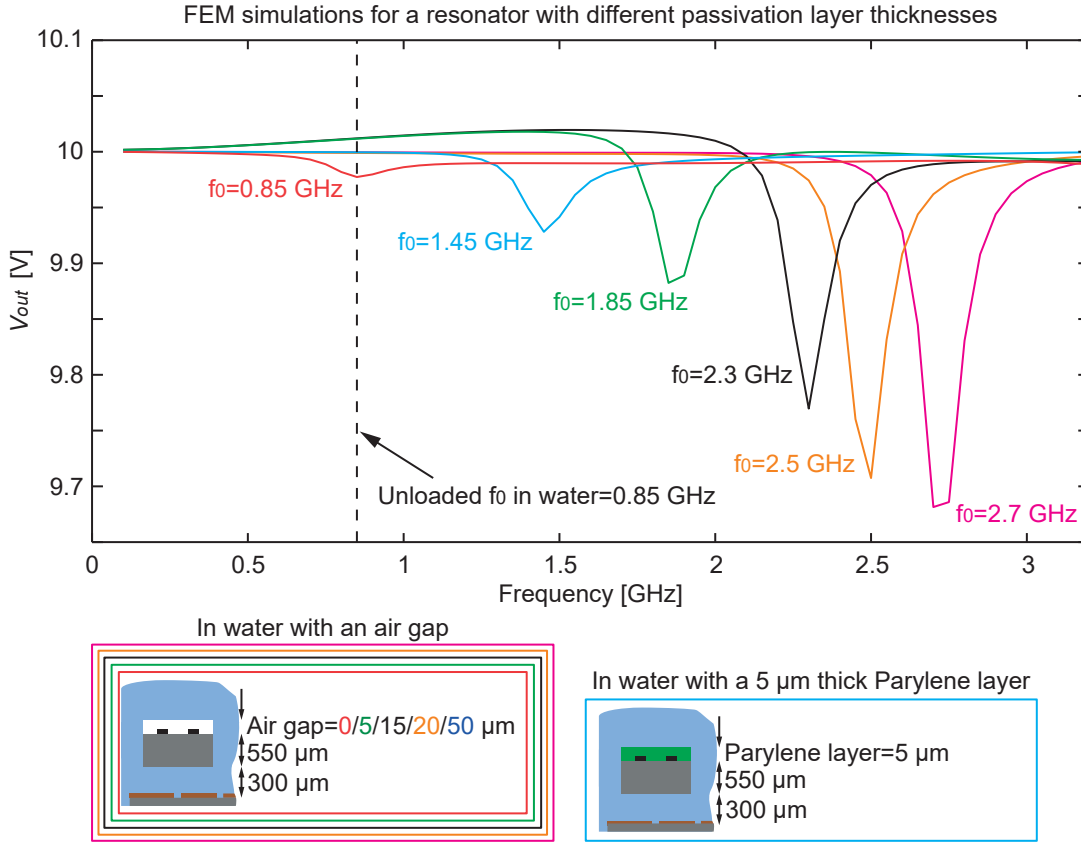
Figure 2.28 – **FEM model - Passivation layer thickness effect.** FEM simulations of the resonance frequency of a resonator in water, for multiple thicknesses of an air gap. Results are also compared to the unloaded resonance frequency of the resonator in water without a passivation layer, and to the resonance with a 5 µm thick Parylene passivation layer. The resonator is facing up, has no meander and its dimensions are $R = 1280$ µm, $W = 160$ µm, $G = 10$ µm, $T = 2$ µm. Because of time concerns, no baseline simulations were performed and the output voltage signal is used instead of the change in the output voltage. The unloaded resonance frequency is computed by FEM simulation using an eigenfrequency study.

The validity of the analytical model in terms of resonance frequency can also be discussed according to values in Table 2.5. In the analytical model, there is no distinction between the resonator facing up or down, as the distance between the CPW and the resonator is not taken into account. The unloaded resonance frequency is computed. It should thus be compared to the resonance of the resonator facing up, since it is the case with the less loading of the resonator by the excitation system.

In air, with and without a Parylene passivation layer, there is a <10% mismatch in the resonance frequency between the analytical model and the FEM/experimental values. This mismatch can be explained by the approximations in the computation of the capacitance and inductance values in the analytical model. In water with a Parylene passivation layer however,

the mismatch of resonance frequency with the FEM value goes up to 33% and is reversed compared to the case in air (f_0 anal. $< f_0$ FEM/meas.).

This difference is hard to explain. As shown in the last line of Table 2.5, when the resonator is in water without a Parylene passivation layer, the analytical model matches again the FEM simulation. Therefore, a possible explanation of the mismatch is to consider that the analytical model is more inaccurate in multi-layers environments. However, the configuration with a Parylene passivation layer in air is also a multi-layer environment and the mismatch is not as dramatic as in water. It is worth noting that in this paragraph, all the analysis is performed according to one specific resonator geometry. Nevertheless, it is also valid for other geometries as shown by the data in Appendix B.

Resonators geometry effect   As shown in Figure 2.26 and Table 2.6, in air, a small gap variation of 10 μm (between resonators A and B) induces a relatively large frequency shift of 0.28 GHz. In water, for the same gap variation, the frequency shift is only 0.01 GHz. As detailed in Appendix B, between resonators A and B, FEM simulations predicted a frequency shift of 0.29 GHz in air and 0.04 GHz in water. Consequently, a smaller frequency shift is expected in water, but it is slightly worse experimentally than computed by FEM simulations. However, our measurements show that obtaining large frequency shifts in water is still possible but requires larger geometrical variations ($\Delta R = 280$ μm, $\Delta f_0 = 0.57$ GHz, between resonators A and D). It is thus not a limitation in itself but an important parameter to consider when designing the resonators.

Meander effect   Finally, as shown in Figure 2.27 and Table 2.7 and similarly to what was observed with the FEM model in Sections 2.3.3 and 2.3.4, adding a meander hot-spot to the resonator has negligible effect on the values of f_0 and Q. Indeed, the resonance frequency decreases by less than 3% and the quality factor by less than 15%, which doesn't affect the overall performance of the resonator.

2.6   Degradation study of the resonators

2.6.1   Introduction

Previous studies showed that Mg degradation rate in aqueous media varies from a few tens of nm/h to a few μm/h. [100]. In this section we study the degradation timescale of our Mg microresonators in terms of material dissolution but also in terms of the resonance of the resonators. Additionally, a study of the degradation mechanisms responsible for the decrease in the performance of the resonator during the degradation is also performed. The degradation is studied in phosphate-buffered saline (PBS) in order to better mimic the in vivo environment compared to simply using water.

2.6.2   Methods

The degradation of the Mg microresonators in PBS is performed as follow. 150 ml of phosphate-buffered saline (PBS, pH 7.4, Merck, Switzerland) is poured in a beaker and placed on a stirring hotplate at 37°C. For the full material dissolution experiment, stirring is set to 250 rpm to have a uniform temperature and pictures are taken every 30 s without removing the sample (2 μm thick, no Parylene passivation) from the solution. For the resonance degradation experiments, stirring is set to 0 rpm. The sample (2 μm thick, no Parylene passivation) is immersed in the solution for a defined amount of time and subsequently dried under a light nitrogen flow. An optical microscope (OM) image is taken and the resonance is measured before immersing the sample in the solution again for the next degradation step. The same characterization setup and measurement principle as described in Section 2.5.2 is used to measure the resonance. SEM images are taken after the last degradation step with an acceleration voltage of 2 kV, a working distance of 7.6 mm, 0° tilt and recorded using a secondary electrons detector. Additionally, an elemental analysis is also performed using an energy-dispersive X-ray (EDX) detector.

2.6.3   Results

Figure 2.30 shows sequential optical images of the Mg microresonators in phosphate-buffered saline at 37°C under gentle stirring. The left image shows the Mg microstructures a few seconds after their immersion in PBS. The center image shows the same sample after 10 minutes, while the right image shows the sample after 50 minutes. Additionally to the material dissolution in itself, it is also interesting to study the degradation of the performance of the resonator, which can be measured by its quality factor. Figure 2.31 shows the resonance of a microresonator ($R = 1360$ μm, $W = 120$ μm, $G = 15$ μm, $T = 2$ μm) in air after several successive immersion steps in PBS without stirring. Between each immersion step in PBS and the subsequent resonance measurement, the chip is dried under a gentle nitrogen flow. We can observe that the quality factor decreases rapidly and the resonance completely vanishes after 250 s.
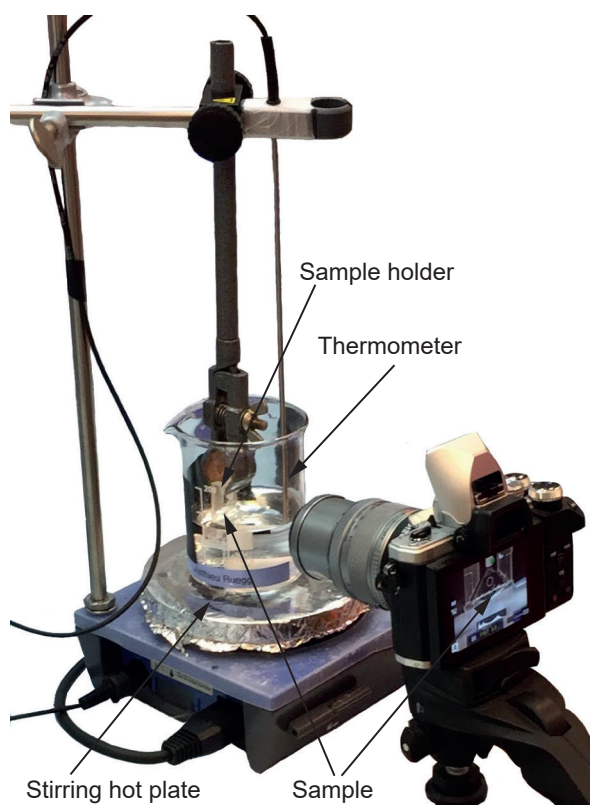
Figure 2.29 – **Degradation setup.** Setup used to characterize the degradation of the Mg resonators. The chip with the Mg resonators is immersed with the sample holder in a 150 ml solution of PBS. A stirring hotplate connected to a thermometer is used to keep a uniform and constant temperature at 37°C.
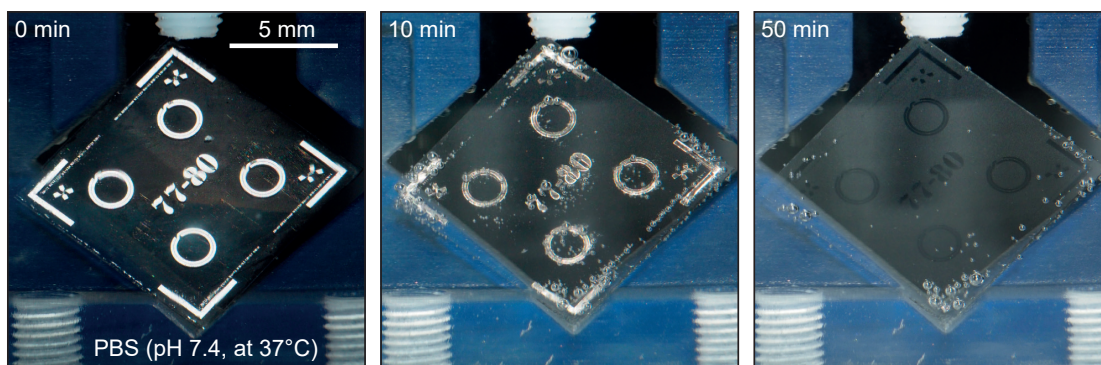
Figure 2.30 – **Full dissolution of Mg microresonators.** Sequential images of Mg microresonators dissolution (2 µm thick) in phosphate-buffered saline (PBS, pH 7.4) at 37°C under gentle stirring. Microresonators in their initial state (0 min, left), during dissolution (10 min, center), and after full dissolution (50 min, right).
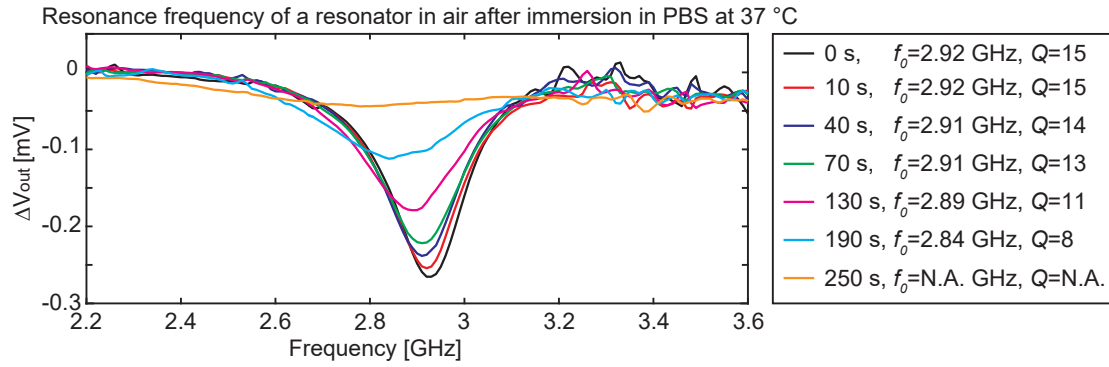
Figure 2.31 – **Degradation of the resonance.** Resonance of a resonator ($R = 1360$ μm, $W = 120$ μm, $G = 15$ μm, $T = 2$ μm) in air after different immersion times in PBS (0–250 s) without stirring.

According to the measurements performed in Figures 2.30 and 2.31, the degradation of the resonance of the resonators occurs more rapidly than the full material dissolution. Therefore, in order to study the underlying mechanisms leading to the failure of the Mg microresonators, sequential OM and SEM images of the resonators at different degradation times are recorded and shown in in Figures 2.32 and 2.33.
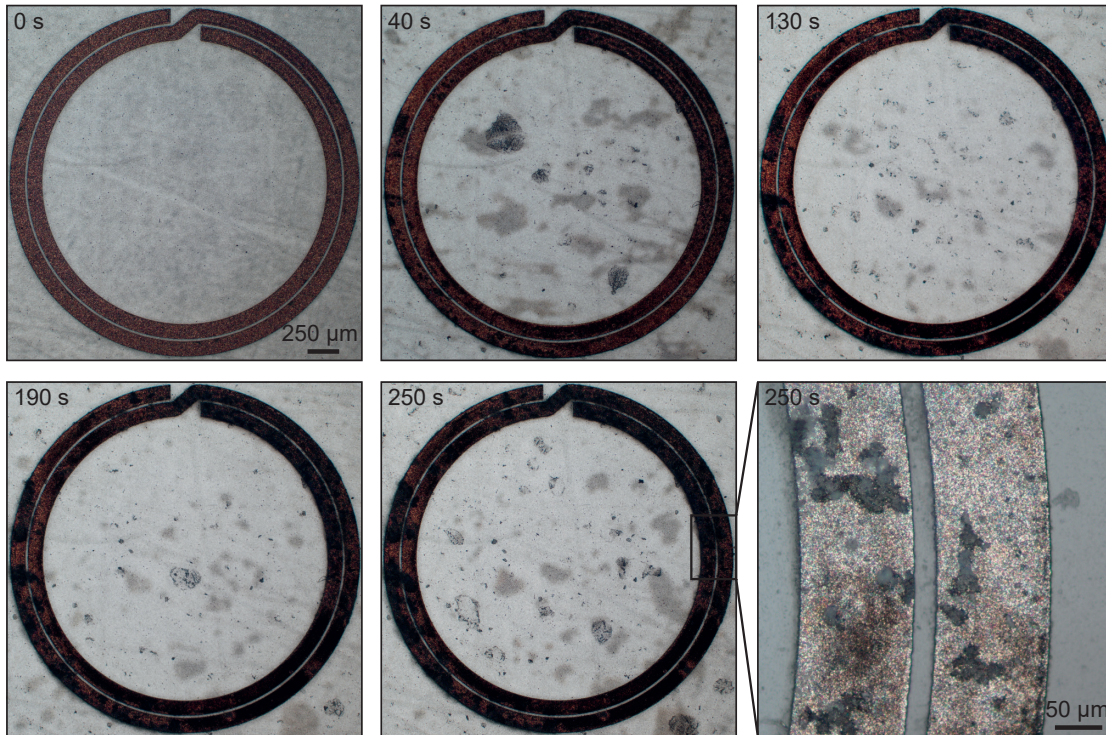
Figure 2.32 – **OM images of the degradation of a resonator.** Sequential optical microscope images of the degradation of the resonator used for the measurements in Figure 2.31.
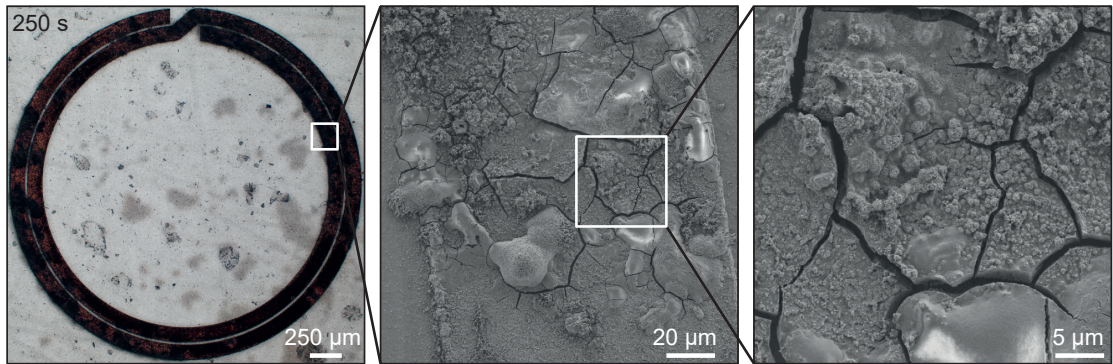
Figure 2.33 – **SEM images of the degradation of a resonator.** Optical microscope (left) and scanning electron microscope (center, right) images of the resonator used for the measurements in Figure 2.31 after 250 s in PBS .

These images clearly show that voids and cracks appear in the Mg resonator during the degradation process. Additionally, Figure 2.34 shows high aspect ratio MgO spikes on the surface of the Mg film during its degradation. The material composition is studied using energy-dispersive X-ray spectroscopy.
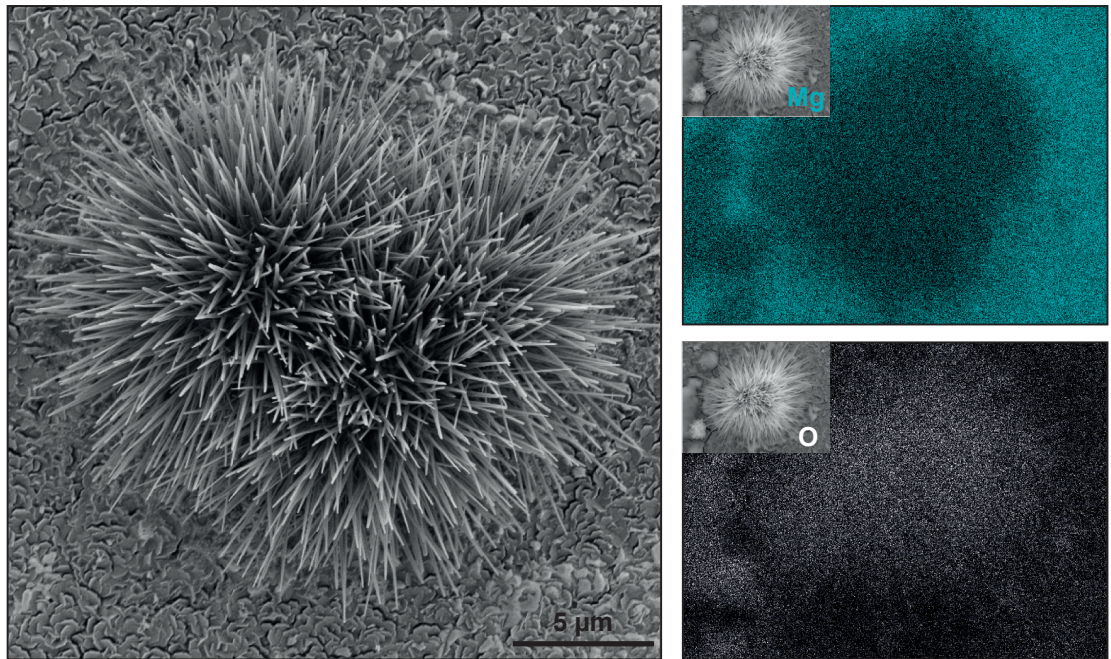
Figure 2.34 – **MgO spikes on Mg during the film degradation.** SEM image (left) of high aspect ratio MgO spikes on the surface of the Mg film during it's dissolution. The composition of the spikes is studied using energy-dispersive X-ray spectroscopy (EDX). The Mg (blue) and O (white) signals are shown on the right side of the figure.

2.6.4 Summary and discussion

Summary   In this section, the degradation of our Mg resonators in PBS was studied. In terms of material dissolution, a full degradation time of 50 min was observed. In terms of the performance of the resonators, the resonance completely disappear after a few minutes already. Additionally, the underlying mechanisms leading to the failure of the resonators were also characterized by imaging the resonators with optical and scanning electron microscopes, at different degradation times.

Material dissolution   In Figure 2.30, hydrogen bubbles that are typical of the Mg dissolution process by hydrolysis are clearly visible. [59] As shown in the right image, after 50 minutes in PBS, the Mg structures are fully dissolved and there are no more bubbles. The contrast pattern visible on the image is due to over-etching of the glass substrate during the ion beam etching step, which was intentionally produced to ensure a complete etching of the Mg layer. As discussed in Section 2.1.1, such a short time window of a few tens of minutes implies that a passivation layer must be used to tailor the degradation time to several days or weeks once implanted in the body. [64] Several materials such as silk, [108] silicon dioxide and nitride, [49, 51, 106] polyanhydrides, [50] or poly(lactic-co-glycolic acid) (PLGA) can be used for this purpose. [48, 49] The degradation time of the entire device is defined first by the degradation rate of the passivation layer, and subsequently by the degradation rate of the actual device layer. Hence, a stable operation regime during several days or weeks followed by a rapid degradation of the device functionality within a few minutes is expected.

Degradation of the resonance   Figure 2.31 shows that already after a few tens of seconds, the Q factor of the resonator begins to decrease. After 190 s the Q factor is reduced by a factor of two, and after 250 s no resonance can be measured anymore. For geometries having fine meander structures, the degradation time until the resonance vanishes is a few tens of seconds only. Such a rapid degradation of the resonance represents an important challenge for their fabrication. Indeed, it confirms that the production of thin Mg resonators is not compatible with the rinsing steps associated to wet etching processes, which would severely damage the finest structures of our device. The use of a manufacturing process which avoids exposing the structures to an aqueous media is thus required.

Failure mechanisms of the resonators   Finally, figures 2.32 and 2.33 show the underlying mechanisms leading to the failure of the Mg microresonators. In its initial state, before immersion in PBS, the Mg film quality is uniform over the entire resonator surface, as shown in Figure 2.21 in Section 2.4.3. However, after 250 s in PBS, the Mg film is not uniform anymore, and some areas of the resonators are partially degraded by hydrolysis. In these areas, voids and cracks propagating across the entire Mg track clearly appear in the optical and scanning electron microscope images. As a result, the electrical resistance of the resonator increases, which leads to a decrease of the Q factor and a degradation of the resonance.

2.7 Wireless heating of the resonators

2.7.1 Introduction

The setup that we designed and used for the electrical characterization of the resonators in Section 2.5 does not amplify the signal generated by the signal generator and is thus not capable to deliver sufficient power to wirelessly heat the meander hot-spot of the resonators until they break. We therefore designed and fabricated a different setup for this purpose, which working principle is detailed below in Section 2.7.2. With this setup, the power coupled into the Mg SRs is increased by using an RF power amplifier as well as by replacing the CPW by a lambda-over-two ($\lambda/2$) CPW resonator. As a result, the magnetic field generated by the $\lambda/2$ CPW resonator is much stronger than the one produced by the transmission line. According to FEM simulations in Sections 2.3.3 and 2.3.4, the induced current in the SR increases by more than an order of magnitude.

This new setup is also able to measure the resonance of the SR in situ. Consequently, it is possible to measure the resonance of the SR before and after applying a high input power into the $\lambda/2$ CPW and hence, to detect if the SR was thermally damaged. The power required to wirelessly heat and break the meander hot-spot of a resonator, or alternatively to damage the 5 µm thick Parylene passivation layer, is studied in this section. Additionally, the selective breaking of one specific resonator when several resonators are exposed to the same RF magnetic field is also demonstrated. Finally the temperature as a function of the power dissipated in the meander is also studied for several meander designs.

2.7.2 Methods

Wireless heating of the resonators In order to generate enough power to wirelessly heat and break the meander hot-spot of the resonators, a new setup was designed. It enables to increase the induced current in the SRs at a specific frequency. The setup is illustrated in Figure 2.35a and its working principle is the following: as for the wireless electrical characterization in Section 2.5, the RF generator generates a 5 kHz pulse modulated RF signal, and sweeps the frequency between 1 and 4 GHz. The signal is amplified using a 15 W RF power amplifier (gain=46 dB, ZHL-15W-422+, Mini-Circuits, USA), and subsequently coupled through a directional coupler (ZGDC6-362HP+, Mini-Circuits, USA) into a $\lambda/2$ CPW resonator. The reflected signal is coupled through the directional coupler and detected at the coupled port using attenuators (-50 dB), and the same detection system as for the wireless electrical characterization.

Using a resonant CPW enables to increase the current in the waveguide at a specific frequency, for a fixed amount of input power. As a result, the generated magnetic field is stronger, which increases the induced current in the coupled SR. The $\lambda/2$ CPW resonator consists of a 50 Ω CPW with a transmission line of a defined length and an open end. To tune its resonance frequency, the length of the CPW is trimmed and a capacitance between the input port and the
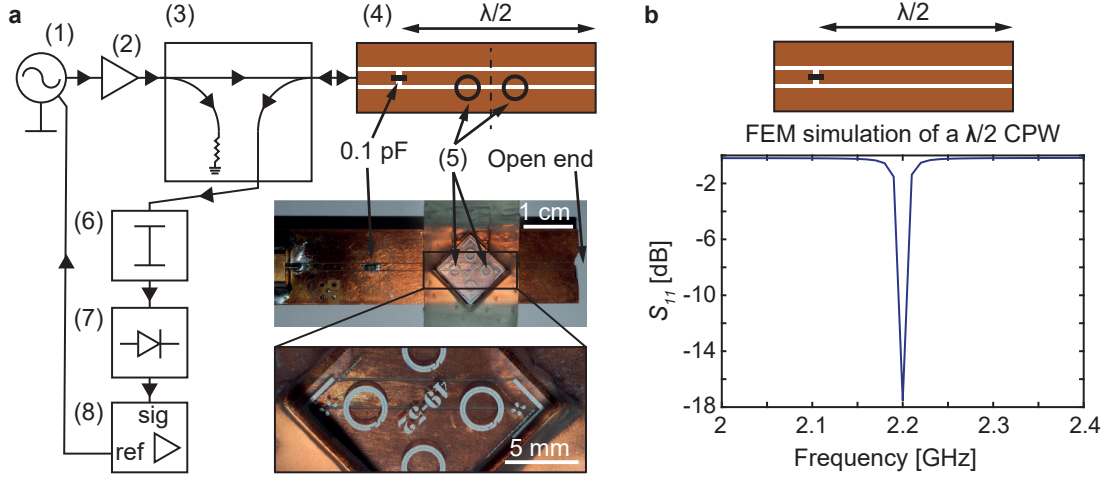
Figure 2.35 – **Wireless heating setup. a**, The wireless heating setup consists of (1) a signal generator, (2) a power amplifier, (3) a directional coupler, (4) a lambda-over-two coplanar waveguide resonator, (5) SRs, (6) attenuators, (7) a power detector, and (8) a lock-in amplifier. Insets show top-view photographs of two SRs aligned on the CPW resonator. A 0.1 pF capacitance is used to match the CPW resonator to 50 Ω. **b**, FEM simulation showing the resonance of the λ/2 CPW resonator when no SR is placed on top of it.

transmission line is used to match it to 50 Ω. As shown in Figure 2.35b, the resonance frequency of the λ/2 CPW resonator is defined as the frequency at which the scattering parameter S_{11} has the lowest value. S_{11} is defined in Equation 2.49, with V_{in} and V_{out} the input and output (reflected) voltage waves at the port of the λ/2 CPW resonator.

$$S_{11} = 20 log_{10}\left(\frac{V_{out}}{V_{in}}\right) \tag{2.49}$$

The relationship between the resonance frequency and the length of the λ/2 CPW resonator is defined in Equation 2.50, with c the speed of light in a free space and ϵ_{er} the effective relative permittivity of the CPW. The quality of the 50 Ω matching is proportional to the value of the attenuation at resonance.

$$l_{\lambda/2} = \frac{c}{2 f_0 \sqrt{\epsilon_{er}}} \tag{2.50}$$

Once the λ/2 CPW resonator is tuned and matched to the same resonance frequency as the SR to heat, a -5 dBm non-modulated signal is generated by the signal generator at the resonance frequency of the system, for a time longer than 2 s. A -5 dBm signal at the output of the signal generator results in a 10 W signal at the input of the λ/2 CPW resonator after amplification. The setup used here enables in-depth characterization of material and device functionalities, with well-controlled and reproducible environmental conditions. For subsequent in vivo experiments a setup able to generate a stronger magnetic field at a larger distance will be required. [48, 50, 55, 75]

Meander temperature measurement In addition to wirelessly heat the resonators, it is also important to characterize the hot-spot temperature as a function of the dissipated electrical power for several meander geometries. The temperature was measured by monitoring, with a four-point probe setup, the change in resistance when a DC current is applied through the meander. To this aim, standalone meander geometries with contact pads are specially designed, as shown in the inset of Figure 2.36. A sourcemeter (Serie 2400, Keithley, USA) is used to generate a current (I) and simultaneously measure the voltage drop (U) across the meander. The current is progressively increased in steps of 5 mA until the meander breaks while the voltage is recorded. The power through the meander (P_m) as well as the resistance of the meander (R_m) for each data points are computed according to Equations 2.51 and 2.52.

$$P_m = UI \qquad [\text{W}] \tag{2.51}$$

$$R_m = \frac{U}{I} \qquad [\Omega] \tag{2.52}$$
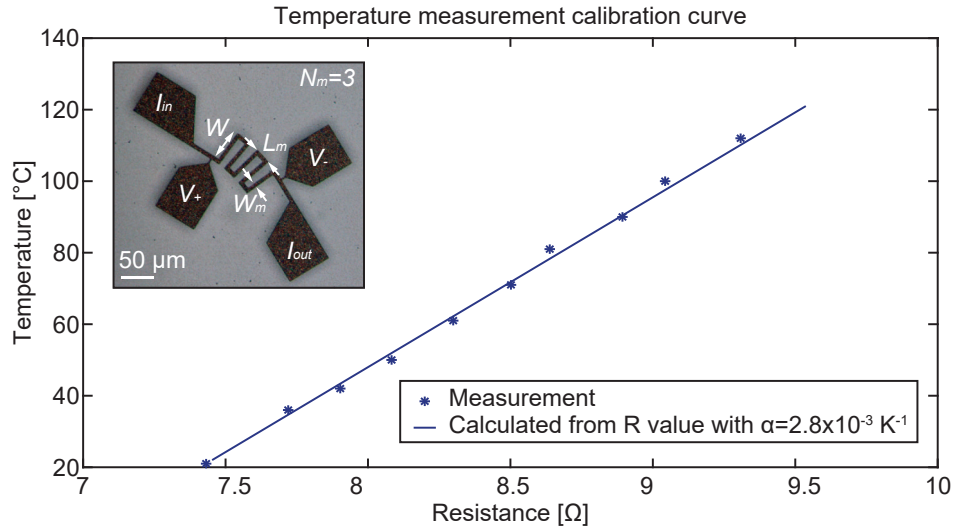
Figure 2.36 – **Temperature measurement calibration.** Temperature of a meander hot-spot as a function of its resistance value. The stars are data points obtained by measuring the resistance of the meander hot-spot when it is placed on a hot plate. The solid line is the calculated temperature obtained using the temperature coefficient $\alpha = 2.8 \times 10^{-3}$ K^{-1} in Equation 2.55. The picture in inset shows a typical standalone meander geometry used in experiments to characterize the hot-spot temperature. It is connected to four contact pads in order to record the voltage drop when a current is applied through the meander with probes.

The average temperature of the meander hot-spot is determined from the meander resistance value and a preliminary calibration discussed hereafter. The temperature effect on the resistance value is described in Equation 2.53, with T the temperature of the meander, R_{T0} the resistance value at room temperature, α the resistance temperature coefficient and ΔT the difference between T and $T0$.

$$R(T) = R_{T0}(1 + \alpha \Delta T) \tag{2.53}$$

By measuring the meander resistance when placed on a hotplate while increasing the temperature between 30°C and 120°C, α can be computed according to Equation 2.54, with $\Delta R = R(T) - R_{T0}$. The numerical values given in Equation 2.54 are the average and standard deviation computed form the α values obtained for each temperature setpoint.

$$\alpha = \frac{\Delta R}{R_{T0}\Delta T} = 2.8\text{x}10^{-3} \pm 1.45\text{x}10^{-4} \qquad [\text{K}^{-1}] \tag{2.54}$$

For comparison $\alpha_{Mg,bulk}$=3.7x10^{-3} K^{-1}. Knowing the value of α, it is possible to compute the temperature for each resistance value measured according to Equation 2.55.

$$T = T0 + \frac{\Delta R}{\alpha R_{T0}} \qquad [\text{°C}] \tag{2.55}$$

Figure 2.36 shows the quality of this calibration by comparing $R(T)$ measured when the meander is placed on the hotplate, with the calculated temperature obtained using Equation 2.55 and $\alpha = 2.8\text{x}10^{-3}$ K^{-1}. The main limitation of this technique is that it assumes a uniform temperature along the whole meander, as it is the case during the calibration on the hotplate. When the meander is heated by Joule heating, if the cooling occurs mainly through the glass substrate, then this assumption is valid. However, if the cooling occurs through the contact pads, then the accuracy of this technique is limited.

2.7.3   Results

Figure 2.37 illustrates the wireless heating and breaking of a meander hot-spot when a 10 W input power is applied into the CPW resonator, for a time longer than 2 s with a signal matching the resonance frequency of the SRs. The top images show an SR without Parylene passivation that was heated in air. The images clearly show that the Mg meander hot-spot is burnt by Joule heating and damaged in the center. The bottom images show an SR with a 5 μm thick Parylene passivation layer heated in water. In this configuration, the heat generated by coupling the external 10 W RF excitation into the SR is strong enough to induce damage to the Parylene layer. As shown in the microscope image, a hole is created through the polymer layer.

In contrast, as shown in Figure 2.38, when applying an input power lower than 10 W into the CPW resonator, the Parylene layer is melted over the whole meander area but no holes are observed. Progressively increasing the power intensity enables to slowly spread the area which is thermally damaged. For each input power, the signal is applied for a time longer than 2 s and experiments are performed in air. Details about the dimensions of the SRs used in this section are summarized in Table C.1 in Appendix C. For all the experiments in this section, the SRs are facing down and lie 300 μm above the λ/2 CPW.
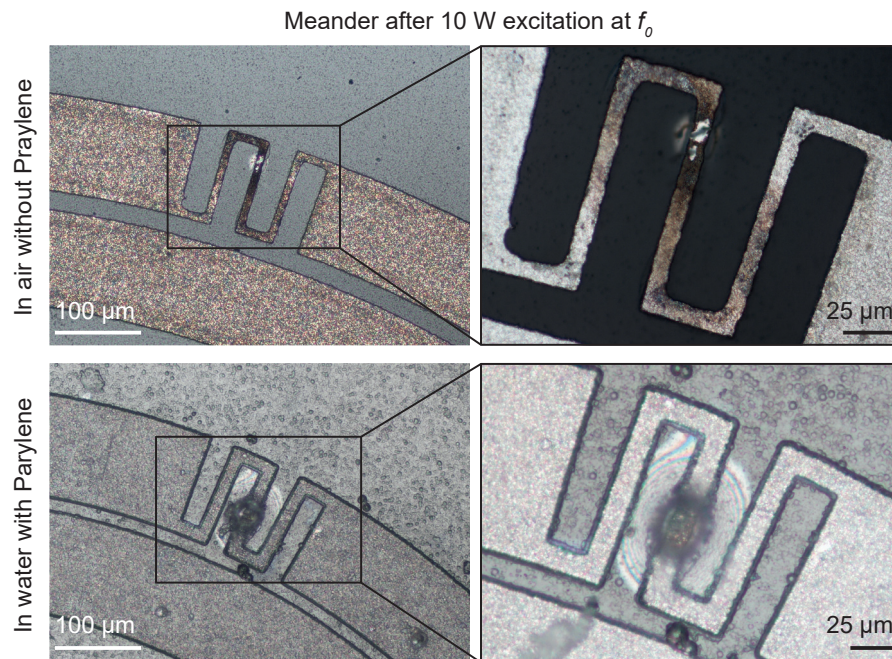
Figure 2.37 – **Wireless heating of the resonators - Surrounding media effect.** OM images of the broken meander hot-spots of the SRs after heating them in air and in water.
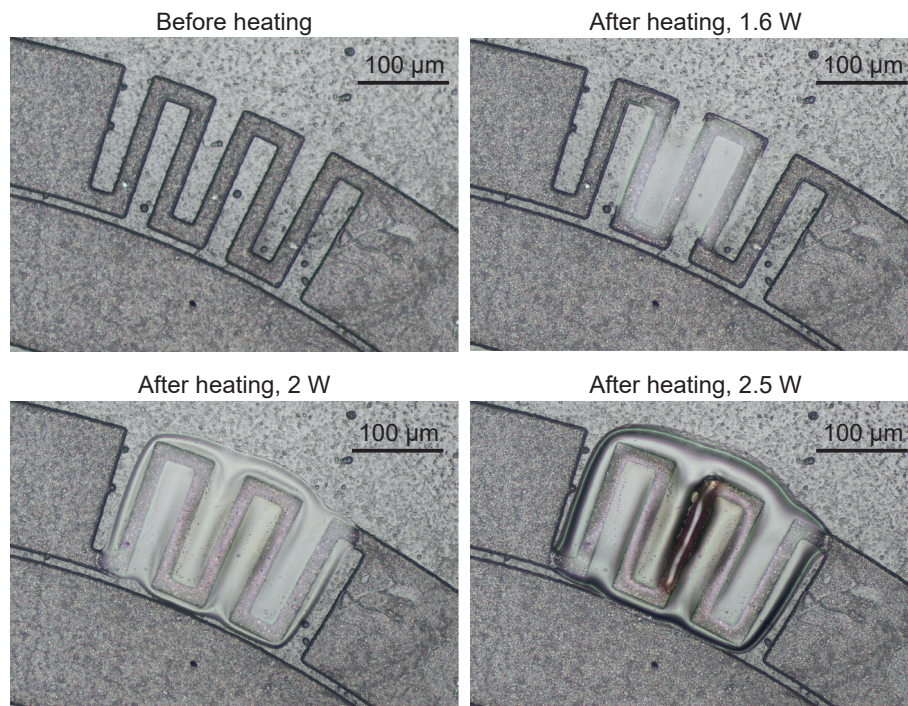
Figure 2.38 – **Wireless heating of the resonators - Power effect.** OM images showing the deterioration of the Parylene passivation layer (5 μm thick) after a progressive heating.

69

Our current setup is able to excite two SRs with different resonance frequencies at the same time and with the same amount of power, in order to demonstrate the selective breaking of only one of the meander hot-spots. To do so, the two SRs are positioned on top of the $\lambda/2$ CPW resonator, symmetrically with respect to the center of the transmission line, as shown in Figure 2.35a. Selective wireless breaking of the meander hot-spot of one resonator, when two SRs with different resonance frequencies are excited at the same time and with the same RF magnetic field, is demonstrated in Figure 2.39. The top images show the broken resonator while the bottom images show the intact resonator.

Meander after 10 W excitation at 2.54 GHz in air
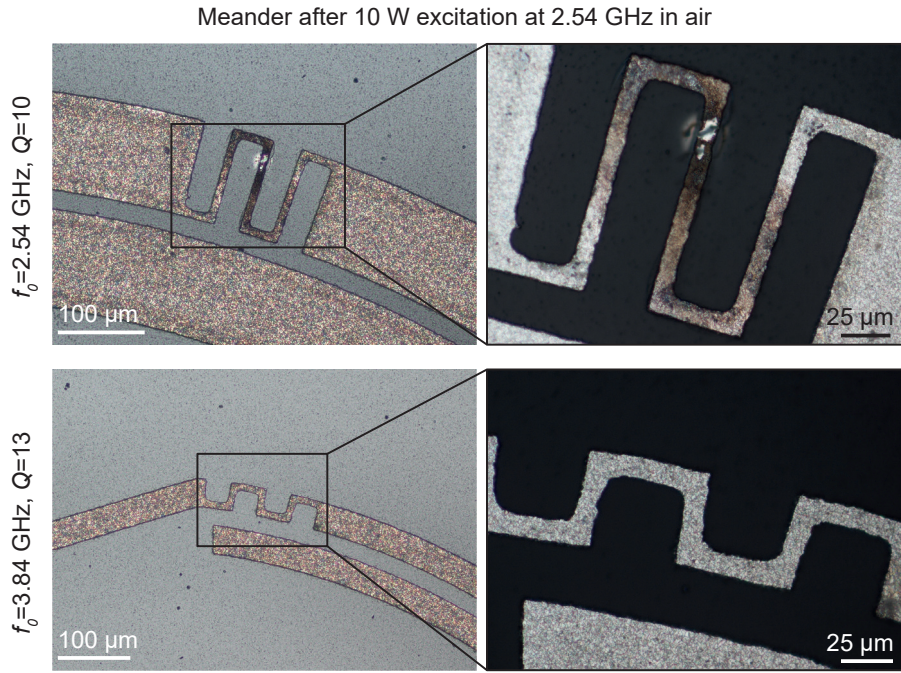
Figure 2.39 – **Wireless heating of the resonators - Selective breaking.** OM images of the meander hot-spots of two resonators with distinct resonance frequencies (top: $f_0 = 2.54$ GHz, Q=10) (bottom: $f_0 = 3.84$ GHz, Q=13) after a simultaneous excitation with a 10 W signal at 2.54 GHz, for a time longer than 2 s.

Although Figures 2.37, 2.38 and 2.39 clearly show that the wireless heating of the SRs damages the meander hot-spot and the Parylene passivation layer, it is not straight forward nor practical to visually determine if the meander is broken or not. Furthermore, it is not possible to optically determine the integrity of an implanted device. The capability of our newly developed excitation setup to electrically measure, in situ, the effective breaking of the SRs in water and in air is demonstrated in Figure 2.40. Indeed, the variation of the impedance matching of the CPW resonator resulting from the meander hot-spot breaking induces a clear signal change in the scattering parameter S_{11}.

In addition to providing a feedback about the SR integrity, the setup also enables to quantitatively determine that a minimum input power of 3.2 W into the CPW resonator is required to break the SR, as shown in Figure 2.41. Sequentially measuring the resonance and exposing
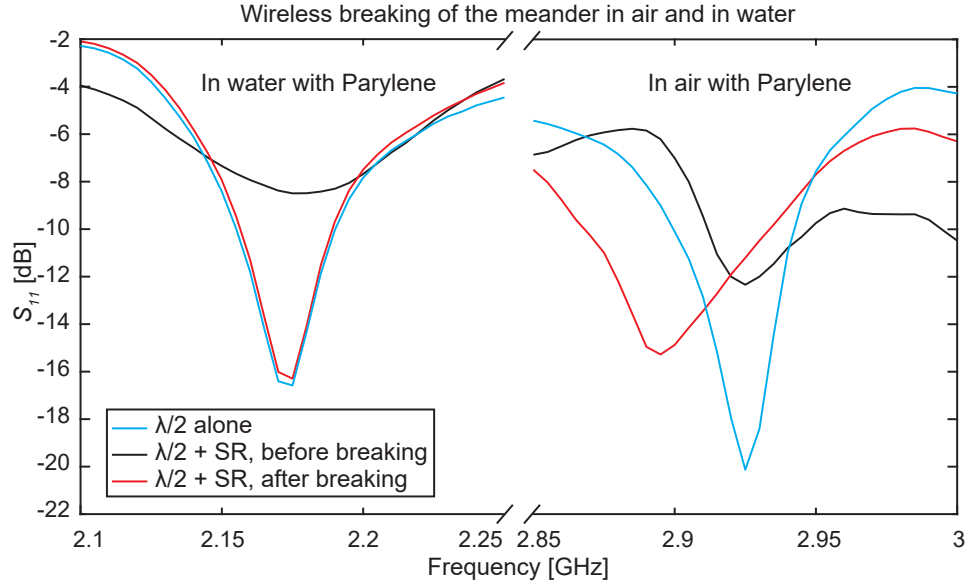
Figure 2.40 – **Wireless heating of the resonators - In situ monitoring.** In situ measurement of the breaking of the meander in water and in air. In both cases, the SRs are passivated with a Parylene layer (5 µm thick). The scattering parameter S_{11} is recorded at the port of the CPW resonator. The cyan line is the measurement of the resonance of the CPW resonator alone, i.e. without an SR on top of it. The black line is the measurement of the resonance of the CPW resonator coupled to an intact SR, whereas the red line is the measurement of the resonance of the CPW resonator coupled to a broken SR, i.e. after heating.

the resonator to a increasing input power enables to determine the breaking point. The dimensions of the resonator used for this experiment are $R = 1280\,\mu m$, $W = 80\,\mu m$, $G = 10\,\mu m$, $T = 2\,\mu m$, $W_m = 20\,\mu m$, $L_m = 30\,\mu m$, $N_m = 3$ and are also summarized in Appendix C, with all the dimensions of the SRs used in this section.

Finally, as shown in in Figure 2.42, the temperature in air as a function of the electrical power dissipated in the meander was also studied for several meander designs. The measurement ends when the meander breaks, as shown in the inset. We observe that independently of the type of meander, the breaking temperature is around 350°C. Additionally, the temperature as a function of the current and the current density in the meander is also shown in Appendix D. Current densities of $4\text{-}7\text{x}10^9$ A/m^2 are required to break the meanders with a DC current.

To conclude the study of the temperature effect on the resonators, we also investigated that heating a resonator up to 140°C for one hour, i.e. well above all realistic in vivo applications requiring continuous heating, does not affect its electrical performance or the Mg degradation rate. No change was observed in terms of resonance frequency and quality factor before and after heating the resonators and degradation times of a few minutes were measured, independently of the heating.
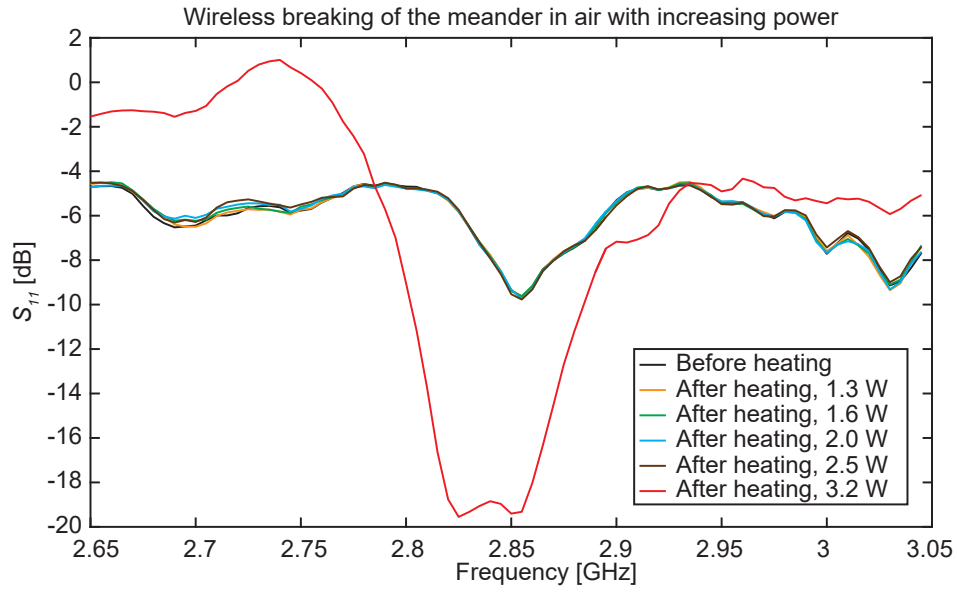
Figure 2.41 – **Wireless heating of the resonators - Minimum power to break the meander.** Wireless heating and breaking of a resonator in air without any passivation layer with increasing power from 1.26 to 3.2 W.
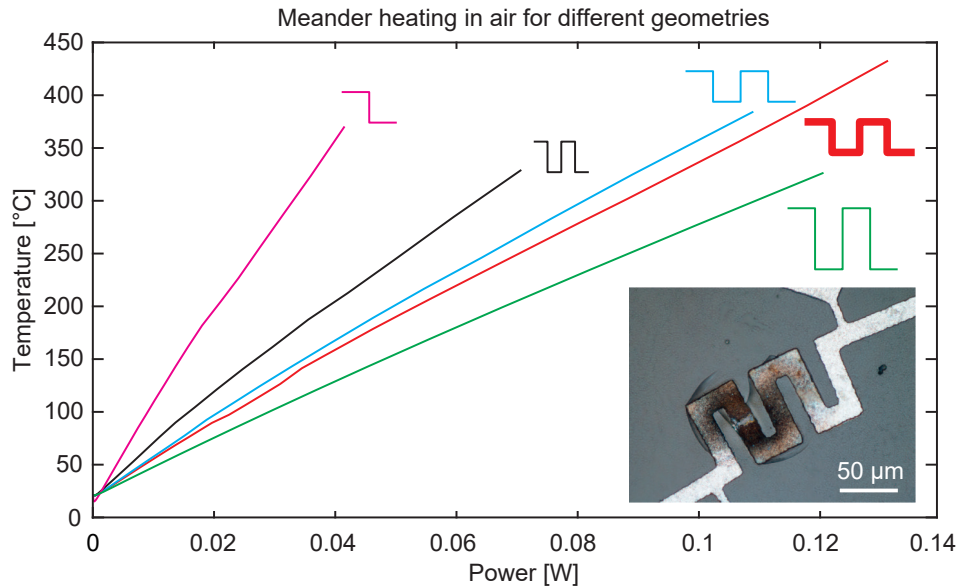
Figure 2.42 – **Temperature of the meander hot-spot.** Meander heating analysis in air. Average temperature of different meander geometries as a function of the DC power applied through the meander with a four-point-probes setup. Inset shows a broken meander after reaching the breaking power.

2.7.4   Summary and discussion

Summary   A new primary excitation setup based on the use of a power amplifier and a $\lambda/2$ CPW resonator enables to generate enough power to wirelessly heat the meander hot-spot of the spiral resonators, under the effect of the induced electrical current. The increase in temperature is such that it leads to the failure of the device by burning the thin meander track. Additionally, when the resonator is passivated with a Parylene layer, the heat generated creates a hole in the polymer above the meander hot-spot location. Using resonators with different geometries enables to selectively heat only one of them. Finally, changing the meander geometrical parameters enables to tune the hot-spot temperature as a function of the dissipated power.

Effect of the meander design on the hot-spot temperature   Figure 2.42 shows that to reach the highest possible temperature for a given input power, the meander area must be minimized and the meander density maximized to concentrate the heat in one spot. However, it is important not to forget that several other parameters should also be taken into account. Firstly, as shown in Equation 2.6, electrical resistance of the meander must be minimized in order to maximize the dissipated power. Secondly, depending on the final application of the microheaters, having the largest temperature possible over a small area, or a slightly lower temperature over a larger area might be required. At this stage, it is impossible to know which scenario is better to break a membrane and release drugs from a drug delivery implant. And third, it is important to keep in mind that all the measurements in Figure 2.42 are performed in air, but the final temperature of the meander strongly depends on the surrounding medium.

Failure mechanism   Figure 2.42 also shows that independently of the meander geometry, the failure occurs around a temperature of 350°C. Temperature seems to be the failure mechanism, as opposed to electrical effects such as electromigration. Indeed, Figure D.1 in Appendix D shows that the current density at which the meander breaks depends on its geometry. Smaller meanders break at larger current densities because their cooling is better. Additionally, Figures 2.37, 2.39 and the inset of Figure 2.42 show that the breaking of the meander occurs in the center of the meander. According to the FEM simulations in Figure 2.16, the current density is higher in the corners of the meander. As a result, if the breaking was due to electromigration, it should occur in the corners and not in the center of the meander. Although the breaking temperature of the meanders is high, it is not harmful for in vivo use thanks to the short time scale and small heated volumes. [21, 37]

Current density considerations   Finally, although the measurements in Figure 2.42 are performed with a DC current applied with microprober needles, they can be related to the wireless heating and breaking of the resonators. As shown in Figure D.1 in Appendix D, current densities of 4-7x10^9 A/m^2 are required to break the meanders with a DC current in air. According to

FEM simulations, a 0.5 W input power in the $\lambda/2$ CPW induces a $5.2\text{x}10^9$ A/m^2 current density in the meander of a typical Mg resonator, with a 300 µm spacing between the $\lambda/2$ CPW and the SR. In this configuration, the magnetic flux density perceived by the SR is 25 µT. Comparing these values with the measured value of 3.2 W reported in Figure 2.41 to wirelessly break the resonator shows that this is within the same order of magnitude. The small mismatch between the simulated and measured values can be attributed to experimental inaccuracies such as the alignment and the gap between the SR and the $\lambda/2$ CPW. According to FEM simulations, a 3.2 W input power in the $\lambda/2$ CPW produces a 75 µT magnetic flux density 300 µm above the CPW.

2.8 Conclusion

The results reported in this chapter demonstrate the design, fabrication and characterizing of selectively addressable biodegradable Mg microresonators. The resonance frequency of the resonators can be conveniently tuned to specific values between 1.5 to 5 GHz in air and 0.5 to 2 GHz in water, by varying their geometrical parameters. The resonance, which is also sensitive to the surrounding environment of the resonators, can be accurately predicted beforehand using an analytical model and FEM simulations.

Biodegradable resonators were obtained through the use of magnesium as a conducting material. Those structures starts to degrade by hydrolysis when immersed in an aqueous media. Consequently, the resonance of the devices is strongly affected after a few tens of seconds due to the fast propagation of cracks through the magnesium thin film. As a result, and to enable magnesium thin film structures, a dry fabrication process is required and was demonstrated in this chapter. It is based on ion beam etching, consists of only 4 steps and doesn't expose the Mg microstructures to any aqueous media.

We also demonstrated that adding a meander to the resonators increases the current density locally by one order of magnitude and creates a hot-spot. Adding a meander doesn't affect much the resonance of the resonators, and enables to create selectively addressable wireless microheaters. Wireless heating in air and in liquid was demonstrated. Temperatures as high as a few hundreds of degree Celsius can be reached, leading to the breaking of the meander hot-spot, or alternatively to the melting of the surrounding environment.

The ability to selectively power and heat up microresonators made of biodegradable materials is a significant step towards the use of such devices as heating and triggering elements in implantable biodegradable devices, in particular for controlled drug release and thermal therapy. [37, 54, 55, 66, 75] In comparison, our device has a 4-24 times smaller coil area, and its fabrication complexity is much reduced since it consists of one single metal layer. Additionally, this design of microheaters enables large frequency shifts by merely inducing small geometrical variations by design. As a result, we can readily integrate several resonators with multiple resonance frequencies in one device without much of an increase in diameter. The novel resonant microheater technology described in this chapter enables the design of more compact and more versatile biodegradable IMDs. Chapter 3 introduces the development of a drug delivery system using theses resonators as triggering elements to selectively release drugs from multiple reservoirs. This is one of many possible integration of the technology described here.

3 A smart implantable capsule for on-demand wireless drug delivery

The purpose of this chapter is to present the design and fabrication of a wirelessly controlled drug delivery capsule enabling the on-demand selective release of drugs from multiple reservoirs. First the principle of knee arthroplasty is introduced. Then the concept of using a wirelessly controlled drug delivery capsule for post-operative pain management is presented, followed by the design considerations and optimization. The fabrication and assembly of the capsule are then discussed. Finally, the capsules electrical characterization is performed and the wireless release of liquids from the capsule is demonstrated.

3.1   Introduction

In Chapter 2, the concept of biodegradable frequency-selective resonant microheaters was introduced. Their ability to generate heat wirelessly to modify the surrounding environment enables their use as heating and triggering elements in implantable biodegradable drug delivery systems. Hereafter we introduce knee arthroplasty, the current post-operative pain treatments associated to this procedure, and how the use of a biodegradable drug delivery implant is beneficial in this context. The main goal here is to replace the current methods of drug administration for post-operative local analgesia after knee arthroplasty, while personalizing and reducing the drug dose and secondary effects.

3.1.1   Knee arthroplasty

Knee joint   The knee is the largest and strongest joint in the body and is used to perform most daily activities. It consists of the lower part of the femur (thighbone), the upper part of the tibia (shinbone) and the patella (kneecap). Bones are linked together and stabilized thanks to ligaments and tendons, and bones extremities are covered with articular cartilage allowing a smooth and easy movement. Menisci, which are located in between the femur and the tibia, absorb shocks in order to prevent injuries. Finally, the remaining surfaces of the knee are covered with synovial bursae, which release synovial fluid lubricating the cartilage. A healthy knee anatomy is shown in Figure 3.1. In normal conditions, the knee allows flexion and extension, as well as limited internal and external rotation movements.
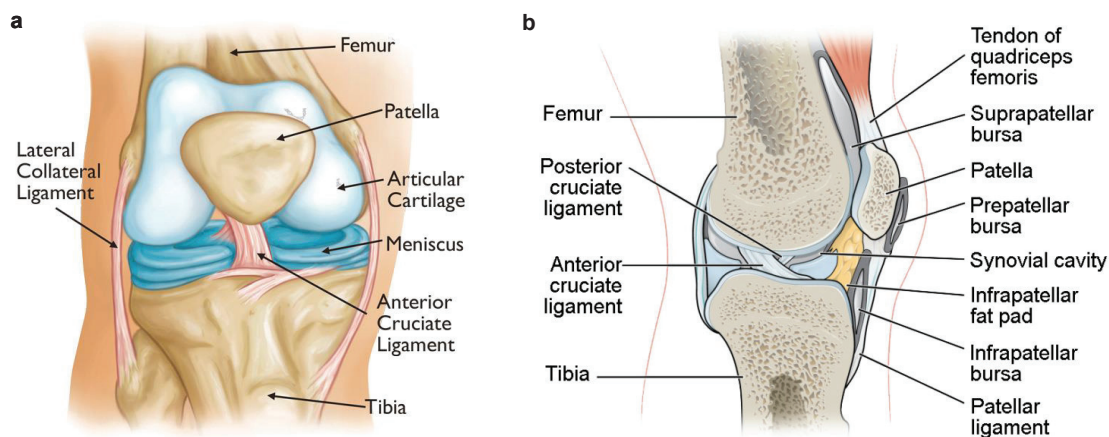
Figure 3.1 – **Healthy knee anatomy. a**, Front view of a healthy knee anatomy showing the bones, the ligaments, the cartilage and the menisci. [138] **b**, Lateral cross-section view of a healthy knee anatomy showing also several of the synovial bursae. [139]

Knee pain   The most common causes of knee pain and disability are osteoarthritis, rheumatoid arthritis and post-traumatic arthritis. Arthritis consists in articular cartilage damage and losses, resulting in bones rubbing against one another. As cartilage is not innervated but

periosteum is, this is causing joint pain, swelling and stiffness. Osteoarthritis is a degenerative form of arthritis, and mainly an age-related problem with cartilage damage due to wear and tear. On the other hand, rheumatoid and post-traumatic arthritis are consequences of diseases and injuries. Damaged cartilage is shown in Figure 3.2a. Worldwide, estimates show that 18% of women and 10% of men aged over 60 years suffer from moderate and severe forms of osteoarthritis. [140] If pain or disability are so strong that it becomes difficult to perform simple activities such as walking or climbing stairs, or if pain occurs even while sitting or lying down, patients' quality of life strongly decreases. In such cases, and if medication or walking supports are not sufficient anymore, knee arthroplasty should be considered, as shown in in Figure 3.2b.
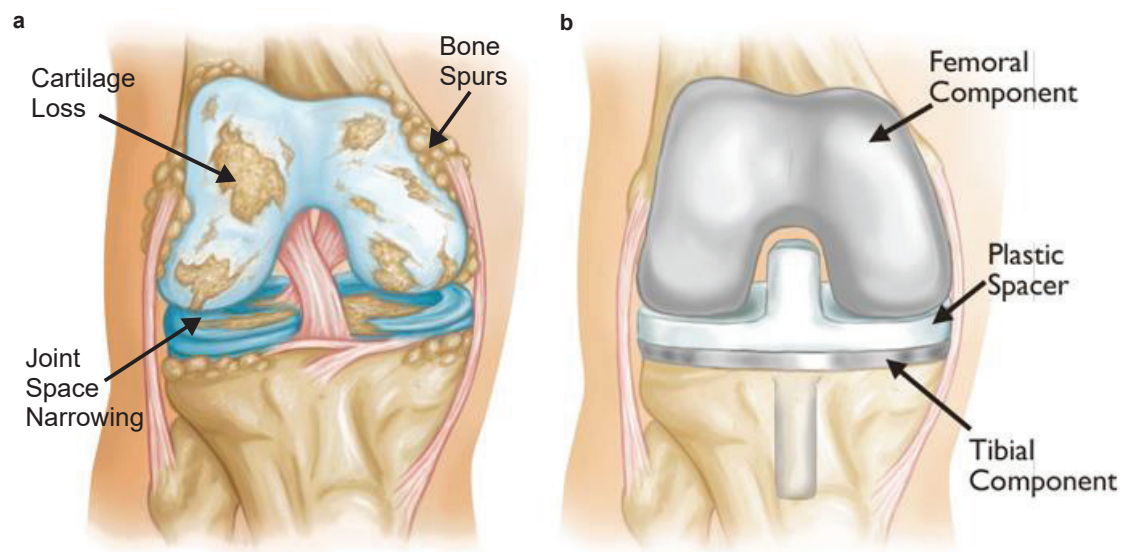
Figure 3.2 – **Damaged cartilage and knee arthroplasty. a**, Damaged cartilage resulting in bone spurs and the narrowing of the joint space. **b**, Total knee arthroplasty showing the different components of the prosthesis. [138]

Knee arthroplasty   Prior to the surgery, an orthopedic evaluation consisting of a medical history, a physical examination, x-rays and sometimes other tests such as a blood test or an MRI scan are required. This evaluation allows first to confirm that knee replacement surgery is the adequate treatment, and second to select the right prosthesis type. X-ray images of healthy, damaged and prosthetic knees are shown in Figure 3.3. Figure 3.3b clearly shows that the space between the femur and tibia is reduced because of arthritis. The first knee replacement surgery was performed in 1968. Nowadays, each year, over 2.2 million people undergo knee replacement surgery and this rate doubled since 2000, which makes it one of the most effective and frequently performed surgery worldwide. [140] Several types of knee arthroplasty exist. The implant can consist of a total knee replacement (TKR) or a partial/unicompartmental knee replacement (PKR). It can be fixed or mobile, and cemented or press-fitted into the bones. However, despite these variations, the implant components and the required surgical

procedure for their implantation are always very similar. A typical surgery lasts from one to two hours in total and consists of four main steps.

- Bone preparation: the damaged cartilage is removed from the femur and tibia ends. Then, bones extremities are resurfaced.

- Metal implants positioning: tibial and femoral metal components of the implant are inserted at the end of the tibia and femur to mimic cartilage, as shown in Figure 3.2b. These parts are usually made of titanium or cobalt-chromium alloys such as CrCoMo. They are attached to the bones using fast-curing bone-cement (polymethylmethacrylate) or cementless fixation. In the latter case, the implants are press-fitted into the bones and new bone growth ensures their stability. To improve the bone growth, cementless implants are coated with specific structured materials. Finally, hybrid designs also exist where the femoral component is cementless and the tibial component is cemented to the bone.

- Patella resurfacing: depending upon the case and the surgeon, the bottom part of the patella may be resurfaced with plastic.

- Spacer insertion: as shown in in Figure 3.2b, a plastic spacer is inserted between the tibial and femoral metal components to allow a smooth gliding and subsequent knee movements. This component is made of medical-grade ultra high molecular-weight polyethylene.
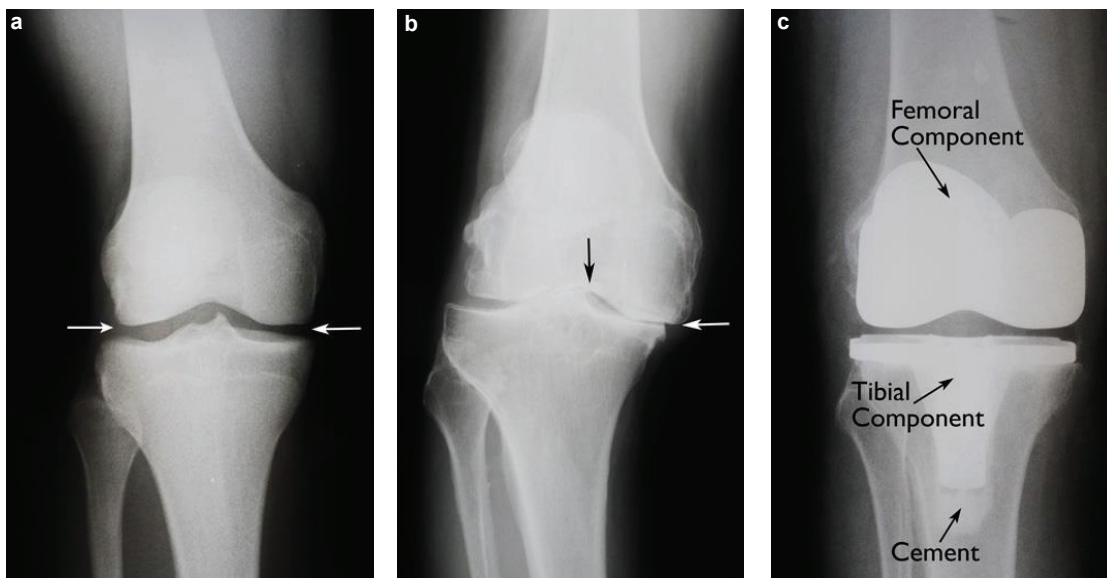
Figure 3.3 – **X-ray images of a knee.** X-ray images of healthy (**a**), damaged (**b**) and prosthetic (**c**) knees. The arrows in **a** and **b** show the location of the cartilage. In **c**, the prosthesis re-aligns the tibia and femur similarly to a healthy knee. [138]

Post-operative complications and risks   Although the general success of joint arthroplasty is beyond dispute, post-operative complications such as infections, blood clots, implant problems, continued pain and neurovascular injuries can still occur. In the specific case of knee replacement, the incidence of periprosthetic infection is of 1.1%. [141] While minor infections can be treated with antibiotics, more serious cases can lead to the implant removal. Therefore, after a joint arthroplasty, skin in proximity of the implant should not be pierced, which limits the methods of drug administration.

After a knee replacement, patients stay in the hospital for a few days up to one week. During hospitalization, several measures are taken to improve patients' recovery. Blood clot and swelling are prevented by using compression boots, and physical therapy improves movements recovery. Additionally, pain management is also important in the healing process, as pain is often the factor limiting physical therapy. Post-operative pain following knee replacement surgeries is usually strong in comparison to other joint replacement surgeries such as hip and shoulder. However, because of the risks of infection, it is not possible to deliver local anesthetics by subcutaneous or intramuscular injections.

Post-operative pain management   Currently, the post-operative pain treatment following a knee arthroplasty consists in combined analgesia. First, 20 to 150 ml of an analgesic solution is infiltrated at several locations in tissues around the knee while the patient is still in the operating room, before closing the wound at the end of the surgery. Typically, the solution contains a local anesthetic such as levobupivacaine or ropivacaine, adrenaline to increase vasoconstriction and an anti-inflammatory drug such as cortisone or ketorolac. [142–144] Unfortunately, the infiltration is effective over a time period of 24 to 48 hours only, doesn't diffuse well within the knee articulation, and the drug dose cannot be adjusted afterwards. This results in an incomplete pain relief. Consequently, in the following days after the surgery, the epidural administration of morphine as well as oral drug delivery are necessary. Such methods of drug administration suffer from a relative discomfort due to the epidural catheter, the systemic toxicity of the drugs, a possible temporary paralysis of the quadriceps, and put the patient at risk of opioid addiction.

Recovery and outcome   For more than 90% of the patients, the knee arthroplasty enables improvements in the performance of daily activities and drastically reduces the pain. [138] Following a knee replacement surgery, high-impact activities such as running or jumping are prohibited, but low-impact activities such as swimming and cycling are possible and recommended. Stitches and staples are removed approximately three weeks after the surgery, while walking aids are kept up to six weeks after the surgery. It takes from four to six weeks to recover driving abilities. During the recovery time at home, preventing blood clots and infections is important and avoiding falls is primordial. When following basic precautions, modern implants are expected to be still functional at least 15 years after their implantation. [138]

3.1.2 Capsule DDS for post-operative pain management

As discussed in Section 3.1.1, post-operative pain management following a knee arthroplasty requires combined analgesia to be fully effective. A solution to improve patients' compliance and overcome systemic toxicity is to use an implantable drug delivery system. This way, a local anesthetic can be released in close proximity to the knee during several days. If the system is active and wirelessly controlled, it enables a precise and controlled drug delivery over time without piercing the skin. Additionally, the use of a biodegradable implant prevents the need for a second surgery to remove it.
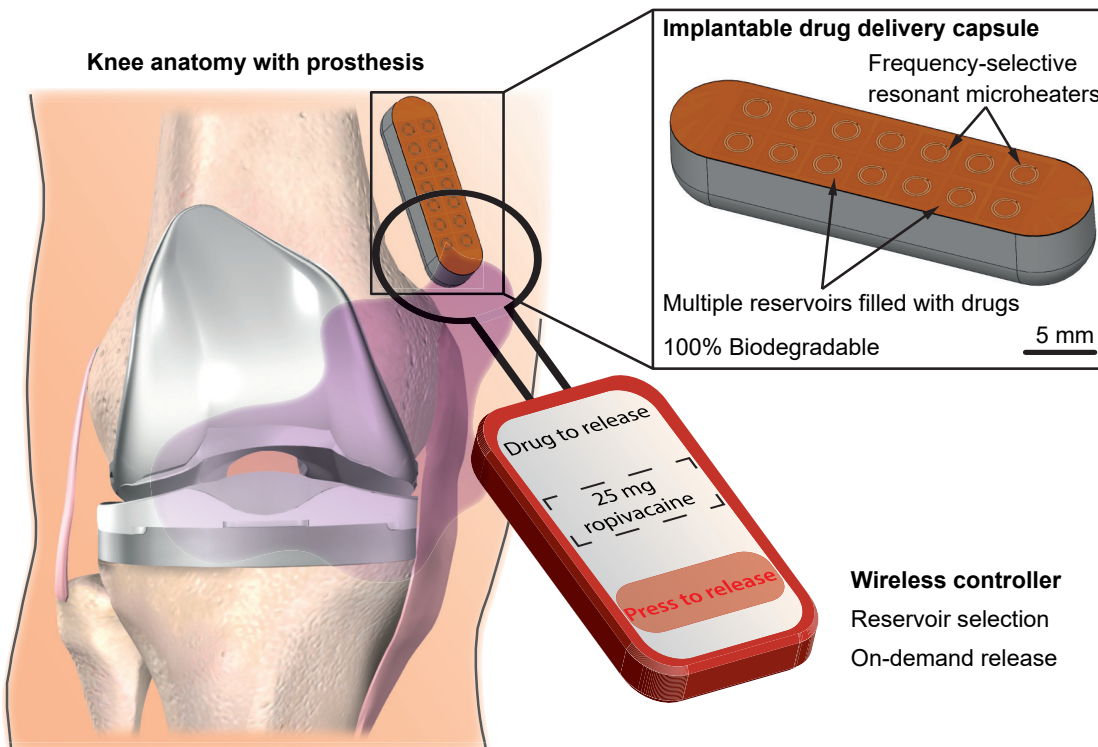
Figure 3.4 – **Biodegradable and wirelessly controlled drug delivery capsule.** The device consists of a biodegradable implantable capsule with multiple reservoirs filled with drugs. Each reservoir can be selectively opened using an external wireless controller. Resonant microheaters are used both as power receivers and electrothermal triggering elements to release the drugs. On-demand drug release enables to precisely control the concentration over time. In the context of local analgesia after a knee arthroplasty, the device is implanted on the top of the knee articulation, a few millimeters to centimeters under the skin. It releases ropivacaine, a local anesthetic, and is naturally eliminated by the body once its action is complete. Image adapted from [145].

We present here the concept of a fully biodegradable and wirelessly controlled drug delivery capsule. As shown in Figure 3.4, drugs can be selectively released on-demand from multiple reservoirs. The resonant microheaters developed in Chapter 2 are used both as power receivers for near-field resonant inductive coupling, and electrothermal triggering elements to release

the drugs. Thus, the device powering and triggering mechanisms are combined into a single element, minimizing the volume of implanted material and maximizing the drug-to-implant volume ratio. The integration and miniaturization of all the components of such a system enables multiple drug reservoirs of several tens of microliters in the smallest possible volume.

In the context of local analgesia after a knee arthroplasty, the reservoirs are filled with ropivacaine, a local anesthetic. The device is implanted at the end of the surgery, before closing the wound. As shown in Figures 3.4 and 3.1b, it is placed in the suprapatellar bursa, on the top of the knee articulation along the quadriceps tendon. Details regarding the drug used, the required amount of drug and the implant dimensions are given in section 3.2.

As shown in Figure 3.5, the device consists of a centimeter-sized capsule with multiple reservoirs filled with drugs. Each reservoir is covered with a membrane plus a spiral resonator with a meander hot-spot. Similar to the technology developed in Chapter 2, each resonator has a different resonance frequency tuned by its geometrical parameters, which makes them selectively addressable. Using an external RF magnetic field, energy is coupled only into the frequency matched resonator where an electrical current is induced by electromagnetic induction (cf. Section 2.1.3). Consequently, the Joule heating of the meander hot-spot breaks the underlying membrane, which releases the drug from one reservoir.

Because of the rapid degradation of the microheaters in aqueous media discussed in Section 2.6, it is necessary to use a bi-layer membrane to encapsulate and protect the electronics. The number of reservoirs in one capsule depends on the application and is further discussed in Section 3.2. However, such a system enables to achieve a similar pharmacokinetic as shown in Figure 1.2d. Additionally, the device can be loaded with multiple different drugs, and the drug release scheme can be personalized for each patient. Finally, once all the reservoirs are empty, the implant naturally degrades.
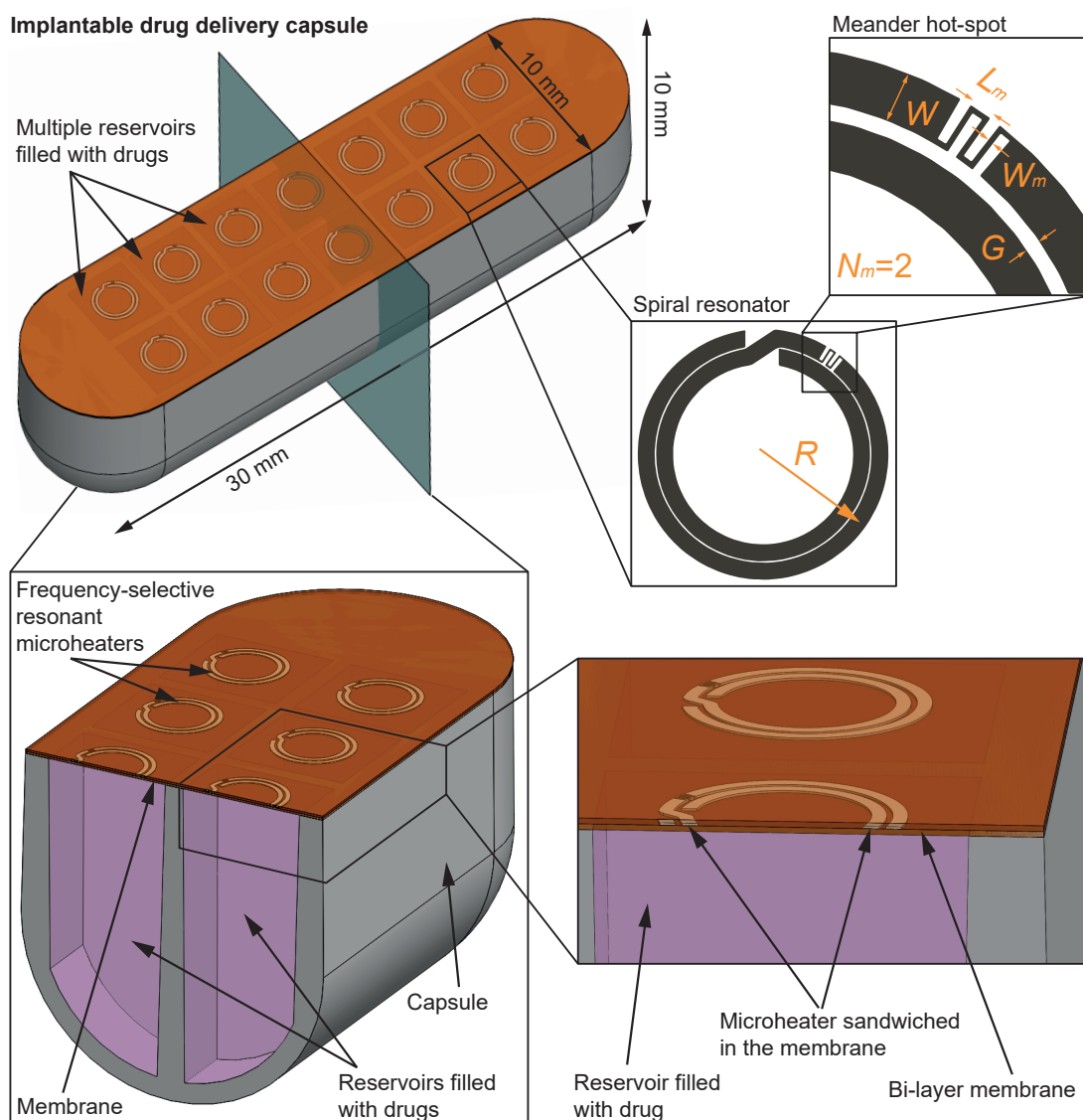
Figure 3.5 – **Design of the drug delivery capsule.** The device consists of a centimeter-sized capsule with multiple reservoirs filled with drugs. Each reservoir is covered with a membrane with an integrated spiral resonator. Each resonator has a different resonance frequency tuned by its geometrical parameters. The heat electrothermally generated by a microheater when it is powered with a matching RF magnetic field breaks the membrane and releases the drug from one reservoir. A bi-layer membrane is used to encapsulate and protect the electronics from a rapid degradation in aqueous media.

Using an implantable biodegradable drug delivery capsule for post-operative pain management following a knee arthroplasty involves several advantages over the current techniques in use.

- Thanks to the local and minimally invasive characteristics of the capsule, the patient's discomfort is reduced compared to the use of an epidural catheter.

- Using an implantable wirelessly controlled capsule suppresses any connection to the outside of the body and thus lowers the risk of infection.

- Precise controlled release of the drug over time with the capsule enables to adjust the dose and administration frequency for each patient. This is currently not possible when using infiltration techniques, nor with bioerodible implants.

- Thanks to its location in the suprapatellar synovial bursa, the capsule allows a better diffusion of the drug in the knee articulation. This enables a more uniform pain relief while reducing the required drug dose compared to current infiltration techniques.

- Multi-drug release can be easily implemented in a future version of the device.

- The system can be modified to be compatible with other orthopedic or local surgeries, such as fracture repair and cardiac surgeries.

Ultimately, the goal is to replace the current methods of drug administration for post-operative local analgesia after a knee arthroplasty, while personalizing and reducing the drug dose and secondary effects.

In this chapter, the functionality of the implant is demonstrated in a non-biodegradable prototype. Its purpose is to demonstrate the wireless release of a liquid from the capsule using our microheaters. The capsule is 3D printed by stereolithography, the microheaters are made of gold, and the membrane is made of polyimide. However, the design of the active elements is such that only one metal layer is required and the fabrication is based on dry processes only. Consequently, this technology can be readily translated to be compatible with biodegradable materials, as detailed in Chapter 4.

3.2 Design considerations

Design of the resonators   The microheaters used in the drug delivery capsule to trigger the drug release are spiral resonators with a meander hot spot, similarly to the technology developed in Chapter 2. However, a few observations from Chapter 2 were taken into account when designing the second version of the resonators used in the capsule.

Firstly, the measurements in Figure 2.26 showed that obtaining large frequency shifts between different resonator geometries in water requires larger geometrical variations than in air. When implanted in the body, the capsule is surrounded by liquid. Thus, the resonance frequency of the resonators is tuned by varying their radius by a few hundreds of microns, and not simply by changing the gap between the two turns of the resonators by a few tens of microns.

Additionally, we want to have resonators with resonance frequencies lower than 4 GHz in air, which was not always the case in the first design. Limiting the resonance frequency in air also limits the resonance frequency in water and thus the tissue losses which are increasing with the frequency. In the new design, the maximum radius of the resonator is increased to 2500 μm to satisfy this condition. In the first version, the maximum radius was 1500 μm. The exact geometries and resonance frequencies of the resonators are discussed in Section 3.3.

Figure 2.42 showed that, for the same amount of dissipated power, thin and dense meanders heat more. Thus, only meanders with $W_m = 15$ μm and $L_m = 25$ μm are considered in the new design. However, the number of meanders still varies from 1 to 4 to see the effect of the hot-spot size on the membrane breaking and the drug release from the capsule.

Finally, as demonstrated in Equation 2.5, to maximize the power dissipated in the meander, its electrical resistance (R_m) should be equal to the electrical resistance of the rest of the resonator (R_r). This condition was not implemented in the first version of the resonators, since a full factorial design was used. The parameters values were simply varied to the bounds of the parameters range without taking into account $R_m = R_r$. In the second version, the geometry of each resonator is optimized to maximize the power dissipation in the meander, for a given resonance frequency, resonator radius and number of meanders. For this purpose, the analytical model developed in Section 2.3 is used, as detailed in Section 3.3.

Design of the capsule   As discussed in Section 3.1.2, the capsule is placed in the suprapatellar bursa, on the top of the knee articulation. To minimize patients' discomfort, the implant should match the shape of the bursa. A cylindrical-shaped capsule with a diameter of 10 mm, a length of 30 mm and no sharp corners is then optimal. Another possible design would be a sheet-shaped implant; large and long but very thin. However, such a design limits the amount of drug that can be loaded in the implant. The design chosen for the capsule is shown in Figure 3.5. It consists of a cylinder with a flat surface to implement the membranes and the microheaters. The size of the capsule is comparable to the size of the screws used in orthopedic surgeries and will thus not seem unreasonable to the surgeons.

Additionally, the orientation of the capsule in the knee is important since the power is transmitted through NRIC. In order to guarantee a good alignment between the capsule and the primary coil, the capsule must be sutured when implanted in the body. Some suture holes can be designed in the final version of the device. The frequency range of the used microheaters is around 0.3 to 1.5 GHz in liquid. As discussed in Section 2.7.4, a magnetic field of 25-75 µT over the resonator surface is required to wirelessly break the meander hot-spot. Generating a field of this intensity in the low GHz frequency range should be possible up to a a few millimeters while respecting the SAR. However, experimental validation is required to corroborate this value.

The thickness of the membrane closing the drug reservoirs is a tradeoff between mechanical stability and the required amount of energy to thermally break it. The membrane must be resistant to the movements of the patient when doing physical therapy. The mechanical stability and the required amount of energy to thermally break the membrane strongly depend on the membrane material. For the non-biodegradable version of the device developed in this chapter, the membrane is made of polyimide, a mechanically and thermally resistant polymer. For this specific material, membrane thicknesses of 1 to 3 µm are used to close reservoirs with a surface area of 3x3 mm^2. Decreasing the area of the membrane is also an efficient way to increase its mechanical stability. However, as discussed in Section 3.7.4, this might affect the drug release dynamics.

If the resonators are made of a water-soluble material such as Mg, the degradation time-scale is only a few tens of seconds once exposed to an aqueous solvent (cf. Section 2.6). Consequently, a bi-layer membrane to encapsulate and protect the electronics is required. For the non-biodegradable prototype developed in this chapter, single-layer membranes with the resonators on top are used, as detailed in Section 3.4.

Finally, the capsule can be filled with liquid by pipetting or by inkjet printing before assembling the membranes, or by designing specific filling apertures. Considerations regarding the amount of drug required to have a therapeutically effective capsule are discussed in the next paragraph. However, for the prototype developed in this chapter, capsules with four reservoirs are used.

Required drug dose As discussed in Section 3.1.1, patients stay in the hospital from a few days up to one week after a knee arthroplasty. For most patients, the pain is critical during the first week following the surgery. Consequently, the drug delivery capsule must be fully functional and able to release drugs in a controlled manner during 7 days. Afterwards, it should degrade to be progressively eliminated by the body.

Currently, 20 to 150 ml of an analgesic solution are infiltrated in the tissues to treat the pain in the hours following the surgery. However, the volume of the drug delivery capsule is intrinsically limited. A 10x10x30 mm^3 implant represents a volume of 3 ml. Changing the administration method from a single bolus dose at the end of the surgery to multiple pulsatile

and localized releases over several days enables to decrease the total drug dose required for a complete pain relief. Nevertheless, increasing the drug concentration is necessary in order to have enough active principle within the volume of the capsule. Modifying the concentration or the method of administration of an existing drug requires a specific care in terms of drug toxicity and stability. Consequently, the capsule would be loaded with only one local anesthetic such as ropivacaine or levobupivacaine to begin with. Since these drugs have a low toxicity and side effects, it is possible to safely increase their concentration.

Practically, during a knee arthroscopy, surgeons administrate to the patient 5 ml of ropivacaine at 0.5% (i.e. 5 mg/ml). This represents an amount of 25 mg of active principle and the effect lasts for 24 to 48 hours. Ropivacaine density as a powder is around 1 g/cm^3. Consequently, in the extreme condition where the drug formulation is a pure powder and is not diluted in a solvent, a volume of 25 µl is required to administrate 25 mg. The current design of the drug delivery capsule enables to have 14 reservoirs of 50 µl each, and is thus compatible with post-operative local analgesia after a knee replacement surgery. Nevertheless, if the drug formulation is a powder, its diffusion out of the capsule reservoirs might be affected, as further discussed in Section 3.7.4.

Even though only one drug would be delivered with the capsule to begin with, it enables to precisely personalize the drug doses release over time for each patient. This is currently not possible when using infiltration techniques, nor with bioerodible implants. Additionally, multi-drug release can be easily implemented in a future version of the device, and the system can be modified to be compatible with other orthopedic or local surgeries, such as fracture repair and cardiac surgeries.

Limitations of the system   Finally, it is also important to keep in mind the few limitations associated to a wirelessly controlled biodegradable drug delivery system. Firstly, all the drug in the device has to be released at some point. In the context of local analgesia after a knee arthroplasty, this is not a major concern since the drugs used have a low toxicity. Additionally, the drug dose loaded in the implant can be slightly underestimated on purpose, and the remaining pain once the implant is empty treated with oral pills. Nevertheless, this may become a serious risk if highly toxic drugs are used.

A second risk is the sudden rupture of the device releasing all the drugs at once. Although tests will be performed to ensure such a failure of the device will not occur, this is a concern especially for highly toxic drugs. The maximum amount of drugs loaded in one implant might be limited accordingly. Similarly, a sudden release could also occur if someone hacks the system and releases all the drugs in one shot. Nevertheless, since the working principle of the device is based on near-field inductive coupling, the hacker would need to be in close proximity with the patient or use a powerful well focused far-field emitter.

Finally, as discussed above, the device will be controlled up to 1 to 2 cm under the skin, which makes it incompatible with overweight persons.

3.3 Optimization of the power dissipation

3.3.1 Introduction

In the analytical model discussed in Section 2.3, Equation 2.40 describes the dissipated power in the meander as a function of the frequency and the electrical parameters of the resonators. Analytically optimizing this equation for a given frequency, is not an easy task because of the non-linear equations describing the resistance, inductance and capacitance values. Nevertheless, the computation of the resonance for one specific resonator geometry with the analytical model takes less than one second. Consequently, the resonance of a large number of resonator geometries can be computed within a reasonable amount of time. In this section, we present a brute-force approach to optimize the power dissipated in the meander of a resonator, at a given frequency and in a given environment. A brute-force approach consists in computing the solutions of a problem using a large set of input parameters and then selecting the optimum solution.

In the specific case of the spiral resonators, the resonance is computed combining a large number of geometrical parameters. For resonators with a meander hot-spot, the optimum solution is the one maximizing the power dissipated in the meander. For resonators without a meander hot-spot, the optimum solution is the one maximizing the quality factor. Two main assumptions are made when using such a technique. Firstly, we consider that the maximum power is dissipated in the meander at the resonance frequency of the resonator. Secondly, we assume that the analytical model is accurate enough to compute the current in the resonator, and thus the dissipated power. As discussed in Sections 2.3.3 and 2.3.4, more comparisons between the analytical model and the FEM simulations are still required to validate the preliminary evidence that the difference in the estimation of the current density is in the order of a factor of two. This means that optimizing the dissipated power using the analytical model is not fully accurate, but it enables us to refine the possible resonator geometries from a large set of parameters.

3.3.2 Methods

The first step consists in defining the set of geometrical parameters to investigate. As shown in Figure 2.4b, in the case of a spiral resonator with a meander hot-spot, there are 7 geometrical parameters (R, W, G, W_m, L_m, N_m, W_o). As discussed in section 3.2, only thin and dense meanders are considered, so W_m is set to 15 μm and L_m to 25 μm. Additionally, varying the opening between the two turns of the resonators (W_o) doesn't change much in terms of resonance so it's value is fixed at $W_o = 250$ μm. The other parameters are varied among the ranges defined in Table 3.1. This represents 282'295 possible combinations. For each combination the validity of the geometry is checked. Indeed, some of the combinations result in errors, for instance if the track width is larger than twice the opening of the resonator ($W > 2W_o$). Details regarding the possible geometrical errors are given in Appendix E.

Table 3.1 – **Geometrical parameters range.** Varying the parameters enables to optimize the design of the spiral resonators in terms of power dissipated in the meander and of quality factor. The parameter range nomenclature is start point : step : end point.

Symbol	Parameter name	Units	Parameter range
R	Radius of the resonator	[µm]	1500 : 10 : 2500
W	Track width	[µm]	20 : 10 : 440
G	Gap between the two turns of the resonator	[µm]	10 : 5 : 70
W_m	Meander width	[µm]	15
L_m	Meander length	[µm]	25
N_m	Number of meanders	-	0 : 1 : 4
W_o	Opening between the two turns of the resonators	[µm]	250

Then, for each valid combination of the parameters, the resonance frequency, the quality factor and the power dissipated in the meander are computed using the analytical model. It is possible to compute these values in multiple surrounding environments. In our case, the resonance was computed in two different surrounding environments: on a 2 µm polyimide substrate in air, and on a 2 µm polyimide substrate with a 5 µm polyimide passivation layer in water. For each case, the environmental parameters used to compute the resonance are given in Table 3.2. In the analytical model the only difference between polyimide, water and air is their relative permittivity.

Table 3.2 – **Environmental parameters.** Environmental parameters used to compute the resonance of the resonators in air and in water.

	In air	In water
Substrate material	polyimide	polyimide
Substrate thickness [µm]	2	2
Coil material	Mg	Mg
Coil thickness [µm]	2	2
Passivation material	-	polyimide
Passivation thickness [µm]	-	5
Surrounding material	air	water
Magnetic flux density [µT]	10	10

Finally, the optimized geometries are selected among the matrix of results for the desired resonance frequencies. Optimized geometries can be defined according to the power dissipated in the meander or to the quality factor of the resonator. It is also possible to set the radius of a resonator to a specific value for a given resonance frequency, in order to generate resonators with larger geometrical variations. This condition is necessary to obtain large frequency shifts in water.

3.3.3 Results

Out of the 282'295 possible combinations of all the geometrical parameters, 169'057 combinations result in valid geometries. Figure 3.6a, shows which combinations of the parameters are valid for resonators with $N_m = 3$. Error 0 means the geometry is valid, while each other value depicts one of the errors detailed in Appendix E. In total, 50 hours are required to compute the resonance for all the valid geometries, in one of the two experimental condition described in Table 3.2. The resonance frequency, the power dissipated in the meander and the quality factor for all the valid geometries with $N_m = 3$ computed in air are shown in Figures 3.6b, 3.6c and 3.6d respectively.
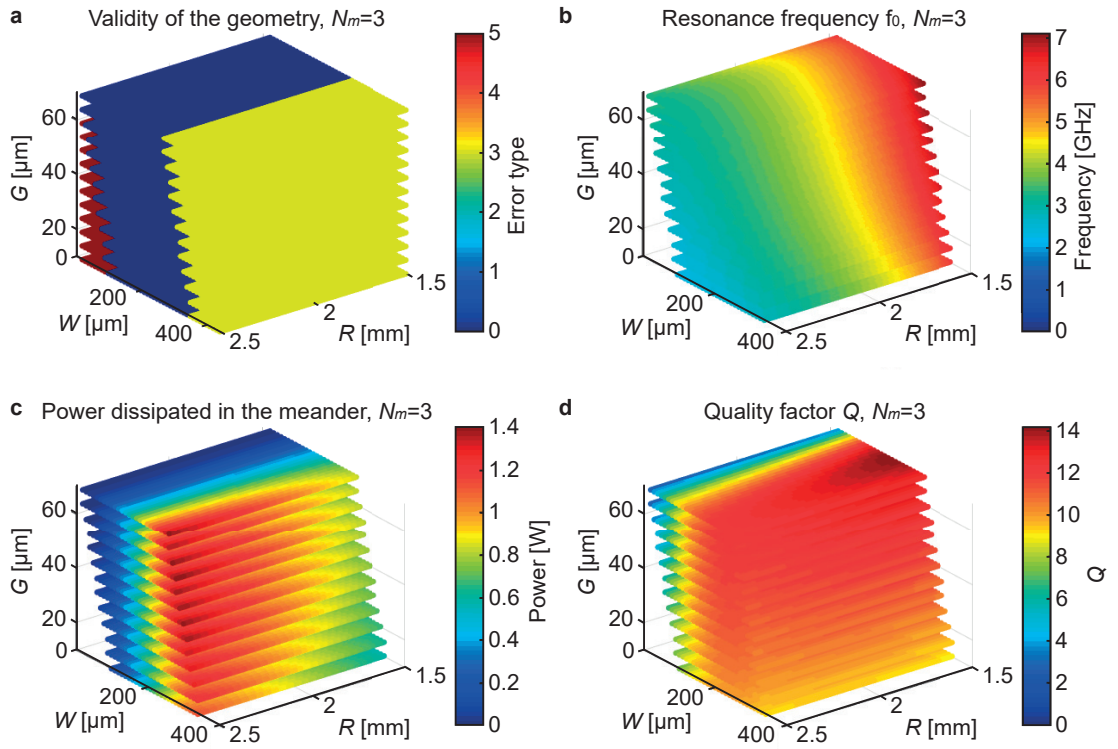
Figure 3.6 – **Power optimization - Full range of parameter. a**, Results of the geometrical validity check for resonators with $N_m = 3$. Error 0 means the geometry is valid. **b,c,d**, Resonance frequency (**b**), power dissipated in the meander (**c**) and quality factor (**d**) for the valid geometries with $N_m = 3$ in air over the full range of parameters.

Additionally, Figure 3.7 analyzes the power dissipated in the meander for valid resonator geometries in some subsets of the frequency domain. This enables us to select the optimum geometry at specific resonance frequencies.
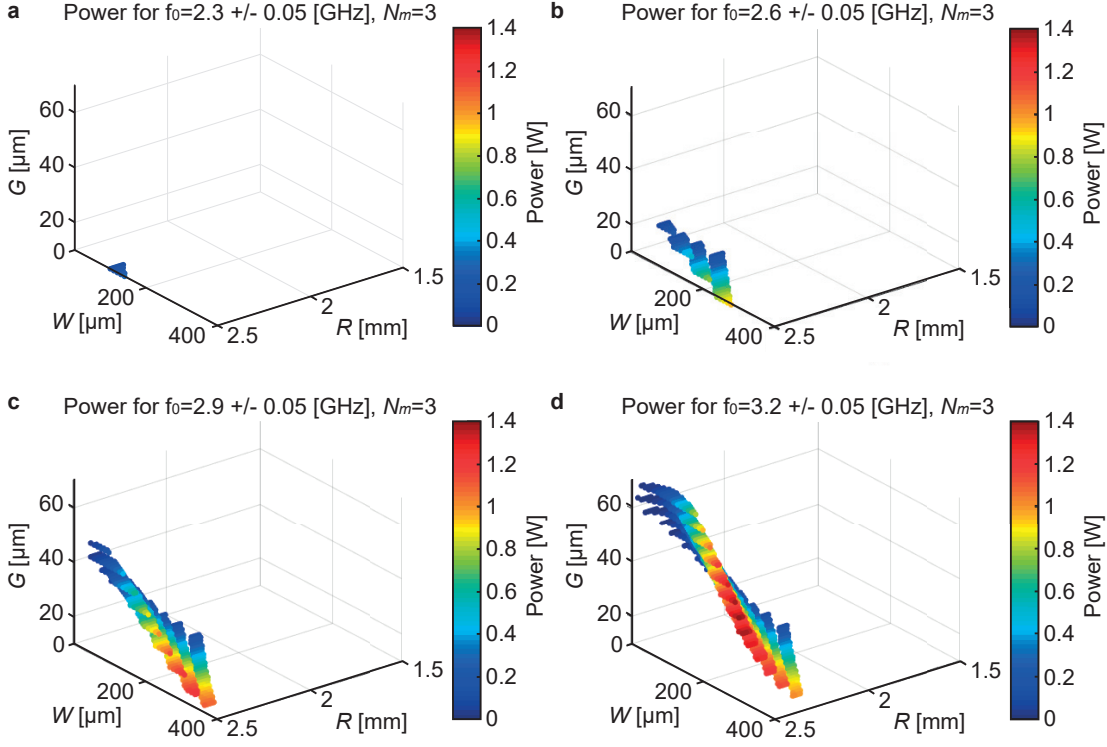
Figure 3.7 – **Power optimization - Frequency selection.** Power dissipated in the meander at specific resonance frequencies for valid geometries with $N_m = 3$ in air. Each plot is a subset of Figure 3.6c according to the resonance frequencies displayed in Figure 3.6b.

Finally, Figure 3.8 performs the same analysis but restricts the radius of the resonators to specific values in steps of 200 μm. The analysis performed here for $N_m = 3$ in air can also be performed for $N_m = 0, 1, 2, 4$ and in water. However, when $N_m = 0$, the quality factor is used to optimize the geometry of the resonators instead of the power dissipated in the meander. The optimum geometrical parameters as well as f_0, P_m and Q values for each numbers of meander, in air and in water, are given in Appendix E.

3.3.4 Summary and discussion

The amount of time required to compute the resonance for all the possible combinations of the geometrical parameters is substantial. However, once it is computed, selecting the optimized resonator geometry for any resonance frequency, with or without restricting the radius of the resonator to specific values, can be done within a few seconds. Additionally, results shown in Figure 3.6 enable us to understand the effect of each geometrical parameter. The resonator radius has the strongest impact on the resonance frequency, with the frequency being inversely proportional to the radius. The power dissipated in the meander scales up mainly with the track width. The power also scales up with the radius of the resonator because of the larger area but is weighted against the associated decrease in the resonance frequency.
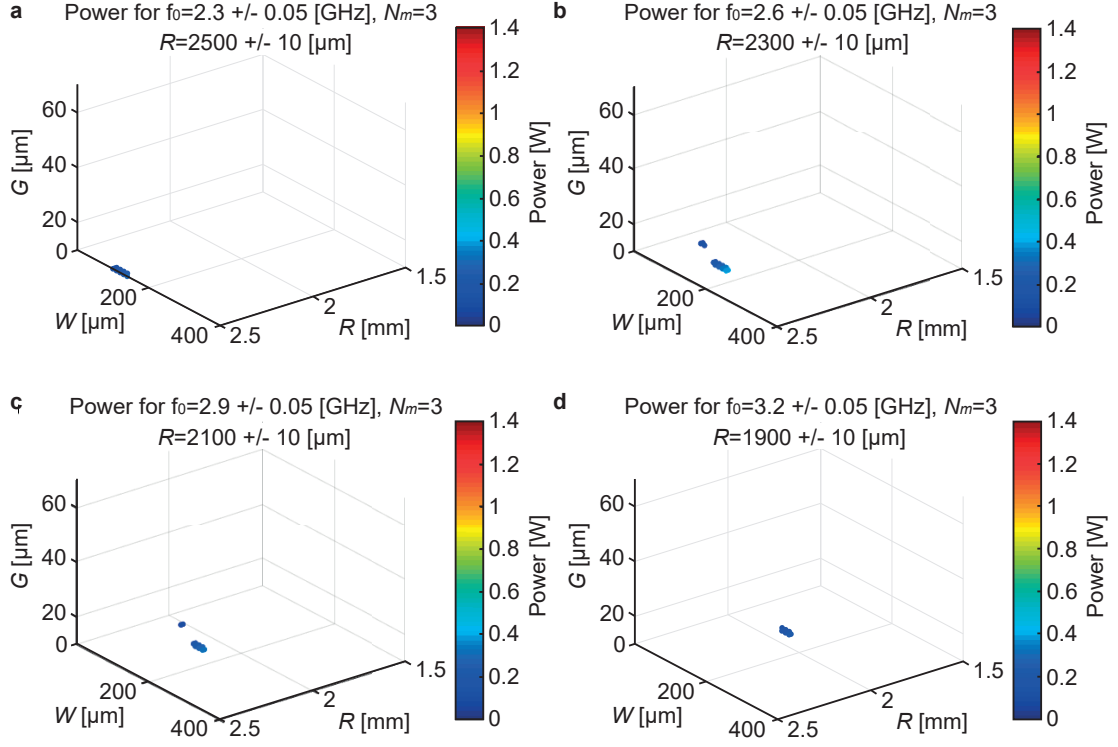
Figure 3.8 – **Power optimization - Specific resonator radius.** Power dissipated in the meander at specific resonance frequencies and for preset radius values in air. Only valid geometries with $N_m = 3$ are displayed. Each plot is a subset of the corresponding plot in Figure 3.7.

Indeed, a larger track width decreases the resistance of the resonator which improves the matching between the resistance of the resonator and the resistance of the meander. Finally, the quality factor also increases with the track width since the total resistance of the resonator is smaller for larger track width. Changing any of the environmental parameters in Table 3.2 changes the values of the results but not the trends. Finally, a last observation from Figure 3.8 is that when restricting the radius of the resonator to specific values, the number of valid geometries for a given resonance frequency is very limited. Consequently, the optimization quality is also limited as illustrated in Table E.1, where the ratio R_m/R_{tot} can be as low as 0.05 for resonators with $N_m = 1$. As discussed in Section 3.2, in the ideal case $R_m = R_r$, which gives a ratio $R_m/R_{tot} = 0.5$.

3.4 Microfabrication of Au resonators on polyimide membranes

3.4.1 Introduction

As discussed in Section 3.2, gold microheaters on polyimide membranes are used for the non-biodegradable prototype developed in this chapter. Polyimide is a mechanically stable and temperature resistant polymer, with a glass transition temperature above 200°C. Therefore, PI is not the best option for a thermally-breakable membrane. However, the choice of this specific material is strongly motivated by the final application which consists of a fully biodegradable drug delivery capsule. As discussed in Section 2.1.2, microfabrication processes based on transfer printing are used to fabricate biodegradable electronics on biodegradable polymeric substrates. [107, 122, 124] With these processes, PI is used as a mechanical layer during the transfer from a non-biodegradable to a biodegradable substrate.

The process we developed here is partially similar because we use a PI layer as a mechanically stable membrane material. First, Au is deposited by sputtering on a stack of materials consisting of a Si wafer, a poly(methyl methacrylate) (PMMA) sacrificial layer and a PI layer. Gold is then patterned using photolithography and ion beam etching, similarly to the process developed in Section 2.4. During a second photolithography step, the PI layer is patterned to define the shape of the membranes. Finally, the PI film with the gold microstructures on top is released by dissolving the PMMA layer in acetone to form PI membranes. At this point of the fabrication process, PI membranes stick to the Si wafer due to van der Waals interactions.

As detailed in Section 3.5, the PI membranes are detached from the wafer only once the capsules have been glued on top of them. The thickness of the PI film directly determines the thickness of the membranes used to close the drug reservoirs of the capsule. Several PI thicknesses between 1 and 3 μm are tested. The optimum thickness is a tradeoff between a thin membrane which can be easily broken thermally, and a thick membrane which is mechanically stable to withstand the handling of the capsule.

3.4.2 Methods

Figure 3.9 shows the details of the process flow used to fabricate Au microheaters on PI membranes. First, a 200 nm thick PMMA sacrificial layer is spin-coated on a Si wafer previously cleaned by oxygen plasma. It is followed by a 5 min soft-bake at 180°C on a hotplate. Secondly, a PI thin film is spin-coated on top of the PMMA layer. Adjusting the spin speed enables to coat films between 1.5 and 3.5 μm thick. The PI layer is cured with two soft-bake steps of 180 s each, at 65 and 105°C on hot plates, plus a hard-bake at 250°C during 1 h in an oven under a nitrogen atmosphere. Then, gold microresonators are fabricated on top of this stack consisting of the Si wafer, the PMMA and the PI layers, using a process very similar to the one developed for Mg in Section 2.4.
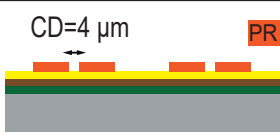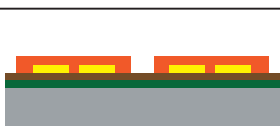
#	Process description	Cross-section
1	**Substrate: silicon** Thickness: 525 µm SRD + 4 min O_2 plasma, 500 W	
2	**PMMA spin-coating** Thickness: 200 nm 950K A4, 4500 rpm Soft-bake: 5 min, 180°C	PMMA
3	**PI spin-coating** Thickness: 1.5 µm PI 2610, 3280 rpm No adhesion promoter Soft-bake: 2x180 s, 65°C + 105°C Hard-bake: 1 h, 250°C under N_2	PI
4	**Au thin film deposition** Activation: 60 s O_2 plasma, 40 W Thickness: 1 µm Sputtering, R=13 Å/s	Au
5	**Photolithography** 10 min dehydration, 120°C AZ9221 2 µm, no EBR, 165 mJ/cm^2	CD=4 µm PR
6	**Reflow** 2 min reflow, 130°C On a hotplate	
7	**Au dry etch** IBE: -10° tilt, 60 nm/min	
8	**PR stripping** 20 s O_2 plasma Acetone - IPA - N_2 1 min O_2 plasma, 500 W	
9	**Photolithography** 10 min dehydration, 135°C AZ9260 10 µm, no EBR, 420 mJ/cm^2 Soft-bake: 4 min, 105°C Relaxation: 30 min, RT	
10	**PI + PMMA etching** O_2 plasma 1.5 µm/min	
11	**PR stripping + PMMA release** Acetone - IPA - N_2 48 h	

Figure 3.9 – **Microfabrication of Au microresonators on PI membranes.** Fabrication process to produce gold microheaters on polyimide membranes.

Firstly, a 1 μm thick Au film is deposited by sputtering (plasma activation 40 W/60 s, 13 Å/s) on top of the PI thin film. Secondly, a photolithography step is performed: after a dehydration step of 10 min on a hotplate at 120°C, a 2 μm thick layer of photoresist (AZ9221, Microchemicals GmbH, Germany) is spin-coated on top of the Au film. Patterns are exposed by direct laser writing, with a dose of 165 mJ/cm^2 at a wavelength of 405 nm. The targeted critical dimension is 4 μm. After developing the resist (AZ400K 1:3.5 in DI water, Microchemicals GmbH, Germany), a reflow is performed at 130°C on a hotplate during 2 min to smoothen the resist profile. This avoids re-deposition of Au on the resist sidewalls during the subsequent ion beam etching step. The Au thin film is etched through by ion beam etching with argon (Ar) ions, at a rate of 60 nm/min and a tilt of -10°.

Finally, the photoresist is removed with a 20 s oxygen plasma, a 10 min immersion step in acetone (rinsed in IPA and dried with N_2), and a subsequent 1 min oxygen plasma at 500 W. For this last oxygen plasma step, a dummy wafer must be placed in front of the wafer with the microstructures in order to prevent the etching of the PI layer.

At this stage of the microfabrication process, the microresonators are fully fabricated but a second photolithography step is required to define the shape of the polyimide membranes, as shown in Figure 3.10.
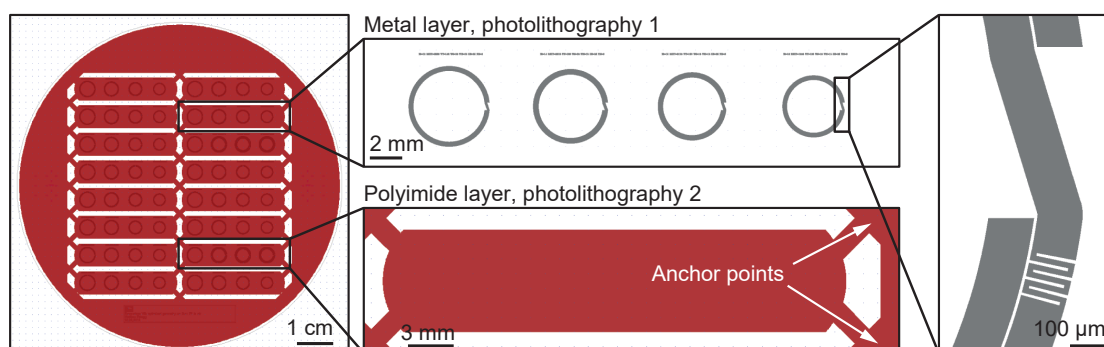
Figure 3.10 – **Wafer layout for the drug delivery capsules.** Layout of the Au resonators on PI membranes on a 4" wafer. The wafer is divided into 16 membranes for capsules, each containing four resonators. The first lithography defines the geometry of the gold microresonators and their meander hot-spots. The second photolithography defines the design of the PI membranes, including some anchor points in order to keep the membranes attached to the wafer after the final release step in acetone.

The design of the membranes is similar to the shape of the capsule (cf. Section 3.5) but anchor points are added in the corners. The purpose of these anchor points is to keep the membranes on the wafer after the final release step in acetone. The second photolithography step is as follows. After a dehydration step of 10 min on a hotplate at 135°C, a 10 μm thick layer of photoresist (AZ9260, Microchemicals GmbH, Germany) is spin-coated on top of the Au microresonators. Because of the thick PR layer, a soft-bake at 105°C during 4 min on a hotplate is required, followed by a 30 min relaxation step at room temperature. Such a thick PR layer is used in order to make sure that the Au microstructures are protected during the whole

subsequent etching step of the PI layer. Patterns are exposed in the PR by direct laser writing, with a dose of 420 mJ/cm^2 at a wavelength of 405 nm. The targeted critical dimension is 1 mm. After developing the resist (AZ400K 1:3.5 in DI water, Microchemicals GmbH, Germany), the PI layer is etched through in an oxygen plasma at a rate of 1.5 µm/min. Finally, the wafer is immersed in acetone during 48 h to remove the PR layer and dissolve the underlying PMMA sacrificial layer under the PI film. The wafer is rinsed in IPA and dried under a gentle N$_2$ flow.

At this stage of the process, the PI membranes with the Au resonators on top are released but remain attached to the wafer through the anchor points. 16 capsules with four resonators each can be produced from one wafer. As discussed in Section 3.3 and Appendix E, the resonators are designed to maximize the power dissipation in the meander while having distinct resonance frequencies within the same capsule.

3.4.3 Results

The resist stripping after the IBE step is a technical but critical difference in the process flow compared to the fabrication of the Mg resonators in Section 2.4. With Mg, the resonators were fabricated directly on a glass wafer, and the resist was stripped with a strong oxygen plasma step followed by an immersion in acetone. The same process is not compatible with the fabrication of Au microresonators on a polyimide film, since the strong oxygen plasma step would etch through the PI layer. Consequently, a shorter and less intense oxygen plasma step is performed before the immersion in acetone, which results in the incomplete dissolution of the PR layer. As shown in Figure 3.11a, a PR crust remains on top of the gold microstructures. Therefore, a second oxygen plasma step is required afterwards to remove this PR crust as shown in Figure 3.11b. Using a dummy wafer to protect the PI layer during this step is mandatory. Finding the right recipe to fully remove the PR layer without damaging the PI film was a key milestone in this fabrication process.
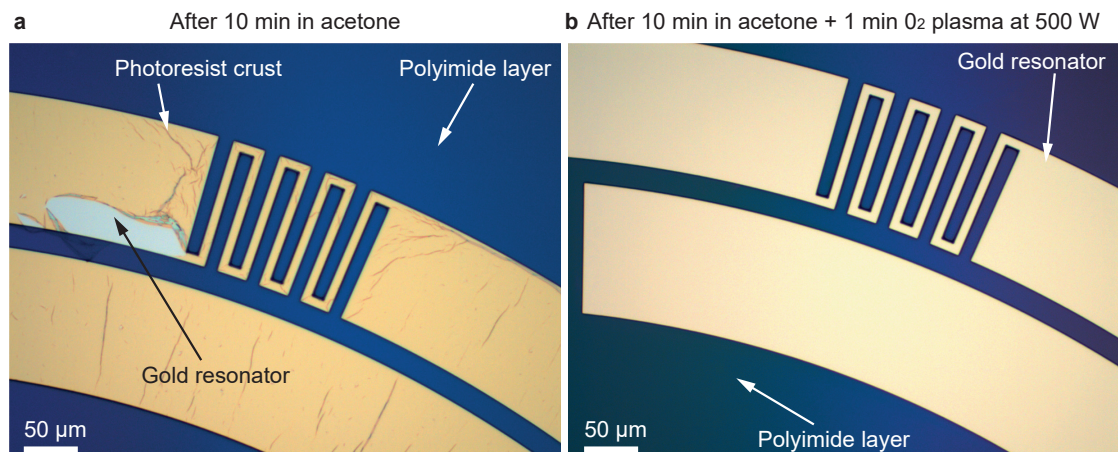
Figure 3.11 – **Photoresist stripping. a,b**, Remaining photoresist crust on the Au resonators after a 10 min immersion step in acetone (**a**), and fully removed photoresist with a subsequent oxygen plasma step (**b**).

The rest of the process doesn't present any major complications, and the wafer before and after the final dissolution of the PMMA layer in acetone to release the PI membranes is shown in Figure 3.12. The release step is relatively long but has a good efficiency. The yield of the overall microfabrication process is close to 100% which enables us to produce 16 PI membranes with four resonators each, with one wafer.
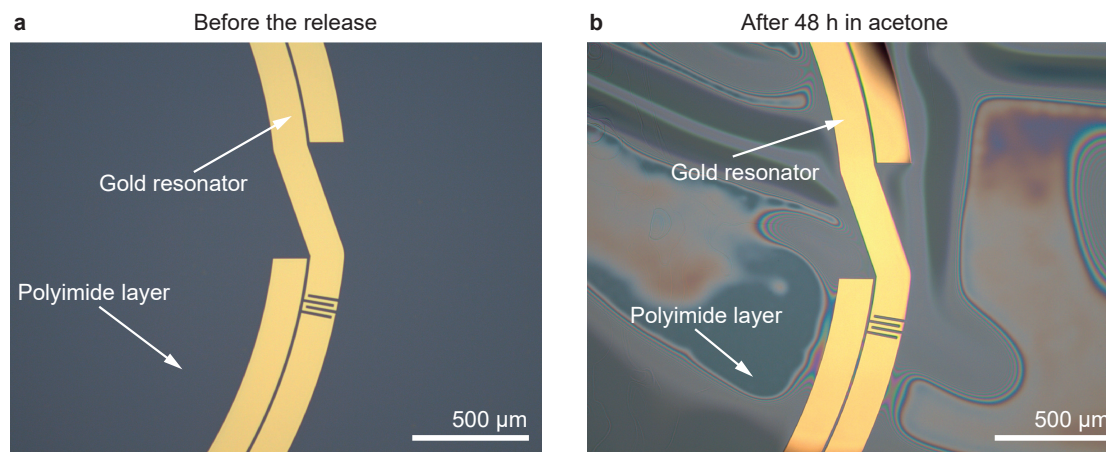
Figure 3.12 – **PMMA dissolution to release the PI membranes. a**,**b**, OM images before (**a**) and after (**b**) the release of the PI membranes by dissolving the underlying PMMA layer during 48 h in acetone.

3.4.4 Summary and discussion

The fabrication of Au microheaters on PI membranes is based on the process developed in Chapter 2 to fabricate Mg microstructures by ion beam etching. Additionally, it also considers the transfer printing process required to fabricate biodegradable resonators on biodegradable membranes. Chapter 4 shows how the process developed in this section can be modified for this purpose. The thickness of all the PI membranes fabricated on one wafer is identical. However, it can be modified from one wafer to another by changing the thickness of the PI layer during the initial spin-coating step. During the fabrication process, the PI layer is exposed several times to oxygen plasma steps. Consequently, at the end of the fabrication, the PI film is approximately 500 nm thinner than just after the initial spin-coating. The change in thickness over the whole fabrication process is reproducible from one wafer to another, and can be taken into account beforehand during the design step.

3.5 Capsule fabrication and assembly

3.5.1 Introduction

At the end of the microfabrication process described in Section 3.4, the polyimide membranes with the gold resonators on top could be detached from the wafer. However, the PI membranes are only a few μm thick and would be difficult to handle. Therefore, the drug delivery capsules are first assembled on top of the PI membranes, while they are still on the wafer. Then, the whole system consisting of the capsule, the membrane and the gold resonators is detached from the wafer. The filling of the capsules occurs afterwards by pipetting some liquid, which acts as the dummy drug here, into the reservoirs through filling holes at the backside of the capsule.

3.5.2 Methods

The design of the drug delivery capsules used to fabricate the non-biodegradable prototype of the system is shown in Figure 3.13. The capsule with its four drug reservoirs, is directly 3D printed by stereolithography (Clear resin, Formlabs, Ireland). Additionally, filling holes are also designed at the backside of the capsule.
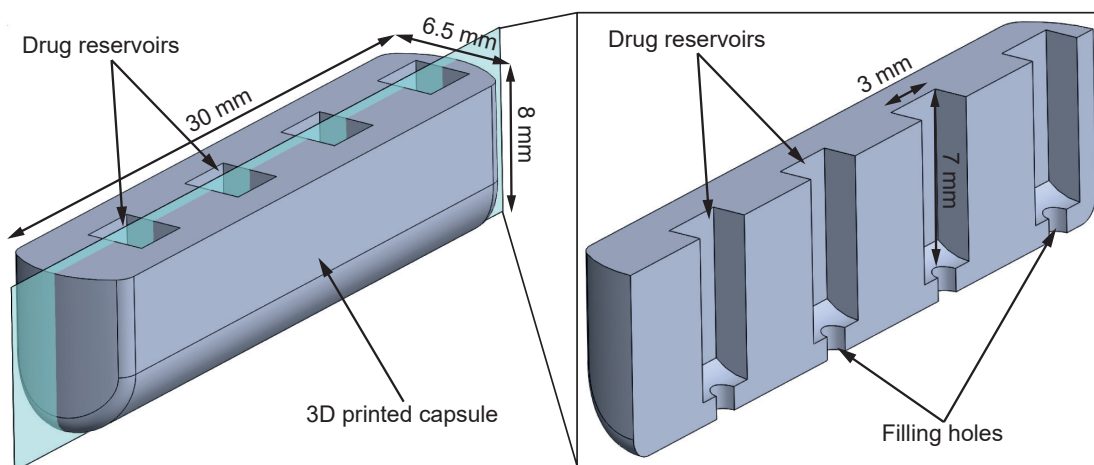
Figure 3.13 – **Design of the 3D printed drug delivery capsule.** The drug delivery capsule is 3D printed by stereolithography. It consists of 4 distinct reservoirs, each with a filling hole at the backside of the capsule. On the front side of the capsule, the drug reservoirs will be closed by the PI membranes with the Au microheaters on top.

To assemble the membrane on the front side of the capsule and seal the drug reservoirs, the capsule is glued on top of the PI membrane and the resonators while they are still attached to the Si wafer. Such a process is illustrated in Figures 3.14 and 3.15. Fast-drying glue is applied to the front side of the capsule using a toothpick, and the capsule is then pressed against the PI membrane. Once the glue has dried, the capsule, together with the PI membrane and the gold resonators are manually peeled-off from the wafer.

99
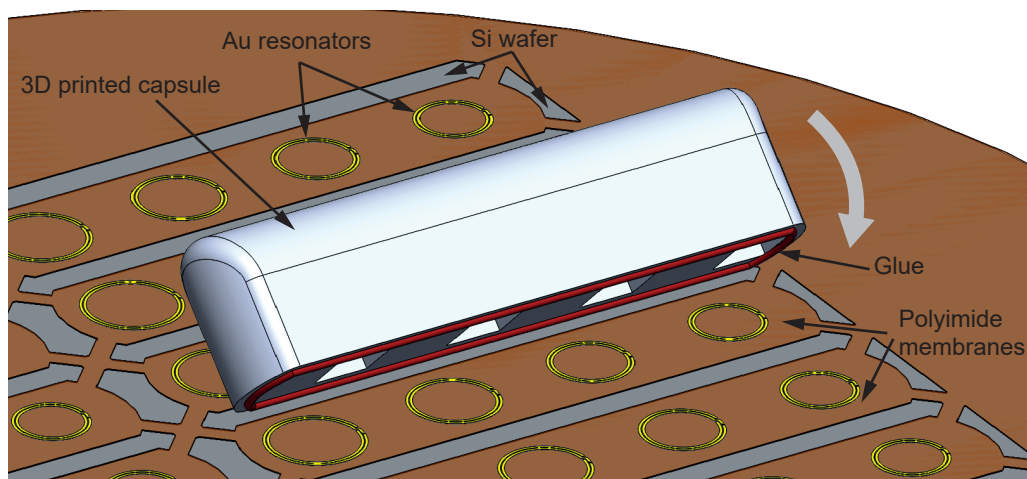
Figure 3.14 – **Assembly of the drug delivery capsule on the PI membrane.** The drug delivery capsule is glued on top of the PI membrane and the gold resonators while they are still attached to the Si wafer thanks to the anchor points. Once the glue has dried, the capsule together with the PI membrane and the gold resonators are manually peeled-off from the wafer.
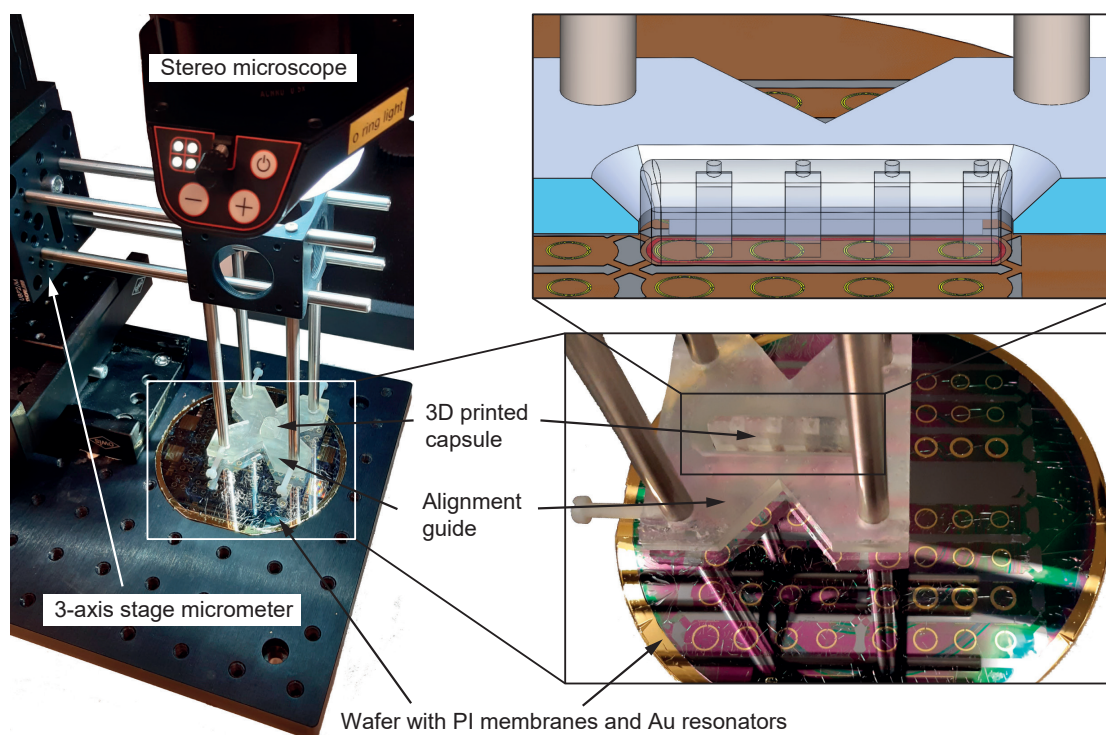
Figure 3.15 – **Alignment of the drug delivery capsule over the PI membrane.** A 3-axis stage micrometer and a stereo microscope are used to align the drug delivery capsule on top of the PI membrane. First, a 3D printed alignment guide is positioned at the right location and pressed down against the wafer. Then, the drug delivery capsule is glued on top of the PI membrane with the help of the alignment guide.

As shown in Figure 3.15, a 3-axis stage micrometer and a stereo microscope are used to precisely align the capsule on top of the PI membrane. This also ensures that the meander hotspots of the resonators are in the center of the drug reservoirs. First, a 3D printed alignment guide is positioned at the right location over the wafer and the PI membranes using the stage micrometer and the microscope. Then, the alignment guide is pressed down against the wafer to prevent any movement. Finally, the drug delivery capsule is glued on top of the PI membrane with the help of the alignment guide.

After peeling-off the capsule with the membrane and the resonators from the wafer, the drug reservoirs are filled with colored DI water, which acts as a dummy drug, by pipetting the solution through the filling holes at the backside of the capsule. The process is illustrated in Figure 3.16. DI water is required because normal water would short-circuit the resonators. Instead of manually pipetting the solution into the capsule, inkjet printing could also be used to increase the throughput and assure the exact amount of drug is in the reservoir. The holes are subsequently sealed with high viscosity glue.
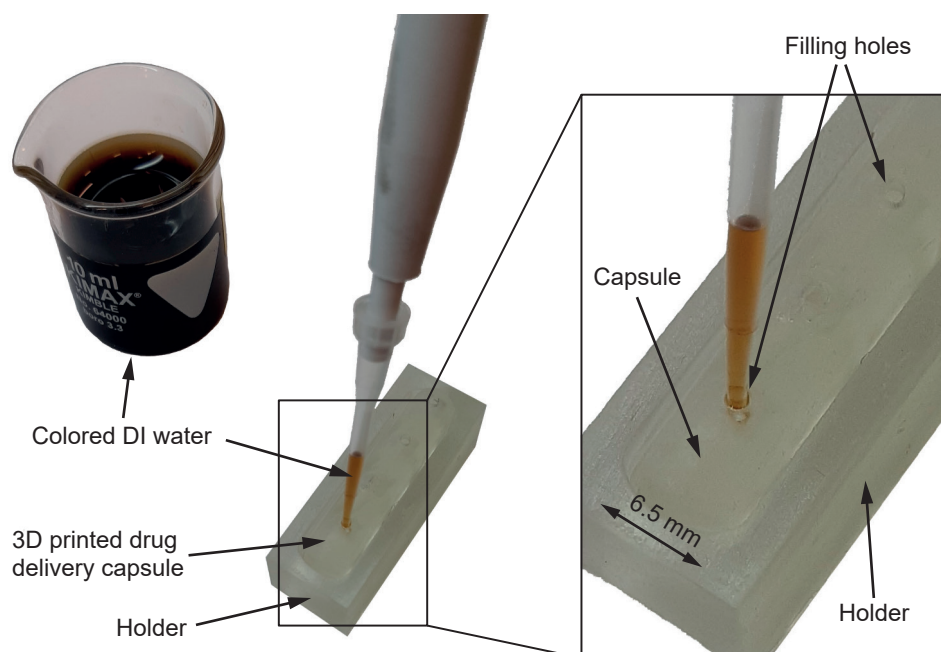
Figure 3.16 – **Dug delivery capsule filling by pipetting.** Colored DI water is manually pipetted into the drug reservoirs through the filling holes at the backside of the capsule. The holes are subsequently sealed with high viscosity glue. The capsule is placed in a holder to facilitate its handling.

3.5.3 Results

A capsule with a 1 µm thick PI membrane and 1 µm thick Au resonators after the final assembly step is shown in Figure 3.17a. After pipetting the water solution into the reservoirs and closing the filling holes with glue, the capsule drug delivery system is immersed in water to demonstrate that the sealing of the reservoirs with the polyimide membrane is leak-free. Figure 3.17b shows the capsule immersed in water after two days.
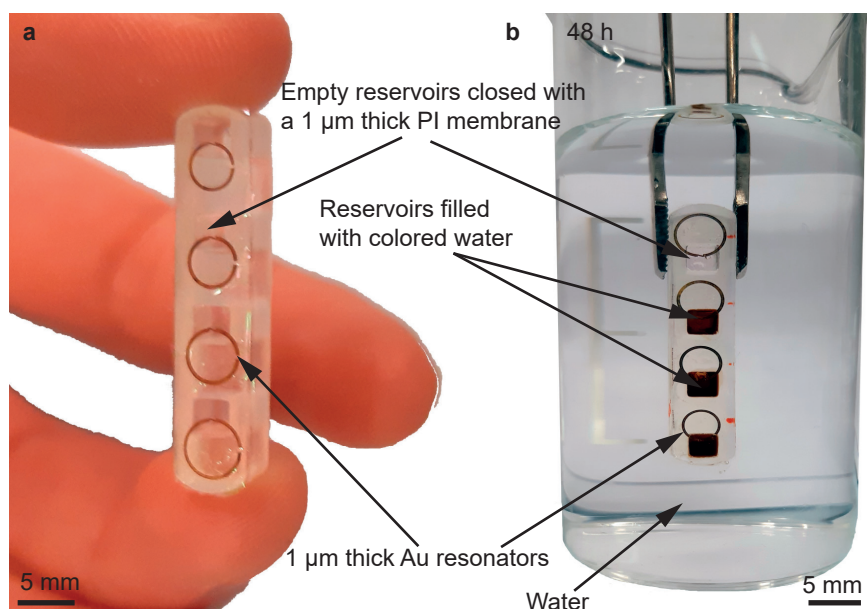
Figure 3.17 – **Assembled drug delivery capsule. a**, Capsule with a 1 µm thick PI membrane and 1 µm thick Au resonators after the final assembly step, before filling the reservoirs. **b**, Capsule drug delivery system immersed in water to demonstrate the leak-free sealing of the reservoirs with the polyimide membrane.

Finally, Figure 3.18 shows a close up view of the PI membrane closing the drug reservoirs. It also demonstrates the reliable alignment of the meander hot-spot of the resonators in the center of the reservoirs.
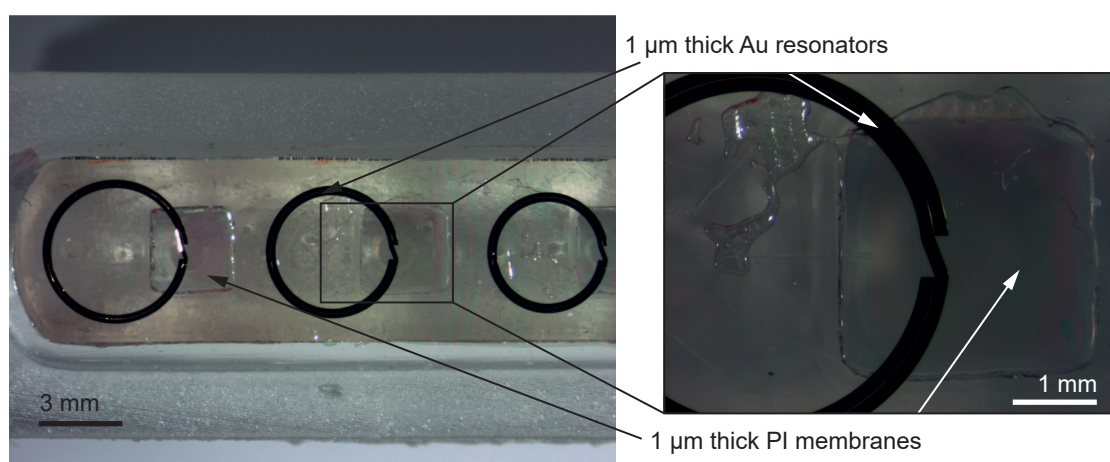
Figure 3.18 – **PI membranes closing the drug reservoirs.** OM images showing the closing of the drug reservoirs with a polyimide membrane as well as the alignment of the meander hot-spot of the resonators in the center of the reservoirs.

3.5.4   Summary and discussion

The final assembly of the system is performed by gluing the 3D printed drug delivery capsule directly on top of the PI membrane and the gold microheaters while they are still attached to the Si wafer. For this purpose, a custom-made alignment setup is used and enables the precise and reliable positioning of the capsule over the PI membrane. Then, the assembled capsule system is peeled-off from the wafer and the reservoirs are filled with colored DI water by pipetting. This assembly method enables a good alignment of the meander hot-spot of the resonators in the center of the drug reservoirs and the leak-free sealing of the reservoirs with the PI membranes.

3.6 Electrical characterization of the capsule

3.6.1 Introduction

Similar to the Mg resonators on a glass substrate in Section 2.5, the gold microresonators on PI membranes are also characterized electrically. The characterization is performed by measuring the resonance frequencies and quality factors of the resonators after the capsule assembly. The resonance is studied before and after filling of the reservoirs with water. Additionally, the resonance of the resonators is compared when measured individually and when measured simultaneously for the four resonators in one capsule.

3.6.2 Methods

The characterization setup used in this section is identical to that used for the Mg resonators on a glass substrate shown in Figure 2.23a. The working principle of the setup is the following. A signal generator (SG384, Stanford Research Systems, USA) creates a -40 dBm RF signal and couples it into a CPW above which is placed a capsule with the resonators to characterize. The signal is pulse-modulated at 5 kHz to perform synchronous detection and, hence suppresses the influence of low frequency noise sources on the measured transmission and reflection spectra.

The signal frequency is swept between 0.1 and 4 GHz, and when it matches the resonance frequency of one of the resonators some electromagnetic energy is coupled from the CPW into the resonator. This results in a drop in the transmitted power and voltage at the output of the CPW. The efficiency of this coupling as a function of the signal frequency is depicted in the transmitted power at the output of the CPW, which is amplified using a power detector (ZX47-60+, Mini-Circuits, USA) and a lock-in amplifier (7260 DSP lock-in amplifier, EG&G Instruments, USA). Finally, an acquisition card is used to record the signal (BNC-2110 + PCIe6361, National Instruments, USA) and the setup control is performed using LabVIEW (National Instruments, USA).

As described in Section 2.3.2, the resonance frequency is defined as the frequency at which the voltage attenuation at the output of the waveguide is maximal. The Q factor is defined as the resonance frequency divided by the full width at half maximum (Δf) of the voltage attenuation signal at the output of the CPW (cf. Equation 2.45). Without a resonator above the CPW, all the energy is transmitted through the CPW and the recorded signal can be used as a baseline. Baseline removal is performed for each measurement by subtracting the signal obtained with a capsule with resonators cut by design on top of the CPW.

Similar to Section 2.5, the center of the resonator is aligned over one of the two gaps of the CPW to maximize the power coupling, and the vertical distance between the device and the CPW is also 300 μm. A shorter vertical distance results in a larger signal but also in a larger shift from the unloaded resonance frequency of the resonator. As shown in Figure 3.19, custom-made

3D printed sample holders are used to precisely set the vertical and horizontal position of the capsule and the resonators respectively to the CPW. Two different holders are used to align the capsule along or perpendicularly to the CPW. This enables to measure the resonance of the four resonators in a capsule simultaneously or individually.
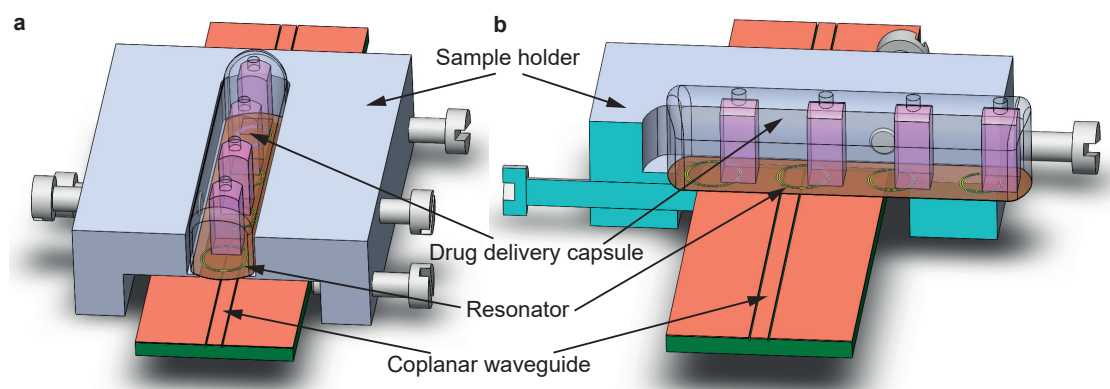
Figure 3.19 – **Sample holders for the electrical characterization of the capsules. a,b**, 3D printed sample holders are used to position the capsules 300 μm over the CPW and to align the resonators with one of the gaps of the CPW. The capsule can either be aligned along the CPW (**a**) in order to measure the resonance of the four resonators simultaneously, or perpendicularly to the CPW (**b**) to position only one resonator on top of the CPW.

3.6.3 Results

Figure 3.20 shows the resonance of an empty capsule in several orientations. The capsule is closed with a 1 μm thick PI membrane and has four Au resonators. As discussed in Sections 3.2 and 3.3 resonators are designed to have distinct resonance frequencies in water. This implies to set their radius to specific values in steps of 200 μm. The resonance of the four resonators can be measured simultaneously when the capsule is aligned along the CPW (top), or individually for each radius value when the capsule is placed perpendicularly to the CPW (bottom). For the simultaneous measurements, the capsule can be flipped by 180° (along a vertical axis) which results in two distinct measurements. For the individual measurements, the capsule is translated along the holder to align one of the resonator over one of the gaps of the CPW. The detailed geometries of each resonator are described at lines 5, 6, 7 and 8 of Table E.1 in Appendix E.
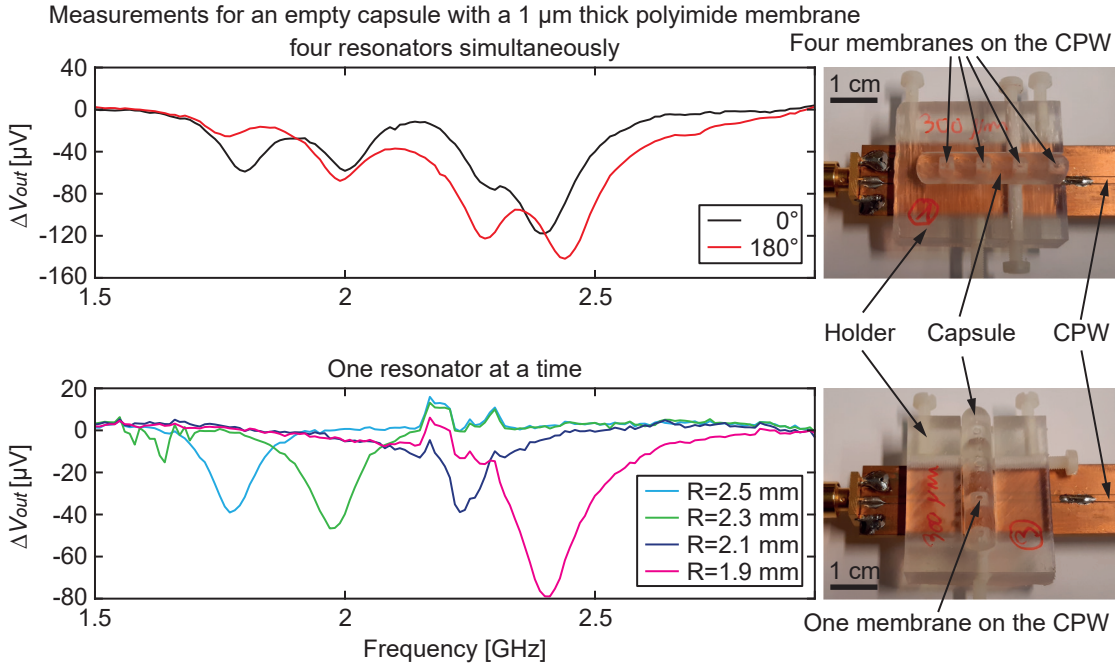
Figure 3.20 – **Capsule electrical characterization - Orientation effect.** Resonance of an empty capsule closed with a 1 µm thick PI membrane measured in several orientations. The black and red curves depict measurements where the capsule is aligned along the CPW with an angle of 0° and 180° to measure the resonance of the four resonators simultaneously. The cyan, green, blue and magenta curves depict measurements where the capsule is placed perpendicularly to the CPW to measure the resonance of each resonator individually. The main geometrical variation between the four resonators used is their radius. The four resonators have the same meander hot-spot and are fully described at lines 5, 6, 7 and 8 of Table E.1 in Appendix E.

In Figure 3.21, the resonance of different resonator geometries is compared between an empty capsule (solid lines) and a capsule filled with DI water (dashed lines). In both cases, a 1 µm thick PI membrane is used to close the reservoirs. The geometrical variations of the resonators, resulting in distinct resonance frequencies, are described in the table in the center and depicted by different colors in the plots. As discussed in the previous paragraph, the main geometrical variation between the different resonators is their radius value. The detailed geometries of each resonator are described at lines 14, 15 and 16 of Table E.1 in Appendix E. Finally, the numerical values of f_0 and Q for each measurement in Figure 3.21 are described in Table 3.3.
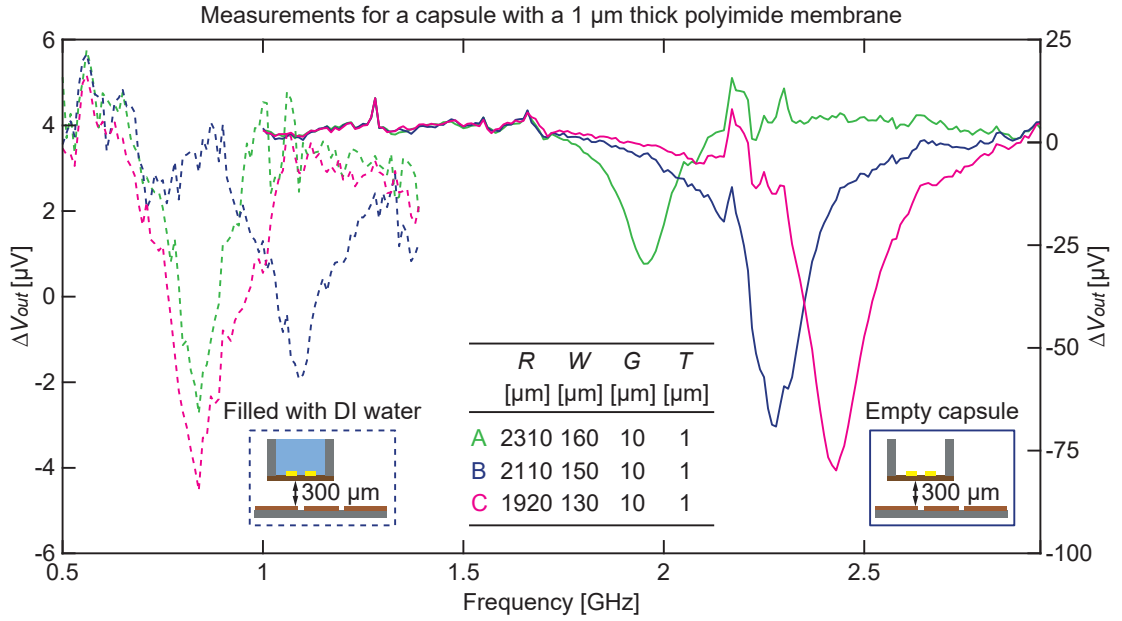
Figure 3.21 – **Capsule electrical characterization - Resonator geometry effect.** Resonance of different resonator geometries on a 1 μm thick PI membrane closing an empty capsule (solid lines, right ordinate axis) and a capsule filled with DI water (dashed lines, left ordinate axis). These two configurations are illustrated by the cross-sections in inset. The geometrical variations of the resonators are described in the table in the center and depicted by different colors in the plots. The main geometrical variation between the three resonators used is their radius. The three resonators have the same meander hot-spot and are fully described at lines 14, 15 and 16 of Table E.1 in Appendix E. The resonance of each resonator is measured individually by placing the capsule perpendicularly to the CPW.

Table 3.3 – **Capsule electrical characterization - Resonator geometry effect.** Resonance frequencies and Q factors of the measurements in Figure 3.21, for several resonator geometries on a 1 μm thick PI membrane closing an empty capsule and a capsule filled with water. * Low signal-to-noise ratio.

	Empty capsule		Filled with water	
	f_0 [GHz]	Q	f_0 [GHz]	Q^*
A	1.95	16	0.84	17
B	2.28	15	1.09	21
C	2.43	15	0.84	8

3.6.4 Summary and discussion

Summary The electrical characterization of the capsules is performed by measuring the resonance frequencies and quality factors of the resonators on the membranes closing the reservoirs. For this purpose, the same wireless characterization setup as in Section 2.5 is used. Its working principle consists in recording the power at the output of a CPW used as the primary excitation system. The capsules are characterized with empty reservoirs and with reservoirs filled with DI water, for multiple resonator geometries. Additionally, the resonance frequencies of the four resonators in a capsule are compared when measured individually or simultaneously.

Simultaneous vs. individual measurement As shown in Figure 3.20, the resonance of the four resonators in a capsule can be measured either simultaneously or individually. A good correlation exists between the two types of measurements, and the simultaneous measurement enables to observe the four resonance peaks distinctly. Another observation is that for the simultaneous measurement, the signal intensity varies slightly for some of the peaks when the capsule is flipped by 180°. This can be explained by standing waves in the CPW. As a result, the magnetic field intensity is lower at some specific locations along the CPW and for specific frequencies. It is also the reason why the intensity of the blue signal for the resonator with a radius of 2.1 mm is lower than for the three other resonators.

Resonators geometry effect As shown in Figure 3.21 and Table 3.3 the resonance frequency of resonators with different geometries varies in air and in water. Setting the radius of the resonators to specific values in steps of 200 μm enables to have distinct frequencies also in water. For all the measurements in Figure 3.21, the geometry of the resonators is optimized in air, as described in Table E.1. Selecting resonators from Table E.2, where the geometry of the resonators is optimized in water, would enable to further increase the frequency shift in water. Additionally, the quality factor of the resonators in air is similar to that of the Mg resonators on a glass substrate in Section 2.5. Since the gold resistivity is higher than that of Mg, slightly higher quality factors were expected, but in the end having similar values doesn't alter the performance of the device. These lower Q factors can be explained by the fact that the resonators are on membranes and also by the fact that their resonance frequencies are lower than that of Mg resonators on glass. Finally, the quality factor of the resonators in water shown in Table 3.3 is not reliable. Indeed, the signal-to-noise ratio for the measurements preformed in water in Figure 3.21 is too low for an accurate computation of Q.

Comparison with the analytical model As described in Section 3.3, the geometry of the resonators is optimized in order to maximize the power dissipated in the meander hot-spot at specific resonance frequencies. The optimized geometries as well as their theoretical resonance characteristics computed with the analytical model are given in Appendix E. When

comparing the expected theoretical resonance frequencies to that measured in Figures 3.20 and 3.21, we observe a mismatch of -25% for the empty capsules and +50% for the capsules filled with DI water. This difference is large but it can be explained. Indeed, the resonators were optimized considering the whole resonator area is on a PI membrane. Practically, the size of the reservoirs is smaller than the diameter of the resonators, and the resonators are shifted to the side in order to have the meander hot-spot in the center of the reservoirs. Consequently, only a small portion of the resonator is actually on the PI membrane area. Since the relative permittivity of the capsule material is higher than that of air but lower than that of water, the measured resonance frequencies for empty capsules are lower than computed. Inversely, the resonance frequencies for reservoirs filled with water are higher than computed. Another effect affecting the resonance frequency is the fact that the PI membranes are not fully flat, which alters the capacitance value of the resonators.

3.7 Wireless release from the capsule

3.7.1 Introduction

The final purpose of the drug delivery capsule developed in this chapter is to release liquid from the reservoirs by wirelessly heating the resonators and breaking the PI membranes. Similar to the wireless heating of the Mg microresonators in Section 2.7, a $\lambda/2$ CPW resonator and a power amplifier are used to generate a strong magnetic field. However, a few adaptations of the setup are made compared to the one used in Section 2.7. They enable to easily tune the resonance frequency of the primary excitation system and to precisely monitor the power required to break the meander hot-spot, and eventually the membrane. In this section, the wireless heating of the meander hot-spot and the membrane breaking mechanism are studied for empty capsules and for capsules filled with DI water.

3.7.2 Methods

The working principle of the primary excitation setup used in this section is identical to the one shown in Figure 2.35 and used to heat the Mg resonators on a glass substrate in Section 2.7. However, its physical implementation is slightly different to facilitate the tuning of the resonance frequency of the system. An RF generator generates a 5 kHz pulse modulated RF signal, and sweeps the frequency between 0.1 and 4 GHz. The signal is amplified using a 15 W RF power amplifier (gain=46 dB, ZHL-15W-422+, Mini-Circuits, USA), and subsequently coupled through a directional coupler (ZGDC6-362HP+, Mini-Circuits, USA) into a $\lambda/2$ CPW resonator. The reflected signal is coupled through the directional coupler and detected at the coupled port using attenuators (-50 dB), and the same detection system as for the wireless electrical characterization.

Using a resonant CPW enables to increase the current in the waveguide at a specific frequency, for a fixed amount of input power. As a result, the generated magnetic field is stronger, which increases the induced current in the coupled SR. The $\lambda/2$ CPW resonator consists of a 50 Ω CPW with a transmission line of a defined length and an open end.

Unlike the setup used in Section 2.7, the resonance frequency of the $\lambda/2$ CPW resonator is not tuned by trimming the waveguide. In the new setup developed in this section, the tuning of the length of the waveguide is performed by sliding a second waveguide on top of the first one, as shown in Figure 3.22. Detailed explanations regarding the computation of the resonance frequency of the $\lambda/2$ CPW resonator are given in Section 2.7.2. Additionally, a 3D printed sample holder is used to set the vertical and horizontal position of the capsule. The SR to heat is placed 300 µm over the $\lambda/2$ CPW resonator, at the half of the total length of the system, and is aligned over one of the gaps of the transmission line.
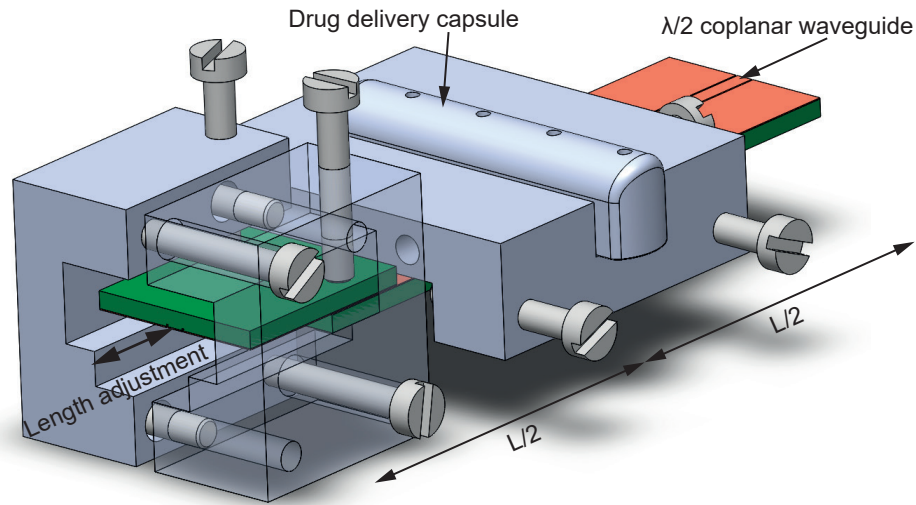
Figure 3.22 – **Tunable setup for the wireless heating of the capsules.** The resonance frequency of the $\lambda/2$ CPW resonator used as the primary excitation system to wirelessly heat the capsules can be tuned by adjusting the length of waveguide. For this purpose, a second CPW is added at the end of the first CPW and translated to adjust the total length of the setup. 3D printed holders are used to hold the two CPWs together as well as to position the capsule at the half of the total length of the system. Indeed, the strongest magnetic field is generated at this specific location.

Once the $\lambda/2$ CPW resonator is tuned and matched to the same resonance frequency as the SR to heat, a -5 dBm non-modulated signal is generated by the signal generator at the resonance frequency of the system, for a time longer than 2 s. A -5 dBm signal at the output of the signal generator results in a 10 W signal at the input of the $\lambda/2$ CPW resonator after amplification. Alternatively, a new LabVIEW program was also developed in order to ramp the power up at different rates and to simultaneously record the reflected signal from the CPW resonator.

The setup used here enables in-depth characterization of material and device functionalities, with well-controlled and reproducible environmental conditions. For subsequent in vivo experiments a setup able to generate a stronger magnetic field at a larger distance will be required. [48, 50, 55, 75]

3.7.3   Results

Figure 3.23 illustrates the wireless heating of two meander hot-spots and their underlying PI membranes above empty reservoirs. In both cases, 1 μm thick Au SRs on 1 μm thick PI membranes are used. In Figure 3.23a a 10 W input power is directly applied into the $\lambda/2$ CPW resonator for a time longer than 2 s, with a signal matching the resonance frequency of the SR. In Figure 3.23b , the power is progressively ramped up from 10 mW to 10 W, first at a rate of 0.01 dBm/s, and then a second time at a rate of 0.1 dBm/s, with a signal matching the

resonance frequency of the SR. The OM images clearly show that the Au meander hot-spots and the PI membranes are altered by the heat but no clear breaking of the membranes can be observed.

Wireless heating of empty capsules, 1 µm thick gold resonators on 1 µm thick polyimide membranes
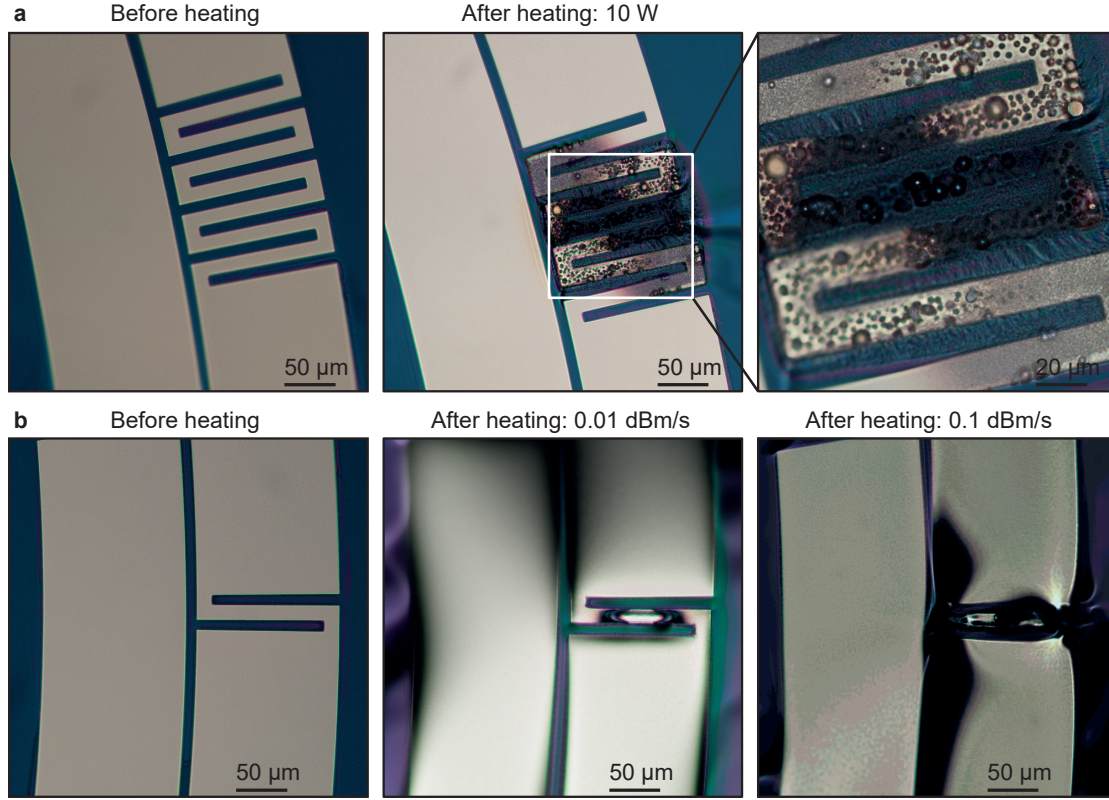
Figure 3.23 – **Wireless heating of empty capsules - OM images. a**, Optical microscope images of the meander hot-spot of a SR before and after applying 10 W into the CPW resonator, for a time longer than 2 s with a signal matching the resonance frequency of the SR. **b**, OM images of the meander hot-spot of a SR before and after ramping up the power into the CPW resonator from 10 mW to 10 W at rates of 0.01 and 0.1 dBm/s, with a signal matching the resonance frequency of the SR. In all the cases, 1 µm thick Au SRs on 1 µm thick PI membranes closing empty capsules are used. However, the experiments in **a** and **b** are performed sequentially with different capsules.

Figure 3.24 shows the in situ recording of the experiment performed in Figure 3.23b, when heating the SR by progressively ramping up the power from 10 mW to 10 W. First at a rate of 0.01 dBm/s and a frequency of 1.715 GHz, and then a second time at a rate of 0.1 dBm/s and a frequency of 1.745 GHz. Figure 3.24a illustrates the resonance of the system before and after the wireless heating steps. It shows that a slow heating rate (0.01 dBm/s) alters the impedance matching of the system, which induces a clear signal change in the scattering parameter S_{11}. However, the signal after a slow heating is not identical to the signal recorded with a resonator cut by design. It is only after the second heating at a fast rate (0.1 dBm/s) that the meander hot-spot breaks and that S_{11} matches the signal recorded with a resonator

cut by design. Additionally, the monitoring of the power sweep for the fast heating rate is shown in Figure 3.24b. This power sweep depicts the change from the green to the red curve in Figure 3.24a and enables to precisely see that the breaking occurs at -8.2 dBm. Indeed, the breaking of the meander hot-spot induces a sudden change in the resonance frequency of the system, which results in a a jump in the power sweep curve.
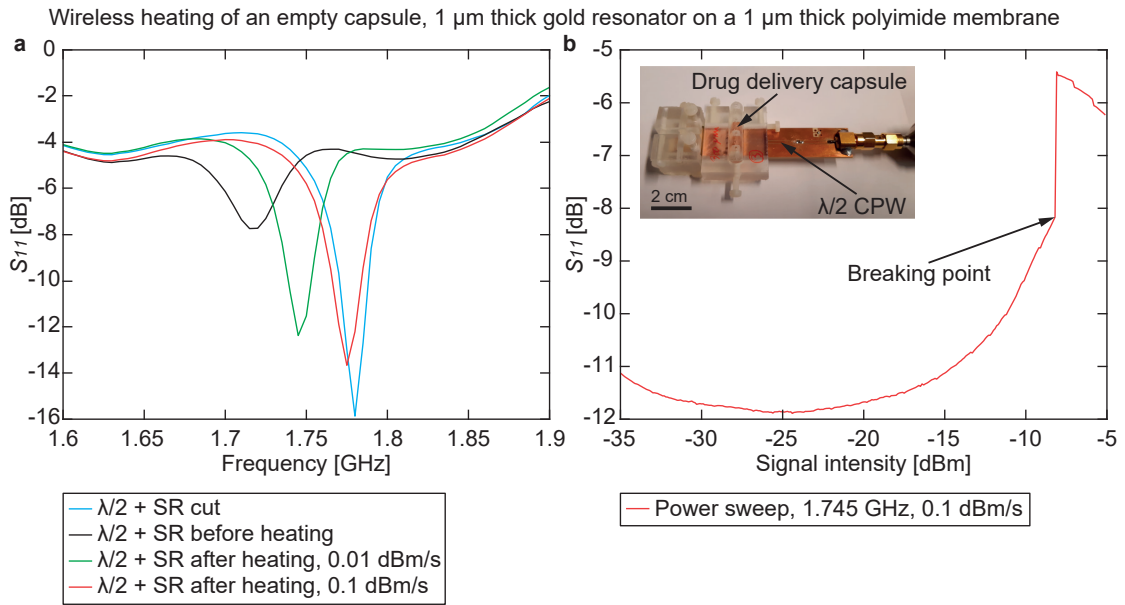
Figure 3.24 – **Wireless heating of empty capsules - Data recording. a**,**b**, In situ measurement of the breaking of the meander hot-spot of a 1 µm thick Au SR on a 1 µm thick PI membrane closing an empty capsule. The scattering parameter S_{11} is recorded at the port of the CPW resonator. **a**, The cyan and black lines are the measurements of the resonance of the CPW resonator with a SR cut by design on top of it and when coupled to an intact SR respectively. The green and red lines are the measurements of the resonance of the CPW resonator coupled to a SR heated beforehand. The heating of the SR was performed by ramping up the power into the CPW resonator from 10 mW to 10 W at rates of 0.01 and 0.1 dBm/s, with a signal matching the resonance frequency of the SR. **b**, Measurement of the power sweep when ramping up the power into the CPW resonator from 10 mW to 10 W at a rate of 0.1 dBm/s and a frequency of 1.745 GHz (i.e. the resonance frequency of the green curve in **a**). The inset shows the setup used and the arrow shows the breaking point of the meander hot-spot.

Figure 3.25 shows a similar experiment as in Figure 3.24 but this time with the reservoirs of the capsule filled with DI water. A 1 µm thick Au SR on 1 µm thick PI membrane is used and the power is ramped up from 10 mW to 10W at a rate of 0.1 dBm/s and a frequency of 1.08 GHz. Figure 3.25a illustrates the resonance of the system before and after the wireless heating and shows that the meander hot-spot breaks. Indeed, after the heating step, S_{11} matches the signal recorded with a resonator cut by design. Additionally, as shown in Figure 3.25b, a jump in the power sweep signal at -11.5 dBm confirms the meander breaking. Finally, after removing the capsule from the sample holder, some colored DI water is observed on the CPW. This confirms

the meander breaking but also demonstrates the breaking of the membrane and the wireless release of some liquid from the reservoir.
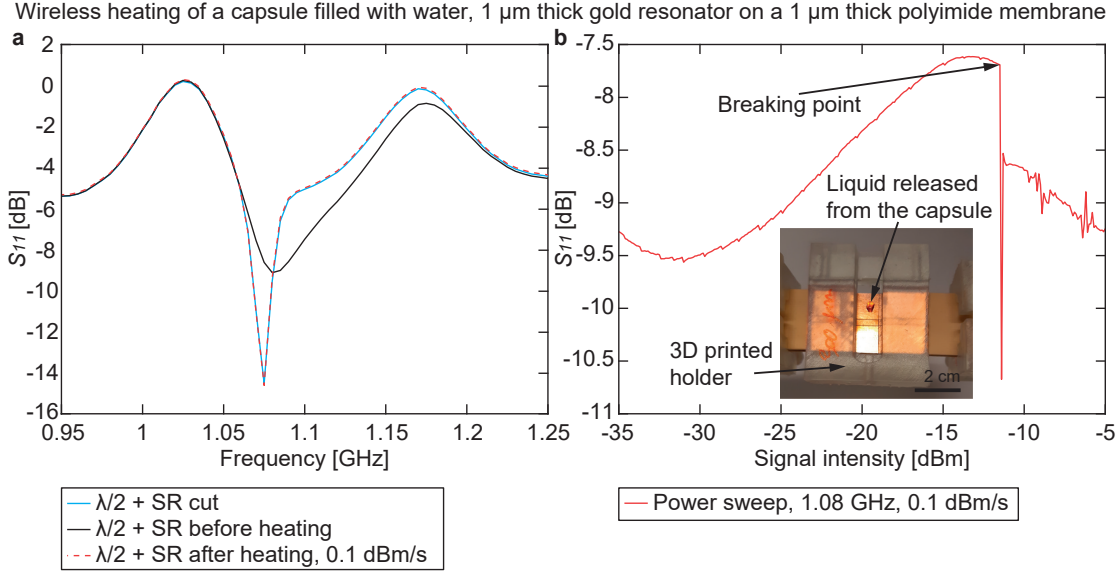
Figure 3.25 – **Wireless heating of capsules filled with DI water - Data recording. a,b**, In situ measurement of the breaking of the meander hot-spot of a 1 μm thick Au SR on a 1 μm thick PI membrane closing a capsule filled with DI water. The scattering parameter S_{11} is recorded at the port of the CPW resonator. **a**, The cyan and black lines are the measurements of the resonance of the CPW resonator with a SR cut by design on top of it and when coupled to an intact SR respectively. The red line is the measurement of the resonance of the CPW resonator coupled to a SR heated beforehand. The heating of the SR was performed by ramping up the power into the CPW resonator from 10 mW to 10 W at a rate of 0.1 dBm/s, with a signal matching the resonance frequency of the SR. **b**, Measurement of the power sweep used to heat the SR in **a**. The power at the input of the CPW resonator is ramped up from 10 mW to 10 W at a rate of 0.1 dBm/s and a frequency of 1.08 GHz (i.e. the resonance frequency of the black curve in **a**). The inset shows the setup used, with the liquid released from the capsule consequently to the breaking of the membrane. The arrow shows the breaking point of the meander hot-spot.

OM images of two PI membranes after the wireless heating of the resonators on top of them when the reservoirs are filled with DI water are shown in Figure 3.26. In both cases, the Au SRs are 1 μm thick and the PI membranes are 1 μm thick. However, the two experiments are performed sequentially and using two different capsules. The membrane opening is large and doesn't consist of only a small hole over the meander hot-spot of the resonator. Nevertheless, the membrane breaking is a consequence of the heating of the SR and not simply due to the heating of the primary excitation system. Indeed, the temperature of the λ/2 CPW resonator after a power sweep up to 10 W is 27.7°C only. Additionally, a control experiment was performed with a capsule filled with water but having a resonator cut by design on the PI membrane. No breaking was observed in this configuration.

Wireless heating of capsules filled with water, 1 µm thick Au resonators on 1 µm thick PI membranes
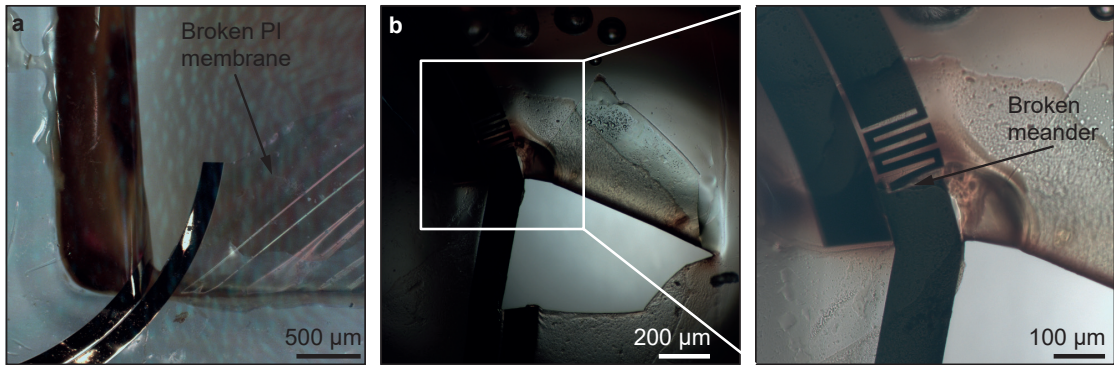
Figure 3.26 – **Wireless heating of capsules filled with DI water - OM images. a,b**, Optical microscope images of broken membranes after wirelessly heating the SRs on top of them. In both cases, the heating of the meander hot-spot was performed by ramping up the power into the CPW resonator from 10 mW to 10 W at a rate of 0.1 dBm/s, with a signal matching the resonance frequency of the SRs. Additionally, in both cases, the Au SRs are 1 µm thick, the PI membranes are 1 µm thick and closing capsules filled with DI water. However, the two experiments are performed sequentially and using two different capsules.

3.7.4 Summary and discussion

Summary   In this section, the wireless breaking of the membranes and the release of liquid from the reservoirs of the capsule was demonstrated. A primary excitation setup based on the use of a power amplifier and a $\lambda/2$ CPW resonator enables to generate enough power to wirelessly heat the meander hot-spot of the spiral resonators, under the effect of the induced electrical current. The increase in temperature is such that it leads to the breaking of the underlying PI membrane when the reservoirs are filled with DI water, but not when the reservoirs are empty. This effect was observed repeatedly for three membranes in each condition which demonstrates the reproducibility of the process. However, as discussed below, further investigations are required in order to fully understand the breaking mechanisms of the membranes and the release dynamics of the liquid from the reservoirs.

Effect of the heating rate   Several parameters affect the heating of the meander hot-spot of the resonators as well as the membrane breaking. As shown in Figures 3.23 and 3.24, the heating rate affects the meander hot-spot breaking. When a slow heating rate is used, the heat propagates and modifies the surrounding environment. Consequently, the resonance frequency of the system shifts. Then, if the excitation frequency is kept constant, the heating efficiency decreases. This shift in the resonance frequency is permanent, even once the resonator has cooled down again to room temperature. On the other hand, when a fast heating rate is used or when a high power is directly applied into the primary excitation system, the heat doesn't have time to spread and to alter the resonance frequency of the system. Higher temperatures are achieved in the close proximity of the meander hot-spot, leading to its failure.

This heating rate related problem can be solved by implementing a feedback mechanism to follow the drift in the frequency.

Membrane breaking mechanism   The breaking of the membranes was only successful for reservoirs filled with water. The membrane can break according to two possible failure mechanisms. [21] The first one is the melting of the membrane due to the heat generated by the meander hot-spot. The second one is the mechanical rupture of the membrane due to the generation of vapor bubbles in close proximity of the membrane. The vapor bubbles arise from the boiling of the liquid due to the heat generated by the meander hot-spot. Additionally, the creation of vapor bubbles increases the thermal insulation of the membrane and has an auto-catalytic effect on the membrane melting.

In our case, because of the high temperature resistance of polyimide and the fact that the membranes only break when the reservoirs are filled with DI water, we suspect a mechanical failure of the membranes due to vapor bubbles. When the reservoirs are empty, the heat generated is not sufficient to melt the PI membranes. To verify this hypothesis, a new primary excitation setup where we can observe the breaking of the membrane with a high-speed camera is required. However, the membrane breaking mechanism strongly depends on the membrane material. Using biodegradable polymers with glass transition temperatures as low as 50°C in the final application is an important parameter to consider. If required, it is also possible to increase the heating efficiency of the system by doping the membrane with magnetic particles. This would create a second source of heating while also increasing the magnetic permeability and the magnetic flux density.

Release dynamics and drug bioavailability   As shown in Figure 3.26, the membrane opening is much larger than the size of the meander hot-spot. The reason might be due to the capillary forces created by the coplanar waveguide as soon as the liquid diffuses out of the membrane through a small opening. To verify this hypothesis, we need to perform an experiment with liquid on both sides of the membrane. For this purpose, a new primary excitation setup is required. In the end, the size of the membrane and the size of the opening in the membrane will strongly affect the release dynamics of the drug out of the capsule. Additionally, the location of the implant in the body also has a strong influence on the drug bioavailability. Placing the implant in a synovial bursa should allow a good diffusion of the drug once out of the implant. Indeed, the synovial liquid and the fact that the hematoma is liquid during the first weeks after the surgery will help the drug diffusion. Consequently, the drug should be able to reach all the painful areas of the articulation, including the periosteum.

An open question that remains is to determine if, in the context of local analgesia after a knee arthroplasty, the ropivacaine released from the capsule should dissolve rapidly or slowly in the synovial fluid. This mainly depends on how the drug acts on the nerves. In addition to controlling the size of the hole in the membrane, the drug formulation can also be modified to

control the release rate from the capsule. If a slow release is required a low solubility powder can be used. On the other hand, if a fast dissolution is required it is possible to prepare the drug as a very thin powder. Additionally, some surfactant and bicarbonate can also be added to improve the wettability and create an effervescent effect.

Further investigations   As mentioned in the previous paragraphs, it is required to design a new primary excitation setup able to generate magnetic fields in the range of 50 μT at a larger distance than the 300 μm spacing currently used. With this new setup, it will be possible to use the capsule in a liquid environment and to visually observe the membrane breaking. This will help us to confirm the breaking mechanism of the membranes and to better understand the release dynamics of the drugs from the capsule. More specifically, the effect of several parameters such as the membrane thickness, the magnetic field intensity, the meander geometry, the surrounding media and the implantation depth could be studied.

Another important consideration which should also be studied is the effect of the membrane thickness on the membrane mechanical stability. Indeed, the membrane needs to be thin enough to be thermally opened, but it also needs to survive the capsule handling, the patients' movements as well as the variations in atmospheric, blood and osmotic pressures. However, all the absolute values of these characteristics are strongly dependent on the membrane material. A special care should be taken with the final biodegradable version of the device, in order to design a system with the optimal resonators geometries, membrane thickness and membrane area.

3.8 Conclusion

The results reported in this chapter demonstrate the design, fabrication and characterizing of a drug delivery capsule with multiple drug reservoirs which can be selectively opened. The resonant microheaters developed in Chapter 2 are used both as power receivers for near-field resonant inductive coupling, and electrothermal triggering elements to release the drugs. The system consists of a 3D printed capsule with several reservoirs filled with drugs. Each reservoir is sealed with a polyimide membrane with a resonant gold microheater on top of it. The integration and miniaturization of all the components of the system enables multiple drug reservoirs of several tens of microliters in a minimal volume. The design of the resonators is optimized to maximize the power dissipated in the meander hot-spot at specific resonance frequencies. This optimization is performed using the analytical model developed in Chapter 2.

The Au microheaters are fabricated on a stack consisting of a Si wafer, a PMMA sacrificial layer and a PI layer. At the end of the fabrication process, the PI layer is released to create PI membranes by dissolving the PMMA sacrificial layer. Similar to the process developed in Section 2.4, the metal etching is based on ion beam etching and the whole fabrication process is water-free. This makes it compatible with the fabrication of biodegradable electronics. The 3D printed capsules are then glued on top of the PI membranes and the gold resonators using a custom-made alignment setup. Finally, the reservoirs are filled with colored DI water, or ultimately the drug solution, by pipetting. The successful fabrication of leak-free capsules was demonstrated in this chapter. Additionally, the electrical performance of the Au resonators on the PI membranes is similar to that of the Mg resonators on a glass substrate in Section 2.5.

We also demonstrated that it is possible to wirelessly heat the resonators and break the underlying PI membranes to release liquid from the reservoirs. However, no breaking occurs with empty reservoirs, which leads us to believe that the breaking mechanism of the membranes is related to vapor bubbles. These bubbles are created in the close proximity of the membrane when the surrounding liquid reaches its boiling point due to the heat generated by the microheater. At this stage of the development of the device, a new primary excitation setup is required to study in more details the release dynamics of the drugs from the reservoirs.

The ability to wirelessly release liquid from the capsule demonstrates the feasibility of using our microheaters as power receivers and triggering elements in implantable medical devices. It is also a significant step towards the development of the final biodegradable version of the device. This drug delivery capsule is very similar in terms of dimension and working principle compared to other non-biodegradable drug delivery systems. [44, 71] However, its design enables the integration of several drug reservoirs which can be selectively opened without the need for complex integrated circuits. Additionally, the microfabrication process developed to produce the microheaters makes this technology easier to fabricate a fully biodegradable version of the drug delivery system. In comparison to other biodegradable

DDS, [28, 54, 55, 66, 67] which consist of polymer layers loaded with drugs, this capsule and its multiple reservoirs of several tens of µl enables the delivery of larger amounts of drugs.

The design of our capsule is compatible with the drug requirements needed in the context of an implantable drug delivery system for local analgesia after a knee arthroplasty. However, such a system is only interesting if it can be fully fabricated from biodegradable materials, to prevent a second surgery to extract the device. Using a biodegradable drug delivery implant to locally treat the pain after a knee replacement surgery shows several advantages compared to the current post-operative pain management techniques. Among others, it would lower the risk of infection, create less discomfort to the patient and enable a personalized and better pain relief while using lower drug doses. Ultimately, the goal is to replace the current methods of drug administration for post-operative local analgesia after a knee arthroplasty, while personalizing and reducing the drug dose and secondary effects.

Then, the next step consists in the development of a fully biodegradable version of the system. The required modifications of the fabrication processes developed in Chapter 2 and in this chapter in order to produce such a device are introduced and discussed in Chapter 4.

4 A fully biodegradable multi-reservoir drug delivery capsule

The purpose of this chapter is to translate the fabrication processes developed in Chapters 2 and 3 in order to fabricate a fully biodegradable version of the drug delivery system presented in Chapter 3. The microresonators are fabricated on a biodegradable membrane using a transfer printing process, while the capsules are micro-molded from biodegradable polymers. At this stage, this work is facing some technological challenges preventing the fabrication of a fully functional prototype. However, it gives some strong guidelines in order to its fulfillment.

4.1 Introduction

In Chapter 2, biodegradable frequency-selective resonant microheaters were fabricated on a glass substrate. In order to use them as triggering elements in a biodegradable version of the drug delivery capsule discussed in Chapter 3, these microheaters must be fabricated on biodegradable membranes. Figure 4.1 illustrates a fabrication process in which the Mg microheaters are directly fabricated on PLGA biodegradable membranes. Concretely, in this process, the glass substrate used in Section 2.4 is simply replaced by a Si wafer covered with a silane anti-adhesion layer and a drop-casted PLGA film on top. Then the Mg microstructures are fabricated by ion beam etching in the same way as on a glass substrate. A second PLGA film is bonded on top of the first PLGA film and the Mg structures to encapsulate and protect the Mg from the body fluids and the drug solution. [104] Finally, a biodegradable capsule is glued on top of the PLGA film and filled by pipetting, similarly to the process developed in Section 3.5. Then, the whole capsule system is peeled-off from the wafer substrate. The biodegradable capsule is micro-molded in PGS or POMaC, two biodegradable elastomers.
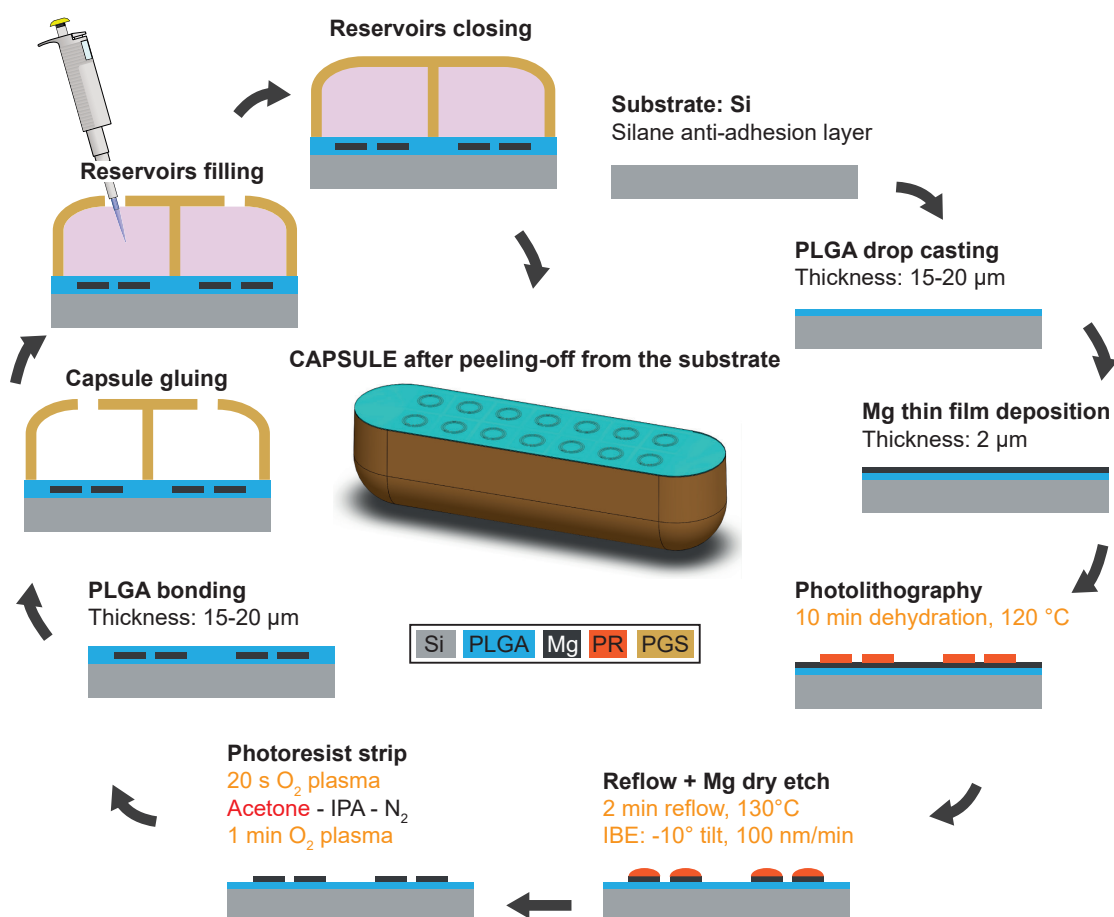
Figure 4.1 – **Direct fabrication on biodegradable membranes.** Fabrication process to produce Mg microresonators directly on biodegradable PLGA membranes. Steps in orange are not fully compatible with the PLGA film, while steps in red are absolutely incompatible.

Nevertheless, this process is not feasible because the PLGA film is incompatible with several of the fabrication steps. Indeed, PLGA is soluble in most solvents and its glass transition temperature is around 50-60°C. Consequently, the dehydration step before the photolithography and the reflow before the ion beam etching should be skipped. Indeed, at these elevated temperatures the PLGA film is liquid.

Additionally, during the IBE step the substrate also heats up. The etching time should be split in several shorter steps. The oxygen plasma steps helping to strip the photoresist are also problematic since the PLGA would be attacked. Further investigations would be required here.

Finally, the main problematic step is the dissolution of the photoresist in acetone since the PLGA film would dissolve after a few seconds already. Because of all these limitations, an alternative process based on the transfer printing of the Mg microstructures from a non-biodegradable substrate to a biodegradable substrate is used, as shown in Figure 4.2.

With this transfer printing process, the Mg microheaters are first fabricated on a substrate consisting of the stack of a Si Wafer, a PMMA sacrificial layer and a PI mechanical layer, similarly to the process developed in Section 3.4. At the end of the fabrication, the PI film with the Mg microresonators on top is released by dissolving the underlying sacrificial PMMA layer in acetone. Then the PI-Mg chips are transferred on a biodegradable substrate using a PDMS stamp. The stamp is pressed against the wafer with the PI-Mg chips and peeled-off manually.

At this point, the PI layer is etched in oxygen plasma and only the Mg microheaters remain on the PDMS stamp. Finally, the stamp is pressed against a wafer covered with a silane anti-adhesion layer and a drop-casted PLGA film on top, heated just below the glass transition temperature of the PLGA. After cooling down to room temperature, the PDMS stamp is peeled-off and the Mg microstructures remain on the PLGA. The end of the process consists of the bonding of a second PLGA layer plus the gluing and filling of the capsules, as discussed above for Figure 4.1.
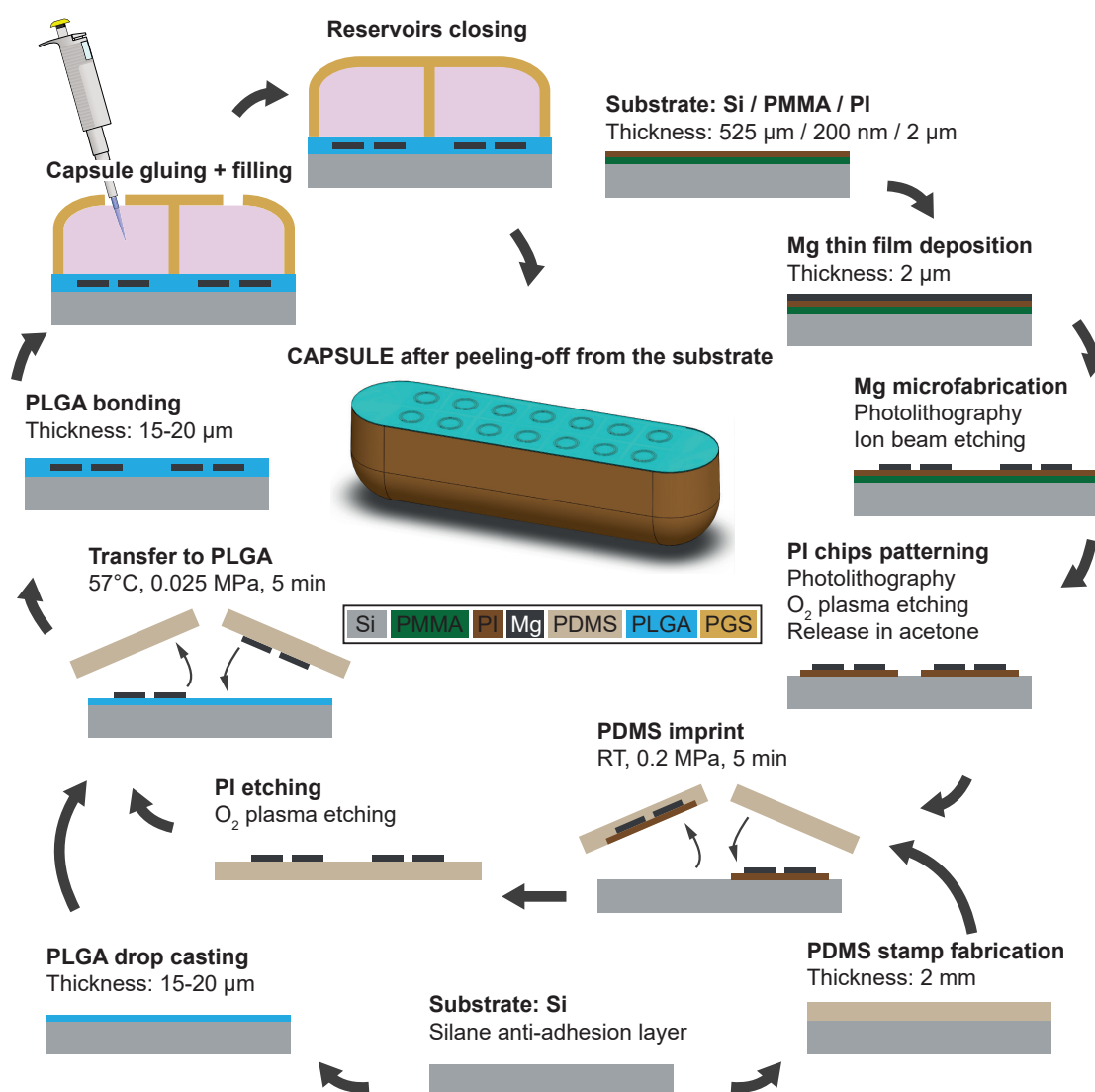
Figure 4.2 – **Fabrication on biodegradable membranes by transfer printing.** Fabrication process to produce Mg microresonators on biodegradable PLGA membranes by transfer printing with a PDMS stamp and a PI mechanical layer.

4.2 Microfabrication of Mg resonators on PLGA membranes

4.2.1 Introduction

In order to produce Mg biodegradable microheaters on PLGA biodegradable membranes, the fabrication processes developed in Sections 2.4 and 3.4 are combined together to develop a transfer printing process.

As introduced in Section 2.1.2, transfer printing-based processes are used to produce biodegradable micro- and nanostructures on delicate biodegradable substrates. [107,122,124] With these processes, metal microstructures or Si nanomembranes are fabricated on a non-biodegradable substrate between two PI layers. Then the stack consisting of the two PI layers with the microstructures sandwiched in between is transferred on a biodegradable substrate using a PDMS stamp. The first PI layer is removed by oxygen plasma when the stack is still on the PDMS stamp, and the second PI layer is removed after the final transfer step on the biodegradable substrate, also by oxygen plasma.

In this section, we developed a similar process with only one PI layer, to avoid the final plasma etching step on our thin PLGA membranes. PLGA is chosen as the membrane material because its degradation can be easily tailored during the synthesis of the polymer. Additionally, using an elastomer such as PGS or POMaC for the membrane material would have increased the risk of cracks in the metal microstructures, as it is the case for gold on PDMS for instance. [146] The first 11 steps of the fabrication process proposed here are identical to the process developed in Section 3.4, except that a Mg thin film deposited by evaporation is used instead of a Au film deposited by sputtering.

4.2.2 Methods

Figures 4.3 and 4.4 show the details of the process flow used to fabricate biodegradable Mg microheaters on biodegradable PLGA membranes by a transfer printing process. Firstly, a 200 nm thick PMMA sacrificial layer is spin-coated on a Si wafer previously cleaned by oxygen plasma. It is followed by a 5 min soft-bake at 180°C on a hotplate. Secondly, a 1.5 µm thick PI film is spin-coated on top of the PMMA layer. The PI layer is cured with two soft-bake steps of 180 s each, at 65 and 105°C on hot plates, plus a hard-bake at 250°C during 1 h in an oven under a nitrogen atmosphere.

Then, magnesium microresonators are fabricated on top of this stack consisting of the Si wafer, the PMMA and the PI layers. Firstly, a 2 µm thick Mg film is deposited by thermal evaporation (2x10^{-6} mbar, 8 Å/s, joule evaporator) on top of the PI thin film. Secondly, a photolithography step is performed: after a dehydration step of 10 min on a hotplate at 120°C, a 2 µm thick layer of photoresist (AZ9221, Microchemicals GmbH, Germany) is spin-coated on top of the Mg film. Patterns are exposed by direct laser writing, with a dose of 150 mJ/cm^2 at a wavelength of 405 nm. The targeted critical dimension is 4 µm. After developing the resist (AZ400K 1:3.5

#	Process description	Cross-section
1	**Substrate: silicon** Thickness: 525 µm SRD + 4 min O_2 plasma, 500 W	
2	**PMMA spin-coating** Thickness: 200 nm 950K A4, 4500 rpm Soft-bake: 5 min, 180°C	PMMA
3	**PI spin-coating** Thickness: 1.5 µm PI 2610, 3280 rpm No adhesion promoter Soft-bake: 2x180 s, 65°C + 105°C Hard-bake: 1 h, 250°C under N_2	PI
4	**Mg thin film deposition** Thermal evaporation Thickness: 2 µm P=2×10^{-6} mbar, R=8 Å/s	Mg
5	**Photolithography** 10 min dehydration, 120°C AZ9221 2 µm, no EBR, 150 mJ/cm^2	CD=4 µm PR
6	**Reflow** 2 min reflow, 130°C On a hotplate	
7	**Mg dry etch** IBE: -10° tilt, 100 nm/min	
8	**PR stripping** 20 s O_2 plasma Acetone - IPA - N_2 1 min O_2 plasma, 500 W	
9	**Photolithography** 10 min dehydration, 135°C AZ9260 10 µm, no EBR, 420 mJ/cm^2 Soft-bake: 4 min, 105°C Relaxation: 30 min, RT	
10	**PI + PMMA etching** O_2 plasma 1.5 µm/min	

Figure 4.3 – **Microfabrication of Mg microresonators on PLGA membranes - Part 1.** Fabrication process to produce magnesium microheaters on PLGA membranes by a transfer printing process. Continued in Figure 4.4

#	Process description	Cross-section
11	**PR stripping + PMMA release** Acetone - IPA - N$_2$ 6-7 h	
12	**PDMS imprint** RT, 0.2 MPa, 5 min 2 mm stamp, 50 g / 5 g	PDMS
13	**PDMS peel-off** Manual peeling, 30 mm/s	
14	**PI etching** 3x10 min O$_2$ plasma, 500 W	
15	**Mg tranfer printing** 57°C, 0.025 MPa, 5 min 20-40 µm PLGA film Si wafer with a silane layer	PLGA
16	**PDMS peel-off** Manual peeling, 1 mm/s, RT	

Figure 4.4 – **Microfabrication of Mg microresonators on PLGA membranes - Part 2.** Fabrication process to produce magnesium microheaters on PLGA membranes by a transfer printing process. Continued from Figure 4.3

in DI water, Microchemicals GmbH, Germany), a reflow is performed on a hotplate at 130°C during 2 min to smoothen the resist profile. This avoids re-deposition of Mg on the resist sidewalls during the subsequent ion beam etching step. The Mg thin film is etched through by ion beam etching with argon (Ar) ions, at a rate of 100 nm/min and a tilt of -10°. Finally, the photoresist is removed with a 20 s oxygen plasma, a 10 min immersion step in acetone (rinsed in IPA and dried with N$_2$), and a subsequent 1 min oxygen plasma at 500 W. For this last oxygen plasma step, a dummy wafer must be placed in front of the wafer with the microstructures in order to prevent the etching of the PI layer.

At this stage of the microfabrication process, the microresonators are fully fabricated but a second photolithography step is required to define the shape of the polyimide chips, as shown in Figure 4.5. The PI chips are 2x2 cm^2 and contain release holes as well as anchor points. During the final transfer step at the end of the fabrication process, the PI layer acts as a mechanical layer and also increases the adhesion of the structures to the PDMS stamp.
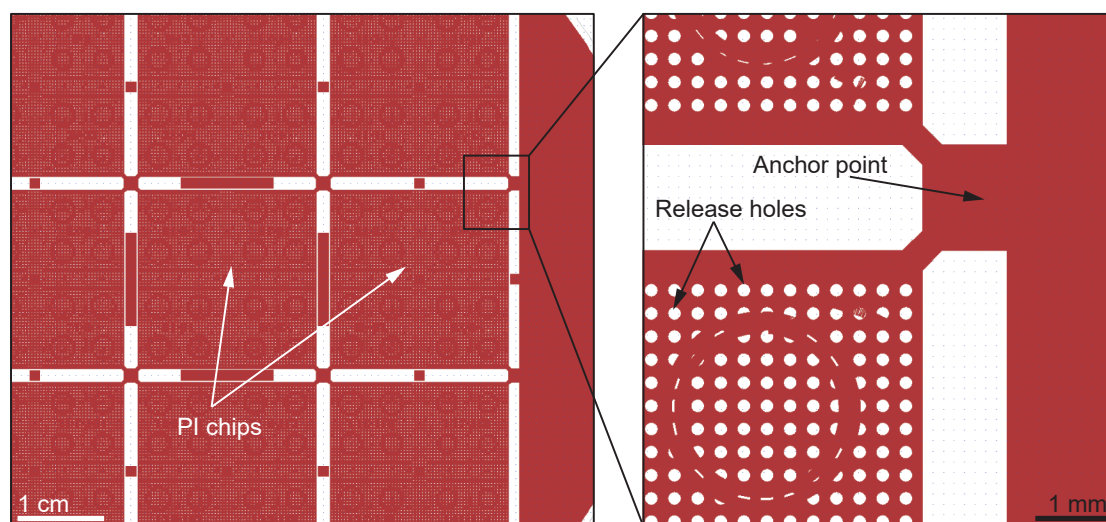
Figure 4.5 – **Polyimide chips with release holes and anchor points.** Layout of the second photolithography mask to create polyimide chips. The release holes enable to decrease the release time in acetone while the anchor points prevent the delimitation of the chips from the wafer. During the transfer step, the PI layer acts as a mechanical layer and also increases the adhesion of the structures to the PDMS stamp.

The second photolithography step is as follows. After a dehydration step of 10 min on a hotplate at 135°C, a 10 µm thick layer of photoresist (AZ9260, Microchemicals GmbH, Germany) is spin-coated on top of the Mg microresonators. Because of the thick PR layer, a soft-bake at 105°C during 4 min on a hotplate is required, followed by a 30 min relaxation step at room temperature. Such a thick PR layer is used in order to make sure that the Mg microstructures are protected during the whole subsequent etching step of the PI layer. Patterns are exposed in the PR by direct laser writing, with a dose of 420 mJ/cm^2 at a wavelength of 405 nm. The targeted critical dimension is 1 mm. After developing the resist (AZ400K 1:3.5 in DI water, Microchemicals GmbH, Germany), the PI layer is etched through in an oxygen plasma at a rate of 1.5 µm/min.

Finally, the wafer is immersed in acetone during 6-7 h to remove the PR layer and dissolve the underlying PMMA sacrificial layer under the PI film. The release holes in the PI chips enable to decrease the release time in acetone while the anchor points prevent the delimitation of the chips from the wafer by the absence of release holes. Additionally, there are no release holes over the Mg structures so that the metal is protected during the previous PI plasma etching step. The wafer is rinsed in IPA and dried under a gentle N_2 flow. At this stage of the process, the PI membranes with the Mg resonators on top are released but remain attached to the wafer through the anchor points.

The final part of the process consists in transfer printing the Mg microstructures on a biodegradable PLGA film. First a 2 mm thick PDMS stamp (base elastomer 50g:5g curing agent, curing: 2 h, 80°C) is pressed against the PI chips with the Mg resonators on top (0.2 MPa, 5 min). Then,

the stamp is manually peeled-off in a rapid movement (~30 mm/s). This process is performed at room temperature and detaches the PI chips and the Mg structures from the Si wafer. The PI chips prevent the formation of cracks in the Mg layer and also increase the adhesion to the PDMS stamp. Both effects contribute to the increase of the transfer yield. At this stage, the PI layer is fully etched down in an oxygen plasma (3x10 min, 500 W). Only the Mg microheaters remain on the PDMS stamp. Finally, the stamp is pressed (0.025 MPa, 5 min) against a wafer covered with a silane anti-adhesion layer and a drop-casted PLGA film on top (20-40 µm). For this step, the PLGA film is heated just below its glass transition temperature (57°C) to increase the adhesion of the Mg microstructures. After cooling down to room temperature, the PDMS stamp is manually peeled-off in a slow movement (~1 mm/s) and the Mg microstructures remain on the PLGA.

The fabrication of the PLGA film on the Si wafer is performed by drop casting. First a silane (Trichloro(1H,1H,2H,2H-perfluorooctyl)silane, Sigma-Aldrich, Switzerland) is deposited on a Si wafer by placing the wafer and ten drops of the silane in a vacuum desiccator overnight. The wafer was previously cleaned in an oxygen plasma (1min, 1000 W). Then, the PLGA film is fabricated by drop casting a solution of PLGA (PLGA 50:50, IV=0.2 dl/g, <1 mm particles, Vornia Biomaterials, Ireland) in ethyl acetate (ACS reagent, ≥ 99.5%, Sigma-Aldrich, Switzerland) on the wafer and letting the solvent slowly dry during 12 h in ambient conditions. 14 ml of solution are required to cover the full surface of the wafer. Varying the concentration of the solution between 2 and 4 % w/v enables to tune the PLGA film thickness between 20 and 40 µm. Experiments showed that if the PLGA film is not heated above its glass transition temperature of 60°C, the film can be easily peeled-off from the wafer.

Before turning to magnesium deposition, gold microresonators are fabricated in the first batches described in Sections 4.2.3 and 4.2.4, gold deposition being more readily available in the cleanroom facilities. This allowed limiting unnecessary delays during the process development. For subsequent batches, Mg microresonators will be deposited in a dedicated equipment outside of the available cleanroom facilities. For the gold deposition and etching, the same parameters as in the process described in Section 3.4.2 are used.

4.2.3   Results

Fabrication results using the process described in Section 4.2.2 are shown in Figure 4.6, 4.7 and 4.8. After the PDMS peel-off, we can see in Figure 4.6 that full resonators are transferred on the PDMS stamp without cracks. Some parts of the resonator are not in contact with the PDMS stamp, for example the black area on the right of the meander hot-spot on the left image. However, no crack formation is observed on the magnified image on the right. Additionally, the meander hot-spot of the resonator is also fully transferred and without damage. As shown in Figure 4.7, after the time consuming PI plasma etching step, many cracks appear in the PDMS stamp and the gold wrinkles on the PDMS. Nevertheless, the resonators as well as the meander hot-spots remain intact.
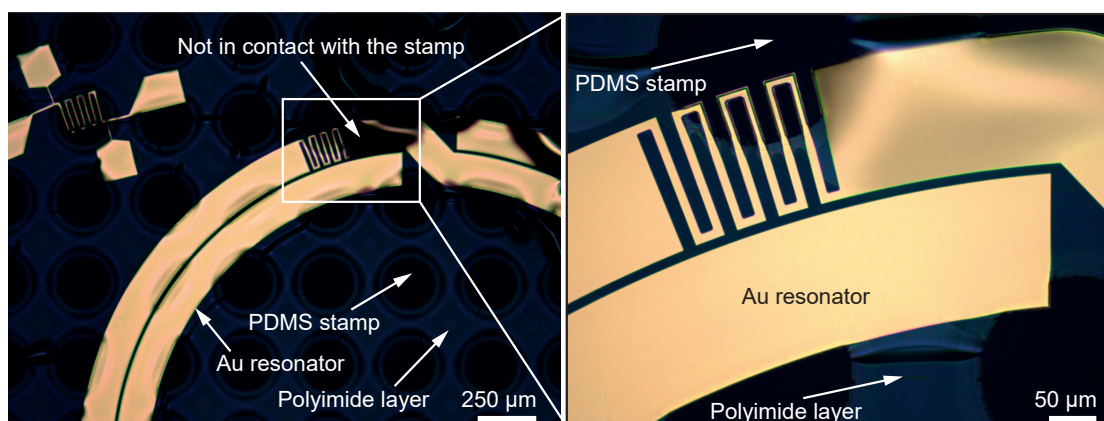
Figure 4.6 – **Au resonator and PI layer on the PDMS stamp.** OM images of a gold resonator and the PI layer on top of the PDMS stamp after successful imprint and peel-off steps. This depicts the situation after step 13 in Figure 4.4. The PDMS stamp is at the bottom with the Au structures on top and finally the PI layer on top of everything. The fine meander hot-spot structure is intact.
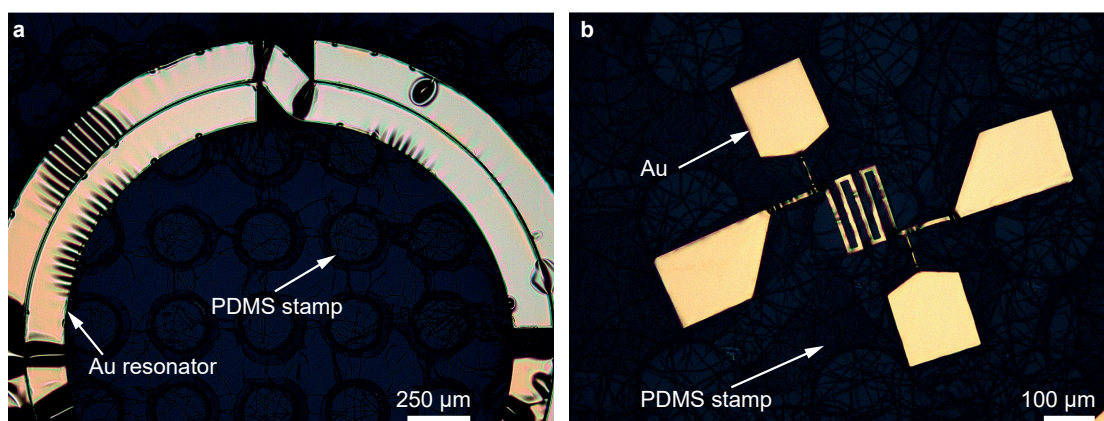
Figure 4.7 – **Au resonator on the PDMS stamp after PI etching. a,b,** OM images of a gold resonator (**a**) and a meander hot-spot (**b**) on top of the PDMS stamp after the etching of the PI layer. This depicts the situation after step 14 in Figure 4.4. The PDMS stamp is at the bottom with the Au structures on top. The fine meander hot-spot structure is intact, but the gold wrinkles on the PDMS stamp and many cracks are visible in the PDMS.

The fabrication of PLGA films on Si wafers by drop-casting results in uniform PLGA films which can be easily peeled-off from the wafer, as shown in Figure 4.8a. Unfortunately, the transfer printing of the resonators on the PLGA film is currently not fully successful since the resonators are damaged during the process as shown in Figure 4.8b. The fine meander hot-spot structure is broken, some gold parts are missing and some gold parts have cracks. Additionally, the cracks from the PDMS stamp visible in Figure 4.7 are also transferred in the PLGA film.
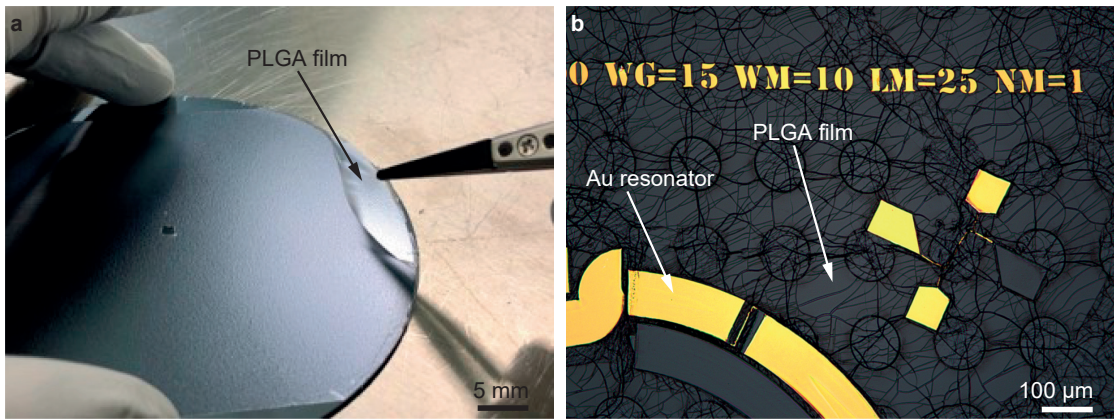
Figure 4.8 – **Au resonator on the PLGA film. a**, Picture of the peeling of a PLGA film from the Si wafer. **b**, OM image of a gold resonator and a meander hot-spot on the PLGA film at the end of the transfer process. This depicts the situation after step 16 in Figure 4.4. The PLGA film is at the bottom with the Au structures on top. The fine meander hot-spot structure is broken, some gold parts are missing and some gold parts have cracks. The cracks in the PLGA film come from the cracks in the PDMS stamp visible in Figure 4.7.

4.2.4 Summary and discussion

Summary   A transfer printing process was developed in order to fabricate Mg microheaters on thin PLGA membranes. Compared to conventional transfer printing processes, only one PI layer is used to avoid the last plasma etching step after the transfer on the biodegradable substrate, which, in our case, is a thin film. All the processing steps until the last transfer step on the PLGA film are now successful and reliable with Au microresonators. However, despite several trials with different, pressure, temperature, and contact time values, the transfer yield after the final transfer on the PLGA film remains around 50% only, and the Au microstructures have cracks.

Further improvements   The cracks in the microstructures appear mainly at sharp edges and could be reduced by avoiding sharp angles by design. Additionally, to improve the mechanical stability during the last transfer step and to avoid wrinkles in the metal layer on the PDMS stamp, using two PI layers as in the initial processes could be considered. The uncertainty would be the quality of the PLGA film following the plasma etching step to remove the second PI layer after the final transfer. Another limitation is due to the manual peel-off of the PDMS stamp. To address this and to improve the final transfer yield, an automatic transfer printing setup could be used. [147]

However, the fabrication process developed in this section is time consuming since it consists of 16 steps, and takes several days to produce microstructures on a PLGA film. Although the transfer yield which is currently only 50% could be improved according to the points discussed above, the resonators must be absolutely crack-free to be fully functional. This is

particularly challenging since they are several mm in diameter and contain microstructures of a few tens of µm. Therefore, it might be worth re-considering an approach based on stencil lithography in this specific case. Finally, as discussed in Section 2.1.1 PLGA swells when immersed in an aqueous solution because of its bulk degradation. [64] Using PLGA with a longer degradation time reduces the swelling, but it might be necessary to use other polymers such as polyanhydrides which degrades by a slow surface erosion for the membranes material. [1]

4.3 Fabrication of biodegradable capsules

4.3.1 Introduction

The choice of the material for the biodegradable capsules is motivated by two considerations. The degradation time and the compliance with the surrounding tissues. The knee articulation consist of hard and soft tissues, such as bones with a Young's modulus of 10-20 GPa, [148] and muscles with a Young's modulus of 1-3 kPa. [149] In order to avoid damaging these soft tissues the capsule design avoids sharp corners, as discussed in Section 3.2. Additionally, using materials with a Young's modulus matching that of the soft tissues also reduces the risk of creating damages.

Biodegradable polymers in the family of polylactides, polyglycolides and their blends are relatively hard with Young's modulus in the range of 2-10 GPa, [57, 150] and are thus not ideal choices. On the other hand, the biodegradable elastomers PGS and POMaC have much lower Young's modulus in the range of 0.1 and 0.5 MPa respectively, [57] which makes them better choices for this application. In terms of degradation time, PLGA degradation can be tuned from a one week to several months, [148, 150] while PGS and POMaC degradation can be tailored from 2 and 3 months and longer. [151, 152] These degradation times are all compatible with the targeted application of local analgesia after a knee arthroplasty.

PGS and POMaC are chosen as materials for the first version of the capsule. One risk associated with the use of elastomers to encapsulate an incompressible liquid in reservoirs is that a small increase of pressure might breaks the thin membranes which are closing the reservoirs. This will be an important parameter to investigate. In case it effectively results in the mechanical breaking of the device, then a hybrid capsule version with a solid 3D printed PLLA core coated with a soft elastomer could be considered.

PGS and POMaC pre-polymers are first synthesized by a polycondensation process. The PGS pre-polymer consists of the polycondensation of glycerol and sebacic acid, while the POMaC pre-polymer consists of the polycondensation of citric acid, maleic anhydride and 1,8-octanediol. Both pre-polymers are then crosslinked by thermal processing. Pouring the pre-polymers in micro-molds before the final thermal crosslinking step enables to produce biodegradable drug delivery capsules. Hybrid 3D printed-PDMS micro-molds with different surface treatments are used to produce PGS and POMaC capsules. Using molds based on 3D printing enables more versatility in the design because of their much lower price and shorter fabrication time compared to metal molds, and due to the ability to 3D print curved surfaces. Compared to the production of microcontainers of a few hundreds of micrometers in diameter by hot-imprinting and hot-punching for oral drug delivery, [153, 154] the overall dimensions of our capsules are incompatible with such fabrication techniques.

4.3.2 Methods

POMaC and PGS pre-polymers synthesis   The POMaC and PGS pre-polymers are synthe-sized by a polycondensation process as detailed in Appendix F. For the POMaC synthesis, the base reagents are 1,8 octanediol (98%, Sigma-Aldrich, Switzerland), citric acid (ACS reagent, ≥ 99.5%, Sigma-Aldrich, Switzerland) and maleic anhydride (puriss., ≥ 99.0% (NT), Sigma-Aldrich, Switzerland), at a molar ratio of 5:2:3. For the PGS, the base reagents are sebacic acid (99%, Sigma-Aldrich, Switzerland) and glycerol (ACS reagent, ≥ 99.5%, Sigma-Aldrich, Switzerland), at a molar ratio of 1:1.

The polycondensation process consists in heating the reagents together in a flask connected to a condensation column. For the POMaC synthesis, the heating occurs during 3 h at 140°C under a N_2 atmosphere. For the PGS synthesis, the heating occurs first during 2 h at 120°C under a N_2 atmosphere, and then during 24-48 h at 120°C under vacuum. After the polycon-densation, the PGS pre-polymer can be used directly for the subsequent micro-molding step, but the POMaC requires a purification step to filter the unreacted monomers. The POMaC pre-polymer is dissolved in cyclopentyl methyl ether (contains 50 ppm BHT as inhibitor, ReagentPlus, ≥ 99.90%, Sigma-Aldrich, Switzerland) and purified by dropwise precipitation in ddH_2O. Finally the POMaC pre-polymer is dried in a rotary evaporator (40-60°C heating, 6-10°C cooling, 100-200 mbar).

Micro-molding process - First trials   The PGS and POMaC capsules are produced by mold-ing the pre-polymers in hybrid 3D printed-PDMS micro-molds. The production of the molds is shown in Figures 4.9 and 4.10, while the molding of PGS or POMaC is shown in Figure 4.11.
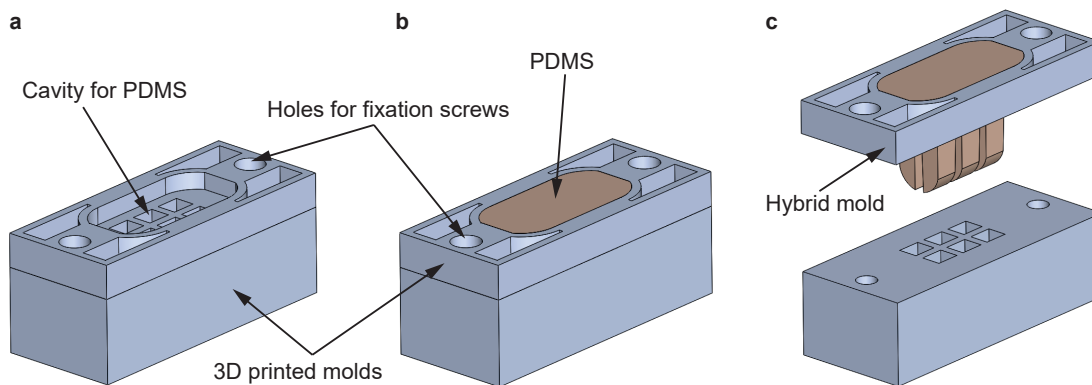
Figure 4.9 – **Top mold fabrication. a,b,c,** Production of the top hybrid 3D printed-PDMS micro-mold for the molding of PGS and POMaC. 3D printed molds before the filling with PDMS (**a**), after the filling with PDMS (**b**), and after the opening of the molds (**c**).

First the hybrid 3D printed-PDMS micro-molds are produced by molding PDMS (10:1 base elastomer:curing agent, curing: 2 h, 80°C) in the 3D printed molds (High Temp resin, Formlabs, USA). Then, these hybrid molds are coated with a silane anti-adhesion layer in vapor phase (Trichloro(1H,1H,2H,2H-perfluorooctyl)silane, Sigma-Aldrich, Switzerland) and used to mold
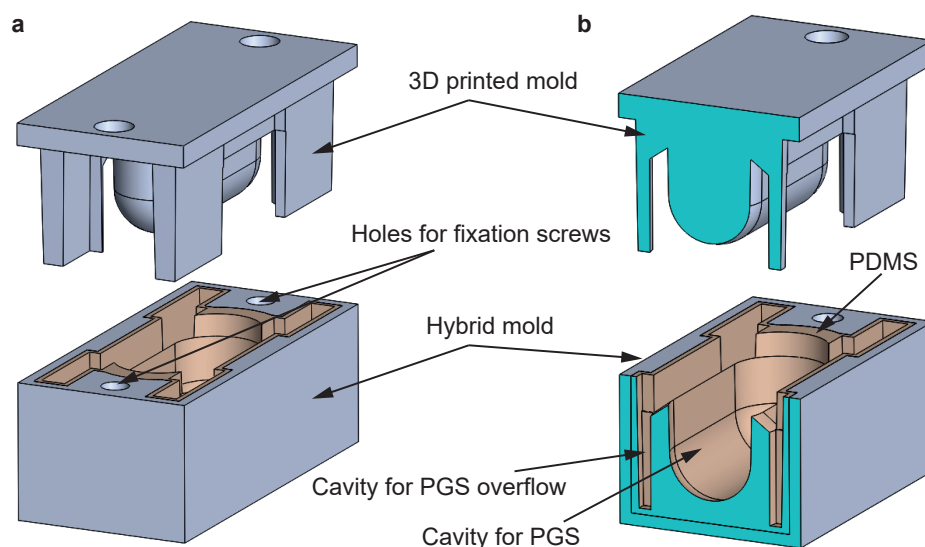
Figure 4.10 – **Bottom mold fabrication. a,b**, Production of the bottom hybrid 3D printed-PDMS micro-mold for the molding of PGS and POMaC. 3D printed molds filled with PDMS after the opening of the molds (**a**) and cross-section showing the cavity to mold PGS as well as the cavity for the PGS overflow (**b**).
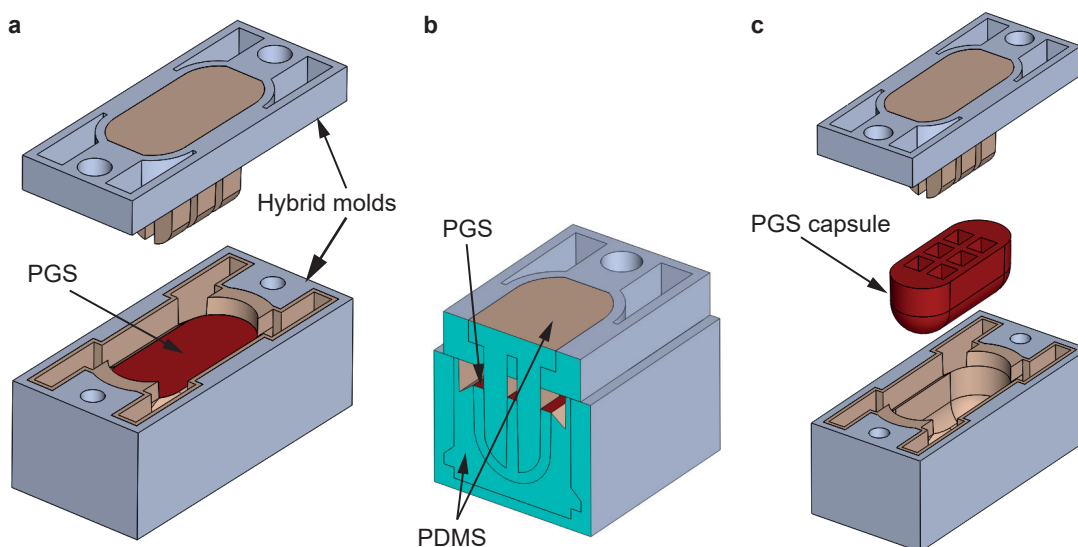
Figure 4.11 – **PGS and POMaC molding. a,b,c**, Molding of PGS or POMaC in the hybrid molds fabricated in Figures 4.9 and 4.10. Hybrid molds filled with PGS before closing the molds (**a**), after closing the molds (**b**), and after the opening of the molds (**c**).

the biodegradable capsules. The design of the hybrid molds is such that the PGS or POMaC pre-polymer is first poured in the bottom mold. The POMaC pre-polymer is liquid enough to be poured directly in the mold. For the PGS however, heating the pre-polymer to 100°C is required to be able to pour it in the mold. The bottom mold filled with the pre-polymer is

then placed in an oven for 2 h at 150°C for the PGS and 75°C for the POMaC. After 2 h, the air bubbles trapped in the pre-polymer are close to the surface and can be removed with a pipette.

At this point, the top mold with the pillars is inserted to define the shape of the drug reservoirs, and secured in place with plastic screws. The excess of PGS or POMaC material overflows from the mold and is collected in some dedicated cavities on the side of the bottom mold. The final crosslinking is performed by placing the closed molds in an oven for 24 h a 150°C for the PGS and 5 days at 75°C for the POMaC. The reason to use hybrid molds is to ease the final demolding step thanks to the soft internal PDMS part. The hard 3D printed external shell is however required to give a structural integrity to the molds.

Micro-molding process - Optimization   As discussed below in Section 4.3.3 the first PGS and POMaC capsules molding trials were not fully successful. The main problems are the tackiness of the PDMS molds, the difficult opening of the molds after the final crosslinking step, the non-uniform upper part of the capsule and the presence of air bubbles. All these issues are tackled by further optimizing the process.

To solve the tacky PDMS issue, an extensive surface treatment study is conducted. First, the 3D printed molds are UV cured (60 min , 405 nm) and thermally cured (180 min, 160°C) after their fabrication. Then, the molds are exposed to one of the following surface treatments or to the combination of two of them: a 1% soap solution in DI water, a 2 µm thick Parylene layer coating, Teflon spray coating and three different silanes (Trichloro(1H,1H,2H,2H-perfluorooctyl)silane, 1H,1H,2H,2H-Perfluorooctyltriethoxysilane, Chlorotrimethylsilane, Sigma-Aldrich, Switzerland).

To solve the difficult opening of the molds after the PGS and POMaC crosslinking, the same surface treatment study is performed with the hybrid 3D printed-PDMS molds when molding PGS. At this stage, the optimization is only performed with PGS and not with POMaC.

Finally, to overcome the formation of bubbles and the non-uniform upper part of the capsules, new hybrid molds are designed, as shown in Figure 4.12. This time, the molds are closed first and the pre-polymer is injected into the cavity of the molds. Before injecting the PGS pre-polymer the molds are heated to 100°C. Then, the molds are placed under vacuum to extract the air bubbles and finally in an oven for the final crosslinking step. A PDMS O-ring is used between the two molds to avoid leakages.

4.3.3   Results

Figure 4.13 shows the PGS and POMaC capsules obtained with the first molding trials. The overall result is promising since 3D capsules were successfully demolded from the molds. However, there are still some challenges to overcome to have fully functional capsules.
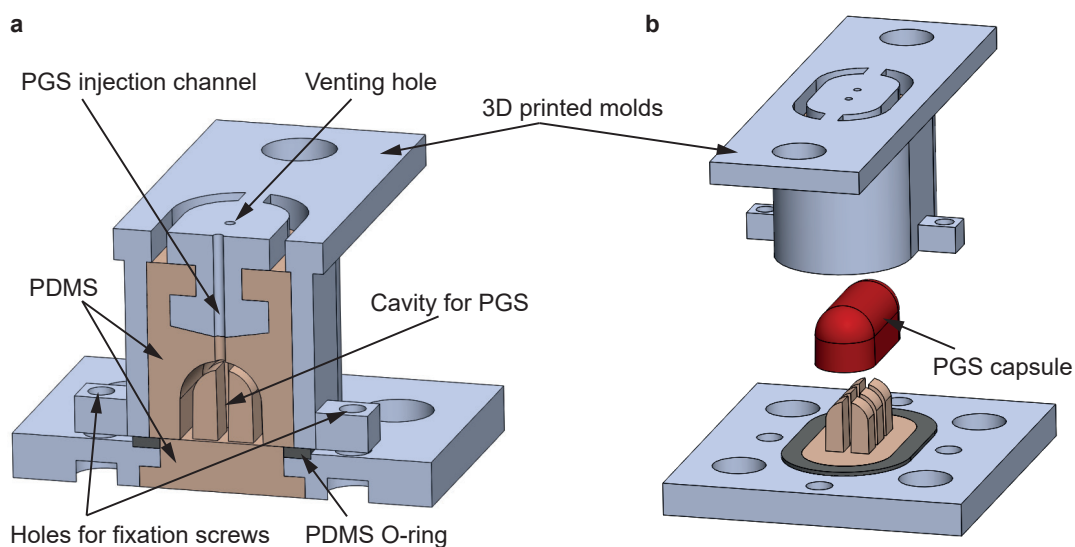
Figure 4.12 – **New mold design. a,b**, Injection molding of PGS or POMaC in the new hybrid molds design. Hybrid molds before filling them with PGS showing the molding cavity (**a**), and after the opening of the molds at the end of the process (**b**).
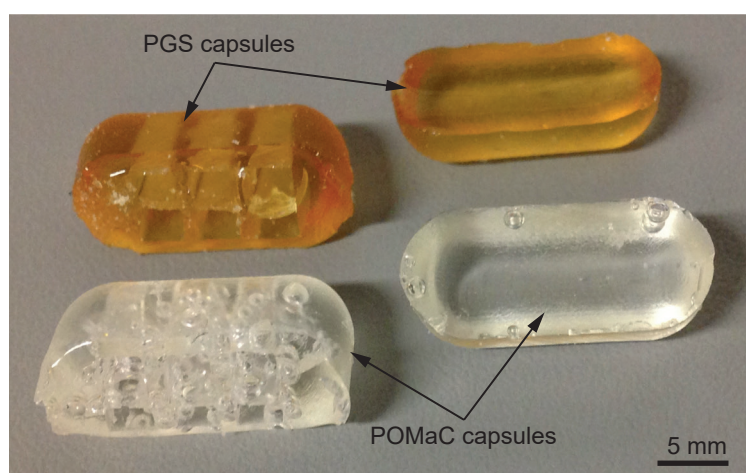
Figure 4.13 – **PGS and POMaC capsules.** PGS and POMaC capsules fabricated by micro-molding. Some capsules were fabricated with the reservoirs for the drug, and some were simply molded in the bottom mold, without closing the mold, and thus without the reservoirs.

The most obvious defect is the presence of air bubbles in the capsules walls. Additionally, the upper part of the capsules, where the membrane is glued to close the reservoirs is not flat. This is due do the fact that the melted pre-polymer is dragged between the pillars of the top mold because of the capillary forces. The design of the molds based on the overflow of the excess PGS or POMaC material is thus not successful. Another problem is the difficult opening of the molds after the final crosslinking step. Finally, the production of the hybrid 3D printed-PDMS molds sometimes results in poor quality molds with a tacky PDMS surface.

The optimization of the molding process resulted in some interesting observations. Curing the 3D printed molds first with UV, then thermally, and finally by immersing them in a soap solution before molding the PDMS enables a non-tacky PDMS surface quality. Additionally, coating the hybrid 3D printed-PDMS molds with a Parylene layer and subsequently immersing them in a soap solution reduces the adhesion between the PGS and the molds. However, opening the molds after the final crosslinking step remains challenging.

The new design of the molds to remove the bubbles and improve the uniformity of the upper part of the capsule was only partially successful. Indeed, with the current size of the venting hole and the cooling of the molds when they are placed under vacuum, large air bubbles remain trapped in the molds. Additionally, when placing the molds under vacuum to extract the air bubbles, some leakages occur at the interface between the top and bottom molds, despite the PDMS O-ring. A stronger pressure between the molds is required to avoid leaks. Nevertheless, the pressure between the molds is currently applied using screws and increasing the pressure results in the breaking of the molds. Finally the molds also often break during the crosslinking step in the oven. This is due to the combination of three effects: the current molds material, the high temperature required to crosslink the PGS, and the current method of applying the pressure with screws. Because of all the molds-related problems discussed here, a further optimization of the molds design is required.

4.3.4   Summary and discussion

Summary   Biodegradable capsules were micro-molded out of two biodegradable elastomers: PGS and POMaC. The pre-polymers were first synthesized by the polycondensation of the reagents materials. Then the crosslinking of the pre-polymers was performed in hybrid micro-molds consisting of a 3D printed outer shell and a soft PDMS inner part. The first molding trials showed promising results but several challenges still need to be solved. Optimizing the molding process enabled us to reliably produce hybrid molds with a non-tacky PDMS surface. This is done by UV and thermally curing the 3D printed molds and immersing them in a soap solution before molding the PDMS. The soap acts as a surfactant on the surface of the molds. Additionally, coating the hybrid molds with Parylene and immersing them in a soap solution enables to decrease the adhesion between the PGS capsule and the molds. Finally, the design of the molds still needs to be improved to solve leakages, mechanical stability and air bubbles-related problems.

Further optimization of the molding process   As discussed above the design of the molds needs to be optimized. Using more points with a larger area to apply the pressure between the top and bottom molds will enable us to apply a higher overall pressure with lower local stresses in the material. This will hopefully reduce the risks of breaking the molds. In order to improve the air bubbles removal, more and larger venting holes should be used and the molds should be heated even when under vacuum. Using a vacuum oven could be a solution here. Another option would be to use POMaC instead of PGS. PGS was initially chosen to

optimize the molding process because of its much shorter crosslinking time (2 h vs. 5 days). However, the curing temperature of POMaC is only 75°C against 150°C for PGS and the POMaC pre-polymer is liquid at room temperature. This means that when using POMaC, the molds don't need to be heated when removing the air bubbles in vacuum. Additionally, the molds will not suffer as much from the combination of high temperature and pressure as with PGS.

Nevertheless, at the end of the crosslinking process, opening the molds remains challenging, even with a Parylene coating and immersing the molds in a soap solution. Another option to consider is to change the molds materials and use Teflon molds or glass molds coated with hyaluronic acid for example. [155] However, some modifications in the capsule design would be required since the technologies to produce molds in these materials are not as versatile as 3D printing, particularly for curved surfaces. Coating the molds with a sucrose sacrificial layer which rapidly dissolves in water could also be investigated. [156] The challenge would be to have a uniform layer all over the molds because of the high aspect-ratio 3D geometry of the capsules. Finally, a last interesting solution would be to directly 3D print the capsules out of biodegradable materials. [157–162]

Sterilization of the capsules   Before implanting the capsules in any living organism, they need to be sterilized. The easiest is to sterilize the final device at the end of the fabrication process. Indeed, if the capsules are sterilized after their fabrication but before the assembly of the membranes and the filling of the reservoirs, these steps must be performed in a sterile environment. This is difficult to setup, especially in an academic environment. Since the final capsules consist of closed cavities, the only compatible sterilization technique is gamma-irradiation, in order to also sterilize the inside of the drug reservoirs.

The sterilization will affect the mechanical and degradation properties of the polymers. The effect of gamma-irradiation on PLGA was studied and resulted in the decrease of the molecular weight of the polymer, leading to a faster degradation and to lower mechanical properties. [148, 163] Limiting the temperature rise during the sterilization, for instance by placing the device in dry ice, should diminish this effect. Recent studies also showed that gamma-irradiation is a suitable technique to sterilize PGS. [164] The gamma-irradiation should not affect the Mg microheaters, nevertheless it will be important to assess the behavior of the overall system after the sterilization to make sure neither the capsule nor the drug functionalities are affected by the sterilization process.

Degradation of the capsules   In-depth degradation tests will also be required to define the total degradation time of the capsules. Parameters such as the weight, shape, rigidity and molecular weight in multiple media (PBS, artificial synovial fluid, blood) should be monitored. An ideal degradation rate would allow the full dissolution of the capsule within three to six weeks after the surgery. This way the patient knows that everything is degraded when the staples or the walking aids are removed, as discussed in Section 3.1.1.

However, according to the degradation times of PGS and POMaC described in Section 4.3.1, such a rapid degradation is not conceivable and the degradation will rather be three months than three weeks. Additionally, with an implant which would fully degrade within three weeks, the risk of having a failure during the first week before releasing all the drugs is high. Nevertheless, in the end, it is not the degradation time that matters the most but how the rigidity and shape of the implant change over time. For instance we could engineer the shape of the implant in a way that it rapidly breaks into several smaller parts. This will probably be the case with the current capsule design because of the relatively thin walls around the drug reservoirs.

4.4   Conclusion

The results reported in this chapter demonstrate a microfabrication process based on transfer printing to fabricate biodegradable Mg microresonators on biodegradable PLGA membranes. Because of the large overall size of the resonators which are several mm in diameter, the crack-free transfer from a non-biodegradable substrate to a biodegradable substrate is not fully functional. Some improvements in the process can be done to improve the transfer yield, but other techniques such as stencil lithography might also be considered.

Additionally it is important to keep in mind that having biodegradable electronics is the best option since it enables the degradation of the whole implanted device. However, in the specific case of our drug delivery capsule, 14 resonators which are 2 µm thick have a total volume of 0.1 mm^3. This represent 0.2 mg of Mg and 2 mg of gold. The daily allowance for Mg is 700 mg/day, so we are well below the limit. [47] For gold, there exist medical therapies which require weekly intramuscular injections of 25 mg of Au. [165] Gold is toxic and start accumulating in the tissues when its concentration in blood is above 3 mg/l. Additionally gold is also present in dietary supplements in doses of 1-2 µg. Thus, the amount of gold in one capsule would not be toxic for the human body. Replacing magnesium with gold would not solve the transfer printing issues we are currently facing, but might open new alternatives to simplify the fabrication process.

We also demonstrated the fabrication of biodegradable capsules made of PGS and POMaC, two biodegradable elastomers, using a micro-molding process. Technical challenges prevent the fabrication of a fully functional prototype. However, some modifications in the design of the molds and possibly in the molds material will solve the remaining problems.

In the end, a fully biodegradable drug delivery capsule would enable to replace the current methods of drug administration for post-operative local analgesia after a knee arthroplasty, while personalizing and reducing the drug dose and secondary effects. The capsule would be functional during one week and then fully resorbs from the body. Once a functional prototype is available, further investigations regarding the sterilization of the device and its in vitro and in vivo biocompatibility and biodegradation should be performed.

5 Conclusion and perspectives

This chapter presents the main outcomes of the thesis and discusses possible future developments.

5.1 Conclusion

Context and motivation   The introduction of this thesis highlighted the importance of bioresorbable implantable medical devices for applications requiring medical care over well-defined periods of time. Once their function is fulfilled, such implants naturally degrade and resorb in the body, which eliminates adverse long-term effects or the need for a secondary surgery to extract the device. However, since biodegradable materials are water-soluble, their fabrication requires special care and relies solely on dry processing steps without exposure to aqueous solutions. Another challenge is the in vivo powering of medical implants that are only constituted of biodegradable materials. The overall objective of this thesis was to develop a fully biodegradable drug delivery implant with multiple reservoirs for on-demand wireless drug delivery. Then to integrate and miniaturize all the components to reduce the volume of material used, whilst limiting the fabrication process complexity.

Biodegradable magnesium wireless microheaters   First, the design, the fabrication and the characterization of selectively addressable biodegradable magnesium microheaters was presented. To this end, an innovative microfabrication process with minimal exposure to aqueous media was developed to fabricate magnesium-based, water-soluble electronic components. It consists of a novel sequence of only four steps: physical vapor deposition, photolithography, ion beam etching and resist stripping in acetone. The microheaters consist of spiral resonators and their resonance frequency is sensitive to the surrounding environment. This could be accurately predicted using an analytical model and FEM simulations.

Coupling an external RF magnetic field with a frequency matching that of one resonator induces an electrical current in this specific resonator. Adding a meander to the resonators

increases the current density locally by one order of magnitude and creates a hot-spot. Slightly varying the geometry of the devices in the design process enables the tuning of their resonance frequency from 0.5 to 5 GHz and makes them selectively addressable. When immersed in an aqueous media, the magnesium starts to degrade by hydrolysis. Consequently, the resonance of the device is strongly affected after a few tens of seconds due to the fast propagation of cracks through the thin magnesium film. The frequency-selective wireless heating of different resonators was demonstrated in air and in liquid. Temperatures as high as a few hundreds of degrees Celsius could be reached, leading to the breaking of the meander hot-spot, or alternatively to the melting of the surrounding environment.

Multi-reservoirs drug delivery capsule   These microheaters were used as power receivers and triggering elements to selectively release drugs on-demand from multiple reservoirs in a wirelessly controlled drug delivery capsule. The first prototype was made of non-biodegradable materials to demonstrate the feasibility of the concept. It consists of a 3D printed capsule with several reservoirs filled with drugs. Each reservoir is sealed with a polyimide membrane with a resonant gold microheater on top of it. The microheaters are used to thermally trigger the breaking of the membranes and release the drugs from the reservoirs. The integration and miniaturization of all the components of the system enables multiple drug reservoirs of several tens of microliters in a minimal volume. Additionally, the powering and triggering mechanisms are combined into one element, minimizing the volume of material and maximizing the drug-to-implant volume ratio. The design of the resonators was optimized to maximize the power dissipated in the meander hot-spot at specific resonance frequencies.

Finally, the successful fabrication of leak-free capsules and the wireless release of liquid from the reservoirs was demonstrated. The breaking mechanism of the membranes appears to be the creation of vapor bubbles in the close proximity of the membrane when the surrounding liquid reaches its boiling point due to the heat generated by the microheater.

Development of a fully biodegradable drug delivery capsule   Finally, the aforementioned fabrication processes are combined to fabricate a fully biodegradable version of the device. Biodegradable microheaters are fabricated on biodegradable membranes by transfer printing, while the capsules are micro-molded from biodegradable elastomers. Because of the large overall size of the resonators which are several mm in diameter, the crack-free transfer from a non-biodegradable substrate to a biodegradable substrate is not working yet. Additionally, some technical challenges also prevent the fabrication of fully functional biodegradable capsules. Some modifications to the design and material of the molds will solve the remaining problems.

Comparison to existing technologies   In comparison to other biodegradable wireless microheaters used in medical implants, the resonators developed in this thesis have a 4-24

times smaller area. Furthermore, their fabrication is less complex, since they consist of one single metal layer. [37, 54, 55, 66, 75] Additionally, this design of microheaters enables large frequency shifts by merely inducing small geometrical variations in the design. As a result, several resonators with multiple resonance frequencies can be readily integrated in one device without much of an increase in diameter.

This drug delivery capsule is very similar in terms of dimension and working principle compared to other non-biodegradable drug delivery systems. [44, 71] However, its design enables the integration of several drug reservoirs which can be selectively opened without the need for complex integrated circuits. Additionally, the microfabrication process developed to produce the microheaters makes this technology easier to fabricate a fully biodegradable version of the drug delivery system (DDS). In comparison, to other biodegradable DDS, [28, 54, 55, 66, 67] which consist of polymer layers loaded with drugs, this capsule and its multiple reservoirs of several tens of microliters enables the delivery of larger amounts of drugs.

5.2 Perspectives

The ability to selectively power and heat up microresonators made of biodegradable materials is a significant step towards the use of such devices in implantable biodegradable devices, in particular for controlled drug release and thermal therapy. Additionally, the ability to wirelessly power and release liquid from a capsule demonstrates the feasibility of using these microheaters as power receivers and triggering elements in implantable medical devices. Finally, the design of the capsule is also compatible with the drug requirements needed in the context of an implantable drug delivery system for local analgesia after a knee arthroplasty. Some improvements that could be implemented and some considerations regarding possible further developments are presented below.

5.2.1 Technological improvements

Biodegradable resonators on biodegradable membranes   As discussed in Section 4.4, the requirement of having biodegradable electronics for such small amounts of material can be questioned since some medical therapies requires the injections of larger amounts of gold. However, the ability to fabricate microheaters on biodegradable membranes is a crucial requirement for the fabrication of a biodegradable version of the drug delivery capsule. Some improvements in the current microfabrication process can be done to improve the transfer yield. This includes avoiding sharp angles in the design of the resonators or using two polyimide layers to improve the mechanical stability during the transfer process. Another limitation is due to the manual peel-off of the PDMS stamp. To address this and to improve the final transfer yield, an automatic transfer printing setup could be used. [147]

However, the resonators must be crack-free to be fully functional. This is particularly challenging since they are several mm in diameter and contain microstructures of a few tens of µm. Therefore, the development of another microfabrication process based on stencil lithography could also be considered. This could include the fabrication of stencils by patterning and etching a polyimide layer on a silicon wafer. This layer could then be transferred to a biodegradable substrate by transfer printing for example.

Molding optimization   To produce defect-free biodegradable capsules, the current molding process needs to be optimized. Some changes in the design of the molds will enable the lowering of local stresses in the material and will reduce the risk of fracture. Additionally, it will also reduce the amount of air bubbles, in combination to heating the molds even when under vacuum. A potential solution would be to use a vacuum oven. Alternatively, another solution would be to use POMaC instead of PGS to fabricate the capsules. The curing temperature of POMaC is only 75°C against 150°C for PGS and the POMaC pre-polymer is liquid at room temperature. Consequently, the molds don't need to be heated when removing the air bubbles in vacuum. Additionally, in comparison to PGS, the molds will not suffer as much from the combination of high temperature and pressure.

Nevertheless, at the end of the crosslinking process, opening the molds remains challenging with the current molds material. Using Teflon molds or glass molds coated with hyaluronic acid for example could be an option. [155] However, some modifications in the capsule design would be required since the technologies to produce molds in these materials are not as versatile as 3D printing, particularly for curved surfaces. Coating the molds with a sucrose sacrificial layer which instantly dissolves in water could also be investigated. [156] The challenge would be to have a uniform layer all over the molds because of the high aspect-ratio 3D geometry of the capsules. Finally, a last interesting solution would be to directly 3D print the capsules out of biodegradable materials. [157–162]

Primary coil design   Finally, the design of a new primary excitation setup is also required to generate magnetic fields in the range of 50 μT at a larger distance than the 300 μm spacing currently used. With this new setup, it will be possible to use the capsule in a liquid environment and to visually observe the membrane breaking. This will help confirm the breaking mechanism of the membranes and to provide a better understanding of the drugs release dynamics from the capsule. It will also allow the capsule to be controlled when implanted in the body. However, having a primary coil enabling and efficient energy transfer in the optimal frequency range is not an easy task. At this stage of the optimization, discussion with experts in the field will be required.

5.2.2   Release studies

The drug delivery capsule prototype developed in this thesis is a tool which opens the way to further in-depth investigations into the drug release from the capsule. In the end, the size of the membrane and the size of the opening in the membrane will strongly affect the release dynamics of the drug out of the capsule. More specifically, the effect of several parameters such as the membrane thickness, the magnetic field intensity, the meander geometry, the surrounding media and the implantation depth could be studied. Another important consideration which should also be studied is the effect of the membrane thickness on the membrane mechanical stability. Indeed, the membrane needs to be thin enough to be thermally opened, but it also needs to survive the capsule handling, the patient's movements as well as the variations in atmospheric, blood and osmotic pressures.

An open question that remains is to determine if, in the context of local analgesia after a knee arthroplasty, the ropivacaine released from the capsule should dissolve rapidly or slowly in the synovial fluid. This mainly depends on how the drug acts on the nerves. In addition to controlling the size of the hole in the membrane, the drug formulation can also be modified to control the release rate from the capsule. If a slow release is required a low solubility powder can be used. On the other hand, if a fast dissolution is required it is possible to prepare the drug as a very thin powder. Additionally, some surfactant and bicarbonate can also be added to improve the wettability and create an effervescent effect.

5.2.3 Clinical outcome

Pain treatment after a knee arthroplasty   Using a biodegradable drug delivery implant to locally treat the pain after a knee replacement surgery shows several advantages compared to the current postoperative pain management techniques. Among others, it would lower the risk of infection, create less discomfort to the patient and enable a personalized and better pain relief while using lower drug doses. Ultimately, the goal is to replace the current methods of drug administration for post-operative local analgesia after a knee arthroplasty, while personalizing and reducing the drug dose and secondary effects. However, several steps need to be validated before being able to use the device clinically.

Sterilization   Before implanting the capsule in a living organism, it needs to be sterilized. The easiest is to sterilize the final device at the end of the fabrication process, to avoid having to assemble and fill the capsule in a sterile environment. Since the capsule consists of closed cavities, the only compatible sterilization technique is gamma-irradiation, in order to also sterilize the inside of the drug reservoirs. The sterilization will affect the mechanical and degradation properties of the polymers. The effect of gamma-irradiation on PLGA was studied and resulted in the decrease of the molecular weight of the polymer, leading to a faster degradation and to lower mechanical properties. [148, 163] Limiting the temperature rise during the sterilization, for instance by placing the device in dry ice, should diminish this effect. Recent studies also showed that gamma-irradiation is a suitable technique to sterilize PGS. [164] The gamma-irradiation should not affect the Mg microheaters, nevertheless it will be important to assess the behavior of the overall system after the sterilization to make sure neither the capsule nor the drug functionalities are affected by the sterilization process.

In vitro and in vivo performance   The biocompatibility of the device and the drug efficacy should be assessed in vitro on cells cultures first in vitro and then in vivo. The in vivo assessment is particularly important in order to determine the bioavailability of the drugs in the knee articulation. Finally, in depth degradation tests will also be required to determine how the swelling of the materials and the infiltration of liquid affect the degradation time of the system. Here, three times are relevant: the time until the device is not responsive anymore, the time until the device breaks and releases the remaining drugs and the time until it is fully degraded. An ideal degradation rate would allow the full dissolution of the capsule within three to six weeks after the surgery, which matches the timeframe for the removal of staples or the walking aids.

However, according to the degradation times of PGS and POMaC described in Section 4.3.1, such a rapid degradation is not conceivable and the degradation will rather be three months than three weeks. Additionally, with an implant which would fully degrade within three weeks, the risk of having a failure during the first week before releasing all the drugs is high. Having a device with the desired degradation time in vivo is a challenging task. [64] Nevertheless,

ultimately, the degradation time is not the most relevant information, but more how the rigidity and shape of the implant change over time. For instance, the shape of the implant could be engineered in a way that it rapidly breaks into several smaller parts. This is most likely to be the case with the current design of the capsule because of the relatively thin walls around the drug reservoirs.

A Matlab code for the analytical model of the spiral resonators

Computation of the SR model

```matlab
function Split_ring=compute_coil_model_v4(Rext,Wt,h,Wgap,Wm,Lm,Nm,Nt,...
Wo,freq_range,Brf,gamma,tau,coil_mat,surr_mat,sub_mat,sub_thick,...
pass_mat,pass_thick,under_mat,under_thick,no_display,varargin)
%COMPUTE_COIL_MODEL_V4
%This function is a model of the RLC resonator used in the CAPSULE device.
%First R,L and C values are computed as a function of frequency and
%geometrical parameters for a spiral resonator with a meander hot-spot.
%Then the resonance frequency, the Q-factor, the current density in the
%meander as well as the energy dissipated in the meander are computed.
%
%
% Syntax: Split_ring=compute_coil_model_v4(Rext,Wt,h,Wgap,Wm,Lm,Nm,Nt,...
% Wo,freq_range,Brf,gamma,tau,coil_mat,surr_mat, sub_mat,sub_thick,...
% pass_mat,pass_thick,under_mat,under_thick,axes_pos,no_display,varargin)
%
% Inputs, all in SI units:
%     - Rext: external radisu of the resonator
%     - Wt: width of the resoanator
%     - h: thickness of the resoantor
%     - Wgap: gap between the two turns of the resonator
%     - Wm: meander width
%     - Lm: meander length
%     - Nm: meander number (can be set to 0 if no meander)
%     - Nt: number of turns (can only be set to 2 in the current version)
%     - Wo: opening between the two turns of the resonator
%     - freq_range: frequeny range in the format [f_min f_max]
%     - Brf: RF mangnetic flux density value
%     - gamma: angle between the coil and the magneitc field
%     - tau: RF magnetif flux density pusle time
%     - coil_mat: string with the coil material
%     - surr_mat: string with thte surrounding material
%     - sub_mat: string with the substrate amterial
```

```matlab
33  %    - sub_thick: substrate thickness
34  %    - pass_mat: string with thte passivation material on top of the coil
35  %    - pass_thick: passsivation material thickness
36  %    - under_mat: string with the underlying material between the
37  %      substrate and the coil
38  %    - under_thick: thickness of the underlying material
39  %    - no_display: set 0 to plot the result in a figure, set to 1
40  %      otherwise
41  %    - varargin: optional pair of intputs to set a specific Mg
42  %      resisitivity using a first argument 'resistivity' and a second
43  %      argument equal to the resistivity value
44  %
45  % Outputs:
46  %    - Split_ring: strucutre containing the resonance parameters
47  %          Split_ring.L: inductance of the coil
48  %          Split_ring.Ctot: capacitance of the coil
49  %          Split_ring.f0: resonance frequency
50  %          Split_ring.Q: quality factor
51  %          Split_ring.Emax: energy dissipated in the menader at resonance
52  %          Split_ring.Rtot: total electrical resistance at
53  %                           resonance
54  %          Split_ring.Rm: electrical resistance of the meander at
55  %          resonance
56  %          Split_ring.RmRtot: ratio Rm/Rtot
57  %          Split_ring.Res_m_DC: DC value of the electrical resistance of
58  %                                the meander
59  %          Split_ring.jm: current density in the meander at resonance
60  %
61  % Example: none
62  %
63  % Other m-files required: compute_resonator_length, P_factor_inductance,
64  %                         F_factor_inductance
65  % Subfunctions: none
66  % MAT-files required: none
67  %
68  % See also: coil_model_v4_GUI.m, coil_model_v4_GUI.fig
69  % Author: Matthieu Ruegg
70  % Work address: EPFL, STI, IMT, LMIS1
71  % email: matthieu.ruegg@gmail.com
72  % Website: http://www.lmis1.epfl.ch
73  % August 2018; Last revision: 09-October-2019
74
75
76  %% Constants and variables definition
77
78  %Constants
79  c=299792458; %Speed of light [m/s]
80  mu0=4*pi*10^(-7); %Vacuum magnetic permeability [H/m]
81  epsilon0=1/(mu0*(c^2)); %Vacuum permittivity = 8.85e-12 [F/m]
82
83  %Metals constants
84
```

```matlab
85  mu_r_Mg=1; %Magnesium is non-magnetic
86  Mg_res=4.39e-8; %Magnesium resistivity: 43.9[nOhm*m] (default value)
87  %Mg_res=10.5e-8; %Magnesium resistivity: 105[nOhm*m] (default value)
88  if ¬isempty(varargin)
89      for i=1:2:length(varargin)-1
90          if strcmp(varargin{i},'resistivity')
91              Mg_res=varargin{i+1};
92          end
93      end
94  end
95
96
97  mu_r_Au=0.999996; %Gold is almost non magnetic
98  %from http://www.antenna-theory.com/definitions/permeability.php
99  Au_res=2.44e-8; %Gold resistivity: 24.4[nOhm*m]
100
101  mu_r_Al=1.00002; %Al is almost non magnetic
102  %from http://www.antenna-theory.com/definitions/permeability.php
103  Al_res=2.82e-8; %Al resistivity: 28.2[nOhm*m]
104
105  mu_r_Cu=0.999994; %Cu is almost non magnetic
106  %from https://en.wikipedia.org/wiki/Permeability_(electromagnetism)
107  Cu_res=1.68e-8; %Cu resistivity: 16.8[nOhm*m]
108
109  %Dielectric constants
110
111  %Relative permittivity of water @37[degree C] from Malmbarbeg, Dielectric
112  %Constant of Water from 0 degree C to 100 degree C, 1956
113  epsilon_r_Water=74;
114
115  %Relative permittivity of parylene @1[Ghz] from
116  %http://www.comelec.ch/en/parylene_tableaux.php. Parylene relative
117  %permittivity is close from that of other polymers from Ahmad, Polymeric
118  %Dielectric Materials, 2012
119  epsilon_r_Parylene=2.8;
120
121  %Relative permittivity of PLGA from Khalid A highly sensitive
122  %biodegradable pressure sensor based on nanofibrous dielectric, 2019
123  epsilon_r_PLGA=4;
124
125  %Relative permittivity of PI, datasheet PI2610
126  epsilon_r_PI=3; %Aprroximative value
127
128  %Relative permittivity of air
129  epsilon_r_Air=1;
130
131  %Relative permittivity of float glass from Adrien Toros' report p.41
132  epsilon_r_Float_glass=6.0;
133
134  %Relative permittivity of FR-4 https://en.wikipedia.org/wiki/FR-4 @1[GHz]
135  epsilon_r_FR4=4.34;
136
```

```matlab
137  %Material varaibles initialisation
138  rho=Mg_res; %To avoid warning later with eval
139  mu=mu0*mu_r_Mg; %To avoid warning later with eval
140  epsilon_r1=epsilon_r_Air; %To avoid warning later with eval
141  epsilon_r2=epsilon_r_Air; %To avoid warning later with eval
142  epsilon_r3=epsilon_r_Air; %To avoid warning later with eval
143  epsilon_r4=epsilon_r_Air; %To avoid warning later with eval
144  epsilon_r5=epsilon_r_Air; %To avoid warning later with eval
145
146  %Define coil variables
147  eval(['rho = ',coil_mat,'_res;']); %Define coil resistivity
148  eval(['mu = mu0*mu_r_',coil_mat,';']); %Define coil permeability
149
150  %Define substrate, passivation, underlying and surrounding materials
151  %variable. Definitions of "epsilon_r1" to "epsilon_r5" and "h1" to "h5"
152  %are related to figure 1b in Chen, Characteristics of coplanar
153  %transmission lines on multilayer substrates: modeling and experiments,
154  %1997
155
156  %Top layers (epsilon_r1 and 2)
157  if(strcmp(pass_mat,'None'))
158      epsilon_r1=epsilon_r_Air; %Because no passivation material
159      h1=Inf; %Doesn't matter as epsilon_r1=epsilon_r_Air
160      %Define surrounding material permittivity
161      eval(['epsilon_r2 = epsilon_r_',surr_mat,';']);
162      h2=Inf; %Surrounding material has infinite thickness
163  else
164      %Define surrounding material permittivity
165      eval(['epsilon_r1 = epsilon_r_',surr_mat,';']);
166      h1=Inf; %Surrounding material has infinite thickness
167      %Define passivation material permittivity
168      eval(['epsilon_r2 = epsilon_r_',pass_mat,';']);
169      h2=pass_thick; %Passivation material thickness
170  end
171
172  %Bottom layers
173  if(strcmp(sub_mat,'None') && strcmp(under_mat,'None'))
174      epsilon_r3=epsilon_r_Air; %Because no underlying material
175      h3=Inf; %Doesn't matter as epsilon_r3=epsilon_r_Air
176      epsilon_r4=epsilon_r_Air; %Because no sunstrate material
177      h4=Inf; %Doesn't matter as epsilon_r4=epsilon_r_Air
178      %Define surrounding material permittivity
179      eval(['epsilon_r5 = epsilon_r_',surr_mat,';']);
180      h5=Inf; %Surrounding material has infinite thickness
181  elseif(strcmp(sub_mat,'None'))
182      epsilon_r3=epsilon_r_Air; %Because no substrate material
183      h3=Inf; %Doesn't matter as epsilon_r3=epsilon_r_Air
184      %Define surrounding material permittivity
185      eval(['epsilon_r4 = epsilon_r_',surr_mat,';']);
186      h4=Inf; %Surrounding material has infinite thickness
187      %Define underlying material permittivity
188      eval(['epsilon_r5 = epsilon_r_',under_mat,';']);
```

```matlab
189        h5=under_thick; %Underlying material thickness
190    elseif(strcmp(under_mat,'None'))
191        epsilon_r3=epsilon_r_Air; %Because no underlying material
192        h3=Inf; %Doesn't matter as epsilon_r3=epsilon_r_Air
193        %Define surrounding material permittivity
194        eval(['epsilon_r4 = epsilon_r_',surr_mat,';']);
195        h4=Inf; %Surrounding material has infinite thickness
196        %Define substrate material permittivity
197        eval(['epsilon_r5 = epsilon_r_',sub_mat,';']);
198        h5=sub_thick; %Substrate material thickness
199    else
200        %Define surrounding material permittivity
201        eval(['epsilon_r3 = epsilon_r_',surr_mat,';']);
202        h3=Inf; %Surrounding material has infinite thickness
203        %Define substrate material permittivity
204        eval(['epsilon_r4 = epsilon_r_',sub_mat,';']);
205        h4=sub_thick; %Substrate material thickness
206        %Define underlying material permittivity
207        eval(['epsilon_r5 = epsilon_r_',under_mat,';']);
208        h5=under_thick; %Underlying material thickness
209    end
210
211    %RF field vriables
212    %Frequencies from user input in GUI
213    freq=linspace(freq_range(1), freq_range(2), 2000);
214    omega=2*pi*freq; %Angular frequency [rad/s]
215
216    %Structure definition to pass as argument in functions
217    Geometry.Rext=Rext;     %External radius
218    Geometry.Wt=Wt;     %Track width
219    Geometry.Wg=Wgap;       %Gap width
220    Geometry.Wm=Wm;     %Meander track width
221    Geometry.Lm=Lm;     %Meander length
222    Geometry.Nm=Nm;     %Number of meanders
223    Geometry.Wo=Wo;     %Opening half width
224
225    %% Compute useful length according to resonator geometry
226    %This function computes the exact geometry defined in the photolithography
227    %design
228
229    length_struct=compute_resonator_length(Geometry);
230
231    %% Resistances computation
232    %This computation doesn't take into account temperature effect: R
233    %increases whith tempereature as detailed in Li, A Parylene MEMS
234    %Electrothermal Valve, 2009
235
236    %Total track length
237    Lt=length_struct.resonator_total_Res-length_struct.meander_arc_Res;
238    %Total length of meander [m]
239    Lmtot=length_struct.meander_total_Res;
240
```

Appendix A. Matlab code for the analytical model of the spiral resonators

```
241  %Resistance computation including skin effect: formula from Boutry,
242  %Characterization of miniaturized RLC resonators made of biodegradable
243  %materials for wireless implant applications, 2013
244  Δ=sqrt(2*rho/mu./omega);   %Skin depth [m]
245  Res_t=rho*Lt./(Wt*Δ.*(1-exp(-h./Δ))); %Track resistance[Ohm]
246  Res_m=rho*Lmtot./(Wm*Δ.*(1-exp(-h./Δ))); %Meander resistance[Ohm]
247  Res_tot=Res_t+Res_m; %Total resistance[Ohm]
248  %Meanders resistance when DC voltage is applied (no skin effect)[Ohm]
249  Res_m_DC=rho*Lmtot/(Wm*h);
250  %Track resistance when DC voltage is applied (no skin effect)[Ohm]
251  Res_t_DC=rho*Lt/(Wt*h);
252  %Total resistance when DC voltage is applied (no skin effect)[Ohm]
253  Res_tot_DC=Res_t_DC+Res_m_DC;
254
255
256  %% Inductance computation
257  %The inductance of a spiral resonator is equivalent to that of a single
258  %ring with a radius equal to the average radius of the spiral resonator,
259  %and a width equal to the track width of the resonator according to Baena,
260  %Equivalent-circuit models for split-ring resonators and complementary
261  %split-ring resonators coupled to planar transmission lines, 2005 and
262  %Marques, Comparative analysis of edge- and broadside- coupled split ring
263  %resonators for metamaterial design - theory and experiments, 2003. In
264  %that case the total inductance is computed using formula from Grover,
265  %Inductance Calculations: Working Formulas and Tables, 1946, p.110 and
266  %Thompson, Inductance Calculation Techniques --- Part II: Approximations
267  %and Handbook Methods, 1999 p.6
268
269  %L computation
270  Ravg=Rext-(Nt*(Wt+Wgap)-Wgap)/2; %Average radius of all the turns [m]
271  %Normalized radial thickness for P and F factors
272  Rnorm=(Nt*(Wt+Wgap)-Wgap)/(2*Ravg);
273  thick_norm=h/(Nt*(Wt+Wgap)-Wgap); %Normalizeed thickness for F factor
274  %Grover 1946 p.113, function of normalized radius: Nt*Wt/(2*Rext)
275  P=P_factor_inductance(Rnorm,0); %Only for 0.01<Rnorm<1
276  F=F_factor_inductance(Rnorm,thick_norm); %Grover 1946 p.108
277  %L=mu0/(4*pi)*(Nt^2)*Ravg*P*F; %Formula from Thompson 1999 p.6 [H]
278  L=mu0/(4*pi)*Ravg*P*F; %Formula considering Nt=1 (cf Baena 2005)
279
280
281  %% Capacitance computation
282
283  %To compute the capacitance of the spiral resonator, the per unit length
284  %capacitance Cpul is first computed in the same way as for coplanar
285  %strips. cf. Ghione, Analytical formulas for coplanar lines in hybrid and
286  %monolithic MICs, 1984, Chen, Characteristics of coplanar transmission
287  %lines on multilayer substrates: modeling and experiments, 1997 and Bahl,
288  %Microwave Solid State Circuit Design, 2003.
289
290  %The formula from Chen 1997 is used but the nomenclature is changed to be
291  %the same as in other references (Ghione 1984, Bahl 2003). Concretely, the
292  %definition of k and k' (and ki and ki') are swapped. This formula assume
```

```
293    %we can neglect tickness of the track.
294
295    %Parallell plate capacitance is also added to take into account resonator
296    %thickness. No fringing field is taken into account as fringes goes from
297    %the backside of infinitely thin parallell plate capacitor. It is thus
298    %already taken into account when computing capacitance of coplanar strips
299
300    %Then to compute the final capacitance, Cpul is multiplied by the total
301    %length of the gap in the spiral resonator.
302
303    %The formula is only valid for NT=2! If Nt>2 => we don't have 2 parallel
304    %strip but 3 or more...we should then correct the formula used.
305
306    %Variables definition
307    s=Wgap;
308    w=Wt;
309    %Use the command vpa to keep use symbloic variable and increase the
310    %precision
311    k=vpa(s/(s+2*w));
312    %Use the command vpa to keep use symbloic variable and increase the
313    %precision
314    k_prime=vpa(sqrt(1-k^2));
315
316    %K(k)/K(k') = elliptic integral ratio according to Bahl, Microwave Solid
317    %State Circuit Design 2003, initially developed by Hilberg, From
318    %Approximations to Exact Relations for Characteristic Impedances, 1969 and
319    %Wen, Coplanar Waveguide: A Surface Strip Transmission Line Suitable for
320    %Nonreciprocal Gyromagnetic Device Applications, 1969
321    if(k<0)
322        error('Error k is smaller than 0, in capacitance computation');
323    elseif(k<(1/sqrt(2)))
324        K_k_ratio=(1/pi*log(2*(1+sqrt(k_prime))/(1-sqrt(k_prime))))^-1;
325    elseif(k<1)
326        K_k_ratio=1/pi*log(2*(1+sqrt(k))/(1-sqrt(k)));
327    else
328        error('Error k is larger than 1, in capacitance computation');
329    end
330
331    %Capacitance when all dielectric are replaced by free space (or air)
332    Ca=epsilon0/K_k_ratio;
333
334    %The computation of elliptical integrals ratios requires high
335    %computational power in some cases when the substrate thickness is thin
336    %which might result in computational errors or code errors. To prevent
337    %these errors some condition to check that we are not in such cases are
338    %added in the code. In case of positive detection then the value of
339    %elliptical integral ratios is computed by extrapolatiing the value using
340    %the last thickness for which the detection is not positive (in steps of
341    %100 nm) and the limit when the thickness tends to 0 (this value is
342    %computed properly). In terms of coding, this is implemented using a while
343    %loop and increasing the thickness at each iteration until there is no
344    %more positive detection. This works also if several layers are very thin
```

```matlab
345  %because the K(i), K_prime(i) and K_ratio(i) computation is independent
346  %of the other layers thicknesses
347
348  H=[h1 h2 h3 h4 h5];
349  H_0=H; %Initial values as a backup
350  %Initialization, use the command vpa to keep use symbloic variable and
351  %increase the precision
352  K=vpa(ones(1,length(H)));
353  %Initialization, use the command vpa to keep use symbloic variable and
354  %increase the precision
355  K_prime=vpa(ones(1,length(H)));
356  Epsilon_r=[epsilon_r1 epsilon_r2 epsilon_r3 epsilon_r4 epsilon_r5];
357  K_ratio=vpa(ones(1,length(H))); %Initialization
358
359  syms f(S,W,X); %Symbolic function to compute ki
360  syms g(S,W); %Symbolic function for when we have indterminations (0/0)
361  %Symbolic function to compute ki
362  f(S,W,X)=sinh(pi*S/(4*X))/sinh(pi/2*(S/2+W)/X);
363
364  for i=1:length(H)
365      %Flag to exit the while loop once the computation of the capacitance
366      %is finished
367      exit=0;
368      %Flag is set to 1 when we detect a positive case => we need to
369      %extrapoalte the final value
370      extrap=0;
371      while(exit==0)
372          %By default we assume we are not in a case where we will have an
373          %error
374          exit=1;
375
376          %K(i) computation, 0<K(i)<k, K(i)=0 when thickness=0 and K(i)=k
377          %when thickness=Inf
378          if(H(i)==Inf) %H(i)=Inf => evaluate the function limit at + inf
379              g(S,W)=limit(f,X,Inf);
380              K(i)=g(s,w); %In this case K(i)=k
381          else
382              if(H(i)==0)
383                  g(S,W)=limit(f,X,0);
384                  K(i)=g(s,w); %In this case K(i)=0
385              else
386                  K(i)=f(s,w,H(i));
387              end
388              %In this specific case it is because H(i) is very small
389              %(i.e. limit toward 0)
390              if(isnan(K(i)))
391                  g(S,W)=limit(f,X,0);
392                  K(i)=g(s,w); %In this case K(i)=0
393              end
394          end
395
396          %K_prime(i) computation, sqrt(1-k^2)<K_prime(i)<1, K_prime(i)=1
```

158

```
397         %when thickness=0 (K=0)
398         K_prime(i)=sqrt(1-K(i)^2);
399
400         %K(ki)/K(ki') = elliptic integral ratio according to Bahl,
401         %Microwave Solid State Circuit Design 2003, initially developed
402         %by Hilberg, From Approximations to Exact Relations for
403         %Characteristic Impedances, 1969 and Wen, Coplanar Waveguide: A
404         %Surface Strip Transmission Line Suitable for Nonreciprocal
405         %Gyromagnetic Device Applications, 1969
406         if(K(i)<0)
407             error(['Error k', num2str(i),[' is smaller than 0, in'...
408                 ' capacitance computation']]);
409         elseif(K(i)<(1/sqrt(2)))
410             %Test if division by 0, i.e if K'=1 => if K=0 => for very thin
411             %layers
412             if(double(1-sqrt(K_prime(i)))==0)
413                 if(H(i)==0) %Thickness is set to 0 by the user
414                     %Compute the limit of K_ratio when K_prime=1 (i.e.
415                     %thickness=0) => K_ratio = 0;
416                     syms q(Z)
417                     q(Z)=(1/pi*log(2*(1+sqrt(Z))/(1-sqrt(Z))))^-1;
418                     K_ratio(i)=limit(q,Z,1);
419                 else %H(i) is too thin to compute K_ratio
420                     %In this case we need to redo the computation of K(i),
421                     %K_prime(i) for a slightly thicker H(i)
422                     exit=0;
423                     %Set the flag to remeber that we where in a positive
424                     %case
425                     extrap=1;
426                     %Increase the layer thickness by 100 nm
427                     H(i)=H(i)+100e-9;
428                 end
429             %Case where there is no computational error risk
430             else
431                 %Test if we detected a positive case before and reach this
432                 %condition now after increasing the thickness
433                 if extrap
434                     %Extrapolate between limith when thickness tends to
435                     %0 and current value (first thickness value wihthout
436                     %high computational error risk).
437
438                     %Compute the limit of K_ratio when K_prime=1 (i.e.
439                     %thickness=0) => K_ratio = 0;
440                     syms q(Z)
441                     q(Z)=(1/pi*log(2*(1+sqrt(Z))/(1-sqrt(Z))))^-1;
442                     K_ratio_zero=limit(q,Z,1);
443
444                     %Compute the value of K_ratio for the minimum
445                     %thickness before requiring high computational cost
446                     K_ratio_first=(1/pi*log(2*(1+sqrt(K_prime(i)))/...
447                                     (1-sqrt(K_prime(i)))))^-1;
448
```

```matlab
449                         %Extrapolate linearly to compute the value of K_ratio
450                         %for the thin thickness requiring too high
451                         %computational power
452                         K_ratio(i)=H_0(i)/H(i)*(K_ratio_first-K_ratio_zero);
453                     %Case where we arrive here directly (normal behavior of
454                     %the code)
455                     else
456                         K_ratio(i)=(1/pi*log(2*(1+sqrt(K_prime(i)))/...
457                                     (1-sqrt(K_prime(i)))))^-1;
458                     end
459                 end
460         elseif(K(i)<1)
461             %Maybe there are some high computational power cases in this
462             %condition but we are ulikely to fall within this condition
463             %with our SR resonators design
464             K_ratio(i)=1/pi*log(2*(1+sqrt(K(i)))/(1-sqrt(K(i))));
465         else
466             error(['Error k', num2str(i),[' is larger than 1, in '...
467                     'capacitance computation']]);
468         end
469     end
470 end
471
472 %Relative permittivity due to dielectric material
473 Epsilon_d=ones(1,length(Epsilon_r)); %Initialization
474 Epsilon_r_d=Epsilon_r-[1 epsilon_r1 1 epsilon_r3 epsilon_r4];
475 for i=1:length(Epsilon_r)
476     %If Epsilon_r_d is not equal to 0, compute the value
477     if(Epsilon_r_d(i))
478         Epsilon_d(i)=0.5*Epsilon_r_d(i)/K_k_ratio*K_ratio(i);
479     %If Epsilon_r_d=0, set the value to 0 to avoid indetermination
480     else
481         Epsilon_d(i)=0;
482     end
483 end
484
485 %Effectife relative permittivity
486 epsilon_eff=1+sum(Epsilon_d);
487
488 %Per unit lenght capacitance due to CPS [F/m]
489 Cpul_CPS=double(Ca*epsilon_eff); %Convert from symbolic to double
490
491 %Per unit length capacitance due to parallell plates (no fringes) [F/m]
492 Cpul_PARR=epsilon0*epsilon_r2*h/Wgap;
493
494 %Per unit lenght capacitance [F/m]
495 Cpul=Cpul_CPS+Cpul_PARR;
496
497 %Length where we have bot capacitances
498 Lc_PARR_CPS=length_struct.resonator_total_Cap-...
499             length_struct.meander_arc_Cap;
500
```

```matlab
501  %Length where we have parallel plate capacitance only
502  Lc_PARR=length_struct.meander_arc_Cap_plate;
503
504  %Length where we have coplanar strip capacitance only
505  Lc_CPS=length_struct.meander_arc_Cap_strip;
506
507  %Total capacitance [F]
508  Ctot=Cpul*Lc_PARR_CPS + Cpul_PARR*Lc_PARR + Cpul_CPS*Lc_CPS;
509
510
511  %% Computation of dissipated energy as a function of frequency
512
513  Vemf=omega*pi*(Ravg^2)*Nt*Brf*cos(gamma); %Induced electromotive force [V]
514
515  %Power dissipated in the meander [W]
516  Pm=((Vemf.^2).*Res_m)./((Res_tot.^2)+(omega*L-1./(omega*Ctot)).^2);
517
518  %Energy dissipated in the meander during one pusle [J]
519  Em=Pm*tau;
520
521  if ¬no_display
522      plot(freq/(10^9),Em*10^3);
523      xlabel('Frequency [GHz]');
524      ylabel('Energy [mJ]');
525      title(['Energy dissipated in meanders as a function of external RF'...
526              'field frequency']);
527      ylim([0 400]);
528  end
529
530  %% Computation of f0, Q factor, P(w0) and E(w0)
531
532  %Resonance frequency without takinng into account that Vemf, Res_m and
533  %Res_t depends on omega
534  omega_res=1/sqrt(L*Ctot); %Resonance pulsation
535  f0=omega_res/(2*pi); %Resonance frequency
536
537  %Resistance computation including skin effect: formula from Boutry,
538  %Characterization of miniaturized RLC resonators made of biodegradable
539  %materials for wireless implant applications, 2013
540  ∆_res=sqrt(2*rho/mu/omega_res);  %Skin depth [m]
541  %Track resistance[Ohm]
542  Res_t_res=rho*Lt/(Wt*∆_res*(1-exp(-h/∆_res)));
543  %Meanders resistance[Ohm]
544  Res_m_res=rho*Lmtot/(Wm*∆_res*(1-exp(-h/∆_res)));
545  Res_tot_res=Res_t_res+Res_m_res; %Total resistance[Ohm]
546
547  Q=1/Res_tot_res*sqrt(L/Ctot); %Q-factor
548
549  %Induced electromotrice force at resonance [V]
550  Vemf_res=omega_res*pi*(Ravg^2)*Nt*Brf*cos(gamma);
551
552  %Power dissipated in the meander at resonance [W]
```

```matlab
553  Pm_res=((Vemf_res^2)*Res_m_res)/(Res_tot_res^2);
554
555  %Current in the meander
556  I_res=Vemf_res/Res_tot_res;
557  Jm_res=I_res/(Wm*Δ_res*(1-exp(-h/Δ_res)));
558
559  %Energy dissipated in the meander at resonance [J]
560  Em_res=Pm_res*tau;
561  Emax=Em_res;
562
563  output_name={'L','Ctot','f0','Q','Emax'};
564  for i=1:length(output_name)
565      eval(['Split_ring.',output_name{i},'=',output_name{i},';']);
566  end
567
568  Split_ring.Rtot=Res_tot_res;
569  Split_ring.Rm=Res_m_res;
570  Split_ring.RmRtot=Res_m_res/Res_tot_res;
571  Split_ring.Res_m_DC=Res_m_DC;
572  Split_ring.jm=Jm_res;
```

SR geometry verification

```matlab
1   function non_valid=check_geometry_resonator(Geometry)
2   %CHECK_GEOMETRY_RESONATOR
3   %Check that the geometry is valid and return a warning flag if not.
4   %
5   % Syntax:  non_valid=check_geometry_resonator(Geometry)
6   %
7   % Inputs:
8   %    - Geometry: strucutre containing all the geometrical parameters
9   %               defining a resonator
10  %         Geometry.Rext: external radius
11  %         Geometry.Wt: track width
12  %         Geometry.Wg: gap width
13  %         Geometry.Wm: meander track width
14  %         Geometry.Lm: meander length
15  %         Geometry.Nm; number of meanders
16  %         Geometry.Wo: opening half width
17  %         Geometry.h: thickness of the resonator
18  %         Geometry.Nt: number of turn == 2 otherwise the model is not
19  %                      valid
20  %         Geometry.pass_thick: thickness of the passivation layer over
21  %                              the Mg resonator
22  %
23  % Outputs:
24  %    - non_valid: flag with values describing the reason of a non valid
25  %    geopmetry:
26  %    0='Valid'
```

```matlab
27  %    1='Too small normalized radius for P value table'
28  %    2='Too large value of Nt, Wt, Wo or Wg for the current value of Rext'
29  %    3='Too small opening for the current value of Wt adn Wg'
30  %    4='Passivation layer thickness is smaller than resonator thickness'
31  %    5='Meander is too long and overlaps the junction between the two
32  %       turns of the resonator'
33  %
34  % Example:
35  %    None
36  %
37  % Other m-files required: compute_resonator_length
38  % Subfunctions: none
39  % MAT-files required: none
40  %
41  % See also: none
42  % Author: Matthieu Ruegg
43  % Work address: EPFL, STI, IMT, LMIS1
44  % email: matthieu.ruegg@gmail.com
45  % Website: http://www.lmis1.epfl.ch
46  % August 2016; Last revision: 15-March-2019
47
48  %Variables definition
49  Rext=Geometry.Rext;    %External radius
50  Wt=Geometry.Wt;      %Track width
51  Wg=Geometry.Wg;      %Gap width
52  Wm=Geometry.Wm;      %Meander track width
53  Lm=Geometry.Lm;      %Meander length
54  Nm=Geometry.Nm;      %Number of meanders
55  Wo=Geometry.Wo;      %Opening half width
56  h=Geometry.h;        %Thickness of the resonator
57  pass_thick=Geometry.pass_thick; %Thickness of the passivation layer over
58                                  %the Mg resonator
59  Nt=Geometry.Nt;      %Number of turn == 2 otherwise the model is not valid
60
61  non_valid=0; %Assume that the geometry is valid
62
63  %Check if geometry is valid
64  if((Nt*(Wt+Wg)-Wg)/(2*(Rext-(Nt*(Wt+Wg)-Wg)/2))<0.01)
65      %disp('Too small normalized radius for P value table');
66      non_valid=1;
67  end
68  if(Rext-Wo<Nt*(Wt+Wg))
69      %disp(['Too large value of Nt, Wt, Wo or Wg for the current value'...
70      %      'of Rext']);
71      non_valid=2;
72  end
73  %if(Wo-Wg<Wt/2)
74  %Initially the condition was: if(Wo-Wg<Wt/2) but it allows steep angles
75  %whcih results in cracks during the fabrication
76  if(Wo-Wg<Wt*69/100)
77      %disp('Too small opening for the current value of Wt and Wg');
78      non_valid=3;
```

```matlab
79  end
80  if(pass_thick<h && h>0)
81      %disp('Passivation layer thickness is smaller than resonator...
82      %       thickness');
83      non_valid=4;
84  end
85  %The function compute_resonator_length also checks if the meander geomety
86  %is not overlaping the junction between the two turns of the resonator.
87  %First check if no previous error detected otherwise it might lead to bugs
88  if non_valid == 0
89      length=compute_resonator_length(Geometry);
90      if length.non_valid == 5
91          %disp(['Meander is too long and overlaps the junction between'...
92          %       'the two turns of the resonator']);
93          non_valid=5;
94      end
95  end
96  end
```

SR length computation

```matlab
1   function length_struct=compute_resonator_length(Geometry)
2   %COMPUTE_RESONATOR_LENGTH
3   %This compute the length of several portions of the resonator.
4   %
5   %It also checks if the meander geomety is not overlaping the junction
6   %between the two turns of the resonator (line 311)
7   %
8   %For geometrical definitions of the points, radius, etc, refer to
9   %handwritten notes in lab notebook 0261-15
10  %
11  % Syntax:  length_struct=compute_resonator_length(Geometry)
12  %
13  % Inputs:
14  %    - Geometry: strucutre containing all the geometrical parameters
15  %                defining a resonator
16  %           Geometry.Rext: external radius
17  %           Geometry.Wt: track width
18  %           Geometry.Wg: gap width
19  %           Geometry.Wm: meander track width
20  %           Geometry.Lm: meander length
21  %           Geometry.Nm; number of meanders
22  %           Geometry.Wo: opening half width
23  %
24  %           %Unecessary parameters for this specific function
25  %           Geometry.h: thickness of the resonator
26  %           Geometry.Nt: number of turn == 2 otherwise the model is not
27  %                        valid
28  %           Geometry.pass_thick: thickness of the passivation layer over
```

```
29   %                                    the Mg resonator
30   %
31   % Outputs:
32   %     - legth_struct: structure with the length of the different parts of
33   %                     the resonators
34   %          length_struct.resonator_total_Res
35   %          length_struct.meander_arc_Res
36   %          length_struct.meander_total_Res
37   %          length_struct.meander_arc_Cap
38   %          length_struct.meander_arc_Cap_plate
39   %          length_struct.meander_arc_Cap_strip
40   %          length_struct.resonator_total_Cap
41   %
42   % Example:
43   %     None
44   %
45   % Other m-files required: circle_arc_length
46   % Subfunctions: none
47   % MAT-files required: none
48   %
49   % See also: compute_coil_model_V4, check_geometry_resonator
50   % Author: Matthieu Ruegg
51   % Work address: EPFL, STI, IMT, LMIS1
52   % email: matthieu.ruegg@gmail.com
53   % Website: http://www.lmis1.epfl.ch
54   % August 2016; Last revision: 15-March-2019
55
56   %% Define constants and variables
57   %All units are in SI units
58
59   %Define geometrical parameters
60   Rext=Geometry.Rext;%External radius
61   Wt=Geometry.Wt;      %Track width
62   Wg=Geometry.Wg;      %Gap width
63   Wm=Geometry.Wm;      %Meander track width
64   Lm=Geometry.Lm;      %Meander length
65   Nm=Geometry.Nm;      %Number of meanders
66   Wo=Geometry.Wo;      %Opening half width
67
68   %Define radius
69   R1=Rext-2*Wt-Wg;    %See schematic in lab notebook for reference geometry
70   R2=Rext-Wt-Wg-Wt/2; %See schematic in lab notebook for reference geometry
71   R3=Rext-Wt-Wg;  %See schematic in lab notebook for reference geometry
72   R4=Rext-Wt; %See schematic in lab notebook for reference geometry
73   R5=Rext-Wt/2;   %See schematic in lab notebook for reference geometry
74   R6=Rext;     %See schematic in lab notebook for reference geometry
75
76   %% Compute the slope of the segment between external and internal tracks
77   %
78   %                              /                    x=(x2,y2)
79   %                             /                    /
80   %                            /                    /
```

```
81  % Upper line: y=ax+b ->    /                    /
82  %                         /                    /
83  %                        /                    /   <- Lower line: y=ax+c
84  %                       /                    /
85  %              (x1,y1)=x                    /
86  %                     /                    /
87  %                    /                    x=(x3,y3)
88  %                   /                    /
89  %
90  % Perpendicular going through (x1,y1) (x3,y3): y=-1/a*x+d
91  % Perpendicular going through (x2,y2) (x20,y20): y=-1/a*x+f
92  % Edit: point 3 is computed below with points 19, 20, 21
93  % Edit2: to understand the computation of the slope and the definition of
94  % alpha 1 and alpha2 refer to handwritten notes in lab notebook 0261-15
95
96  %Computation of pt1
97  R_pt1=R3;
98  opening_angle_pt1=asin((Wo-Wg)/R_pt1);  %Computation of the opening angle
99  theta_pt1=opening_angle_pt1+pi/2; %Conversion in polar coord. 2nd quadrant
100 x1=R_pt1*cos(theta_pt1);   %Conversion in cartesian coordinates
101 y1=R_pt1*sin(theta_pt1);   %Conversion in cartesian coordinates
102
103 %Computation of pt2
104 R_pt2=R4;
105 opening_angle_pt2=asin((Wo-Wg)/R_pt2);  %Computation of the opening angle
106 theta_pt2=pi/2-opening_angle_pt2; %Conversion in polar coord. 1st quadrant
107 x2=R_pt2*cos(theta_pt2);   %Conversion in cartesian coordinates
108 y2=R_pt2*sin(theta_pt2);   %Conversion in cartesian coordinates
109
110 %Compute distance between pt 1 and 2
111 %See top right corner of handwritten note in 0261-15 to understand
112 %computation
113 dist_pt1_pt2=sqrt((x2-x1)^2+(y2-y1)^2);
114 alpha1=atan((y2-y1)/(x2-x1));
115 alpha2=asin(Wt/dist_pt1_pt2);
116 a=tan(alpha1+alpha2);
117 b=y1-a*x1;
118 c=y2-a*x2;
119 d=y1+x1/a;
120 f=y2+x2/a;
121 e=(b+c)/2; %Centerline is in between upper line ax+b and lower line ax+c
122
123
124 %% Computation of points 3, 19, 20, 21
125 % Pts 19 and 21 are defined on a line going through the resonator center
126 % and pts 2 and 1 respectiverly
127 % Pts 20 and 3 are defined by the intersection of lines perpendicular to
128 % the track through pts 2 and 1 respectively
129
130 R_pt19=R6;
131 theta_pt19=theta_pt2;     %Same angle as point 2
132 x19=R_pt19*cos(theta_pt19);    %Conversion in cartesian coordinates
```

```
133   y19=R_pt19*sin(theta_pt19);    %Conversion in cartesian coordinates
134
135   R_pt21=R1;
136   theta_pt21=theta_pt1;     %Same angle as point 1
137   x21=R_pt21*cos(theta_pt21);    %Conversion in cartesian coordinates
138   y21=R_pt21*sin(theta_pt21);    %Conversion in cartesian coordinates
139
140   x3=(d-c)/(a+1/a); % a*x+c=-1/a*x+d
141   y3=a*x3+c;
142   R_pt3=sqrt(x3^2+y3^2);
143   theta_pt3=atan(y3/x3);
144   %Correction depending on in which quadrant is the point
145   if x3<0 %2nd and 3rd quadrant
146       theta_pt3=theta_pt3+pi;
147   elseif y3<0 %4th quadrant
148       theta_pt3=theta_pt3+2*pi;
149   end
150
151   x20=(f-b)/(a+1/a); % a*x+b=-1/a*x+f
152   y20=a*x20+b;
153   R_pt20=sqrt(x20^2+y20^2);
154   theta_pt20=atan(y20/x20);
155   %Correction depending on in which quadrant is the point
156   if x20<0 %2nd and 3rd quadrant
157       theta_pt20=theta_pt20+pi;
158   elseif y20<0 %4th quadrant
159       theta_pt20=theta_pt20+2*pi;
160   end
161
162
163   %% Computation of Pts 8, 9, 22, 23, 24, 25
164
165   %Computation of pt9
166   R_pt9=R5;
167   opening_angle_pt9=asin(Wo/R_pt9);    %Computation of opening angle
168   theta_pt9=opening_angle_pt9+pi/2; %Conversion in polar coord. 2nd quadrant
169   x9=R_pt9*cos(theta_pt9);    %Conversion in cartesian coordinates
170   y9=R_pt9*sin(theta_pt9);    %Conversion in cartesian coordinates
171
172   %Computation of pt8
173   R_pt8=R2;
174   opening_angle_pt8=asin(Wo/R_pt8);    %Computation of the opening angle
175   theta_pt8=pi/2-opening_angle_pt8; %Conversion in polar coord. 1st quadrant
176   x8=R_pt8*cos(theta_pt8);    %Conversion in cartesian coordinates
177   y8=R_pt8*sin(theta_pt8);    %Conversion in cartesian coordinates
178
179   % Computation of Pts 22, 23, 24, 25
180   % Pts 22 and 25 are defined on a line going through the resonator center
181   % and pts 1 and 2 respectiverly
182   % Pts 23 and 24 are defined by the intersection of lines perpendicular to
183   % the track through pts 1 and 2 respectively
184
```

```matlab
185  R_pt22=R2;
186  theta_pt22=theta_pt1;     %Same angle as point 1
187  x22=R_pt22*cos(theta_pt22);   %Conversion in cartesian coordinates
188  y22=R_pt22*sin(theta_pt22);   %Conversion in cartesian coordinates
189
190  R_pt25=R5;
191  theta_pt25=theta_pt2;     %Same angle as point 2
192  x25=R_pt25*cos(theta_pt25);   %Conversion in cartesian coordinates
193  y25=R_pt25*sin(theta_pt25);   %Conversion in cartesian coordinates
194
195  x23=(d-e)/(a+1/a); % a*x+e=-1/a*x+d
196  y23=a*x23+e;
197  R_pt23=sqrt(x23^2+y23^2);
198  theta_pt23=atan(y23/x23);
199  %Correction depending on in which quadrant is the point
200  if x23<0 %2nd and 3rd quadrant
201      theta_pt23=theta_pt23+pi;
202  elseif y23<0 %4th quadrant
203      theta_pt23=theta_pt23+2*pi;
204  end
205
206  x24=(f-e)/(a+1/a); % a*x+b=-1/a*x+f
207  y24=a*x24+e;
208  R_pt24=sqrt(x24^2+y24^2);
209  theta_pt24=atan(y24/x24);
210  %Correction depending on in which quadrant is the point
211  if x24<0 %2nd and 3rd quadrant
212      theta_pt24=theta_pt24+pi;
213  elseif y24<0 %4th quadrant
214      theta_pt24=theta_pt24+2*pi;
215  end
216
217
218  %% Computation of points 10, 11, 12 and 13
219
220  R_pt10=R6;
221  opening_angle_pt10=asin(Wo/R_pt10);    %Computation of opening angle
222  theta_pt10=opening_angle_pt10+pi/2;%Convert in polar coord. 2nd quadrant
223  x10=R_pt10*cos(theta_pt10);   %Conversion in cartesian coordinates
224  y10=R_pt10*sin(theta_pt10);   %Conversion in cartesian coordinates
225
226  R_pt11=R4;
227  opening_angle_pt11=asin(Wo/R_pt11);    %Computation of opening angle
228  theta_pt11=opening_angle_pt11+pi/2;%Convert in polar coord. 2nd quadrant
229  x11=R_pt11*cos(theta_pt11);   %Conversion in cartesian coordinates
230  y11=R_pt11*sin(theta_pt11);   %Conversion in cartesian coordinates
231
232  R_pt12=R3;
233  opening_angle_pt12=asin(Wo/R_pt12);    %Computation of the opening angle
234  theta_pt12=pi/2-opening_angle_pt12;%Convert in polar coord. 1st quadrant
235  x12=R_pt12*cos(theta_pt12);   %Conversion in cartesian coordinates
236  y12=R_pt12*sin(theta_pt12);   %Conversion in cartesian coordinates
```

```matlab
237
238  R_pt13=R1;
239  opening_angle_pt13=asin(Wo/R_pt13);    %Computation of the opening angle
240  theta_pt13=pi/2-opening_angle_pt13;%Convert in polar coord. 1st quadrant
241  x13=R_pt13*cos(theta_pt13);   %Conversion in cartesian coordinates
242  y13=R_pt13*sin(theta_pt13);   %Conversion in cartesian coordinates
243
244
245  %% Computation of points 6 and 7
246  %Not used anymore with rounded corners
247
248  R_pt6=R6;
249  R_pt7=R1;
250  centerx=0;   %Resonator is centered at (0,0)
251  centery=0;   %Resonator is centered at (0,0)
252
253  [x6,y6]=linecirc(a,b,centerx,centery,R_pt6);  %Solutions for pt6
254  [x7,y7]=linecirc(a,c,centerx,centery,R_pt7);  %Solutions for pt7
255
256  %Find which of the two solutions is correct: it is always the upper point
257  if y6(2)>y6(1)
258      x6=x6(2); %Correct solution for (x6,y6)
259      y6=y6(2); %Correct solution for (x6,y6)
260  else
261      x6=x6(1); %Correct solution for (x6,y6)
262      y6=y6(1); %Correct solution for (x6,y6)
263  end
264
265  if y7(2)>y7(1)
266      x7=x7(2); %Correct solution for (x7,y7)
267      y7=y7(2); %Correct solution for (x7,y7)
268  else
269      x7=x7(1); %Correct solution for (x7,y7)
270      y7=y7(1); %Correct solution for (x7,y7)
271  end
272
273  %Convert from cartesian into polar coordinates
274  theta_pt6=atan(y6/x6);
275  if theta_pt6 < 0
276      theta_pt6=theta_pt6+pi; %Correction because it is in second quadrant
277  end
278  theta_pt7=atan(y7/x7);
279  if theta_pt7 < 0
280      theta_pt7=theta_pt7+pi; %Correction because it is in second quadrant
281  end
282
283
284  %% Total length computation
285  %We need to compute it here in order to compute the meander location and
286  %the meander related points and geometry
287
288  %Compute external track length (from pt9 to pt25)
```

```matlab
289  angle_pt9_pt25=2*pi-(theta_pt9-theta_pt25);
290  length_pt9_pt25=R_pt9*angle_pt9_pt25;
291
292  %Compute internal track length (from pt22 to pt8)
293  angle_pt22_pt8=2*pi-(theta_pt22-theta_pt8);
294  length_pt22_pt8=R_pt22*angle_pt22_pt8;
295
296  %Compute inter-track segment length (from pt23 to pt24)
297  length_pt23_pt24=sqrt((x23-x24)^2+(y23-y24)^2);
298
299  %Compute external rounded corner length (from pt24 to pt25)
300  length_pt24_pt25=circle_arc_length(theta_pt24, theta_pt25, R_pt24,...
301                                     R_pt25, x2, y2, Wt/2, 'clockwise');
302
303  %Compute internal rounded corner length (from pt22 to pt23)
304  length_pt22_pt23=circle_arc_length(theta_pt22, theta_pt23, R_pt22,...
305                                     R_pt23, x1, y1, Wt/2, 'anticlockwise');
306
307  %Compute total lenght of the resonator
308  resonator_length=length_pt9_pt25 + length_pt22_pt8 + length_pt23_pt24 +...
309                   length_pt24_pt25 + length_pt22_pt23;
310
311
312  %% Computation of points 14, 15, 16, 17 and 18
313
314  %Initialize the geometry as valid
315  length_struct.non_valid=0;
316
317  %if Nm≠0
318      R_pt18=R5;
319      %The center of the meander is at the half lenght of the resonator
320      angle_for_half_length=resonator_length/2/R_pt18;
321      theta_pt18=theta_pt9+angle_for_half_length;
322      if theta_pt18 ≥ 2*pi
323          %Correction if the meander is in the 1st quadrant
324          theta_pt18=theta_pt18-2*pi;
325      end
326      x18=R_pt18*cos(theta_pt18);   %Conversion in cartesian coordinates
327      y18=R_pt18*sin(theta_pt18);   %Conversion in cartesian coordinates
328
329      meander_total_length=2*Nm*Lm;
330      meander_total_angle=meander_total_length/R_pt18;
331
332      theta_pt14=theta_pt18+meander_total_angle/2;
333      if theta_pt14 ≥ 2*pi
334          theta_pt14=theta_pt14-2*pi; %Correction if in 1st quadrant
335      end
336      theta_pt15=theta_pt18+meander_total_angle/2;
337      if theta_pt15 ≥ 2*pi
338          theta_pt15=theta_pt15-2*pi; %Correction if in 1st quadrant
339      end
340      theta_pt16=theta_pt18-meander_total_angle/2;
```

```matlab
341        if theta_pt16<0
342            theta_pt16=theta_pt16+2*pi; %Correction if in 4th quadrant
343        end
344        theta_pt17=theta_pt18-meander_total_angle/2;
345        if theta_pt17<0
346            theta_pt17=theta_pt17+2*pi; %Correction if in 4th quadrant
347        end
348
349        R_pt14=R6;
350        R_pt15=R4;
351        R_pt16=R6;
352        R_pt17=R4;
353
354        x14=R_pt14*cos(theta_pt14);   %Conversion in cartesian coordinates
355        y14=R_pt14*sin(theta_pt14);   %Conversion in cartesian coordinates
356        x15=R_pt15*cos(theta_pt15);   %Conversion in cartesian coordinates
357        y15=R_pt15*sin(theta_pt15);   %Conversion in cartesian coordinates
358        x16=R_pt16*cos(theta_pt16);   %Conversion in cartesian coordinates
359        y16=R_pt16*sin(theta_pt16);   %Conversion in cartesian coordinates
360        x17=R_pt17*cos(theta_pt17);   %Conversion in cartesian coordinates
361        y17=R_pt17*sin(theta_pt17);   %Conversion in cartesian coordinates
362
363        %Test if meander is possible (i.e. if pt 14 is in 1st quadrant and is
364        %not overlaping pt 19)
365        if (theta_pt14<3*pi/2 && theta_pt14>theta_pt19)
366            %disp('Meander is too long and overlaps the junction between...
367            %     the two turns of the resonator');
368            length_struct.non_valid=5;
369        end
370 %end
371
372 %% Computation of the meander length for resistance computation
373
374 if Nm≠0
375        %The meander arc length is defined as the average of the outer arc
376        %length (pt 14 to 16)and the inner arc length (pt 15 to 17). We also
377        %have to substract the two extremities where the meander is already
378        %back to standard track dimensions. See handwritten notes in lab
379        %notebook 0261-15 for details.
380        outer_meander_arc=circle_arc_length(theta_pt15, theta_pt17, R_pt15,...
381                                    R_pt17, 0, 0, R_pt15, 'clockwise');
382        inner_meander_arc=circle_arc_length(theta_pt14, theta_pt16, R_pt14,...
383                                    R_pt16, 0, 0, R_pt14, 'clockwise');
384        meander_arc_length_Res=(outer_meander_arc+inner_meander_arc)/2-...
385                            2*R_pt18*asin(Wm/2/R_pt18);
386
387        %Meander total length is equal to meander_arc_length + the (2Nm-1)
388        %radial parts of the meanders which have a lenght of (Wt-Wm)
389        meander_total_length_Res=meander_arc_length_Res + (2*Nm-1)*(Wt-Wm);
390 else
391        meander_arc_length_Res=0;
392        meander_total_length_Res=0;
```

```
393  end
394
395
396  %% Computation of the meander length for capacitance computation
397  %We need to compute two length: one length for the parallel plate
398  %capcitance which consists of the part of the meander inner boundary close
399  %to the resonator internal track and one length for the parallel strip
400  %capacitance which is approximated to the arc lenght of the perpendicular
401  %meander stripes
402  if Nm≠0
403      %Compute length from pt 15 to pt 17 in the gap between the tracks
404      angle_pt15_pt17=theta_pt15-theta_pt17;
405      meander_arc_length_Cap=(R_pt9+R_pt8)/2*angle_pt15_pt17;
406
407      %Compute the part where we have to take into account the parallel
408      %plate capacitance
409      meander_arc_length_Cap_plate=Nm*(R_pt8+R_pt9)/2*Lm/R_pt18+(2*Nm+1)*...
410                              (R_pt8+R_pt9)/2*asin(Wm/2/R_pt18);
411
412      %Compute the part where we have to take into account the coplanar
413      %strip capacitance
414      meander_arc_length_Cap_strip=4*Nm*(R_pt8+R_pt9)/2*asin(Wm/2/R_pt18);
415  else
416      meander_arc_length_Cap=0;
417      meander_arc_length_Cap_plate=0;
418      meander_arc_length_Cap_strip=0;
419  end
420
421
422  %% Computation of the total length for the capacitance
423  %This is the whole resonator except the transition part between external
424  %and interanl tracks
425
426  %Compute length from pt 9 to pt 8 in the gap between the tracks
427  angle_pt9_pt8=2*pi-(theta_pt9-theta_pt8);
428  length_total_Cap=(R_pt9+R_pt8)/2*angle_pt9_pt8;
429
430
431  %% Save values into output structure
432  length_struct.resonator_total_Res=resonator_length;
433  length_struct.meander_arc_Res=meander_arc_length_Res;
434  length_struct.meander_total_Res=meander_total_length_Res;
435  length_struct.meander_arc_Cap=meander_arc_length_Cap;
436  length_struct.meander_arc_Cap_plate=meander_arc_length_Cap_plate;
437  length_struct.meander_arc_Cap_strip=meander_arc_length_Cap_strip;
438  length_struct.resonator_total_Cap=length_total_Cap;
439
440  end
```

Computation of the length of an arc of circle

```matlab
function length=circle_arc_length(theta_start, theta_end, R_start,...
                                  R_end, xcenter, ycenter, R, direction)
%CIRCLE_ARC_LENGTH
%Computes the length of a specific arc of circle
%
% Syntax:  length=circle_arc_length(theta_start, theta_end, R_start,...
%                                   R_end, xcenter, ycenter, R, direction)
%
% Inputs:
%    - theta_start + R_start: polar coordinates of the starting point of
%      the arc in the main referential
%    - theta_end + R_end: polar coordinates of the ending point of the arc
%      in the main referential
%    - xcenter: x coordinate of the center of the circle on which to
%      measure the arc length
%    - ycenter: y coordinate of the center of the circle on which to
%      measure the arc length
%    - R: radius of the circle on which to measure the arc length
%    - direction: 'clockwise' or 'anticlockwise'
%
% Outputs:
%    - length: length of the arc measured
%
% Example:
%    length_pt24_pt25=circle_arc_length(theta_pt24, theta_pt25, R_pt24,...
%                                       R_pt25, x2, y2, Wt/2, 'clockwise');
%    length_pt22_pt23=circle_arc_length(theta_pt22, theta_pt23, R_pt22,...
%                                       R_pt23, x1, y1, Wt/2,...
%                                       'anticlockwise');
%
% Other m-files required: none
% Subfunctions: none
% MAT-files required: none
%
% See also: none
% Author: Matthieu Ruegg
% Work address: EPFL, STI, IMT, LMIS1
% email: matthieu.ruegg@gmail.com
% Website: http://www.lmis1.epfl.ch
% January 2017; Last revision: 15-March-2019

%Need to reposition the circle if center is not (0,0)
if xcenter≠0 || ycenter≠0
    %Shift circle to (0,0)
    xstart=R_start*cos(theta_start)-xcenter;
    ystart=R_start*sin(theta_start)-ycenter;
    xend=R_end*cos(theta_end)-xcenter;
    yend=R_end*sin(theta_end)-ycenter;

```

```matlab
50      %Compute new values of theta_start and theta_end
51      theta_start=atan(ystart/xstart);
52      theta_end=atan(yend/xend);
53
54      %Correction depending on in which quadrant is the point
55      if xstart<0 %2nd and 3rd quadrant
56          theta_start=theta_start+pi;
57      elseif ystart<0 %4th quadrant
58          theta_start=theta_start+2*pi;
59      end
60      if xend<0 %2nd and 3rd quadrant
61          theta_end=theta_end+pi;
62      elseif yend<0 %4th quadrant
63          theta_end=theta_end+2*pi;
64      end
65  end
66
67  %Compute angle for the arc from theta_start to theta_end
68  if strcmp(direction,'anticlockwise')
69      if theta_end==theta_start
70          angle=0;
71      %If end angle is between start angle and 2pi
72      elseif theta_end>theta_start
73          angle=theta_end-theta_start;
74      else    %If end angle is between 0 and start angle
75          angle=2*pi-(theta_start-theta_end);
76      end
77  end
78  if strcmp(direction,'clockwise')
79      if theta_end==theta_start
80          angle=0;
81      %If end angle is between 0 and start angle
82      elseif theta_end<theta_start
83          angle=theta_start-theta_end;
84      else %If end angle is between start angle and 2pi
85          angle=2*pi-(theta_end-theta_start);
86      end
87  end
88
89  length=R*angle;
90
91  end
```

Correction factor P for the inductance computation

```matlab
1  function [p] = P_factor_inductance(Rnorm)
2  %P_FACTOR_INDUCTANCE
3  %This function interpolates the P value for the computation of a disc
4  %coil inductance using table 26 p.113 in Grover, Inductance Calculations:
```

```matlab
5   %Working Formulas and Tables, 1946. Interpolation is performed using a 2nd
6   %degree polynomial
7   %
8   % Syntax: [p] = P_factor_inductance(Rnorm,thick_norm)
9   %
10  % Inputs:
11  %    - Rnorm: normalized radius c/2a in Grover 1946
12  %
13  % Ouputs:
14  %    - p = interpolated p value for Rnorm
15  %
16  % Examples: none
17  %
18  % Other m-files required: none
19  % Subfunctions: none
20  % MAT-files required: P.mat
21  %
22  % See also: compute_coil_model_v4
23  % Author: Matthieu Ruegg
24  % Work address: EPFL, STI, IMT, LMIS1
25  % email: matthieu.ruegg@gmail.com
26  % Website: http://www.lmis1.epfl.ch
27  % October 2016; Last revision: 31-March-2019
28  %
29  %Edit:
30  %MR 13.10.2016: added exceptions for Rnorm=0.01 and Rnorm=1
31
32  %Table containting values from table 26 (p.113) in Grover, Inductance
33  %Calculations: Working Formulas and Tables, 1946
34  load('P.mat');
35  p=P(1,2); %P value for Rnorm = 0.01
36
37  if(disp_flag);
38      handle_P=figure;
39      set(gcf,'WindowStyle', 'docked');
40      plot(P(:,1),P(:,2),'+'); %Plot P values table
41  end
42
43  [Min,Ind]=min(abs(P(:,1)-Rnorm)); %Find closest point from Rnorm in P
44  Ind=[Ind-1 Ind Ind+1]; %Take the three closest points
45  if Ind(1)==0
46      %If Rnorm=0.01 => it's closest to the first point of the vector =>
47      %there is no previous point
48      Ind=Ind+1;
49  elseif Ind(3)==101
50      %If Rnorm=1 => it's closest to the last point of the vector =>
51      %there is no next point
52      Ind=Ind-1;
53  end
54  coeff=polyfit(P(Ind,1),P(Ind,2),2);
55  p=polyval(coeff,Rnorm);
```

Correction factor F for the inductance computation

```matlab
1  function [f] = F_factor_inductance(Rnorm,thick_norm)
2  %F_FACTOR_INDUCTANCE
3  %This function interpolates the F value for the computation of a disc
4  %coil inductance using table 26 p.113 in Grover, Inductance Calculations:
5  %Working Formulas and Tables, 1946.
6  %
7  % Syntax: [f] = F_factor_inductance(Rnorm,thick_norm)
8  %
9  % Inputs:
10 %    - Rnorm: normalized radius c/2a in Grover 1946
11 %    - thick_norm = normalized thickness b/c in Grover 1946
12 %
13 % Ouputs:
14 %    - f = interpolated f value for Rnorm
15 %
16 % Examples: none
17 %
18 % Other m-files required: none
19 % Subfunctions: none
20 % MAT-files required: F.mat
21 %
22 % See also: compute_coil_model_v4
23 % Author: Matthieu Ruegg
24 % Work address: EPFL, STI, IMT, LMIS1
25 % email: matthieu.ruegg@gmail.com
26 % Website: http://www.lmis1.epfl.ch
27 % October 2016; Last revision: 31-March-2019
28
29 %Table containting values from table 24 (p.108) in Grover, Inductance
30 %Calculations: Working Formulas and Tables, 1946.
31 load('F.mat');
32 f=1; %F value for a coil where h/c=0
33
34 %Find closest point from thick_norm in F
35 [Min_line,Ind_line]=min(abs(F(2:end,1)-thick_norm));
36 %Find closest point from Rnorm in F
37 [Min_col,Ind_col]=min(abs(F(1,2:end)-Rnorm));
38
39 Ind_line=Ind_line+1; %Because first line is values of Rnorm
40 Ind_col=Ind_col+1; %Because first column is values of thick_norm
41 f=F(Ind_line,Ind_col);
```

B Full comparison of the resonance between models and experimental data

Tables B.1 and B.2 compare the resonance frequencies and quality factors values measured experimentally, with the values computed by FEM simulations or with the analytical model. Several resonator geometries, in multiple media and configuration are considered. The media and orientation description is similar to that given in Figure 2.25 and Table 2.5 in Section 2.5.3. The geometries of the resonators used in Tables B.1 and B.2 are described in Table B.3.

Table B.1 – **Full comparison between experimental data and models - Part 1.** Comparison of the resonance frequencies and Q factors measured experimentally, computed by FEM simulation and with the analytical model, in several media and orientations for multiple resonator geometries. Resonator geometries are described in Table B.3. For the analytical model, there is no difference between the up and down configurations, since it doesn't take into account the distance between the CPW and the resonator, as explained in Section 2.3.4. This table contains only resonators without a meander hot-spot.

SR #	Medium and orientation	f_0 [GHz]			Q		
		Measured	FEM	Anal.	Measured	FEM	Anal.
	SRs 117 to 119 are resonators without meander, with two different track width, two different gap and all the same diameter						
117	In air, down	2.78	2.74	2.78	13	N.A.	7
	In air, up	2.63	2.58		16	N.A.	
	In air with Parylene, down	2.54	2.50	2.67	14	N.A.	7
	In air with Parylene, up	N.A.	2.47		N.A.	N.A.	
	In water with Parylene, down	1.64	1.34	0.89	9	N.A.	3
	In water with Parylene, up	1.57	1.30		N.A.	N.A.	
	In water no Parylene, up	N.A.	N.A.	0.78	N.A.	N.A.	2
118	In air, down	N.A.	3.00	3.07	N.A.	N.A.	8
	In air, up	N.A.	2.84		N.A.	N.A.	
	In air with Parylene, down	2.77	2.80	2.99	12	N.A.	8
	In air with Parylene, up	N.A.	2.75		N.A.	N.A.	
	In water with Parylene, down	1.64	1.39	0.97	11	N.A.	3
	In water with Parylene, up	N.A.	1.35		N.A.	N.A.	
	In water no Parylene, up	N.A.	N.A.	0.88	N.A.	N.A.	3
119	In air, down	3.13	3.12	3.12	15	19	13
	In air, up	2.93	2.92		17	21	
	In air with Parylene, down	2.85	2.87	3.03	18	19	13
	In air with Parylene, up	2.80	2.81		19	20	
	In water with Parylene, down	1.63	1.38	0.97	10	6	5
	In water with Parylene, up	1.57	1.33		10	7	
	In water no Parylene, up	N.A.	0.85	0.87	N.A.	4	4
120	In air, down	3.31	3.40	3.41	16	N.A.	14
	In air, up	N.A.	3.18		N.A.	N.A.	
	In air with Parylene, down	3.13	3.16	3.34	18	N.A.	13
	In air with Parylene, up	N.A.	3.10		N.A.	N.A.	
	In water with Parylene, down	1.64	1.42	1.04	13	N.A.	5
	In water with Parylene, up	N.A.	1.37		N.A.	N.A.	
	In water no Parylene, up	N.A.	N.A.	0.97	N.A.	N.A.	5

Table B.2 – **Full comparison between experimental data and models - Part 2.** Comparison of the resonance frequencies and Q factors measured experimentally, computed by FEM simulation and with the analytical model, in several media and orientations for multiple resonator geometries. Resonator geometries are described in Table B.3. For the analytical model, there is no difference between the up and down configurations, since it doesn't take into account the distance between the CPW and the resonator, as explained in Section 2.3.4. This table contains resonators with a meander hot-spot.

| SR # | Medium and orientation | f_0 [GHz] | | | Q | | |
		Measured	FEM	Anal.	Measured	FEM	Anal.
	SRs 53 to 56 have the same R, W and G as SR 119 but they have different meander shapes						
119	In air, down	3.13	3.12	3.12	15	19	13
	In air with Parylene, down	2.85	2.87	3.03	18	19	13
	In water with Parylene, down	1.63	1.38	0.97	10	6	5
53	In air, down	3.18	N.A.	3.13	8	N.A.	12
	In air with Parylene, down	2.86	N.A.	3.04	16	N.A.	11
	In water with Parylene, down	1.6	N.A.	0.97	8	N.A.	4
54	In air, down	3.05	N.A.	3.13	11	N.A.	9
	In air with Parylene, down	2.82	N.A.	3.05	12	N.A.	8
	In water with Parylene, down	1.55	N.A.	0.97	9	N.A.	3
55	In air, down	3.13	3.08	3.13	13	16	12
	In air with Parylene, down	2.89	2.84	3.05	16	16	11
	In water with Parylene, down	1.59	1.37	0.97	10	6	4
56	In air, down	3.01	N.A.	3.16	11	N.A.	8
	In air with Parylene, down	2.79	N.A.	3.07	14	N.A.	8
	In water with Parylene, down	1.55	N.A.	0.98	5	N.A.	3

Table B.3 – **Resonator geometries for the full comparison between experimental data and models.** Geometrical parameters of the resonators used in Tables B.1 and B.2. For all the SRs, $W_o = 115\,\mu$m.

SR #	R [μm]	W [μm]	G [μm]	T [μm]	W_m [μm]	L_m [μm]	N_m
53	1280	160	10	2	20	30	1
54	1280	160	10	2	20	30	3
55	1280	160	10	2	20	50	1
56	1280	160	10	2	20	50	3
117	1280	80	10	2	-	-	-
118	1280	80	20	2	-	-	-
119	1280	160	10	2	-	-	-
120	1280	160	20	2	-	-	-

C Dimensions of the resonators used in Section 2.7

Table C.1 – **Geometries of the resonators used in Section 2.7.** Geometrical parameters plus measured f_0 and Q values of the resonators used for the wireless and DC heating experiments. The resonance frequency and Q factor are not available for the last five lines since the structures are not resonators but standalone meanders with contact pads as shown in Figure 2.36. For all the SRs, $W_o = 115\,\mu m$.

Figure reference	R [µm]	W [µm]	G [µm]	T [µm]	W_m [µm]	L_m [µm]	N_m	f_0 [GHz]	Q
Figure 2.37, top	1528	120	15	2	15	40	2	2.54	10
Figure 2.37, bottom	1000	120	15	2	15	40	2	2.18	8
Figure 2.38	1280	160	10	2	20	50	3	2.93	11
Figure 2.39, top	1528	120	15	2	15	40	2	2.54	10
Figure 2.39, bottom	1000	45	15	2	15	40	2	3.84	13
Figure 2.40, water	1000	120	15	2	15	40	2	2.18	8
Figure 2.40, air	1280	160	10	2	20	50	3	2.93	11
Figure 2.41	1280	80	10	2	20	30	3	2.83	11
Figure 2.42, green	-	160	-	2	10	50	3	-	-
Figure 2.42, red	-	80	-	2	20	50	3	-	-
Figure 2.42, cyan	-	80	-	2	10	50	3	-	-
Figure 2.42, black	-	80	-	2	10	30	3	-	-
Figure 2.42, pink	-	80	-	2	10	50	1	-	-

D Temperature of the meander hot-spot
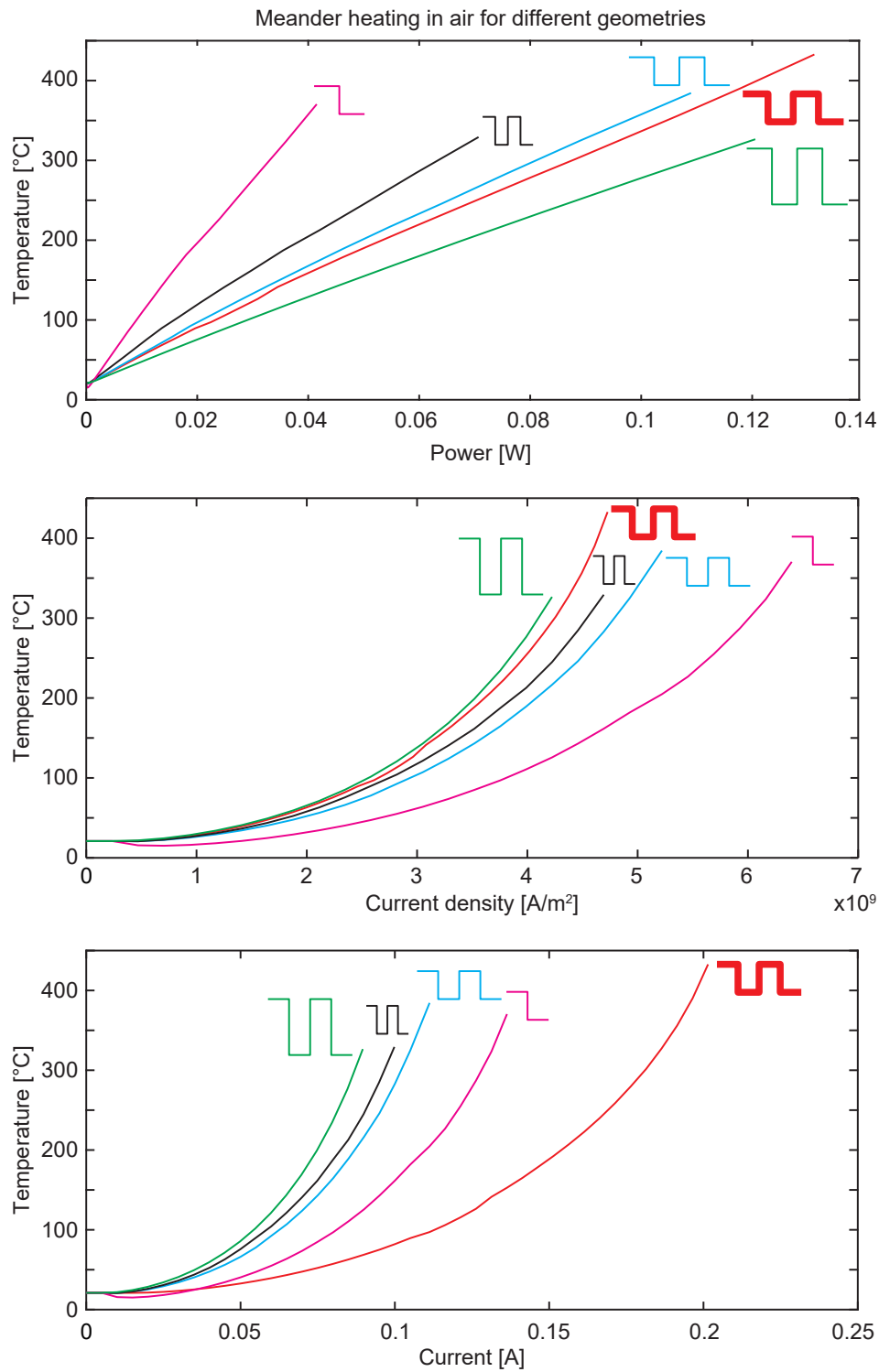
Figure D.1 – **Temperature of the meander hot-spot - Full study.** Meander heating analysis in air. Average temperature of different meander geometries as a function of the DC power, the current density and the current applied through the meander with a four-point-probes setup. The dimensions of the meanders are given in Appendix C.

E Optimization of the power dissipated in the meander hot-spot

Geometrical errors   When checking the validity of a resonator geometry, five error types can occur and are described hereafter, with the mathematical equation used to detect the error and the error message displayed.

1. If $(N_t \cdot (W + G) - G)/(2 \cdot (R - (N_t \cdot (W + G) - G)/2)) < 0.01$, the normalized radius is too small for the P value table. This errors means the computation of the inductance is not possible because the geometry is out of the range of the lookup table describing the P correction factor used in Equation 2.16.

2. If $R - W_o < N_t \cdot (W + G)$, the value of N_t, W, W_o or G is too large for the current value of R. This error means the resonator radius is too small for the current track width and gap values.

3. If $W_o - G < W \cdot 69/100$, the opening between the two turns of the resonators is too small for the current value of W and G.

4. If $pass\_thick < h$, the thickness of the passivation layer is smaller than the thickness of the resonator.

5. The meander is too long and overlaps the junction between the two turns of the resonator. The condition to test this error is not trivial and requires to compute the exact location of the first point of the meander. It is therefore not detailed here. The detailed computation is given at lines 312 to 370 of the Matlab code given in Section SR length computation in Appendix A. The problem originates in the fact that the meander hot-spot is always located at the half of the length of the resonator.

Optimized geometries in air and in water   Tables E.1 and E.2 describe the optimized resonator geometries in terms of power dissipation in the meander (or in terms of quality factor for $N_m = 0$) in air and in water respectively. The detailed environmental parameters for these

two conditions are given in Table 3.2. The values of the resonance frequency, the power dissipated in the meander, the quality factor and the ratio of the electrical resistance of the meander divided by the total resistance of the resonator (R_m/R_{tot}) are also given. For each value of N_m, the resonator geometry is optimized for four resonance frequencies and the radius of the resonator is restricted to specific values in steps of 200 µm. The first 20 lines of the table depicts these conditions for $N_m = 0, 1, 2, 3, 4$. In the last four lines, the geometry is optimized for $N_m = 2$ without restricting the radius of the resonator to specific values. It is important to note that for the experiments performed in Sections 3.6 and 3.7, the membrane area is smaller than the area of the resonator. The values computed here are thus not comparable. The resonance frequency in air is lower in reality and the resonance frequency in water is higher in reality.

Table E.1 – **Optimized resonator geometries in air.** Geometries of 2 μm thick Mg resonators optimized on a 2 μm thick PI substrate in air. Each subset is for one value of N_m and optimized for four distinct resonance frequencies. The values of f_0, Q, P_m and R_m/R_{tot} are also given. In the first 20 lines of the table the radius of the resonator is restricted to specific values in steps of 200 μm for $N_m = 0, 1, 2, 3, 4$. In the last four lines, the geometry is optimized for $N_m = 2$ without restricting the radius of the resonator to specific values. For all the SRs, $W_o = 250$ μm.

SR #	R [μm]	W [μm]	G [μm]	W_m [μm]	L_m [μm]	N_m	f_0 [GHz]	Q	P_m [mW]	R_m/R_{tot}
1	2500	140	10	15	25	0	2.34	11	0	0.00
2	2300	160	10	15	25	0	2.64	13	0	0.00
3	2110	160	10	15	25	0	2.95	14	0	0.00
4	1910	130	10	15	25	0	3.24	13	0	0.00
5	2500	140	10	15	25	1	2.34	11	85	0.05
6	2300	160	10	15	25	1	2.65	12	123	0.07
7	2110	160	10	15	25	1	2.95	13	124	0.07
8	1910	130	10	15	25	1	3.24	12	71	0.06
9	2500	140	10	15	25	2	2.35	10	205	0.13
10	2310	160	10	15	25	2	2.63	11	281	0.17
11	2110	150	10	15	25	2	2.92	11	238	0.17
12	1920	130	10	15	25	2	3.22	11	167	0.15
13	2500	140	10	15	25	3	2.35	9	289	0.20
14	2310	160	10	15	25	3	2.63	10	377	0.26
15	2110	150	10	15	25	3	2.92	10	321	0.25
16	1920	130	10	15	25	3	3.23	10	231	0.22
17	2500	140	10	15	25	4	2.35	8	349	0.25
18	2310	160	10	15	25	4	2.64	9	434	0.33
19	2110	150	10	15	25	4	2.93	9	371	0.32
20	1920	130	10	15	25	4	3.23	9	274	0.28
21	2500	140	10	15	25	2	2.35	10	205	0.13
22	2500	280	10	15	25	2	2.64	12	889	0.38
23	2500	340	15	15	25	2	2.92	13	1264	0.47
24	2500	310	35	15	25	2	3.17	14	1358	0.43

Caption above table: Optimized for 2 μm thick Mg resonators on a 2 μm thick PI substrate in air, $B = 10$ μT

Appendix E. Optimization of the power dissipated in the meander hot-spot

Table E.2 – **Optimized resonator geometries in water.** Geometries of 2 µm thick Mg resonators optimized on a 2 µm thick PI substrate passivated with a 5 µm thick PI layer in water. Each subset is for one value of N_m and optimized for four distinct resonance frequencies. The values of f_0, Q, P_m and R_m/R_{tot} are also given. In the first 20 lines of the table the radius of the resonator is restricted to specific values in steps of 200 µm for $N_m = 0, 1, 2, 3, 4$. In the last four lines, the geometry is optimized for $N_m = 2$ without restricting the radius of the resonator to specific values. For all the SRs, $W_o = 250$ µm.

	Optimized for 2 µm thick Mg resonators on a 2 µm thick PI substrate passivated with a 5 µm thick PI layer in water, $B = 10$ µT									
SR #	R [µm]	W [µm]	G [µm]	W_m [µm]	L_m [µm]	N_m	f_0 [GHz]	Q	P_m [mW]	R_m/R_{tot}
1	2490	290	10	15	25	0	0.33	3	0	0.00
2	2200	340	15	15	25	0	0.42	4	0	0.00
3	1920	310	35	15	25	0	0.55	5	0	0.00
4	1640	310	35	15	25	0	0.70	5	0	0.00
5	2500	290	10	15	25	1	0.33	2	11	0.18
6	2220	340	15	15	25	1	0.42	3	16	0.26
7	1930	310	35	15	25	1	0.55	3	15	0.26
8	1660	310	35	15	25	1	0.69	4	15	0.29
9	2500	290	10	15	25	2	0.33	2	17	0.39
10	2220	310	35	15	25	2	0.45	2	22	0.46
11	1930	310	35	15	25	2	0.55	2	20	0.50
12	1660	280	55	15	25	2	0.71	3	18	0.50
13	2500	290	10	15	25	3	0.33	1	18	0.52
14	2220	280	55	15	25	3	0.47	2	23	0.54
15	1940	260	70	15	25	3	0.58	2	20	0.54
16	1660	260	70	15	25	3	0.73	2	18	0.59
17	2500	290	10	15	25	4	0.33	1	17	0.60
18	2220	280	55	15	25	4	0.47	1	22	0.62
19	1940	260	70	15	25	4	0.58	2	19	0.62
20	1660	260	70	15	25	4	0.73	2	16	0.66
21	2500	290	10	15	25	2	0.33	2	17	0.39
22	2370	310	35	15	25	2	0.41	2	23	0.44
23	1980	280	55	15	25	2	0.55	2	21	0.44
24	1690	280	55	15	25	2	0.70	2	19	0.49

F POMaC and PGS pre-polymers synthesis

In this appendix, the chemical synthesis of POMaC and PGS pre-polymers by polycondensation is detailed.

POMaC and PGS pre-polymers synthesis

Setup preparation

- Vacuum line or pump
- N$_2$ line or bottle
- 2 horizontal metal mounts
- 1 vertical metal mount
- 5 metal-silicone lab clamps for glassware
- 3-neck flask
- Dry hot plate for 3-neck flask
- Glass valve (#9) + yellow plastic clamp
- Silicone/rubber plug for 3-neck flask
- Condensation column + red plastic clamp
- Schlenk line + glass valves (#6, 7, 8)
- Cold trap glassware + Dewar flask + lift table + liquid N2 + 2 metal clamps
- L-shaped glass tube with valve (#4)
- Bubbler
- Orange hose for vacuum
- PTFE valves for vacuum (#1, 2)
- Transparent hose for water and N2
- Wheel flow meter for water (#10)
- Separatory funnel
- Rotavap
- 1,8 octanediol
- Citric acid
- Maleic anhydride
- 1,4-dioxane or THF or CPME
- Glycerol
- Sebacic acid

Courtesy of Clémentine Boutry
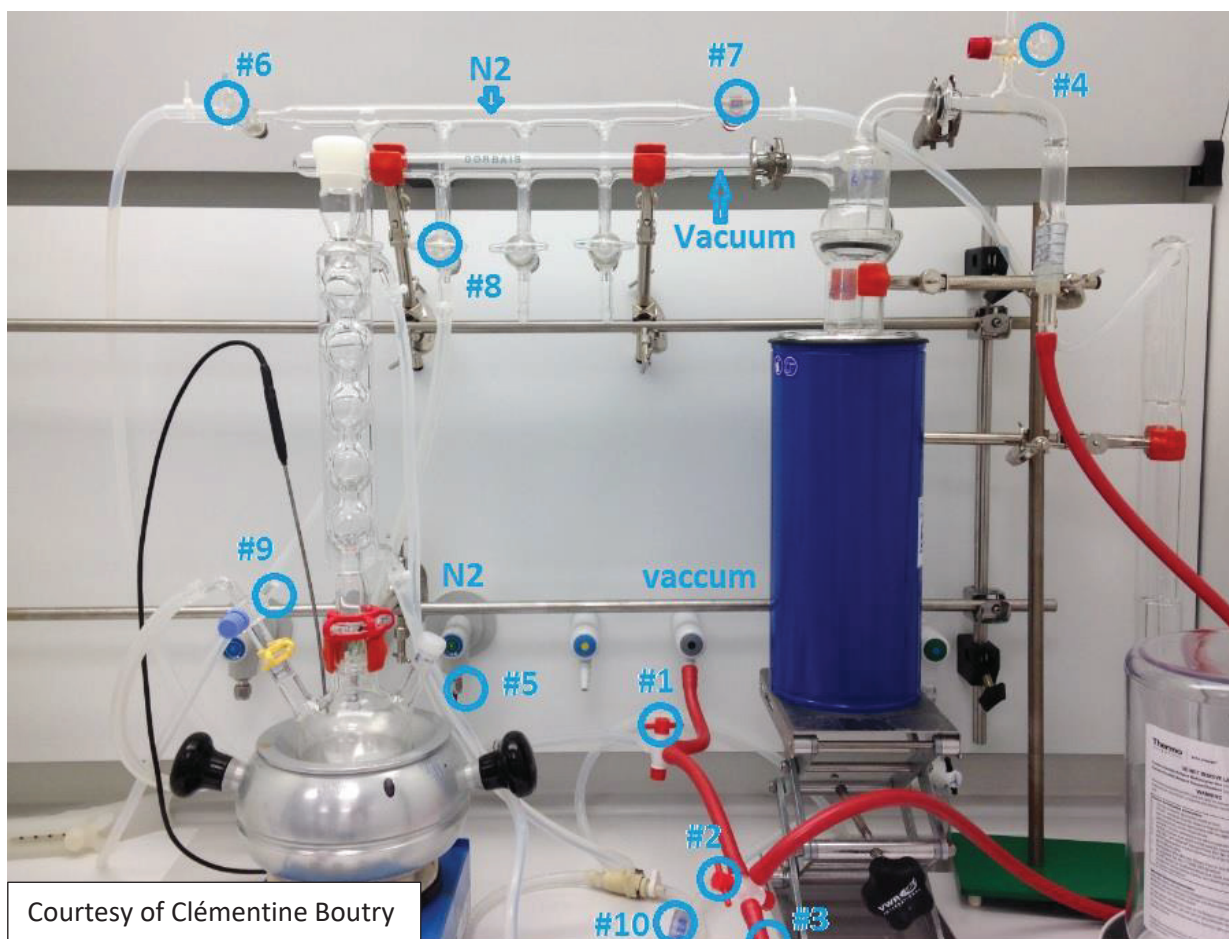
1. Close all the valves:
   a. Close #8 (all 4 valves, horizontal).
   b. Close #6 (vertical).
   c. #7 stays open (horizontal).

POMaC and PGS pre-polymer synthesis by polycondensation

        d. #4 always closed (horizontal).
2. Set vacuum valves:
        a. Close the access to the desiccator (#3, ask other users before).
        b. Valves #1, #2 closed.
3. Open N2:
        a. Open valve #6 (horizontal).
        b. Open N_2 (big black knob, first open the gray valve red-> green), look at flux, 3 bar ok.
        c. Regulate N_2 flux with valve #5 (wall)
        d. For the N_2-vacuum cycles, we need a high flux (lots of bubbles in the bubbler)..
4. Mounting of the 3 neck flask:
        a. Weight out reagents:
            i. POMaC: 1,8 octanediol, citric acid and maleic anhydride — at a molar ratio of 5:2:3:
                1. ___ g of 1,8 octanediol (molar mass: **146.23 g/mol**, ___ mol)
                2. ___ g of citric acid (molar mass: **192.12 g/mol**, ___ mol)
                3. ___ g of maleic anhydride (molar mass: **98.06 g/mol,** ___ mol)
            ii. PGS: sebacic acid and glycerol — at a molar ratio of 1:1:
                1. ___ g of sebacic acid (molar mass: **202.25 g/mol**, ___ mol)
                2. ___ g of glycerol (molar mass: **92.09 g/mol**, ___ mol)
        b. Pour all the chemicals + the magnetic bar in the flask.
        c. Close the 3rd neck with a rubber plug.
        d. Place the flask on the dry hot plate.
        e. Place the glass valve on the 1st neck, check that there is enough vacuum grease (the glass must become transparent), secure the valve with the yellow plastic clamp.
        f. Align the 2nd neck with the metal-silicone clamp (no closed yet, just finger pressed), place the column on top, check that there is enough vacuum grease (the glass must become transparent), secure the column with the red plastic clamp, close the metal-silicone clamp.
        g. The flask should be in good contact with the hotplate, the column should be vertical.
        h. Close valve #9.
5. Open the water:
        a. Big knob (below the 2nd hood), the blue wheel should turn (#10), but not too fast.
6. Preparation vaccum-N_2 cycles:
        a. At this point, the ramp is filled with N_2 → N_2 ok.
        b. Start the vacuum pump, open the big grey knob (below the 2nd hood).
        c. Check that valve #3 is closed, open valves #1 and #2.
        d. Check that the trap is sealed (black ring in the cold trap) → Vacuum ok.
        e. Verify that the N_2 flux is large enough to compensate for the vacuum suction in the bubbler when we will perform the vacuum-N_2 cycles.
7. Vaccum-N_2 cycles: connect the flask to vacuum → ok, **connect the flask to N_2 → be careful!**
        a. Open valve #8 (clockwise, up vertical) → the hose is now under vacuum.
        b. Open valve #9 (aligned with the hose) → the flask in under vacuum. Wait a bit.
        c. Close valve #9.
        d. Open #8 (anti-clockwise, up vertical) → the hose is now full of N_2.
        e. **Open valve #9 VERY SLOWLY:**
            i. Look at the bubbler. Quite large N_2 flux (the oil is white).
            ii. When we see that the bubbles decrease and that there are almost no more bubbles, wait until the bubbles come back in bubbler. The N_2 enter the flask, the vacuum goes out and we need to reach an equilibrium. The objective is to avoid having oil going up in the bubbler column. Open valve #9 fully. Wait 2-3 min to fill the flask with N_2.

   iii. If some oil goes up in the bubbler column, the problem is the air bubbles will go in the N_2 ramp. In such a case, we need to start from scratch the vacuum-N_2 process.

  f. Start again 3 times: close valve #9, open valve #8 (clockwise, up vertical), open valve #9 … stop when the flask is under N_2.

Melting and pre-polymerization

8. Start the heating:
  a. Start the dry hot plate:
   i. POMaC: start at 165°C and after melting go back to 140°C.
   ii. PGS: start at 150°C and after melting go back to 120°C.
  b. Start the magnetic stirring.
9. After melting the powders, create a flux of N_2 in the flask:
  a. Plug a needle (short pink large needle) through the silicon cap of the 3rd neck, leave valve #7 open (to continue bubbling), check that there is enough N_2 flux in the flask by placing a balloon at the needle output. It should inflate.
  b. Another option is to do the same as above, but close the valve #7. Then all the N_2 goes out through the needle.
10. Keep the reaction for:
  a. POMaC: 3h under a N_2 flux.
  b. PGS: 2h under a N_2 flux + 24-48h under vacuum.

Disconnecting the setup

11. At the end of the reaction, disconnect the setup to bring back everything to atmospheric pressure:
  a. Close the N_2 ramp: remove the needle from the 3rd neck, close valve #9, close valve #8, close the big N_2 knob. The bubbles slowly stop in the bubbler.
  b. Close the vacuum ramp: close valve #2, stop the pump, slowly open valve #4. Close it again for the next process.
  c. Stop the water (big knob).
  d. Disconnect the flask: open the metal-silicone clamp, remove the red clip, remove the column slowly, remove the yellow clip, remove the glass valve from the 1st neck, take the flask. That's it!

Pre-polymer purification (for POMaC only)

12. Allow cooling to room temperature. Then, add 1,4-dioxane (or THF or CMPE, which are less toxic and were found suitable for this step as well) into the flask to completely dissolve the POMaC pre-polymer.

13. Pour the dissolved pre-polymer into a separatory funnel and place it above a beaker filled with ddH2O. Purify the POMaC pre-polymer by dropwise precipitation. This is done at room temperature and at a rate of one drop/s. Slowly drip the POMaC solution into the beaker to ensure the separation of the low-molecular-weight monomer reactants from the higher-molecular-weight POMaC pre-polymer. High-molecular-weight POMaC pre-polymer precipitates at the bottom of the beaker and takes a white color.

14. Decant the water from the beaker and collect the precipitated POMaC pre-polymer from the bottom of the beaker.

Drying in rotavap (for POMaC only)

Courtesy of Clémentine Boutry
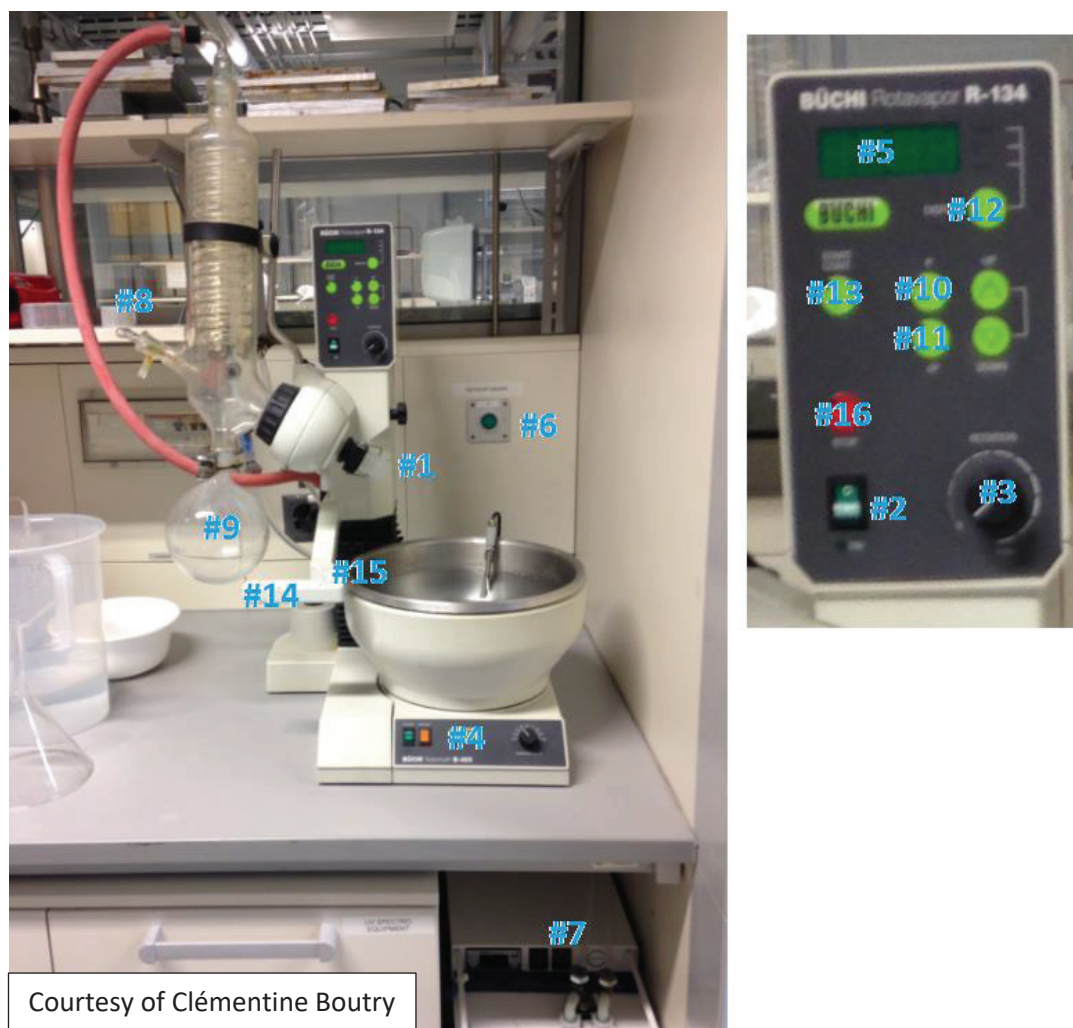
15. Start the rotavap:
    a. Fix the flask with the pre-polymer to dry on the rotavap: apply some vacuum grease to ensure a good vacuum (the glass should become transparent), and secure the setup with the screw (#1).
    b. Start the machine (#2), start the rotation (#3) (not too fast).
    c. Start heating the bath (#4) to a temperature between 40°C and 60°C. The temperature is displayed on the screen (#5).
    d. Start the vacuum pump (#6).
    e. Start the cooling liquid flow (#7). It's possible to change the temperature of the cooling liquid by pressing on "set" next to #7 (use arrows to regulate). 8°C-10°C is ok. Check on the blue wheel that the cooling liquid is indeed flowing. Check that there are no bubbles.
    f. The tap #8 should always been in a closed position (towards the user).
    g. Check that there is a balloon to collect the solvent (#9), and that it is empty.
    h. Apply vacuum (#10) (delta P is given by #11). We can navigate in the menu with #12. Start the vacuum by pressing on #13 (typically here 200 mbar).
    i. Bring the flask with the pre-polymer in the warm water (#14), take care that it doesn't touch the bath when in rotation (#15). It should touch the water, but not be completely immersed.

j. Check that we see the first droplets re-condensate in the solvent flask (#9) (to make sure that it doesn't go in the vacuum pump). In case of problems, for instance if no re-condensation occurs after 5-10min, it can be due to several things. 1) The vacuum is too strong. 2) There is a problem with the re-condensation, so we should check the temperature of the cooling liquid. 3) The combination pressure/temperature is too high, so we should decrease a bit the temperature or go back to room temperature and increase a bit the pressure. We MUST have re-condensation in the solvent flask (#9).

16. When the process is done, stop the rotavap:

a. Keep the rotation and the cooling water flux and stop the vacuum (#16). It goes back to atmospheric pressure.

b. Bring the flask up (#14).

c. Stop the rotation (#3), stop the heating (#4). We can let the flask cool down a little bit, then stop the cooling (#6). This stops the vacuum pump and the cooling liquid flux.

d. Detach the flask (#1), stop the rotavap (#2).

Bibliography

[1] G. D. Cha, D. Kang, J. Lee, and D.-H. Kim, "Bioresorbable Electronic Implants: History, Materials, Fabrication, Devices, and Clinical Applications," *Advanced Healthcare Materials*, vol. 8, no. 11, p. 1801660, 2019.

[2] M. W. Tibbitt, J. E. Dahlman, and R. Langer, "Emerging Frontiers in Drug Delivery," *Journal of the American Chemical Society*, vol. 138, no. 3, pp. 704–717, Jan. 2016.

[3] H. J. Lee, N. Choi, E.-S. Yoon, and I.-J. Cho, "MEMS devices for drug delivery," *Advanced Drug Delivery Reviews*, vol. 128, pp. 132–147, Mar. 2018.

[4] A. N. Khan, A. Ermakov, G. Sukhorukov, and Y. Hao, "Radio frequency controlled wireless drug delivery devices," *Applied Physics Reviews*, vol. 6, no. 4, p. 041301, Sep. 2019.

[5] A. C. Anselmo and S. Mitragotri, "An overview of clinical and commercial impact of drug delivery systems," *Journal of Controlled Release*, vol. 190, pp. 15–28, Sep. 2014.

[6] M. Bikram and J. L. West, "Thermo-responsive systems for controlled drug delivery," *Expert Opinion on Drug Delivery*, vol. 5, no. 10, pp. 1077–1091, Oct. 2008.

[7] S. D. Fitzpatrick, L. E. Fitzpatrick, A. Thakur, M. A. J. Mazumder, and H. Sheardown, "Temperature-sensitive polymers for drug delivery," *Expert Review of Medical Devices*, vol. 9, no. 4, pp. 339–351, Jul. 2012.

[8] Y.-J. Zhu and F. Chen, "pH-Responsive Drug-Delivery Systems," *Chemistry – An Asian Journal*, vol. 10, no. 2, pp. 284–305, 2015.

[9] G. Y. Kim, B. M. Tyler, M. M. Tupper, J. M. Karp, R. S. Langer, H. Brem, and M. J. Cima, "Resorbable polymer microchips releasing BCNU inhibit tumor growth in the rat 9L flank model," *Journal of Controlled Release*, vol. 123, no. 2, pp. 172–178, Nov. 2007.

[10] H. K. Makadia and S. J. Siegel, "Poly Lactic-co-Glycolic Acid (PLGA) as Biodegradable Controlled Drug Delivery Carrier," *Polymers*, vol. 3, no. 3, pp. 1377–1397, Sep. 2011.

[11] D. C. Hyun, "A Polymeric Bowl for Multi-Agent Delivery," *Macromolecular Rapid Communications*, vol. 36, no. 16, pp. 1498–1504, Aug. 2015.

Bibliography

[12] J. Hanuš, M. Ullrich, J. Dohnal, M. Singh, and F. Štěpánek, "Remotely Controlled Diffusion from Magnetic Liposome Microgels," *Langmuir*, vol. 29, no. 13, pp. 4381–4387, Apr. 2013.

[13] M. Beccani, G. Aiello, N. Gkotsis, H. Tunc, A. Taddese, E. Susilo, P. Völgyesi, Á. Lédeczi, E. D. Momi, and P. Valdastri, "Component based design of a drug delivery capsule robot," *Sensors and Actuators A: Physical*, vol. 245, pp. 180–188, Jul. 2016.

[14] A. Shademani, H. Zhang, J. K. Jackson, and M. Chiao, "Active Regulation of On-Demand Drug Delivery by Magnetically Triggerable Microspouters," *Advanced Functional Materials*, vol. 27, no. 6, p. 1604558, Feb. 2017.

[15] M. Raoof, B. T. Cisneros, A. Guven, S. Phounsavath, S. J. Corr, L. J. Wilson, and S. A. Curley, "Remotely triggered cisplatin release from carbon nanocapsules by radiofrequency fields," *Biomaterials*, vol. 34, no. 7, pp. 1862–1869, Feb. 2013.

[16] M. Nafea, A. Nawabjan, and M. S. Mohamed Ali, "A wirelessly-controlled piezoelectric microvalve for regulated drug delivery," *Sensors and Actuators A: Physical*, vol. 279, pp. 191–203, Aug. 2018.

[17] H. R. Cheong, N.-T. Nguyen, M. K. Khaw, B. Y. Teoh, and P. S. Chee, "Wirelessly activated device with an integrated ionic polymer metal composite (IPMC) cantilever valve for targeted drug delivery," *Lab on a Chip*, vol. 18, no. 20, pp. 3207–3215, Oct. 2018.

[18] J. T. Santini, M. J. Cima, and R. Langer, "A controlled-release microchip," *Nature*, vol. 397, no. 6717, pp. 335–338, Jan. 1999.

[19] H.-K. A. Tsai, E. A. Moschou, S. Daunert, M. Madou, and L. Kulinsky, "Integrating Biosensors and Drug Delivery: A Step Closer Toward Scalable Responsive Drug-Delivery Systems," *Advanced Materials*, vol. 21, no. 6, pp. 656–660, Feb. 2009.

[20] P.-Y. Li, R. Sheybani, C. A. Gutierrez, J. T. W. Kuo, and E. Meng, "A Parylene Bellows Electrochemical Actuator," *Journal of Microelectromechanical Systems*, vol. 19, no. 1, pp. 215–228, Feb. 2010.

[21] J. M. Maloney, S. A. Uhland, B. F. Polito, N. F. Sheppard Jr., C. M. Pelta, and J. T. Santini Jr., "Electrothermally activated microchips for implantable drug delivery and biosensing," *Journal of Controlled Release*, vol. 109, no. 1–3, pp. 244–255, Dec. 2005.

[22] N. M. Elman, H. L. Ho Duc, and M. J. Cima, "An implantable MEMS drug delivery device for rapid delivery in ambulatory emergency care," *Biomedical Microdevices*, vol. 11, no. 3, pp. 625–631, Jun. 2009.

[23] Y.-J. Huang, H.-H. Liao, P.-L. Huang, T. Wang, Y.-J. Yang, Y.-H. Wang, and S.-S. Lu, "An Implantable Release-on-Demand CMOS Drug Delivery SoC Using Electrothermal Activation Technique," *ACM Journal on Emerging Technologies in Computing Systems (JETC)*, vol. 8, no. 2, pp. 12:1–12:22, Jun. 2012.

[24] J.-W. Jeong, J. G. McCall, G. Shin, Y. Zhang, R. Al-Hasani, M. Kim, S. Li, J. Y. Sim, K.-I. Jang, Y. Shi, D. Y. Hong, Y. Liu, G. P. Schmitz, L. Xia, Z. He, P. Gamble, W. Z. Ray, Y. Huang, M. R. Bruchas, and J. A. Rogers, "Wireless Optofluidic Systems for Programmable In Vivo Pharmacology and Optogenetics," *Cell*, vol. 162, no. 3, pp. 662–674, Jul. 2015.

[25] W.-J. Jo, S.-K. Baek, and J.-H. Park, "A wireless actuating drug delivery system," *Journal of Micromechanics and Microengineering*, vol. 25, no. 4, p. 045014, Apr. 2015.

[26] B. P. Timko, M. Arruebo, S. A. Shankarappa, J. B. McAlvin, O. S. Okonkwo, B. Mizrahi, C. F. Stefanescu, L. Gomez, J. Zhu, A. Zhu, J. Santamaria, R. Langer, and D. S. Kohane, "Near-infrared–actuated devices for remotely controlled drug delivery," *Proceedings of the National Academy of Sciences*, vol. 111, no. 4, pp. 1349–1354, Jan. 2014.

[27] M. K. Gupta, F. Meng, B. N. Johnson, Y. L. Kong, L. Tian, Y.-W. Yeh, N. Masters, S. Singama-neni, and M. C. McAlpine, "3D Printed Programmable Release Capsules," *Nano Letters*, vol. 15, no. 8, pp. 5321–5329, Aug. 2015.

[28] D. Son, J. Lee, D. J. Lee, R. Ghaffari, S. Yun, S. J. Kim, J. E. Lee, H. R. Cho, S. Yoon, S. Yang, S. Lee, S. Qiao, D. Ling, S. Shin, J.-K. Song, J. Kim, T. Kim, H. Lee, J. Kim, M. Soh, N. Lee, C. S. Hwang, S. Nam, N. Lu, T. Hyeon, S. H. Choi, and D.-H. Kim, "Bioresorbable Electronic Stent Integrated with Therapeutic Nanoparticles for Endovascular Diseases," *ACS Nano*, vol. 9, no. 6, pp. 5937–5946, Jun. 2015.

[29] Y. Zhou, H. Ye, Y. Chen, R. Zhu, and L. Yin, "Photoresponsive Drug/Gene Delivery Systems," *Biomacromolecules*, vol. 19, no. 6, pp. 1840–1857, Jun. 2018.

[30] J. Kost, K. Leong, and R. Langer, "Ultrasound-enhanced polymer degradation and release of incorporated substances," *Proceedings of the National Academy of Sciences*, vol. 86, no. 20, pp. 7663–7666, Oct. 1989.

[31] S. Mitragotri, "Healing sound: The use of ultrasound in drug delivery and other ther-apeutic applications," *Nature Reviews Drug Discovery*, vol. 4, no. 3, pp. 255–260, Mar. 2005.

[32] F. Stewart, B. Cox, J. Vorstius, A. Verbeni, Y. Qiu, and S. Cochran, "Capsule-based ultrasound-mediated targeted gastrointestinal drug delivery," in *2015 IEEE International Ultrasonics Symposium (IUS)*, Oct. 2015, pp. 1–4.

[33] J.-H. Park, M. G. Allen, and M. R. Prausnitz, "Biodegradable polymer microneedles: Fabrication, mechanics and transdermal drug delivery," *Journal of Controlled Release*, vol. 104, no. 1, pp. 51–66, May 2005.

[34] A. S. Rzhevskiy, T. R. R. Singh, R. F. Donnelly, and Y. G. Anissimov, "Microneedles as the technique of drug delivery enhancement in diverse organs and tissues," *Journal of Controlled Release*, vol. 270, pp. 184–202, Jan. 2018.

[35] W. Li, R. N. Terry, J. Tang, M. R. Feng, S. P. Schwendeman, and M. R. Prausnitz, "Rapidly separable microneedle patch for the sustained release of a contraceptive," *Nature Biomedical Engineering*, vol. 3, no. 3, pp. 220–229, Mar. 2019.

[36] T. Tang, S. Smith, B. Flynn, J. Stevenson, A. Gundlach, H. Reekie, A. Murray, D. Renshaw, B. Dhillon, A. Ohtori, Y. Inoue, J. Terry, and A. Walton, "Implementation of wireless power transfer and communications for an implantable ocular drug delivery system," *IET Nanobiotechnology*, vol. 2, no. 3, pp. 72–79, Sep. 2008.

[37] R. Farra, N. F. Sheppard, L. McCabe, R. M. Neer, J. M. Anderson, J. T. Santini, M. J. Cima, and R. Langer, "First-in-Human Testing of a Wirelessly Controlled Drug Delivery Microchip," *Science Translational Medicine*, vol. 4, no. 122, pp. 122ra21–122ra21, Feb. 2012.

[38] S. Rahimi and K. Takahata, "A wireless implantable drug delivery device with hydrogel microvalves controlled by field-frequency tuning," in *2011 IEEE 24th International Conference on Micro Electro Mechanical Systems (MEMS)*, Jan. 2011, pp. 1019–1022.

[39] P. S. Chee, M. N. Minjal, P. L. Leow, and M. S. M. Ali, "Wireless powered thermo-pneumatic micropump using frequency-controlled heater," *Sensors and Actuators A: Physical*, vol. 233, pp. 1–8, Sep. 2015.

[40] J. Fong, Z. Xiao, and K. Takahata, "Wireless implantable chip with integrated nitinol-based pump for radio-controlled local drug delivery," *Lab on a Chip*, vol. 15, no. 4, pp. 1050–1058, Feb. 2015.

[41] Y. Yi, A. Zaher, O. Yassine, J. Kosel, and I. G. Foulds, "A remotely operated drug delivery system with an electrolytic pump and a thermo-responsive valve," *Biomicrofluidics*, vol. 9, no. 5, p. 052608, Jul. 2015.

[42] A. Cobo, R. Sheybani, H. Tu, and E. Meng, "A wireless implantable micropump for chronic drug infusion against cancer," *Sensors and Actuators A: Physical*, vol. 239, pp. 18–25, Mar. 2016.

[43] F. Forouzandeh, X. Zhu, A. Alfadhel, B. Ding, J. P. Walton, D. Cormier, R. D. Frisina, and D. A. Borkholder, "A nanoliter resolution implantable micropump for murine inner ear drug delivery," *Journal of Controlled Release*, vol. 298, pp. 27–37, Mar. 2019.

[44] R. Qazi, A. M. Gomez, D. C. Castro, Z. Zou, J. Y. Sim, Y. Xiong, J. Abdo, C. Y. Kim, A. Anderson, F. Lohner, S.-H. Byun, B. C. Lee, K.-I. Jang, J. Xiao, M. R. Bruchas, and J.-W. Jeong, "Wireless optofluidic brain probes for chronic neuropharmacology and photostimulation," *Nature Biomedical Engineering*, vol. 3, no. 8, pp. 655–669, Aug. 2019.

[45] C. Li, C. Guo, V. Fitzpatrick, A. Ibrahim, M. J. Zwierstra, P. Hanna, A. Lechtig, A. Nazarian, S. J. Lin, and D. L. Kaplan, "Design of biodegradable, implantable devices towards clinical translation," *Nature Reviews Materials*, vol. 5, no. 1, pp. 61–81, Jan. 2020.

[46] S. Oldreive, "Safe intakes of vitamins and minerals: Recommendations from the Expert Group on Vitamins and Minerals," *Nutrition Bulletin*, vol. 28, no. 2, pp. 199–202, 2003.

[47] Y. F. Zheng, X. N. Gu, and F. Witte, "Biodegradable metals," *Materials Science and Engineering: R: Reports*, vol. 77, no. Supplement C, pp. 1–34, Mar. 2014.

[48] J. Koo, M. R. MacEwan, S.-K. Kang, S. M. Won, M. Stephen, P. Gamble, Z. Xie, Y. Yan, Y.-Y. Chen, J. Shin, N. Birenbaum, S. Chung, S. B. Kim, J. Khalifeh, D. V. Harburg, K. Bean, M. Paskett, J. Kim, Z. S. Zohny, S. M. Lee, R. Zhang, K. Luo, B. Ji, A. Banks, H. M. Lee, Y. Huang, W. Z. Ray, and J. A. Rogers, "Wireless bioresorbable electronic system enables sustained nonpharmacological neuroregenerative therapy," *Nature Medicine*, vol. 24, no. 12, p. 1830, Dec. 2018.

[49] K. J. Yu, D. Kuzum, S.-W. Hwang, B. H. Kim, H. Juul, N. H. Kim, S. M. Won, K. Chiang, M. Trumpis, A. G. Richardson, H. Cheng, H. Fang, M. Thompson, H. Bink, D. Talos, K. J. Seo, H. N. Lee, S.-K. Kang, J.-H. Kim, J. Y. Lee, Y. Huang, F. E. Jensen, M. A. Dichter, T. H. Lucas, J. Viventi, B. Litt, and J. A. Rogers, "Bioresorbable silicon electronics for transient spatiotemporal mapping of electrical activity from the cerebral cortex," *Nature Materials*, vol. advance online publication, Apr. 2016.

[50] S.-K. Kang, R. K. J. Murphy, S.-W. Hwang, S. M. Lee, D. V. Harburg, N. A. Krueger, J. Shin, P. Gamble, H. Cheng, S. Yu, Z. Liu, J. G. McCall, M. Stephen, H. Ying, J. Kim, G. Park, R. C. Webb, C. H. Lee, S. Chung, D. S. Wie, A. D. Gujar, B. Vemulapalli, A. H. Kim, K.-M. Lee, J. Cheng, Y. Huang, S. H. Lee, P. V. Braun, W. Z. Ray, and J. A. Rogers, "Bioresorbable silicon electronic sensors for the brain," *Nature*, vol. 530, no. 7588, pp. 71–76, Feb. 2016.

[51] J. Shin, Y. Yan, W. Bai, Y. Xue, P. Gamble, L. Tian, I. Kandela, C. R. Haney, W. Spees, Y. Lee, M. Choi, J. Ko, H. Ryu, J.-K. Chang, M. Pezhouh, S.-K. Kang, S. M. Won, K. J. Yu, J. Zhao, Y. K. Lee, M. R. MacEwan, S.-K. Song, Y. Huang, W. Z. Ray, and J. A. Rogers, "Bioresorbable pressure sensors protected with thermally grown silicon dioxide for the monitoring of chronic diseases and healing processes," *Nature Biomedical Engineering*, vol. 3, no. 1, p. 37, Jan. 2019.

[52] D. Liu, J. Chen, T. Jiang, W. Li, Y. Huang, X. Lu, Z. Liu, W. Zhang, Z. Zhou, Q. Ding, H. A. Santos, G. Yin, and J. Fan, "Biodegradable Spheres Protect Traumatically Injured Spinal Cord by Alleviating the Glutamate-Induced Excitotoxicity," *Advanced Materials*, vol. 30, no. 14, p. 1706032, Apr. 2018.

[53] Q. Yang, S. Lee, Y. Xue, Y. Yan, T.-L. Liu, S.-K. Kang, Y. J. Lee, S. H. Lee, M.-H. Seo, D. Lu, J. Koo, M. R. MacEwan, R. T. Yin, W. Z. Ray, Y. Huang, and J. A. Rogers, "Materials, Mechanics Designs, and Bioresorbable Multisensor Platforms for Pressure Monitoring in the Intracranial Space," *Advanced Functional Materials*, vol. n/a, no. n/a, p. 1910718, 2020.

[54] A. Tamayol, A. H. Najafabadi, P. Mostafalu, A. K. Yetisen, M. Commotto, M. Aldhahri, M. S. Abdel-wahab, Z. I. Najafabadi, S. Latifi, M. Akbari, N. Annabi, S. H. Yun, A. Memic,

M. R. Dokmeci, and A. Khademhosseini, "Biodegradable elastic nanofibrous platforms with integrated flexible heaters for on-demand drug delivery," *Scientific Reports*, vol. 7, no. 1, p. 9220, Aug. 2017.

[55] H. Tao, S.-W. Hwang, B. Marelli, B. An, J. E. Moreau, M. Yang, M. A. Brenckle, S. Kim, D. L. Kaplan, J. A. Rogers, and F. G. Omenetto, "Silk-based resorbable electronic devices for remotely controlled therapy and in vivo infection abatement," *Proceedings of the National Academy of Sciences*, vol. 111, no. 49, pp. 17 385–17 389, Dec. 2014.

[56] C. M. Boutry, Y. Kaizawa, B. C. Schroeder, A. Chortos, A. Legrand, Z. Wang, J. Chang, P. Fox, and Z. Bao, "A stretchable and biodegradable strain and pressure sensor for orthopaedic application," *Nature Electronics*, vol. 1, no. 5, p. 314, May 2018.

[57] C. M. Boutry, L. Beker, Y. Kaizawa, C. Vassos, H. Tran, A. C. Hinckley, R. Pfattner, S. Niu, J. Li, J. Claverie, Z. Wang, J. Chang, P. M. Fox, and Z. Bao, "Biodegradable and flexible arterial-pulse sensor for the wireless monitoring of blood flow," *Nature Biomedical Engineering*, vol. 3, no. 1, pp. 47–57, Jan. 2019.

[58] S.-K. Kang, J. Koo, Y. K. Lee, and J. A. Rogers, "Advanced Materials and Devices for Bioresorbable Electronics," *Accounts of Chemical Research*, vol. 51, no. 5, pp. 988–998, May 2018.

[59] S.-W. Hwang, H. Tao, D.-H. Kim, H. Cheng, J.-K. Song, E. Rill, M. A. Brenckle, B. Panilaitis, S. M. Won, Y.-S. Kim, Y. M. Song, K. J. Yu, A. Ameen, R. Li, Y. Su, M. Yang, D. L. Kaplan, M. R. Zakin, M. J. Slepian, Y. Huang, F. G. Omenetto, and J. A. Rogers, "A Physically Transient Form of Silicon Electronics," *Science*, vol. 337, no. 6102, pp. 1640–1644, Sep. 2012.

[60] L. Hall-Stoodley, J. W. Costerton, and P. Stoodley, "Bacterial biofilms: From the Natural environment to infectious diseases," *Nature Reviews Microbiology*, vol. 2, no. 2, pp. 95–108, Feb. 2004.

[61] M. Maytin and L. M. Epstein, "Lead Extraction Is Preferred for Lead Revisions and System Upgrades: When Less Is More," *Circulation: Arrhythmia and Electrophysiology*, vol. 3, no. 4, pp. 413–424, Aug. 2010.

[62] J. Kzhyshkowska, A. Gudima, V. Riabov, C. Dollinger, P. Lavalle, and N. E. Vrana, "Macrophage responses to implants: Prospects for personalized medicine," *Journal of Leukocyte Biology*, vol. 98, no. 6, pp. 953–962, 2015.

[63] K. K. Fu, Z. Wang, J. Dai, M. Carter, and L. Hu, "Transient Electronics: Materials and Devices," *Chemistry of Materials*, vol. 28, no. 11, pp. 3527–3539, Jun. 2016.

[64] R. Li, L. Wang, D. Kong, and L. Yin, "Recent progress on biodegradable materials and transient electronics," *Bioactive Materials*, vol. 3, no. 3, pp. 322–333, Sep. 2018.

[65] S. Chatterjee, M. Saxena, D. Padmanabhan, M. Jayachandra, and H. J. Pandya, "Futuristic medical implants using bioresorbable materials and devices," *Biosensors and Bioelectronics*, vol. 142, p. 111489, Oct. 2019.

[66] C. H. Lee, H. Kim, D. V. Harburg, G. Park, Y. Ma, T. Pan, J. S. Kim, N. Y. Lee, B. H. Kim, K.-I. Jang, S.-K. Kang, Y. Huang, J. Kim, K.-M. Lee, C. Leal, and J. A. Rogers, "Biological lipid membranes for on-demand, wireless drug delivery from thin, bioresorbable electronic implants," *NPG Asia Materials*, vol. 7, no. 11, p. e227, Nov. 2015.

[67] J. Lee, H. R. Cho, G. D. Cha, H. Seo, S. Lee, C.-K. Park, J. W. Kim, S. Qiao, L. Wang, D. Kang, T. Kang, T. Ichikawa, J. Kim, H. Lee, W. Lee, S. Kim, S.-T. Lee, N. Lu, T. Hyeon, S. H. Choi, and D.-H. Kim, "Flexible, sticky, and biodegradable wireless device for drug delivery to brain tumors," *Nature Communications*, vol. 10, no. 1, p. 5205, Dec. 2019.

[68] P. Nadeau, D. El-Damak, D. Glettig, Y. L. Kong, S. Mo, C. Cleveland, L. Booth, N. Roxhed, R. Langer, A. P. Chandrakasan, and G. Traverso, "Prolonged energy harvesting for ingestible devices," *Nature Biomedical Engineering*, vol. 1, no. 3, pp. 1–8, Feb. 2017.

[69] M. S. M. Ali and K. Takahata, "Wireless microfluidic control with integrated shape-memory-alloy actuators operated by field frequency modulation," *Journal of Micromechanics and Microengineering*, vol. 21, no. 7, p. 075005, 2011.

[70] R. Sheybani, A. Cobo, and E. Meng, "Wireless programmable electrochemical drug delivery micropump with fully integrated electrochemical dosing sensors," *Biomedical Microdevices*, vol. 17, no. 4, pp. 1–13, Jul. 2015.

[71] Y. Zhang, A. D. Mickle, P. Gutruf, L. A. McIlvried, H. Guo, Y. Wu, J. P. Golden, Y. Xue, J. G. Grajales-Reyes, X. Wang, S. Krishnan, Y. Xie, D. Peng, C.-J. Su, F. Zhang, J. T. Reeder, S. K. Vogt, Y. Huang, J. A. Rogers, and R. W. Gereau, "Battery-free, fully implantable optofluidic cuff system for wireless optogenetic and pharmacological neuromodulation of peripheral nerves," *Science Advances*, vol. 5, no. 7, p. eaaw5296, Jul. 2019.

[72] R. Jegadeesan, K. Agarwal, Y.-X. Guo, S.-C. Yen, and N. V. Thakor, "Wireless Power Delivery to Flexible Subcutaneous Implants Using Capacitive Coupling," *IEEE Transactions on Microwave Theory and Techniques*, vol. 65, no. 1, pp. 280–292, Jan. 2017.

[73] J. S. Ho, A. J. Yeh, E. Neofytou, S. Kim, Y. Tanabe, B. Patlolla, R. E. Beygui, and A. S. Y. Poon, "Wireless power transfer to deep-tissue microimplants," *Proceedings of the National Academy of Sciences*, vol. 111, no. 22, pp. 7974–7979, Jun. 2014.

[74] D. R. Agrawal, Y. Tanabe, D. Weng, A. Ma, S. Hsu, S.-Y. Liao, Z. Zhen, Z.-Y. Zhu, C. Sun, Z. Dong, F. Yang, H. F. Tse, A. S. Y. Poon, and J. S. Ho, "Conformal phased surfaces for wireless powering of bioelectronic microdevices," *Nature Biomedical Engineering*, vol. 1, no. 3, pp. 1–9, Mar. 2017.

[75] K. N. Noh, S. I. Park, R. Qazi, Z. Zou, A. D. Mickle, J. G. Grajales-Reyes, K.-I. Jang, R. W. Gereau, J. Xiao, J. A. Rogers, and J.-W. Jeong, "Optofluidic Systems: Miniaturized, Battery-Free Optofluidic Systems with Potential for Wireless Pharmacology and Optogenetics (Small 4/2018)," *Small*, vol. 14, no. 4, p. 1870015, Jan. 2018.

[76] S. Ozeri and D. Shmilovitz, "Ultrasonic transcutaneous energy transfer for powering implanted devices," *Ultrasonics*, vol. 50, no. 6, pp. 556–566, May 2010.

[77] C. Dagdeviren, S.-W. Hwang, Y. Su, S. Kim, H. Cheng, O. Gur, R. Haney, F. G. Omenetto, Y. Huang, and J. A. Rogers, "Transient, Biocompatible Electronics and Energy Harvesters Based on ZnO," *Small*, vol. 9, no. 20, pp. 3398–3404, 2013.

[78] Q. Zheng, Y. Zou, Y. Zhang, Z. Liu, B. Shi, X. Wang, Y. Jin, H. Ouyang, Z. Li, and Z. L. Wang, "Biodegradable triboelectric nanogenerator as a life-time designed implantable power source," *Science Advances*, vol. 2, no. 3, p. e1501478, Mar. 2016.

[79] G. Lee, S.-K. Kang, S. M. Won, P. Gutruf, Y. R. Jeong, J. Koo, S.-S. Lee, J. A. Rogers, and J. S. Ha, "Fully Biodegradable Microsupercapacitor for Power Storage in Transient Electronics," *Advanced Energy Materials*, vol. 7, no. 18, p. 1700157, 2017.

[80] L. Yin, X. Huang, H. Xu, Y. Zhang, J. Lam, J. Cheng, and J. A. Rogers, "Materials, Designs, and Operational Characteristics for Fully Biodegradable Primary Batteries," *Advanced Materials*, vol. 26, no. 23, pp. 3879–3884, Jun. 2014.

[81] M. Tsang, A. Armutlulu, A. W. Martinez, S. A. B. Allen, and M. G. Allen, "Biodegradable magnesium/iron batteries with polycaprolactone encapsulation: A microfabricated power source for transient implantable devices," *Microsystems & Nanoengineering*, vol. 1, p. 15024, Oct. 2015.

[82] J. P. Esquivel, P. Alday, O. A. Ibrahim, B. Fernández, E. Kjeang, and N. Sabaté, "A Metal-Free and Biotically Degradable Battery for Portable Single-Use Applications," *Advanced Energy Materials*, vol. 7, no. 18, p. 1700275, 2017.

[83] X. Jia, C. Wang, V. Ranganathan, B. Napier, C. Yu, Y. Chao, M. Forsyth, F. G. Omenetto, D. R. MacFarlane, and G. G. Wallace, "A Biodegradable Thin-Film Magnesium Primary Battery Using Silk Fibroin–Ionic Liquid Polymer Electrolyte," *ACS Energy Letters*, vol. 2, no. 4, pp. 831–836, Apr. 2017.

[84] X. Huang, D. Wang, Z. Yuan, W. Xie, Y. Wu, R. Li, Y. Zhao, D. Luo, L. Cen, B. Chen, H. Wu, H. Xu, X. Sheng, M. Zhang, L. Zhao, and L. Yin, "A Fully Biodegradable Battery for Self-Powered Transient Implants," *Small*, vol. 14, no. 28, p. 1800994, 2018.

[85] D. She, M. Tsang, and M. Allen, "Biodegradable batteries with immobilized electrolyte for transient MEMS," *Biomedical Microdevices*, vol. 21, no. 1, p. 17, Feb. 2019.

[86] S.-K. Kang, G. Park, K. Kim, S.-W. Hwang, H. Cheng, J. Shin, S. Chung, M. Kim, L. Yin, J. C. Lee, K.-M. Lee, and J. A. Rogers, "Dissolution Chemistry and Biocompatibility of

Silicon- and Germanium-Based Semiconductors for Transient Electronics," *ACS Applied Materials & Interfaces*, vol. 7, no. 17, pp. 9297–9305, May 2015.

[87] L. Lu, Z. Yang, K. Meacham, C. Cvetkovic, E. A. Corbin, A. Vázquez-Guardado, M. Xue, L. Yin, J. Boroumand, G. Pakeltis, T. Sang, K. J. Yu, D. Chanda, R. Bashir, R. W. Gereau, X. Sheng, and J. A. Rogers, "Biodegradable Monocrystalline Silicon Photovoltaic Microcells as Power Supplies for Transient Biomedical Implants," *Advanced Energy Materials*, vol. 8, no. 16, p. 1703035, Jun. 2018.

[88] M. Luo, A. Martinez, C. Song, F. Herrault, and M. Allen, "A Microfabricated Wireless RF Pressure Sensor Made Completely of Biodegradable Materials," *Journal of Microelectromechanical Systems*, vol. 23, no. 1, pp. 4–13, Feb. 2014.

[89] C. Boutry, "Biodegradable Passive Resonant Circuits for Wireless Implant Applications," Ph.D. dissertation, ETHZ, 2012.

[90] B. Lenaerts and R. Puers, *Omnidirectional Inductive Powering for Biomedical Implants*, ser. Analog Circuits and Signal Processing. Dordrecht: Springer Netherlands, 2009.

[91] K. Agarwal, R. Jegadeesan, Y.-X. Guo, and N. V. Thakor, "Wireless Power Transfer Strategies for Implantable Bioelectronics," *IEEE Reviews in Biomedical Engineering*, vol. 10, pp. 136–161, 2017.

[92] "IEEE Standard for Safety Levels with Respect to Human Exposure to Radio Frequency Electromagnetic Fields, 3 kHz to 300 GHz," *IEEE Std C95.1-2005 (Revision of IEEE Std C95.1-1991)*, pp. 1–238, Apr. 2006.

[93] A. K. Skrivervik, M. Bosiljevac, and Z. Sipus, "Fundamental Limits for Implanted Antennas: Maximum Power Density Reaching Free Space," *IEEE Transactions on Antennas and Propagation*, vol. 67, no. 8, pp. 4978–4988, Aug. 2019.

[94] H. Jiang, J. Zhang, D. Lan, K. K. Chao, S. Liou, H. Shahnasser, R. Fechter, S. Hirose, M. Harrison, and S. Roy, "A Low-Frequency Versatile Wireless Power Transfer Technology for Biomedical Implants," *IEEE Transactions on Biomedical Circuits and Systems*, vol. 7, no. 4, pp. 526–535, Aug. 2013.

[95] R. Matthes and J. H. Bernhardt, Eds., *Guidelines on Limiting Exposure to Non-Ionizing Radiation: A Reference Book Based on the Guidelines on Limiting Exposure to Non-Ionizing Radiation and Statements on Special Applications*, ser. ICNIRP. Oberschleißheim: International Commission on Non-Ionizing Radiation Protection, 1999, no. 7.

[96] M. T. Vlaardingerbroek and J. A. den Boer, *Magnetic Resonance Imaging: Theory and Practice*, 2nd ed. Berlin Heidelberg: Springer-Verlag, 1999.

[97] C. Di Mario, H. Griffiths, O. Goktekin, N. Peeters, J. Verbist, M. Bosiers, K. Deloose, B. Heublein, R. Rohde, V. Kasese, C. Ilsley, and R. Erbel, "Drug-Eluting Bioabsorbable

Magnesium Stent," *Journal of Interventional Cardiology*, vol. 17, no. 6, pp. 391–395, 2004.

[98] R. Erbel, C. Di Mario, J. Bartunek, J. Bonnier, B. de Bruyne, F. R. Eberli, P. Erne, M. Haude, B. Heublein, M. Horrigan, C. Ilsley, D. Böse, J. Koolen, T. F. Lüscher, N. Weissman, and R. Waksman, "Temporary scaffolding of coronary arteries with bioabsorbable magnesium stents: A prospective, non-randomised multicentre trial," *The Lancet*, vol. 369, no. 9576, pp. 1869–1875, Jun. 2007.

[99] H. Hermawan, D. Dubé, and D. Mantovani, "Developments in metallic biodegradable stents," *Acta Biomaterialia*, vol. 6, no. 5, pp. 1693–1697, May 2010.

[100] L. Yin, H. Cheng, S. Mao, R. Haasch, Y. Liu, X. Xie, S.-W. Hwang, H. Jain, S.-K. Kang, Y. Su, R. Li, Y. Huang, and J. A. Rogers, "Dissolvable Metals for Transient Electronics," *Advanced Functional Materials*, vol. 24, no. 5, pp. 645–658, Feb. 2014.

[101] S.-W. Hwang, X. Huang, J.-H. Seo, J.-K. Song, S. Kim, S. Hage-Ali, H.-J. Chung, H. Tao, F. G. Omenetto, Z. Ma, and J. A. Rogers, "Materials for Bioresorbable Radio Frequency Electronics," *Advanced Materials*, vol. 25, no. 26, pp. 3526–3531, Jul. 2013.

[102] S. Zhang, X. Zhang, C. Zhao, J. Li, Y. Song, C. Xie, H. Tao, Y. Zhang, Y. He, Y. Jiang, and Y. Bian, "Research on an Mg–Zn alloy as a degradable biomaterial," *Acta Biomaterialia*, vol. 6, no. 2, pp. 626–640, Feb. 2010.

[103] W. Bai, J. Shin, R. Fu, I. Kandela, D. Lu, X. Ni, Y. Park, Z. Liu, T. Hang, D. Wu, Y. Liu, C. R. Haney, I. Stepien, Q. Yang, J. Zhao, K. R. Nandoliya, H. Zhang, X. Sheng, L. Yin, K. MacRenaris, A. Brikha, F. Aird, M. Pezhouh, J. Hornick, W. Zhou, and J. A. Rogers, "Bioresorbable photonic devices for the spectroscopic characterization of physiological status and neural activity," *Nature Biomedical Engineering*, vol. 3, no. 8, pp. 644–654, Aug. 2019.

[104] W. Bai, H. Yang, Y. Ma, H. Chen, J. Shin, Y. Liu, Q. Yang, I. Kandela, Z. Liu, S.-K. Kang, C. Wei, C. R. Haney, A. Brikha, X. Ge, X. Feng, P. V. Braun, Y. Huang, W. Zhou, and J. A. Rogers, "Flexible Transient Optical Waveguides and Surface-Wave Biosensors Constructed from Monocrystalline Silicon," *Advanced Materials*, vol. 30, no. 32, p. 1801584, 2018.

[105] H.-S. Kim, S. M. Yang, T.-M. Jang, N. Oh, H.-S. Kim, and S.-W. Hwang, "Bioresorbable Silicon Nanomembranes and Iron Catalyst Nanoparticles for Flexible, Transient Electrochemical Dopamine Monitors," *Advanced Healthcare Materials*, vol. 7, no. 24, p. 1801071, 2018.

[106] S.-K. Kang, S.-W. Hwang, H. Cheng, S. Yu, B. H. Kim, J.-H. Kim, Y. Huang, and J. A. Rogers, "Dissolution Behaviors and Applications of Silicon Oxides and Nitrides in Transient Electronics," *Advanced Functional Materials*, vol. 24, no. 28, pp. 4427–4434, 2014.

[107] S.-W. Hwang, D.-H. Kim, H. Tao, T.-i. Kim, S. Kim, K. J. Yu, B. Panilaitis, J.-W. Jeong, J.-K. Song, F. G. Omenetto, and J. A. Rogers, "Materials and Fabrication Processes for Transient and Bioresorbable High-Performance Electronics," *Advanced Functional Materials*, vol. 23, no. 33, pp. 4087–4093, Sep. 2013.

[108] M. A. Brenckle, H. Cheng, S. Hwang, H. Tao, M. Paquette, D. L. Kaplan, J. A. Rogers, Y. Huang, and F. G. Omenetto, "Modulated Degradation of Transient Electronic Devices through Multilayer Silk Fibroin Pockets," *ACS Applied Materials & Interfaces*, vol. 7, no. 36, pp. 19 870–19 875, Sep. 2015.

[109] S. Hofmann, C. T. Wong Po Foo, F. Rossetti, M. Textor, G. Vunjak-Novakovic, D. L. Kaplan, H. P. Merkle, and L. Meinel, "Silk fibroin as an organic polymer for controlled drug delivery," *Journal of Controlled Release*, vol. 111, no. 1–2, pp. 219–227, Mar. 2006.

[110] L. Uebersax, M. Mattotti, M. Papaloïzos, H. P. Merkle, B. Gander, and L. Meinel, "Silk fibroin matrices for the controlled release of nerve growth factor (NGF)," *Biomaterials*, vol. 28, no. 30, pp. 4449–4460, Oct. 2007.

[111] X.-S. Zhang, J. Brugger, and B. Kim, "A silk-fibroin-based transparent triboelectric generator suitable for autonomous sensor network," *Nano Energy*, vol. 20, pp. 37–47, Feb. 2016.

[112] H. Tao, J. M. Kainerstorfer, S. M. Siebert, E. M. Pritchard, A. Sassaroli, B. J. B. Panilaitis, M. A. Brenckle, J. J. Amsden, J. Levitt, S. Fantini, D. L. Kaplan, and F. G. Omenetto, "Implantable, multifunctional, bioresorbable optics," *Proceedings of the National Academy of Sciences of the United States of America*, vol. 109, no. 48, pp. 19 584–19 589, Nov. 2012.

[113] J.-K. Chang, H.-P. Chang, Q. Guo, J. Koo, C.-I. Wu, and J. A. Rogers, "Biodegradable Electronic Systems in 3D, Heterogeneously Integrated Formats," *Advanced Materials*, vol. 30, no. 11, p. 1704955, 2018.

[114] Y. K. Lee, J. Kim, Y. Kim, J. W. Kwak, Y. Yoon, and J. A. Rogers, "Room Temperature Electrochemical Sintering of Zn Microparticles and Its Use in Printable Conducting Inks for Bioresorbable Electronics," *Advanced Materials*, vol. 29, no. 38, p. 1702665, 2017.

[115] C. M. Boutry, A. Nguyen, Q. O. Lawal, A. Chortos, S. Rondeau-Gagné, and Z. Bao, "A Sensitive and Biodegradable Pressure Sensor Array for Cardiovascular Monitoring," *Advanced Materials*, vol. 27, no. 43, pp. 6954–6961, Nov. 2015.

[116] Z.-J. Sun, C. Chen, M.-Z. Sun, C.-H. Ai, X.-L. Lu, Y.-F. Zheng, B.-F. Yang, and D.-L. Dong, "The application of poly (glycerol–sebacate) as biodegradable drug carrier," *Biomaterials*, vol. 30, no. 28, pp. 5209–5214, Oct. 2009.

[117] G. C. J. Engelmayr, M. Cheng, C. J. Bettinger, J. T. Borenstein, R. Langer, and L. E. Freed, "Accordion-like honeycombs for tissue engineering of cardiac anisotropy," *Nature Materials*, vol. 7, no. 12, p. 1003, Dec. 2008.

Bibliography

[118] B. Zhang, M. Montgomery, M. D. Chamberlain, S. Ogawa, A. Korolj, A. Pahnke, L. A. Wells, S. Massé, J. Kim, L. Reis, A. Momen, S. S. Nunes, A. R. Wheeler, K. Nanthakumar, G. Keller, M. V. Sefton, and M. Radisic, "Biodegradable scaffold with built-in vasculature for organ-on-a-chip engineering and direct surgical anastomosis," *Nature Materials*, vol. 15, no. 6, pp. 669–678, Jun. 2016.

[119] M. Tsang, F. Herrault, R. Shafer, and M. Allen, "Methods for the microfabrication of magnesium," in *2013 IEEE 26th International Conference on Micro Electro Mechanical Systems (MEMS)*, Jan. 2013, pp. 347–350.

[120] S.-W. Hwang, S.-K. Kang, X. Huang, M. A. Brenckle, F. G. Omenetto, and J. A. Rogers, "Materials for Programmed, Functional Transformation in Transient Electronic Systems," *Advanced Materials*, vol. 27, no. 1, pp. 47–52, 2015.

[121] O. Vazquez-Mena, L. Gross, S. Xie, L. Villanueva, and J. Brugger, "Resistless nanofabrication by stencil lithography: A review," *Microelectronic Engineering*, vol. 132, pp. 236–254, Jan. 2015.

[122] S.-W. Hwang, J.-K. Song, X. Huang, H. Cheng, S.-K. Kang, B. H. Kim, J.-H. Kim, S. Yu, Y. Huang, and J. A. Rogers, "High-Performance Biodegradable/Transient Electronics on Biodegradable Polymers," *Advanced Materials*, vol. 26, no. 23, pp. 3905–3911, Jun. 2014.

[123] D. N. Rockwood, R. C. Preda, T. Yücel, X. Wang, M. L. Lovett, and D. L. Kaplan, "Materials fabrication from Bombyx mori silk fibroin," *Nature Protocols*, vol. 6, no. 10, pp. 1612–1631, Oct. 2011.

[124] J.-K. Chang, H. Fang, C. A. Bower, E. Song, X. Yu, and J. A. Rogers, "Materials and processing approaches for foundry-compatible transient electronics," *Proceedings of the National Academy of Sciences*, vol. 114, no. 28, pp. E5522–E5529, Jul. 2017.

[125] X. Huang, Y. Liu, S.-W. Hwang, S.-K. Kang, D. Patnaik, J. F. Cortes, and J. A. Rogers, "Biodegradable Materials for Multilayer Transient Printed Circuit Boards," *Advanced Materials*, vol. 26, no. 43, pp. 7371–7377, Nov. 2014.

[126] B. K. Mahajan, X. Yu, W. Shou, H. Pan, and X. Huang, "Mechanically Milled Irregular Zinc Nanoparticles for Printable Bioresorbable Electronics," *Small*, vol. 13, no. 17, p. 1700065, 2017.

[127] J. Baena, J. Bonache, F. Martin, R. Sillero, F. Falcone, T. Lopetegi, M. Laso, J. Garcia-Garcia, I. Gil, M. Portillo, and M. Sorolla, "Equivalent-circuit models for split-ring resonators and complementary split-ring resonators coupled to planar transmission lines," *IEEE Transactions on Microwave Theory and Techniques*, vol. 53, no. 4, pp. 1451–1461, Apr. 2005.

[128] C. M. Boutry, H. Chandrahalim, P. Streit, M. Schinhammer, A. C. Hänzi, and C. Hierold, "Characterization of miniaturized RLC resonators made of biodegradable materials for

wireless implant applications," *Sensors and Actuators A: Physical*, vol. 189, pp. 344–355, Jan. 2013.

[129] R. Marques, F. Mesa, J. Martel, and F. Medina, "Comparative analysis of edge- and broadside- coupled split ring resonators for metamaterial design - theory and experiments," *IEEE Transactions on Antennas and Propagation*, vol. 51, no. 10, pp. 2572–2581, Oct. 2003.

[130] F. W. Grover, *Inductance Calculations: Working Formulas and Tables.* Dover Phoenix Editions, 1946.

[131] Thompson, "Inductance Calculation Techniques — Part II: Approximations and Handbook Methods," *Power Control and Intelligent Motion*, vol. 25, no. 12, Dec. 1999.

[132] C. P. Wen, "Coplanar Waveguide: A Surface Strip Transmission Line Suitable for Nonreciprocal Gyromagnetic Device Applications," *IEEE Transactions on Microwave Theory and Techniques*, vol. 17, no. 12, pp. 1087–1090, Dec. 1969.

[133] V. Fouad Hanna, "Finite boundary corrections to coplanar stripline analysis," *Electronics Letters*, vol. 16, no. 15, pp. 604–606, Jul. 1980.

[134] G. Ghione and C. Naldi, "Analytical formulas for coplanar lines in hybrid and monolithic MICs," *Electronics Letters*, vol. 20, no. 4, pp. 179–181, Feb. 1984.

[135] I. Bahl and P. Bhartia, *Microwave Solid State Circuit Design*, 2nd ed. Wiley, 2003.

[136] E. Chen and S. Y. Chou, "Characteristics of coplanar transmission lines on multilayer substrates: Modeling and experiments," *IEEE Transactions on Microwave Theory and Techniques*, vol. 45, no. 6, pp. 939–945, Jun. 1997.

[137] S. E. Maxwell, H. D. Delaney, and K. Kelley, *Designing Experiments and Analyzing Data: A Model Comparison Perspective, Second Edition*, 2nd ed. Mahwah, N.J: Routledge, Jul. 2003.

[138] "Total Knee Replacement - OrthoInfo - AAOS," https://www.orthoinfo.org/en/treatment/total-knee-replacement/.

[139] "Synovial Joints | Anatomy and Physiology I," https://courses.lumenlearning.com/ap1/chapter/synovial-joints/.

[140] OECD (2019), "Health at a Glance 2019: OECD Indicators," *OECD Publishing, Paris*, pp. https://doi.org/10.1787/4dd50c09–en.

[141] L. Pulido, E. Ghanem, A. Joshi, J. J. Purtill, and J. Parvizi, "Periprosthetic joint infection: The incidence, timing, and predisposing factors," *Clinical Orthopaedics and Related Research*, vol. 466, no. 7, pp. 1710–1715, Jul. 2008.

[142] D. R. Kerr and L. Kohan, "Local infiltration analgesia: A technique for the control of acute postoperative pain following knee and hip surgery: A case study of 325 patients," *Acta Orthopaedica*, vol. 79, no. 2, pp. 174–183, Jan. 2008.

[143] F. Carli, A. Clemente, J. F. Asenjo, D. J. Kim, G. Mistraletti, M. Gomarasca, A. Morabito, and M. Tanzer, "Analgesia and functional outcome after total knee arthroplasty: Periarticular infiltration vs continuous femoral nerve block," *British Journal of Anaesthesia*, vol. 105, no. 2, pp. 185–195, Aug. 2010.

[144] R. Rikalainen-Salmi, J. G. Förster, K. Mäkelä, P. Virolainen, K. A. Leino, M. T. Pitkänen, P. J. Neuvonen, and K. S. Kuusniemi, "Local infiltration analgesia with levobupivacaine compared with intrathecal morphine in total hip arthroplasty patients," *Acta Anaesthesiologica Scandinavica*, vol. 56, no. 6, pp. 695–705, Jul. 2012.

[145] "Partial knee replacement vs total knee replacement," https://en.wikipedia.org/wiki/File:Pkrvstotalknee.jpg.

[146] S. Lacour, J. Jones, S. Wagner, T. Li, and Z. Suo, "Stretchable Interconnects for Elastic Electronic Surfaces," *Proceedings of the IEEE*, vol. 93, no. 8, pp. 1459–1467, Aug. 2005.

[147] A. Carlson, A. M. Bowen, Y. Huang, R. G. Nuzzo, and J. A. Rogers, "Transfer Printing Techniques for Materials Assembly and Micro/Nanodevice Fabrication," *Advanced Materials*, vol. 24, no. 39, pp. 5284–5318, 2012.

[148] J. C. Middleton and A. J. Tipton, "Synthetic biodegradable polymers as orthopedic devices," *Biomaterials*, vol. 21, no. 23, pp. 2335–2346, Dec. 2000.

[149] E. Chen, J. Novakofski, W. Jenkins, and W. O'Brien, "Young's modulus measurements of soft tissues with application to elasticity imaging," *IEEE Transactions on Ultrasonics, Ferroelectrics, and Frequency Control*, vol. 43, no. 1, pp. 191–194, Jan. 1996.

[150] P. Gentile, V. Chiono, I. Carmagnola, and P. V. Hatton, "An Overview of Poly(lactic-co-glycolic) Acid (PLGA)-Based Biomaterials for Bone Tissue Engineering," *International Journal of Molecular Sciences*, vol. 15, no. 3, pp. 3640–3659, Feb. 2014.

[151] Y. Wang, G. A. Ameer, B. J. Sheppard, and R. Langer, "A tough biodegradable elastomer," *Nature Biotechnology*, vol. 20, no. 6, pp. 602–606, Jun. 2002.

[152] R. T. Tran, P. Thevenot, D. Gyawali, J.-C. Chiao, L. Tang, and J. Yang, "Synthesis and characterization of a biodegradable elastomer featuring a dual crosslinking mechanism," *Soft Matter*, vol. 6, no. 11, pp. 2449–2461, May 2010.

[153] R. S. Petersen, R. Mahshid, N. K. Andersen, S. S. Keller, H. N. Hansen, and A. Boisen, "Hot embossing and mechanical punching of biodegradable microcontainers for oral drug delivery," *Microelectronic Engineering*, vol. 133, pp. 104–109, Feb. 2015.

[154] Z. Abid, S. Strindberg, M. M. Javed, C. Mazzoni, L. Vaut, L. H. Nielsen, C. Gundlach, R. S. Petersen, A. Müllertz, A. Boisen, and S. S. Keller, "Biodegradable microcontainers – towards real life applications of microfabricated systems for oral drug delivery," *Lab on a Chip*, vol. 19, no. 17, pp. 2905–2914, 2019.

[155] K.-W. Lee and Y. Wang, "Elastomeric PGS Scaffolds in Arterial Tissue Engineering," *Journal of Visualized Experiments : JoVE*, no. 50, Apr. 2011.

[156] C. J. Bettinger, B. Orrick, A. Misra, R. Langer, and J. T. Borenstein, "Microfabrication of poly (glycerol–sebacate) for contact guidance applications," *Biomaterials*, vol. 27, no. 12, pp. 2558–2565, Apr. 2006.

[157] H. N. Chia and B. M. Wu, "Recent advances in 3D printing of biomaterials," *Journal of Biological Engineering*, vol. 9, Mar. 2015.

[158] T. Guo, T. R. Holzberg, C. G. Lim, F. Gao, A. Gargava, J. E. Trachtenberg, A. G. Mikos, and J. P. Fisher, "3D printing PLGA: A quantitative examination of the effects of polymer composition and printing parameters on print resolution," *Biofabrication*, vol. 9, no. 2, p. 024101, 2017.

[159] A. V. Mironov, A. M. Grigoryev, L. I. Krotova, N. N. Skaletsky, V. K. Popov, and V. I. Sevastianov, "3D printing of PLGA scaffolds for tissue engineering," *Journal of Biomedical Materials Research Part A*, vol. 105, no. 1, pp. 104–109, Jan. 2017.

[160] L. Chen, L. Shao, F. Wang, Y. Huang, and F. Gao, "Enhancement in sustained release of antimicrobial peptide and BMP-2 from degradable three dimensional-printed PLGA scaffold for bone regeneration," *RSC Advances*, vol. 9, no. 19, pp. 10 494–10 507, Apr. 2019.

[161] Y.-C. Yeh, C. B. Highley, L. Ouyang, and J. A. Burdick, "3D printing of photocurable poly(glycerol sebacate) elastomers," *Biofabrication*, vol. 8, no. 4, p. 045004, 2016.

[162] Y.-C. Yeh, L. Ouyang, C. B. Highley, and J. A. Burdick, "Norbornene-modified poly(glycerol sebacate) as a photocurable and biodegradable elastomer," *Polymer Chemistry*, vol. 8, no. 34, pp. 5091–5099, Aug. 2017.

[163] F. Alexis, "Factors affecting the degradation and drug-release mechanism of poly(lactic acid) and poly[(lactic acid)-co-(glycolic acid)]," *Polymer International*, vol. 54, no. 1, pp. 36–46, Jan. 2005.

[164] R. Rai, M. Tallawi, J. A. Roether, R. Detsch, N. Barbani, E. Rosellini, J. Kaschta, D. W. Schubert, and A. R. Boccaccini, "Sterilization effects on the physical properties and cytotoxicity of poly(glycerol sebacate)," *Materials Letters*, vol. 105, pp. 32–35, Aug. 2013.

[165] P. Dolara, "Occurrence, exposure, effects, recommended intake and possible dietary use of selected trace compounds (aluminium, bismuth, cobalt, gold, lithium, nickel, silver)," *International Journal of Food Sciences and Nutrition*, vol. 65, no. 8, pp. 911–924, Dec. 2014.

MATTHIEU RÜEGG

PhD STUDENT IN BIOMEDICAL ENGINEERING

✉ matthieu.ruegg@gmail.com   ☎ +4179-673-0174   🌐 Swiss, French   ★ May 27, 1991
in linkedin.com/in/matthieuruegg   📍 Avenue du Mont d'Or 27, 1007 Lausanne, Switzerland

EDUCATION

PhD

Ecole Polytechnique Fédérale de Lausanne (EPFL)

📅 August 2015 – ongoing   📍 Lausanne, Switzerland

Thesis topic: Transient electronics for smart biodegradable medical implants.

- Development of a novel and innovative microfabrication process to manufacture biodegradable electronics made of water-soluble, temperature and solvent sensitive materials.
- Design and modeling of radio-frequency microresonators with specific resonance frequencies.
- Fabrication and integration of biodegradable microresonators as power receivers and microheaters for implantable transient medical devices.
- Supervision of eleven students projects and interns. Project leader in the development of a new massive open online course (MOOC) about microfabrication.
- Lectures about the management of innovation and technology transfer as well as in the field of medical devices regulations.

Master Thesis

Columbia University in the City of New York

📅 October 2014 – April 2015   📍 New York City, USA

- Design, assembly and testing of a portable fluorometer for glucose sensing.
- Low cost system compatible with consumer electronics and wearable devices.

M. Sc. in Micro- and Nanosystems & Minor in Biomedical Technologies

Ecole Polytechnique Fédérale de Lausanne (EPFL)

📅 September 2012 – April 2015   📍 Lausanne, Switzerland

- Modeling of the optical detector of a spectrometer for blood glucose analysis. In collaboration with the start-up Leman Micro Devices.
- Modification of an existing atomic force microscope (AFM) setup to measure the conductivity of single molecules.
- Design and fabrication of a system to handle magnetic beads inside a microfluidic chip.

B. Sc. in Microengineering

Ecole Polytechnique Fédérale de Lausanne (EPFL)

📅 September 2009 – July 2012   📍 Lausanne, Switzerland

- Located at the crossroads of mechanics, electronics, materials, and computer science, my job as a microengineer is to harness the physical laws which govern the miniaturization processes.

OBJECTIVE

In the past five years, I pursued a PhD where I developed fabrication processes and found solutions to engineer new types of smart implantable medical devices. I am now looking forward to draw upon the skills I acquired during that time by working in industrial research and development in the fields of medical devices and biomedical engineering.

STRENGTHS

Hard-working   Tenacious   Innovative
Resourceful   Systematic   Optimistic

SKILLS

Biomedical engineering:

biodegradable materials, drug delivery systems, implantable medical devices, glucose monitoring devices, immunoassays, cellular biology, physiology

Electronics:

microresonators, embedded electronics, RF electronics, finite element modeling, optical detectors, printed circuit board design, sensors, actuators, signal processing

Microfabrication:

AFM, SEM, PVD, ALD, UV photolithography, wet etching, dry etching, mechanical profilometry, ellipsometry, thermal scanning probe lithography, microfluidics, CMP

Soft skills:

creative thinking, innovation, problem solving, decision making, project management, oral and written communication

IT:

C language, ASM language, MATLAB, COMSOL, LabVIEW, Eagle, Autodesk Inventor, SolidWorks, LaTeX

WORK EXPERIENCE

Short Term Researcher
The University of Tokyo

📅 May 2015 – July 2015 📍 Tokyo, Japan

- Development and automation of a process to characterize the shape of 3D high aspect ratio nanostructures by atomic force microscopy (AFM).
- Unconventional AFM measurements without modifying the hardware of an existing setup and implementation of a reliable characterization process within three months.

Engineering Intern
IBM Research

📅 February 2014 – August 2014 📍 Rüschlikon, Switzerland

- Design and implementation of a new setup and process for high resolution polymer patterning by laser induced heating.
- Integration of the setup into an existing tool for nanoscale lithography which resulted in a commercial product called DLS laser writer.

Cleanroom Engineer
EPFL Center of MicroNano Technology

📅 January 2012 – December 2013 📍 Lausanne, Switzerland

- Optimization of microfabrication processes to improve results reliability and accuracy.
- Training and assistance to cleanroom users.
- Work at 20% in parallel of my studies.

PUBLICATIONS AND PATENTS

- M. Rüegg, C. Gonnelli, G. Boero, and J. Brugger, "A smart implantable capsule for on-demand wireless drug delivery," Manuscript in preparation.
- M. Rüegg, R. Blum, G. Boero, and J. Brugger, "Biodegradable Frequency-Selective Magnesium Radio-Frequency Microresonators for Transient Biomedical Implants," Adv. Funct. Mater., Aug. 2019.
- C. Rawlings, Yu Kyoung Ryu, Matthieu Rüegg et al., "Fast turnaround fabrication of silicon point-contact quantum-dot transistors using combined thermal scanning probe lithography and laser writing," Nanotechnology, Oct. 2018.
- F. Yesilkoy, V. Flauraud, M. Rüegg, B. Kim, and J. Brugger, "3D nanostructures fabricated by advanced stencil lithography," Nanoscale, Feb. 2016.
- C. Ruffert, Q. Ramadan, M. Rüegg, G. Vergères, and M. A. M. Gijs, "Integrated Microfluidic Chip for Cell Culture and Stimulation and Magnetic Bead-Based Biomarker Detection," Micro and Nanosystems, 2014.
- Samuel K. Sia, Matthieu Rüegg, Nalin Tejavibulya. Devices and systems for optically determining a concentration of an analyte in a living subject using hydrogel-based, fluorescent microneedles and methods of manufacture thereof. WO2016141307A1, Priority Date 2015-03-05
- Christopher Elliott, Marc-Eric Jones, Arushi Varshney, Matthieu Rüegg. Non-invasive blood analysis. US20160015301A1, EP2922468B1, Priority Date 2013-02-13

LANGUAGES

French: Native Proficiency

- -

English: Full Professional Proficiency

- -

German: Limited Working Proficiency

AWARDS

START Lausanne Contest, Lausanne, 2012
- Contest to raise money to create a start-up (team project).
- Qualification round: elevator pitch among the 10 best over 30 teams.
- Final round: realization of a business plan.

- -

International Contest of Applications in Nano-Micro Technologies, Beijing, 2011
- Contest to create a business idea using sensors (team project).
- 1st place in the Swiss qualification. Best Contribution Award in the final in Beijing.
- Design, fabrication and programming of an electronic device controller by arm movement detection.

INTERESTS

- Entrepreneurship
- Start-ups
- Triathlon
- Rock climbing
- Skiing